2012-03-01

Electron Microscopy Characterization of Vanadium Dioxide Thin Films and Nanoparticles

Felipe Rivera
Brigham Young University - Provo

Electron Microscopy Characterization of Vanadium Dioxide Thin Films and Nanoparticles

Felipe Rivera

A dissertation submitted to the faculty of
Brigham Young University
in partial fulfillment of the requirements for the degree of

Doctor of Philosophy

Richard R. Vanfleet, Chair
Robert C. Davis
Juliana Boerio-Goates
Branton J. Campbell
David D. Allred

Department of Physics and Astronomy

Brigham Young University

April 2012

ABSTRACT

Electron Microscopy Characterization of Vanadium Dioxide
Thin Films and Nanoparticles

Felipe Rivera
Department of Physics and Astronomy, BYU
Doctor of Philosophy

Vanadium dioxide (VO_2) is a material of particular interest due to its exhibited metal to insulator phase transition at 68°C that is accompanied by an abrupt and significant change in its electronic and optical properties. Since this material can exhibit a reversible drop in resistivity of up to five orders of magnitude and a reversible drop in infrared optical transmission of up to 80%, this material holds promise in several technological applications. Solid phase crystallization of VO_2 thin films was obtained by a post-deposition annealing process of a $VO_{x,x\approx 2}$ amorphous film sputtered on an amorphous silicon dioxide (SiO_2) layer. Scanning electron microscopy (SEM) and electron-backscattered diffraction (EBSD) were utilized to study the morphology of the solid phase crystallization that resulted from this post-deposition annealing process. The annealing parameters ranged in temperature from 300°C up to 1000°C and in time from 5 minutes up to 12 hours. Depending on the annealing parameters, EBSD showed that this process yielded polycrystalline vanadium dioxide thin films, semi-continuous thin films, and films of isolated single-crystal particles. In addition to these films on SiO_2, other VO_2 thin films were deposited onto a-, c-, and r-cuts of sapphire and on $TiO_2(001)$ heated single-crystal substrates by pulsed-laser deposition (PLD). The temperature of the substrates was kept at ∼500°C during deposition. EBSD maps and orientation imaging microscopy were used to study the epitaxy and orientation of the VO_2 grains deposited on the single crystal substrates, as well as on the amorphous SiO_2 layer. The EBSD/OIM results showed that: 1) For all the sapphire substrates analyzed, there is a predominant family of crystallographic relationships wherein the rutile $VO_2\{001\}$ planes tend to lie parallel to the sapphire's $\{10\bar{1}0\}$ and the rutile $VO_2\{100\}$ planes lie parallel to the sapphire's $\{1\bar{2}10\}$ and $\{0001\}$. Furthermore, while this family of relationships accounts for the majority of the VO_2 grains observed, due to the sapphire substrate's geometry there were variations within these rules that changed the orientation of VO_2 grains with respect to the substrate's normal direction. 2) For the TiO_2, a substrate with a lower lattice mismatch, we observe the expected relationship where the rutile VO_2 [100], [110], and [001] crystal directions lie parallel to the TiO_2 substrate's [100], [110], and [001] crystal directions respectively. 3) For the amorphous SiO_2 layer, all VO_2 crystals that were measurable (those that grew to the thickness of the deposited film) had a preferred orientation with the the rutile VO_2 [001] crystal direction tending to lie parallel to the plane of the specimen. The use of transmission electron microscopy (TEM) is presented as a tool for further characterization studies of this material and its applications. In this work TEM diffraction patterns taken from cross-sections of particles of the a- and r-cut sapphire substrates not only solidified the predominant family mentioned, but also helped lift the ambiguity present in the rutile $VO_2\{100\}$ axes. Finally, a focused-ion beam technique for preparation of cross-sectional TEM samples of metallic thin films deposited on polymer substrates is demonstrated.

Keywords: vanadium dioxide, electron microscopy, SEM, TEM, FIB, focused ion beam, thin films, characterization

ACKNOWLEDGMENTS

This work could not have been completed without the help of many, many people in different groups and throughout various geographic locations.

From my graduate committee I would first like to express a great deal of appreciation to my research advisor, Dr. Richard Vanfleet, who has given of his time, support, and guidance and has made use of his personal acquaintances to help me succeed in this project. He has proven to be quite patient, very understanding, exceedingly supportive, and an excellent mentor, and for that I feel truly thankful. I am also grateful to: Dr. Robert C. Davis for his persistent, careful attention to this project, for his counsel, and useful insights; to Dr. Branton J. Campbell, for providing useful instruction, availability, and quite useful software resources and an excellent understanding of the "inside-outside, upside-down, backwards space;" to Dr. David D. Allred and Dr. Juliana Boerio-Goates for their sound "down-to-earth" research advice to expedite the completion of this work. As a committee, these people have indeed helped me to make this research possible.

This research would not have taken place without various collaborators and researchers who not only provided samples for analysis, but also their expertise. Dr. Kevin Coffey of the University of Central Florida, and Dr. Richard Haglund and Dr. Joyeeta Nag from Vanderbilt University whose expertise in deposition proved significantly helpful in obtaining high quality vanadium dioxide crystalline films on various substrates. Dr. Jeffrey Farrer of Brigham Young University, who provided the necessary training, expertise, and troubleshooting for the electron microscopes used. There were also several undergraduate students to whom I am indebted, namely: Laurel Burk, from the University of Nebraska at Lincoln; Michael Miller, from the University of California, Los Angeles; Brady Cox and Michael Rawlings, from Brigham Young University; and Carol Chase from Brigham Young University, Hawaii. All of whom took the time to learn the intricacies of electron microscopy and sample preparation, and as a consequence allowed me to learn a from their successes and struggles.

I would further like to thank Michael Clemens and Hiram Conley both of whom were invaluable assets in performing Atomic Force Microscope electrical measurements. The help obtained from many of these wonderful students would not have been possible without the funding provided by the NSF-REU program in the Physics and Astronomy Department at BYU.

The funding and facilities for this research were provided by the Physics and Astronomy Department at Brigham Young University. Additional funding was also provided by a Graduate Fellowship Grant from Brigham Young University's Office of Research and Creative Activities Proposal No.161010. Additional funding provided by *Millenniata, Inc.* and *Moxtek, Inc*.

Most of all, I would like to thank my beloved and beautiful wife, Nancy Rivera, for her encouragement which empowered me to pursue graduate education, and for her formidable patience, love, and continuing reassurance all these years, and for her motivational encouragement during my final year. Also my children, Felipe, Cassandra, Carolina, Samantha, and Viviana, who, unknowingly, gave me that extra drive to complete this work. And to my parents, who have constantly supported, encouraged, and motivated me. Though I cannot name every single person that has given me their support, I would like to extend my gratitude to my relatives, friends, teachers, and mentors who have also given me of their support.

Contents

List of Figures

List of Tables

Chapter 1

An Overview to this Work

For several decades electron microscopy has helped further the study and understanding of materials. Just over 50 years from Richard Feyman's lecture[1] "There is Plenty of Room at the Bottom,"[†] electron microscopy has allowed the study of many materials down to the atomic level with resolving power in the order of angstroms. In these short decades, these advances in microscopy have also allowed a wider observation of how the properties of materials change as their size shrinks, including interesting physical phenomena observed in a wide range of materials.

As an example, some transition metal oxides exhibit phase transitions and varied electronic behavior,[2–7] and recently there has been an effort to use the properties of these materials in novel applications.[5,8–18] One such material of particular interest is Vanadium Dioxide (VO_2). This interest is due to its exhibited metal to insulator phase transition at 68°C that is accompanied by an abrupt and significant change in its electronic and optical properties.

In this work, several scanning electron microscopy techniques were employed to study and characterize thin films of vanadium dioxide thin films and nanoparticles, and also explores the use of transmission electron microscopy for the study of VO_2. This work also introduces a method

[†] Arguably, this lecture gave birth to the modern field of nanotechnology with its "invitation to enter a new field of physics".[1]

through which TEM samples of metallic thin films deposited on polymer substrates may be prepared with the use of a focused ion beam.

Chapter 2 gives an introduction to some of the known properties exhibited by VO_2. From the stoichiometry of related vanadium oxides, to the properties exhibited during the phase transition of crystalline VO_2. Further, several methods used to characterize these properties are introduced, as well as common methods currently used to obtain crystalline VO_2 thin films.

This is then followed by a broad overview to electron microscopy in chapter 3 wherein interactions between an electron beam and a samples are presented and how these interactions may be used to analyze materials. The basics of scanning electron microscopy and transmission electron microscopy are described. This chapter also includes a description of the use of focused ion beams as a tool for imaging, analysis, and sample preparation for TEM.

The bulk of the work on VO_2 is presented in chapters 4 and 5 wherein several scanning electron microscopy techniques are employed to study the morphology of vanadium dioxide thin films. In chapter 4, scanning electron microscopy (SEM) is used to image the morphology of vanadium dioxide thin films that were crystallized by a method called solid phase crystallization, while electron backscattered diffraction (EBSD) is used to verify crystallinity. These samples start from amorphous $VO_{x,x\sim2}$ films deposited onto amorphous SiO_2 obtained from the University of Central Florida. While observed morphological changes are imaged through (SEM), there are several observed limitations to the use of EBSD for verification of the crystallinity of the resulting particles. Within the observed limitations from chapter 4, the use of EBSD is further used in chapter 5 to generate EBSD maps for orientation imaging microscopy (OIM). In chapter 5 OIM is performed not only in some of the samples mentioned in chapter 4, but also in additional samples provided by Vanderbilt University deposited on various substrates including several cuts of single-crystal sapphire and c-cut single-crystal TiO_2. The preferred orientation(s) of VO_2 grains onto these various substrates is presented here. The work included here on the orientation of VO_2 grains on SiO_2

substrates has been published in Thin Solid Films,[19] while the work on the orientation of VO_2 grains on the sapphire and TiO_2 substrates has been submitted for publication to Physical Review B (Feb 2012).

Chapter 6 furthers the use of electron microscopy by showing some results from transmission electron microscopy (TEM) in the study of VO_2. Within this chapter some imaging and analytical techniques are shown including selected area transmission electron diffraction (SAED) and electron energy-loss spectroscopy (EELS).

Since TEM techniques are applicable to a wide range of materials, TEM work was done on additional metallic films deposited on polymer substrates. Chapter 7 covers separate work in which some analytical TEM techniques were applied to a variety of separate samples obtained from two local companies. Considering that TEM sample preparation for samples on polymers is non-trivial, in this chapter, a focused-ion beam technique for preparation of cross-sectional TEM samples of metallic thin films deposited on polymer substrates is demonstrated. This method for cross-sectional TEM sample preparation of metallic thin films deposited polymers has been submitted for publication in Microscopy and Microanalysis (Feb 2012)*.

All the results reported in this work have been presented (in sections) at both regional and national conferences.

*This sample preparation method was utilized in a published study of the thin metallic films that comprised the reflective layers on various archival-grade DVDs[20,21]

Chapter 2

A Primer on the Properties of Vanadium Dioxide

Several transition metal oxides form a wide range of materials in which to explore interesting physical phenomena. Some of these oxides exhibit phase transitions and varied electronic behavior that are widely observed in condensed matter physics.[2–7] Even though the study of these materials has been taking place for several decades, recently there has been an effort to use the properties of these materials in novel applications as well as to understand the underlying phenomena observed in these materials.[5,8–18]

One property of interest is insulator to metal phase transitions. This type of property describes a material that can (depending on certain parameters) behave as either an insulating material or a conductive one. Vanadium is one such transition metal. In fact, vanadium has several oxides that undergo a metal-to-insulator transition (MIT)[†] at some characteristic temperature.[2,3,22]

There are several transition metal oxides that show metallic properties.[4] These metallic properties have been modeled and are often attributed to the 3d electron orbitals forming a narrow

[†]Also referred to as a semiconductor-to-metal transition (SMT)

conductive band.[2,4] However, in the case of vanadium dioxide, and despite the work that has been done on this material, the nature of the phase transition still is very much debated.[11,23–29]

2.1 Vanadium and its oxides

Vanadium is a transition metal with several oxides that undergo a metal-to-insulator transition at some characteristic temperature.[2,30] The reason for these many oxides can be attributed, in part, to the many varied valence states of Vanadium. As a consequence, the synthesis of vanadium dioxide is a non trivial matter since the valence states of vanadium allow it to have various oxide stoichiometries all with different properties. Even when vanadium may be found in a single valence state in oxides such as VO, V_2O_3, VO_2 and V_2O_5 (where the valence state is V^{2+}, V^{3+}, V^{4+}, and V^{5+} respectively),[3] a wide variety of mixed valence oxides also exist.[3,22] Interestingly enough, the vanadium to oxygen ratio affects the structure and the properties of the material greatly. For example, C. Hébert reports that, "VO is a metal with rock-salt structure. V_2O_3 is in a paramagnetic metallic phase with corundum structure (α–Al_2O_3) above 165 K and an anti-ferromagnetic insulator with monoclinic structure below 165 K. VO_2 undergoes a first order transition from a diamagnetic semiconductor phase below 340 K to a paramagnetic metallic state with rutile structure above 340 K. V_2O_5 is a diamagnetic insulator at room temperature with orthorhombic structure."[3]

The phase diagram for the vanadium – oxygen system shows various oxide stoichiometries that vanadium may undertake. Figure 2.1 shows the V–O phase diagram and emphasizes the region encompassing from VO up to and including V_2O_5 showing not only the homogeneous phases mentioned above and the intermediate Magnéli phases corresponding to the series V_nO_{2n-1},[31] but also the mixed-phase regions.[8,32–36]

The change in electrical conductivity was first used to study the metal-to-insulator phase transition in different materials. Thus, the conductivity of various vanadium oxides have been studied

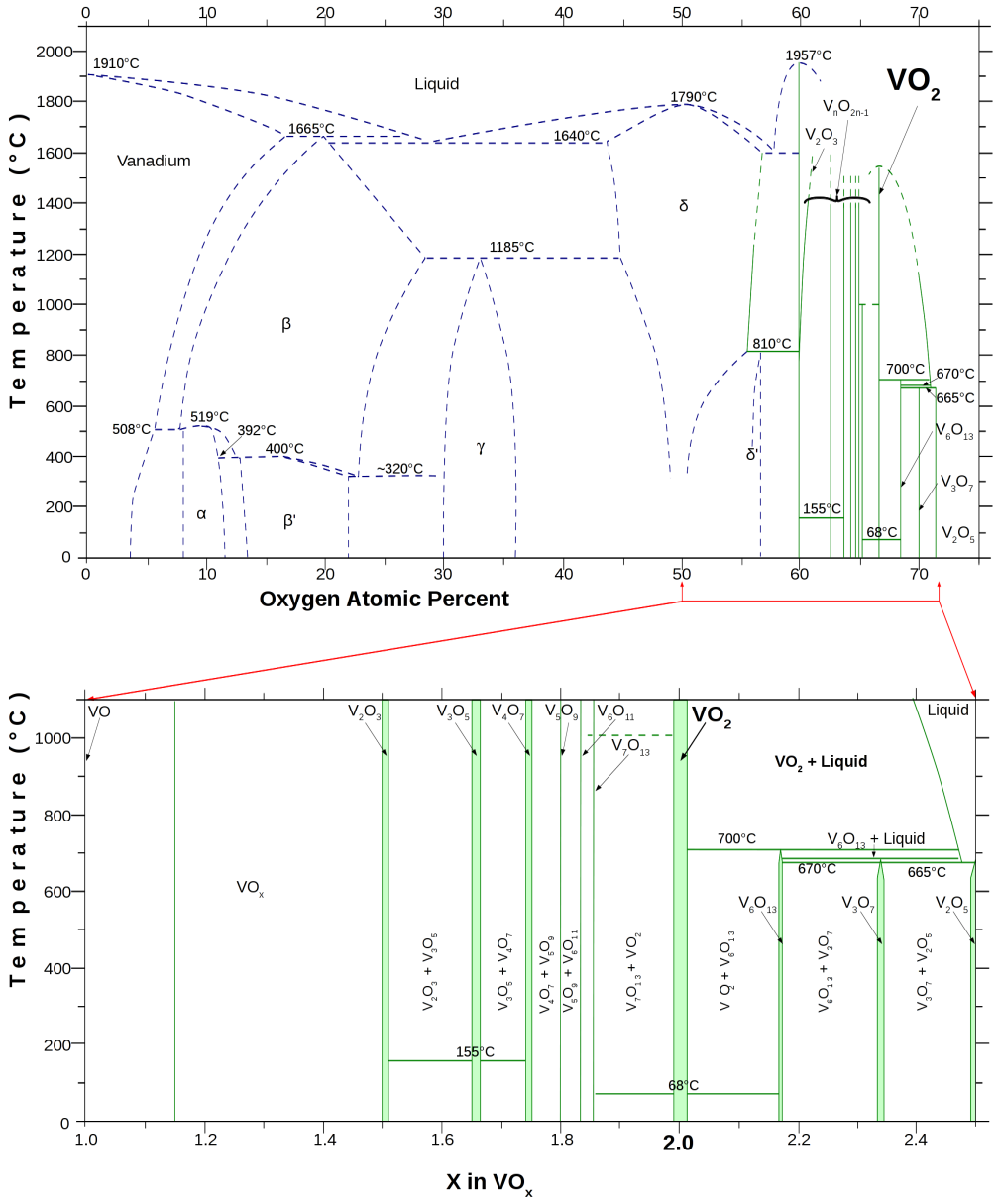

Figure 2.1 Phase diagram of the vanadium – oxygen system. Compiled from the *Binary Alloy Phase Diagrams (1990)*[35] second edition, and other references.[8,32–34,36] The region encompassing from VO to V_2O_5 has been expanded to emphasize the intermediate Magnéli phases corresponding to the series V_nO_{2n-1}. and the mixed-phase regions in the V–O system.

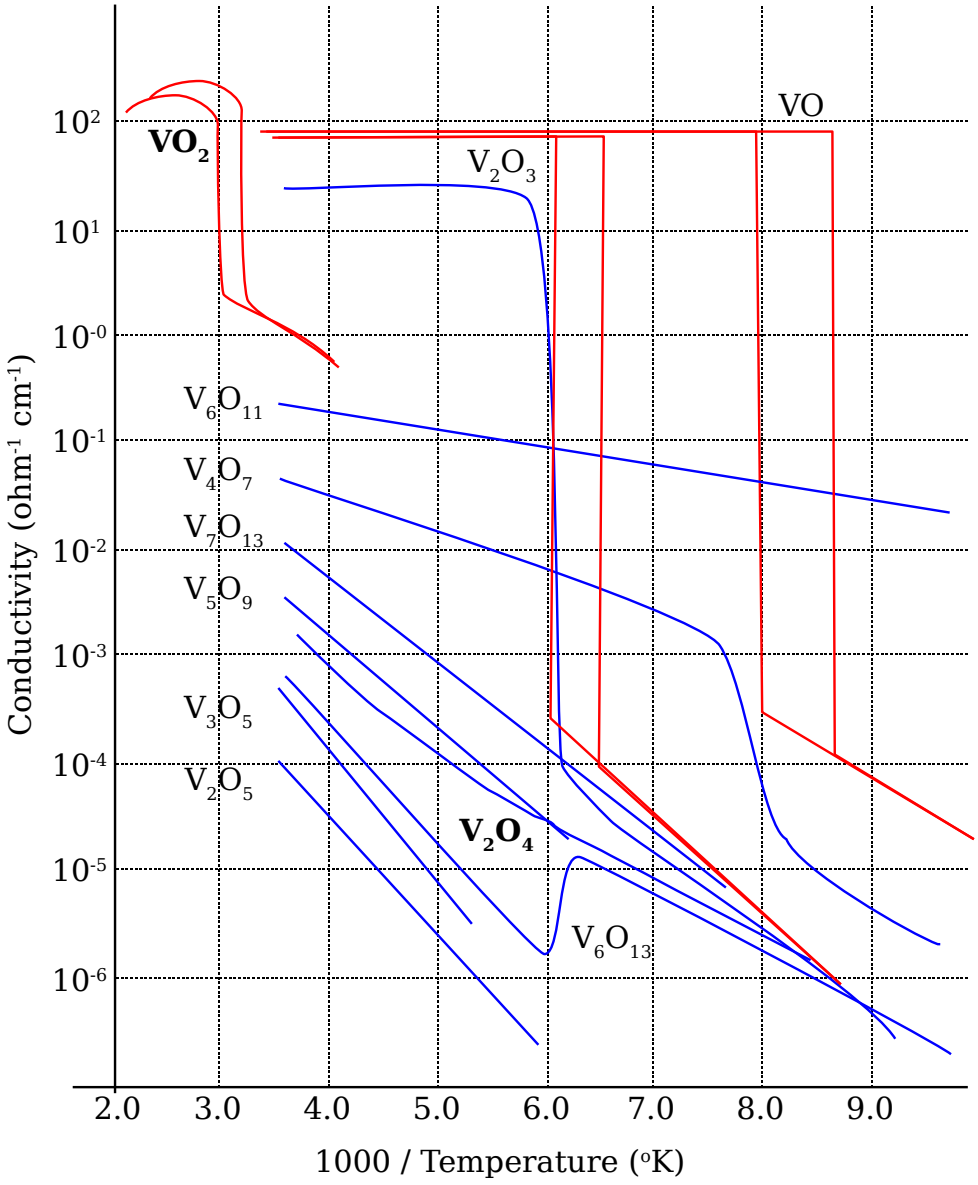

Figure 2.2 Conductivity as a function of reciprocal temperature for varied vanadium oxides, including V_2O_3, V_3O_5, V_4O_7, V_5O_9, V_6O_{11}, V_7O_{13}, V_2O_4, V_6O_{13}, and V_2O_5. These conductivities were reported in 1959 by Morin[2] (in red) and in 1963 by Kachi.[22] Notice there is an entry for VO_2 reported by Morin and one for V_2O_4 as reported by Kachi. Though the phase transition for VO_2 is not as dramatic as the transitions for VO or V_2O_3, it still exhibits a conductivity change of several orders of magnitude.

since the initial report performed by Morin in 1959.[2] It was observed that slight deviations in the vanadium to oxygen ratio greatly changed the properties of the material. In addition to the vanadium oxides studies by Morin in 1959,[2] Sujeki Kachi performed a study in 1963[22] on the electrical conductivity of V_2O_3, V_3O_5, V_4O_7, V_5O_9, V_6O_{11}, V_7O_{13}, V_2O_4, V_6O_{13}, and V_2O_5. These stoichiometries are slight variations in the vanadium to oxygen ratio, yet their electrical properties are remarkably different. Figure 2.2 qualitatively summarizes the differences in electrical conductivity found in the studies performed by Morin (1959) and Kachi (1963).[2,22] The figure shows eleven vanadium oxides with stoichiometries that vary from a 2:2 vanadium to oxygen ratio (VO) to a 2:5 vanadium to oxygen ratio (V_2O_5). Phase transitions are evident for VO, V_2O_3, and VO_2.

Variations in the oxidation states of vanadium not only have an effect in the electrical conductivity of the material, as figure 2.2 qualitatively shows, but these materials also exhibit different magnetic properties, and some (not all) do show metal to insulator transitions.[22,37–39]

Different crystal structures for selected VO_x

In addition to the different conductivities measured by Morin and Kachi, another aspect that distinguishes between different stoichiometries of the known vanadium oxides is their crystal structure. Table 2.1 shows the different lattice parameters between different stoichiometries in several vanadium oxides at room temperature. Some of these differences can be observed in the diagrams of their crystal structures shown in figure 2.3.

The synthesis of vanadium dioxide is non-trivial due to the many possible oxides. As shown in figure 2.1, the phase diagram of the V-O system contains over twelve different phases between VO and V_2O_5, including the homogeneous phases and the intermediate Magnéli phases.[8,31,33,34,36,41–43] Despite these difficulties (and to our benefit) the remarked distinctions (structurally and electrically) between the various oxides help to determine the quality of the material produced by a specific process.

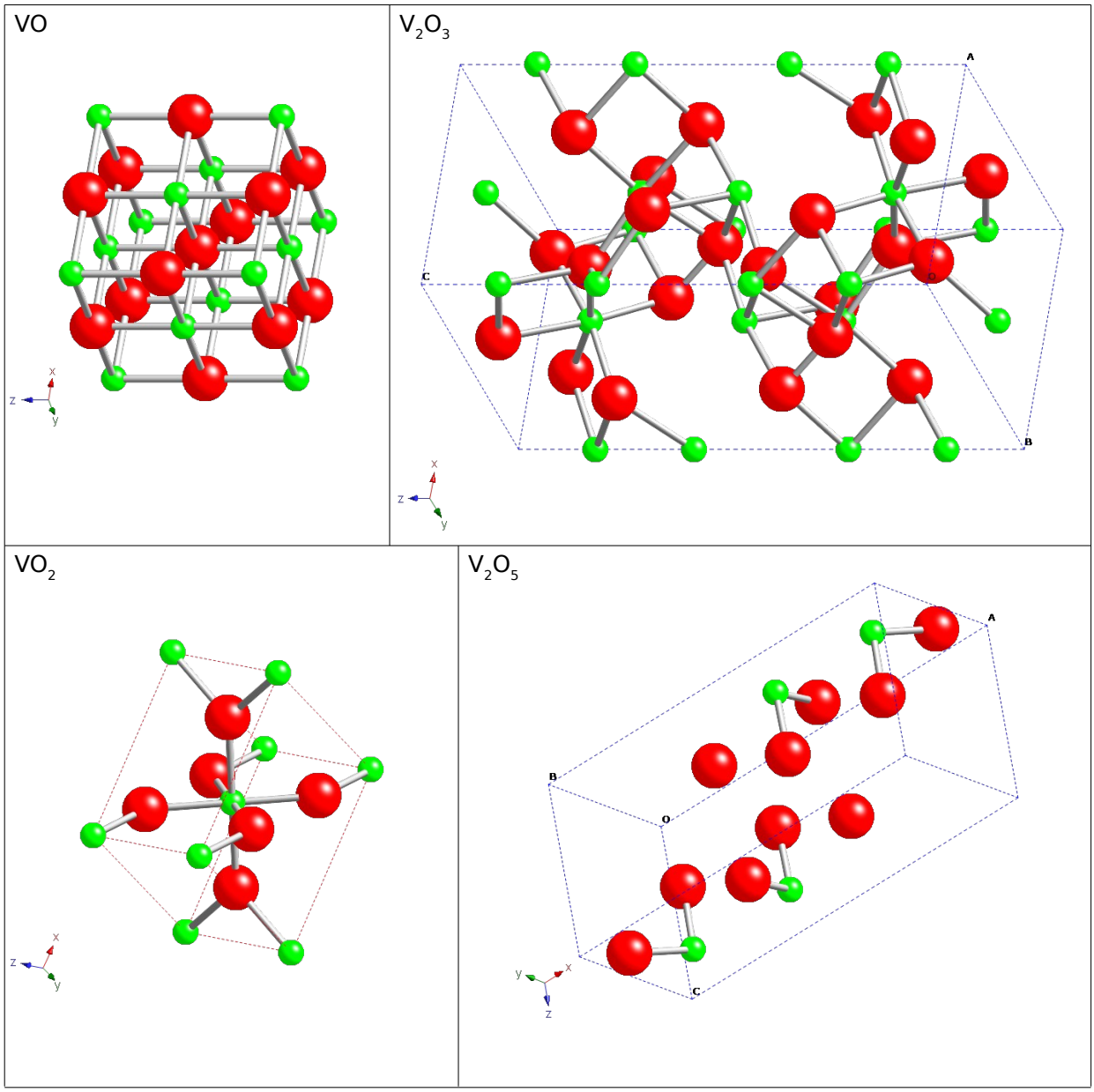

Figure 2.3 Crystal Structures for VO, V_2O_3, VO_2, and V_2O_5. The vanadium dioxide structure modeled corresponds to the high temperature tetragonal structure.[31,33,34,36,40–44] Changes in the vanadium to oxygen ratio affect the crystal structure.

Material	$a1$ (Å)	$a2$ (Å)	$a3$ (Å)	α	β	γ
VO	4.120	4.120	4.120	90.0	90.0	90.0
V_2O_3	4.978	4.978	13.965	90.0	90.0	120.0
VO_2	5.753	4.526	5.383	90.0	122.6	90.0
V_2O_5	10.011	3.564	4.368	90.0	90.0	90.0

Table 2.1 Lattice Parameters for known crystal structures of several vanadium oxides at room temperature.[31,33,34,36,40–44]

2.2 Properties specific to vanadium dioxide

Out of all of the different stoichiometries of VO_x, vanadium dioxide (VO_2) has been a material of particular interest since the observation of its phase transition by F. Morin in 1959.[2] In his paper, Morin reported the conductivity and phase transitions for VO, VO_2, V_2O_3 and two other transition metal oxides. The reported change in conductivity during the transition for crystalline VO_2 is not as dramatic as that for VO or V_2O_3. However, crystalline VO_2 still exhibits a reversible resistivity change of several orders of magnitude.* Furthermore, one of the compelling aspects that makes vanadium dioxide (VO_2) interesting to study (over the other vanadium oxide stoichiometries) is the temperature of its transition and its accompanying hysteresis. 340 K ($\approx 68^{\circ}$C)[23,30,45] is a temperature easy to achieve, and this allows the use of many probing techniques to study the material as the metal–to–insulator transition takes place.

In single crystals, vanadium dioxide undergoes significant, abrupt, and reversible changes in several of its properties during its phase transition. These changes to its properties include: 1) A structural change from a low temperature semi-conducting monoclinic phase to a high-temperature tetragonal metallic phase; 2) a resistivity change of several orders of magnitude; and 3) a sharp

*Figure 2.2 summarizes some of the results obtained by Morin as well as other results obtained by Kachi.

change in optical transmittance in the infrared region. Furthermore, as seen in figure 2.2, there is an associated hysteresis with the metal-to-insulator transition in VO_2 wherein a bi-stable temperature regime exists. These optical and electronic properties, as well as the associated hysteresis, that vanadium dioxide exhibits due to its phase transition hint at the use of this material for optical[46–50] and electronic[51,52] applications, such as thermochromic coatings for windows, fast optical and electronic switches, or thermal sensors.

The synthesis of high-quality vanadium dioxide is not a trivial matter due to the many oxidation states available for vanadium (as discussed in section 2.1 and shown in figure 2.1). Nonetheless, different methods have been used to successfully produce high-quality vanadium dioxide thin films[†].[45] The quality of these deposited films has been determined by examining some of the properties that are characteristic of vanadium dioxide such as conductivity, IR transmittance/reflectance, crystal structure, transition temperature[‡], and others.[2,46,47,51,52,52–56]

2.2.1 Crystal structure change during the phase transition

In single crystals, vanadium dioxide (VO_2) undergoes a structural phase transition near 68°C. Structurally, VO_2 shifts between a low temperature low-symmetry monoclinic structure[§] to a high temperature, higher-symmetry tetragonal structure.[3,53–55] Table 2.2 shows three of the documented structures for VO_2. The lattice parameters for these three structures were found in the Inorganic Crystal Structure Database (ICSD),[40] along with other references.[8,31,33,34,36,41–44,57–60]

Since the electronic band structure of a material is dependent on the crystal structure, a change

[†] See Section 2.5

[‡] Naturally, a change in one of these properties at, or near, the transition temperature is often quoted as an indicator of the quality of the VO_2 crystals produced. Nevertheless, this is not always the case, sometimes, the crystal structure is used as the determining factor to determine the quality of the VO_2 crystals produced.

[§] The monoclinic structure of vanadium dioxide can be altered by other factors such as stress, and doping. However, this tetragonal structure seems to be well accepted.

Tetragonal T> 68°C	Monoclinic T< 68°C	Monoclinic Stressed T< 68°C
4.55350 Å $a1$	5.38250 Å $a3$	4.52550 Å $a3$
4.55350 Å $a2$	4.52630 Å $a2$	9.06640 Å $a1$
2.84940 Å $a3$	5.75290 Å $a1$	5.79700 Å $a2$
$\alpha = 90°$	$\beta = 122.8°$	$\gamma = 90°$
$\beta = 90°$	$\alpha = 90°$	$\alpha = 90°$
$\gamma = 90°$	$\gamma = 90°$	$\beta = 91.88°$

Table 2.2 Lattice Parameters from three known VO_2 crystal structures.[8,36,40,44,57–60] The order is such as to show the corresponding change in the lattice parameter as the transition takes place.

in the crystal structure comes with a change in the band structure. These crystal structures have been studied and modeled in attempts to explain the nature of the transition.[23–25] The computational models show changes in the band structure of VO_2 as the transition takes place.[¶] Though the nature of the transition in VO_2 still is under debate, the theoretical studies have shed light on the band structure, Fermi levels, band gap, and electronic properties of the material.[23–25]

The knowledge of the crystal structure allows for the use of scattering techniques (such as x-ray diffraction) to probe the transition of crystalline vanadium dioxide.[53–55,61] Figures 2.4, 2.5, and 2.6 show some of the structural differences between three known phases in vanadium dioxide as seen from three different directions (100, 010, and 001 of the tetragonal phase respectively).[‖]

As seen from the figures the overall changes may be subtle, however, some of the differences are significant enough that scattering experiments are used to observe the phase transition.[53,54] As the VO_2 crystals transition from the high-temperature tetragonal (R) phase to the low-temeprature

[¶]Unfortunately, many of the computational models are unable to obtain a band gap at the Fermi level in the monoclinic structure.[25]

[‖]A useful tool that helps model the phase transition is isodisplace.[62] See appendix B

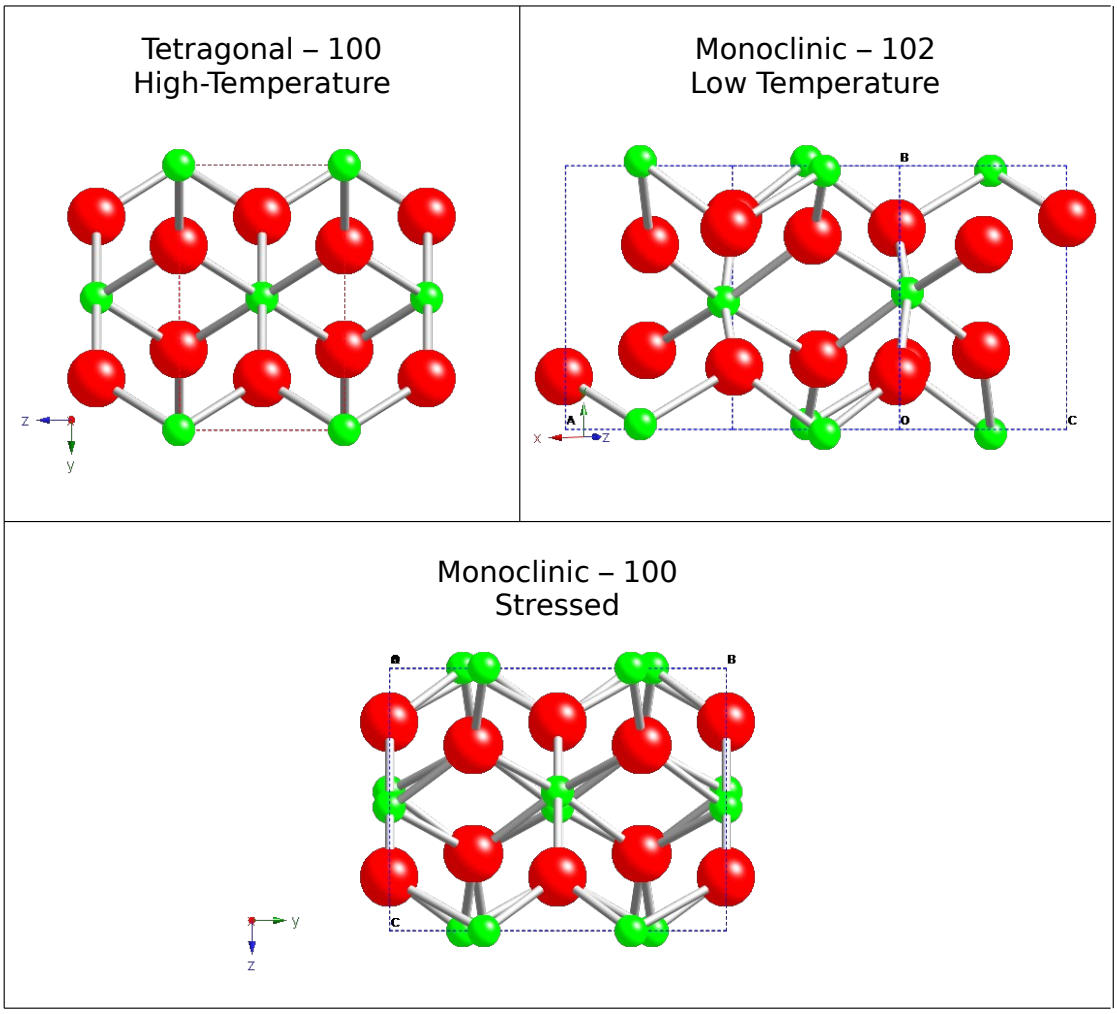

Figure 2.4 Comparison of three known vanadium dioxide structures. The monoclinic structures are oriented in such a way as to correspond with the 100 view of the tetragonal phase

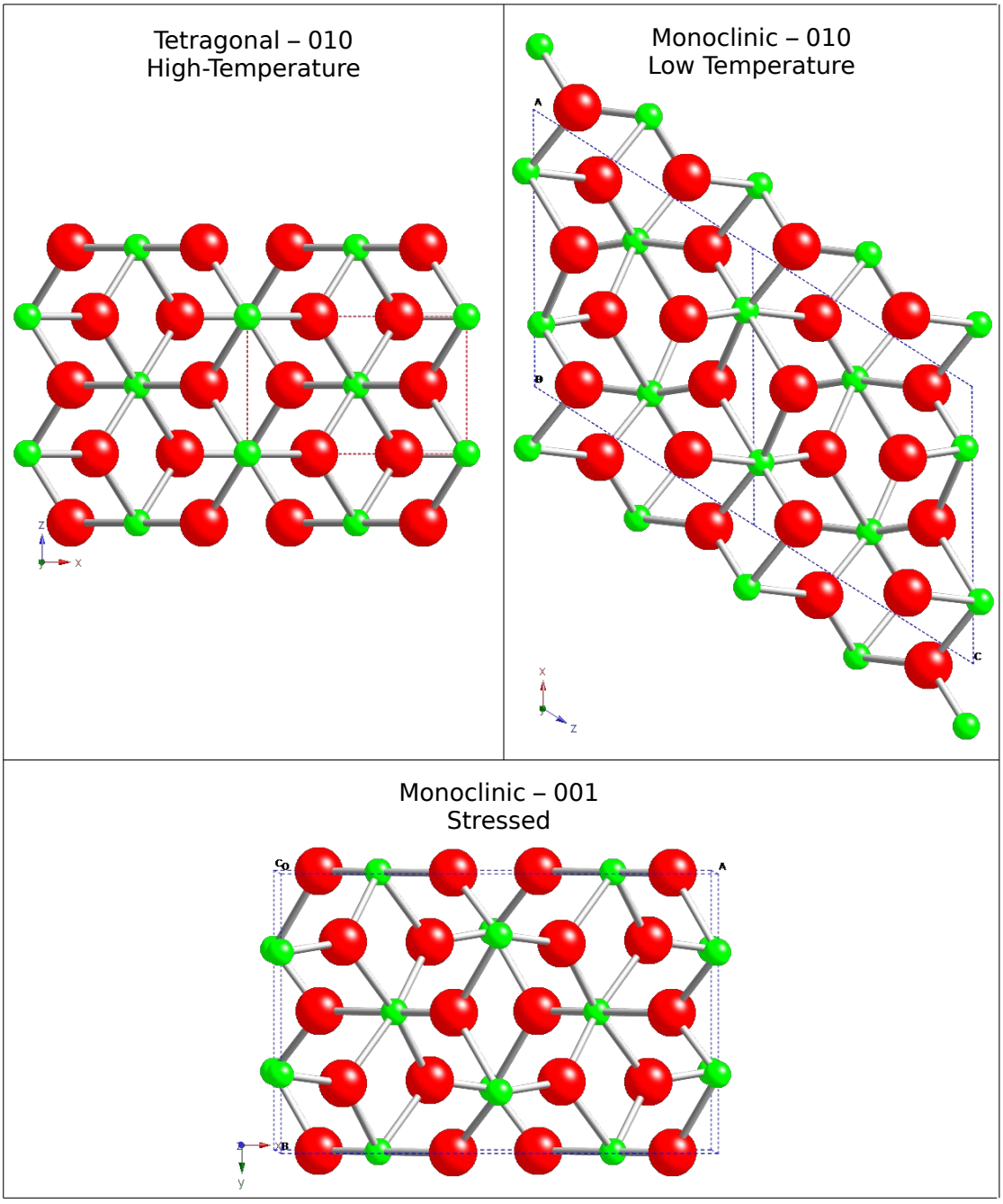

Figure 2.5 Comparison of three known vanadium dioxide structures. The monoclinic structures are oriented in such a way as to correspond with the 010 view of the tetragonal phase

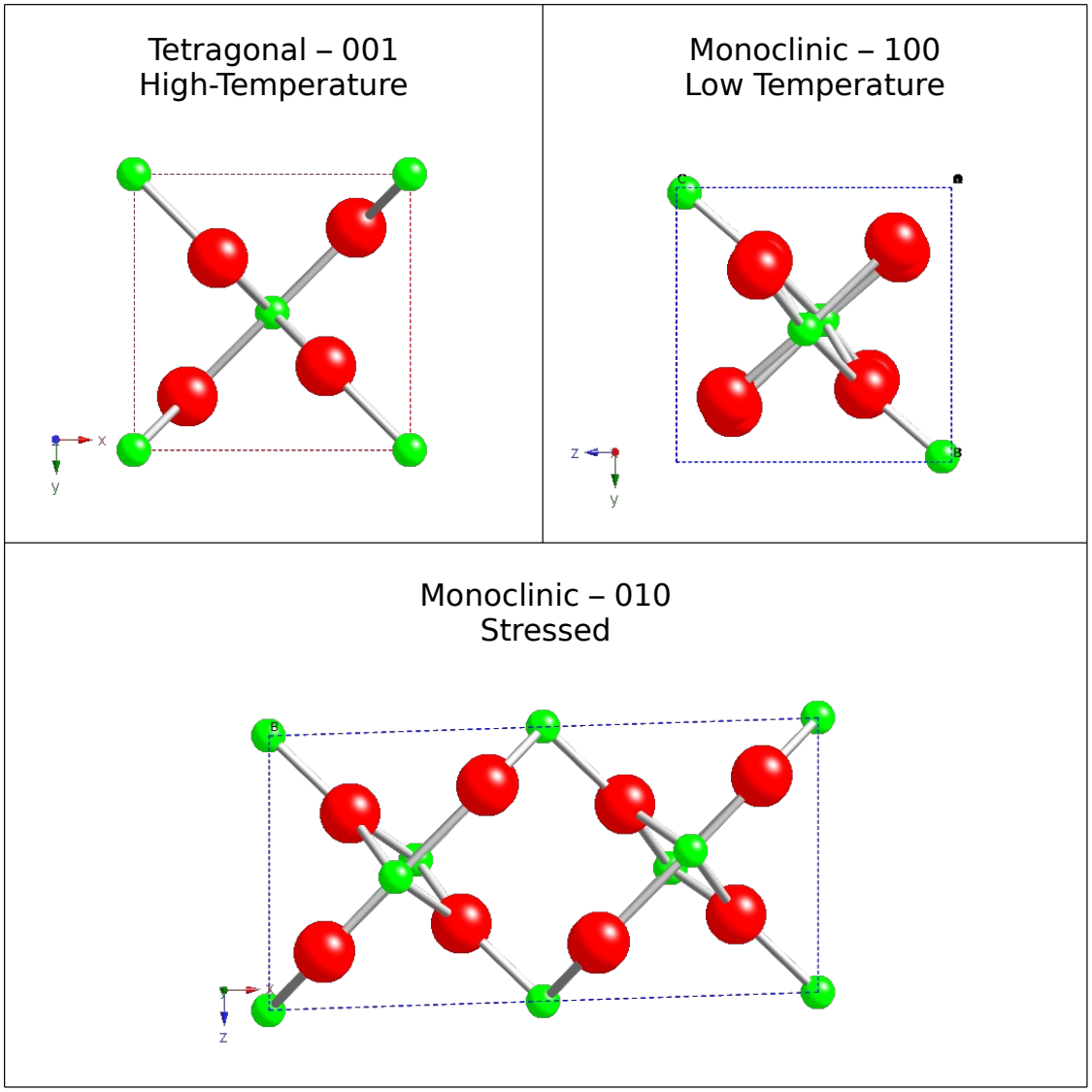

Figure 2.6 Comparison of three known vanadium dioxide structures. The monoclinic structures are oriented in such a way as to correspond with the 001 view of the tetragonal phase

monoclinic (M1) phase there is a 0.94% expansion along the c-axis (of the rutile phase) accompanied with an a and b-axes contraction of 0.42% and 0.59% respectively. The break in symmetry takes place along a and c-axes of the rutile phase where the atoms move from being collinear along these axes to being staggered along these directions. Further, the spacing between the vanadium atoms along the rutile a-axis now alternates between 4.836 Å and 4.258 Å, while the atoms along the rutile c-axis alternate between 2.602 Å and 3.190 Å. This staggering doubles the unit cell along these directions. A diagram of the subtle differences in the position of the vanadium atoms, as well as the overall deformation of a VO_2 tetragonal frame, is shown in figure 2.7. This figure shows the positions of the vanadium atoms in the monoclinic (M1) phase (in white) relative to the positions of the vanadium atoms in the tetragonal (R) phase, as well as the deformation that the tetragonal unit cell undergoes.

2.2.2 Electrical conductivity change during the phase transition

The original observation where vanadium dioxide underwent a metal to insulator phase transition was done by electrical conductivity[2] (see figure 2.2). Below the 68°C transition temperature crystalline VO_2 is found in a semiconducting phase. However, above the transition temperature crystalline vanadium dioxide exhibits a change wherein resistivity drops by as much as 5 orders of magnitude** as it transitions into the metallic phase.[46,51,63] Though the change in electrical conductivity is a rather dramatic change that is easily observable, other electrical changes (such as a change in capacitance) may also be observed.[52]

**Figure 2.2 shows an electrical conductivity change of 2 orders of magnitude. This difference is attributed to grain boundaries, percolation effects and polycrystallinity.[46,51,63]

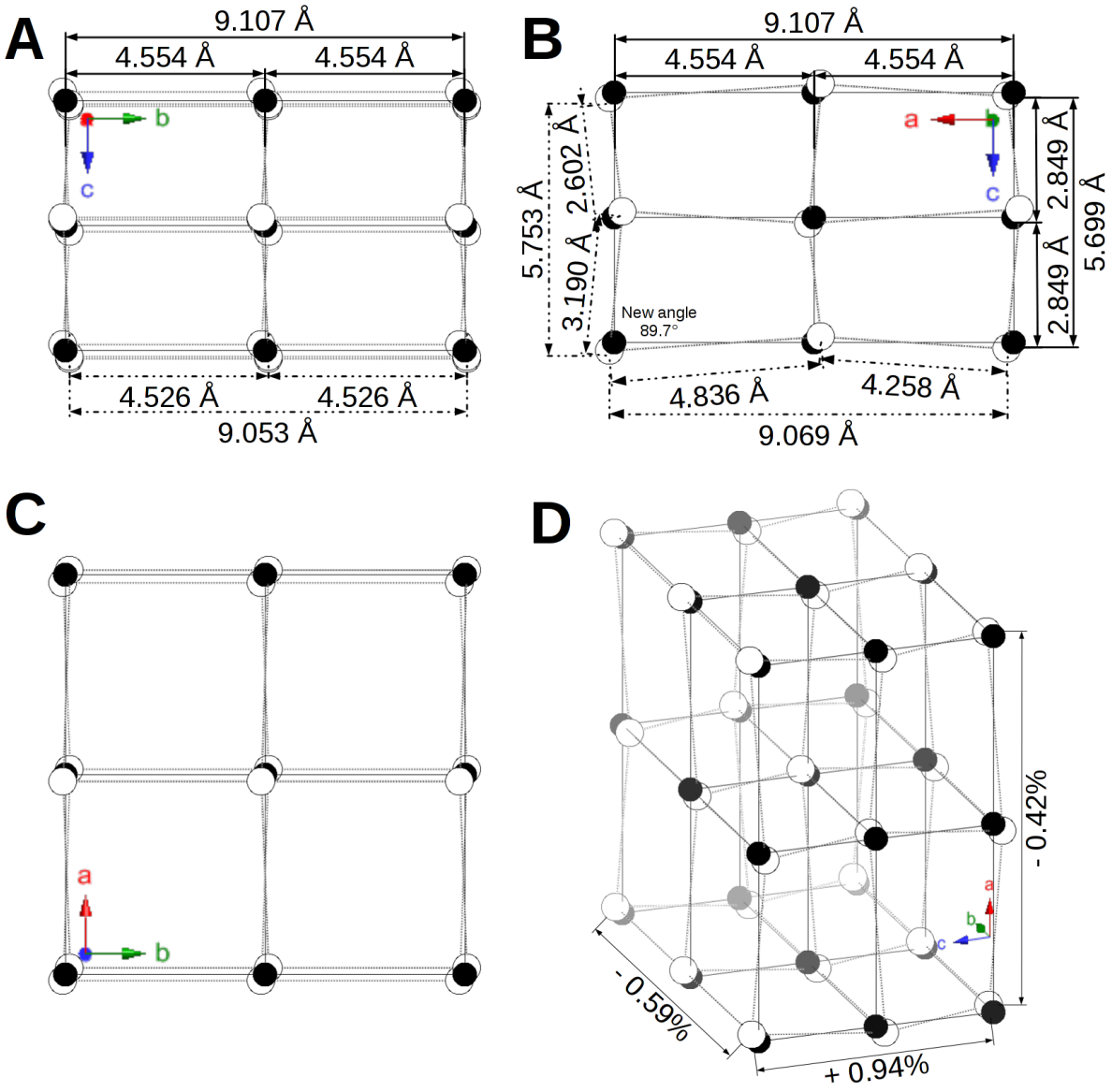

Figure 2.7 Diagram of the positions of the vanadium atoms in the high-temperature VO_{2-R} (black) and low-temperature VO_{2-M1} phases. The diagram shows the structural deformation in the tetragonal frame of $2 \times 1 \times 2$ unit cells of the high-temperature rutile VO_2 phase during the phase transition looking down along the respective (a,b,c) crystal directions of the tetragonal phase and (d) overall view of the deformed cells. The solid black circles and lines represent the reference positions of the vanadium atoms in the high-temperature rutile structure. The axis labels correspond to the rutile VO_2 phase. The white circles represent the new positions for those respective vanadium atoms in the monoclinic phase.

2.2.3 Optical changes during the phase transition

As vanadium dioxide single crystals transition from a semiconducting to a metallic phase the electronic configuration of the material changes, and just as there are changes in the conductivity of the material, there are also significant changes in the material's optical properties. The optical properties of vanadium dioxide began to be studied shortly after Morin's 1959 paper.[2] H. W. Verleur reported in 1968 the optical transmission and the optical constants of 100 nm polycrystalline thin films[††] and single crystals of VO_2 using photon energies from .25 eV to 5 eV.[46]

Figure 2.8 shows the transmission versus temperature for light at 0.31 eV, with the dotted line showing the expected transmission values based on measured resistivity[†] of the film as reported by Verleur. As seen from the figure, as the film transitions from its low-temperature semiconducting phase to its high-temperature metallic phase the film becomes opaque showing a drop in infrared transmission of upto 80%.

Notice that this work by Verleur also was one of the first to hint at differences between the optical and electrical measurements in thin VO_2 films. The dotted line in figure 2.8 is the expected optical IR transmission calculated from resistivity measurements made on the same film[†], however, the film began to drop in IR transmission at a lower temperature than expected. Recently, this observed difference between the electrical and optical behavior has recently been attributed to the polycrystallinity of the film, percolation effects, grain boundaries, and grain size effects.[46,51,56,63]

This change in the relative transmittance of VO_2 thin films is more easily observed in the infrared region,[47–50,64–66] and has been used to study the hysteresis and speed of the transition. It is interesting to note that this optical change during the phase transition of VO_2 has been timed to take place in the sub-pico second regime by using optical pulse-probe techniques.[64,66]

[††] Films deposited on sapphire and rutile (TiO_2) substrates by reactive sputtering.

[†] The films showed a reported resistivity change of $\Delta\rho \sim 10^4$.

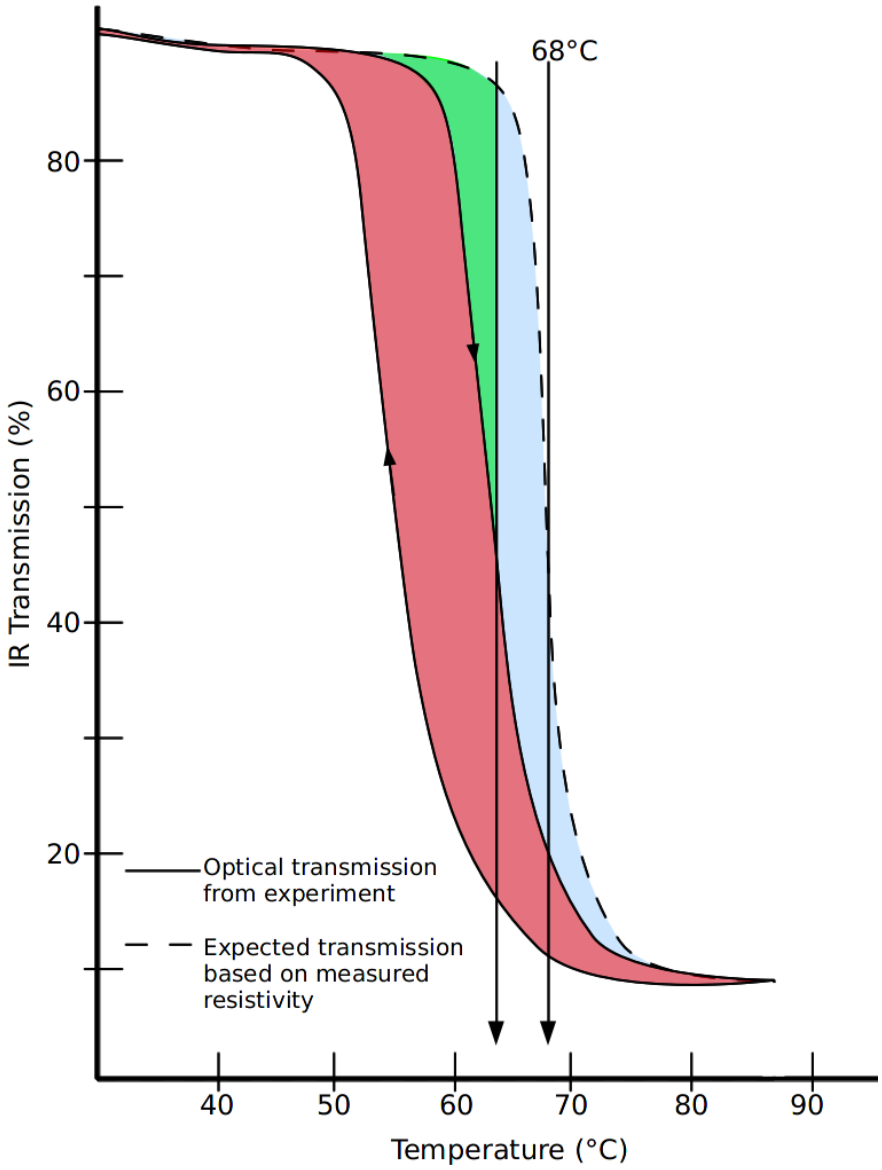

Figure 2.8 Optical transmission of a 100 nm VO_2 thin film compared with the expected transmission based on the measured thin film resistivity.
$h\omega = 0.31eV$. Reported by H. W. Verleur, Bell Labs (1968).[46]

2.3 Methods used for the characterization and differentiation of the different phases of VO_2.

There are various methods used to obtain vanadium dioxide thin films deposited on a variety of substrates (see section 2.5). Since the deposition of vanadium dioxide thin films is no trivial matter (see figure 2.1 and sections 2.1 and 2.5) it is imperative to determine the quality of the films produced. Naturally, these methods make use of the properties that set vanadium dioxide apart from the other stoichiometries of vanadium oxides (see section 2.2). Though there are several methods employed to determine the quality of vanadium dioxide thin films, these can be categorized in three main groups: 1) Methods that rely on the crystal structure of vanadium dioxide; 2) Methods that rely on the oxidation state of vanadium; and 3) Methods that can observe the metal-to insulator phase transition that vanadium dioxide undergoes.

2.3.1 Methods of characterization based on the crystal structure change during the phase transition

As mentioned in section 2.2.1, the room-temperature state of crystalline vanadium dioxide is a monoclinic structure. This structure changes to a tetragonal structure at a higher temperature[‡‡]. With the knowledge of the crystal structure, diffraction experiments may be conducted to help determine the quality of the resulting films. Diffraction methods constitute X-Ray Diffraction, Neutron Diffraction, and Electron Diffraction, with their derivatives.

Even though there is a subtle relocation of the atoms between the VO_{2-M1} and VO_{2-R} phases, this is enough to cause a break in the symmetry of the unit cell. The staggering mentioned in section 2.2.1 causes the tetragonal unit cell to double along the a- and c- axis (see figure 2.7). As a consequence of this doubling in the tetragonal unit cell, the diffraction patterns between the

[‡‡]Refer to table 2.2 for the different lattice parameters in these structures

VO_{2-M1} and VO_{2-R} phases change by introducing a new set of diffraction peaks halfway between some of the tetragonal diffraction peaks. Therefore, not only can diffraction methods differentiate VO_2 from other stoichiometries of vanadium oxides, but it also differentiates among the different phases within VO_2 itself.

Since the VO_{2-M1} and VO_{2-R} phases belong to two different crystallographic groups[†‡], and due to standardized crystallographic nomenclature, the lattice parameters take on different directions from one VO_2 phase to another. As a matter of reference, figure 2.9 shows a diagram to map the relationships of the crystallographic axes between the high-temperature VO_{2-R} and the low-temperature VO_{2-M1} phases. Both views are projections down the b axis of that phase. The unit cell is shown in red and the axes in black (shown in both) are for the M1 phase. However, in the R phase the axes are labeled according to R. This allows the relationships between the phases to be determined.

The tetragonal symmetry of the high-temperature phase poses an ambiguity in the a and b axis when the transition is drawn schematically, therefore there are various mappings from the rutile phase to the monoclinic.[44] We prefer and use the mapping shown in figure 2.9 as we feel it is somewhat simpler with b_R matching to b_{M1} and it makes the matching of atomic positions clearer.[§] Still, it is noteworthy to point out that, due to the symmetry of a tetragonal unit cell, there is an ambiguity between the a- and b- axes.

2.3.2 Characterization Based on the Valence States of Vanadium

The chemical composition of the films may also be examined through various characterization methods. The knowledge of the ratio of vanadium to oxygen atoms is another indicator of the

[†] VO_{2-R} structure: (#136 $P4_2/mnm$) $a = b = 4.554$ Å and $c = 2.849$ Å

[‡] VO_{2-M1} structure (#14 $P2_1/c$) $a = 5.7529$ Å, $b = 4.5263$ Å, $c = 5.3825$ Å, and $\beta = 122.6°$

[§] For example, in the Andersson mapping the $[001]_R$ and $[100]_{M1}$ do not appear to be a good mapping until the rutile unit cell is shifted to the body centered position.

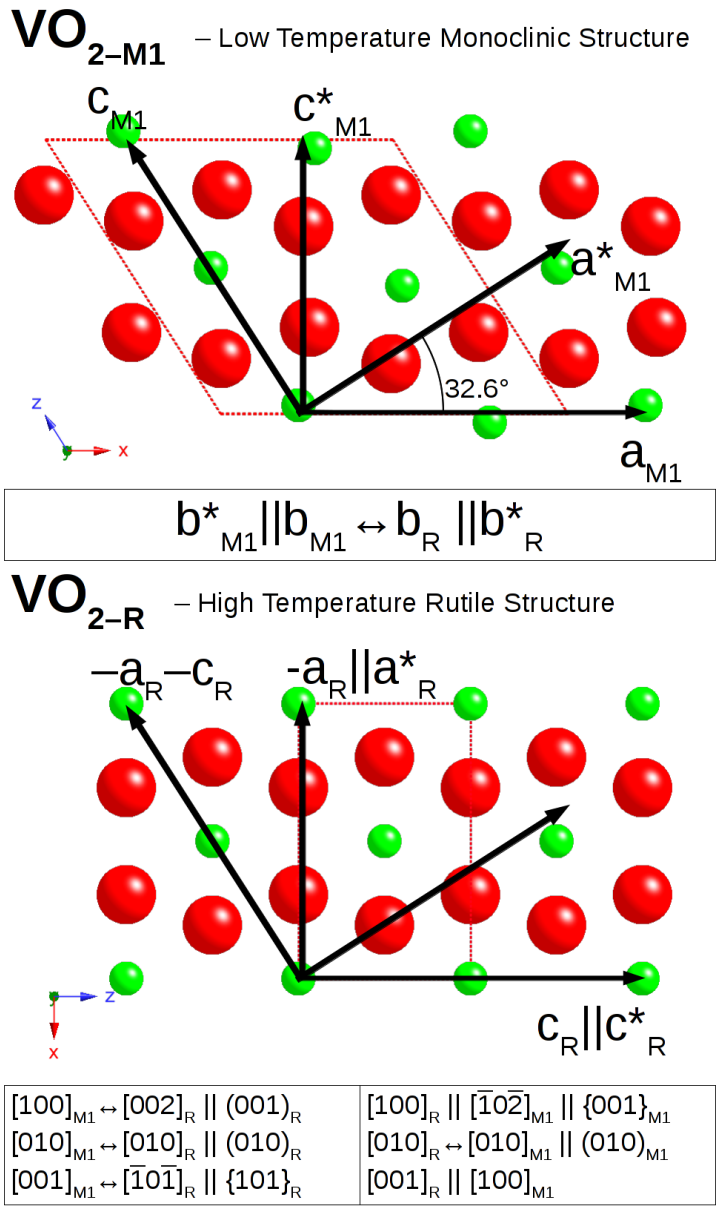

Figure 2.9 Diagram to map the relationships of the crystallographic axes between the low-temperature VO_{2-M1} (top) and the high-temperature VO_{2-R} (bottom) phases.

quality of the deposited films. Spectroscopic techniques often yield information about chemical composition, and in some cases, they can also yield information about the valence states of some of the atoms. As mentioned in section 2.1, vanadium dioxide is only one of the many different vanadium oxides available. Thus knowledge of the oxidation state can help differentiate vanadium dioxide from other vanadium oxide stoichiometries.

Some of the techniques available that yield this kind of information include: X-ray Photoelectron Spectroscopy,[67–74] Photo-Emission Spectroscopy, Raman Spectroscopy,[59,61,70,73,75,76] Energy Dispersive X-Ray Spectroscopy, Electron Energy Loss Spectroscopy,[3,77–81] and others. Usually during a spectroscopic study, a particular spectrum is collected and used as a "fingerprint" to determine the chemical composition, as well as the bonding states of the sample.

2.3.3 Characterization Based on the Electronic Change During the Metal to Insulator Transition

The other two types of characterization methods (that were just discussed in 2.3.1 and 2.3.2) may be applied to a large variety of materials. However, the type of characterization where there is an observable electronic change seems to be somewhat particular to materials that undergo a metal-to-insulator transition. In the case of vanadium dioxide, the metal-to-insulator transition has been observed both optically and electrically.

Optical methods such as infrared laser spectroscopy, pulse-probe techniques, and measurements in infrared transmission, absorbance, and reflection are used to observe the MIT and thus help determine the quality of the deposited vanadium dioxide.[46,56,65,68,81–86]

Similarly, electrical measurements, such as resistivity, also help observe the MIT. In fact, Morin's original report[2] on vanadium dioxide's MIT was done through a resistivity measurement, and this method still is used today.[51,87–91]

Though the electronic and optical methods are closely related, and while they both probe the

internal electronic structure of the VO_2 crystals, they will be discussed separately. The motivation for this separation is discussed in section 2.2.3 and figure 2.8.[46,51,56,63]

Methods of characterization based on the electrical conductivity change during the phase transition

For bulk samples and continuous thin films, a commonly used test is a two-point probe resistance test. This method goes in line to that originally used by Morin in 1959, where the sample is heated above 68°C and there is an observable resistance change.[2]) Similar variations to this technique can incorporate the use of four-point probes, or any number of electrodes connected to the VO_2 sample.[8]

Even though this is a quick test of the presence of VO_2, for this technique to be useful a conductive path is requisite. For example, while Morin[2] and other groups[28,64,92,93] have reported a resistivity change near two orders of magnitude for crystalline VO_2, there have also been reports of changes in resistivity of up to 5 orders of magnitude for crystalline VO_2 thin films.[63,74,87,90] This range of changes in resistivity is attributed to several factors including grain boundaries and film continuity.

Methods of characterization based on the optical changes during the phase transition

The metallic or insulating state of vanadium dioxide thin films and nanoparticles can also be probed optically. Similar to the electrical conductivity test, a sample can be heated above the transition temperature and the optical properties measured.[46] In contrast to the electrical conductivity test, a conductive path is not required. In the case of VO_2, reports of up to an 80% drop in transmission in the infrared has been observed[46,51,56,63] (Naturally, the optical properties of the substrates must also be taken into account).

Verleur's work shown in figure 2.8 shows a comparison between the VO_2 film's transition

optically and the expected optical transition based on the resistivity measurements of the same film. As mentioned in section 2.2.3, this difference between optical and resistive properties is attributed to different factors[46,51,56,63] including polycrystallinity of the film and percolation effects. It is worth pointing out that a resistivity change was not observed until $\sim 50\%$ of the grains in the film had switched to a metallic phase as measured optically, indicating a need for an electrically conductive path for the change to be observed through a resistivity change.

Since a conductive path is not a requisite for this technique, the use of optical probing techniques is advantageous to study isolated non-continuous particles of VO_2.[50,94,95] This advantage is shown in work done by E. Donev and R. Lopez in arrays of isolated size-controlled VO_2 nanoparticles.[56,65,86,94] While there is no electrically conductive path for these samples, the transition of the VO_2 nanoparticles can still be probed optically.

2.4 Methods shown to modulate or induce the phase transition in VO_2

Even though the phase transition for vanadium dioxide is cited to be 68°C (it was first induced by temperature[2]) there are several factors that will modify, tune, alter, or even induce the phase transition. Variations in stoichiometry, particle size, stress, misorientations between grains, morphological faults, dopants, and other "imperfections" have been used qualitatively to describe changes in the transition temperature, hysteresis, and sharpness of the transition.[49,56,63,65] Further, the phase transition in vanadium dioxide has also been induced by methods other than temperature. Some optical measurements have been performed using a pulse-probe technique to induce and time the phase transition.[64,66] According to Cavalleri, the transition was induced by "prompt hole photo-doping."[64]

2.5 Common Deposition methods for VO_2 thin films

Thin film deposition is an inexpensive method of integrating materials because there is no need to create large bulk samples and it is relatively easy to deposit and pattern onto a variety of substrates. In the case for vanadium dioxide, large single crystals have not been used technically as they fracture due to mechanical tensions that occur during the phase transition. Fortunately, these ruptures have not been observed in thin films.[52] As mentioned in previous sections, due to the many oxidation states available for vanadium, the synthesis of high-quality vanadium dioxide is not a trivial matter. Nonetheless, different methods have been used to successfully produce high-quality vanadium dioxide thin films on a variety of substrates. Though the deposition details vary from paper to paper in the literature, deposition methods include: RF and DC magnetron reactive sputtering, sol-gel deposition, reactive ion-beam sputtering, reactive evaporation, chemical vapor deposition (including chemical metal-organic vapor deposition),[45] pulsed laser deposition,[96,97] ion implantation,[56,65,94] and others. Since it is difficult to produce stoichiometric vanadium dioxide using these methods, often a post annealing process is used to produce crystalline stoichiometric vanadium dioxide.[52] The quality of these deposited films is usually determined by optical and electrical conductivity measurements[52,65,94,97] as mentioned in section 2.3.3.

2.5.1 Applied Deposition Methods in this Work

The samples used for the studies presented in this work were provided by Dr. Kevin Coffey at the University of Central Florida and from Dr. Richard Haglund at Vanderbilt University.[†]

[†]Details on the deposition parameters for these films can be found in appendix A

Samples obtained from UCF

The samples obtained from the University of Central Florida were deposited on silicon wafers with thermally grown amorphous silicon dioxide layers. A layer of amorphous vanadium oxide (VO_x), close in stoichiometry to vanadium dioxide was sputtered on top of the thermally grown oxide mentioned above. The sputtering took place by means of RF Magnetron Sputtering of a vanadium target in a reactive environment with an oxygen partial pressure as part of the plasma. Since the sample remained unheated, the deposition of vanadium and oxygen remained amorphous. The wafers obtained are summarized as follows:

- 50 nm VO_x layer on top of a 380 nm thick SiO_2 Layer
- 10 nm VO_x layer on top of a 90 nm thick SiO_2 Layer
- 5 nm VO_x layer on top of a 90 nm thick SiO_2 Layer

The deposited vanadium oxide wafers, as described, was obtained from Dr. Kevin Coffey at the University of Central Florida.[‡]

Samples from Vanderbilt University

At Vanderbilt University, vanadium dioxide was deposited onto various substrates by means of pulsed laser deposition (PLD). In contrasts to the samples obtaind from UCF, these substrates were heated to $\sim 500^{\circ}C$ during deposition to generate crystalline VO_2 thin films. The deposited VO_2 films were $\sim$ 80 nm nominal thickness. The substrates used for deposition are summarized as follows:

- 80 nm VO_2 on $(1\bar{2}10)$ Al_2O_3 – (a-cut sapphire)
- 80 nm VO_2 on (0001) Al_2O_3 – (c-cut sapphire)

[‡]For more details on the deposition parameters for the UCF samples, refer to Appendix A.1

- 80 nm VO_2 on $(1\bar{1}02)$ Al_2O_3 – (r-cut sapphire)
- 80 nm VO_2 on (001) TiO_2 – (c-cut TiO_2)

The deposited VO_2 thin films on various substrates from Vanderbilt University[§], as described above, were obtained from Dr. Joyeeta Nag and Dr. Richard Haglund.

[§]For more details on the deposition parameters for the Vanderbilt University samples, refer to Appendix A.2

Chapter 3

Overview of Electron Microscopy

The wave-particle duality of electrons, in addition to the interactions they have with matter, have made possible several imaging and analytical tools for the study of materials. On one end, the scanning electron microscope takes advantage of the particle nature of the electrons, by rastering (or scanning) over a surface, and detecting the electrons that "bounce back" surface images can be generated. On the other end, with electrons behaving like waves, the transmission electron microscope can focus an electron beam in a manner similar to that of optical microscopes and transmission images can be generated. Furthermore, it is possible to use the electron beams from these instruments to probe the properties of materials, with spatial resolution near the size of the probe.

The purpose of this chapter is to give a brief overview of some techniques that are available thanks to the electron microscope.

3.1 Electron-solid interactions

Beam energy is one of the parameters that determines the type of interactions that the electrons will have with a particular specimen. Due to the wave-particle duality of electrons, the higher the

energy, the lower the wavelength, but also the higher the penetration into a sample. This duality plays an interesting role in scanning electron microscopy. A Monte Carlo simulation showing the interaction volume of an electron beam into a sample at various accelerating voltages is presented in figure 3.1*.

While a higher energy implies a shorter wavelength and a corresponding higher spatial resolution, figure 3.1 shows the overall interaction within the bulk that the electron beam has at different energies. Since in electron microscopy images are generated by means of an electron beam interacting with a specimen, the interaction of the electrons within the sample cannot be neglected. An advantage of having a higher energy beam is also the availability of other electron-generated signals that can be used to probe the properties of a material.

Figure 3.2 shows some of the signals generated when an electron beam interacts with a specimen. These signals include:

- Backscattered Electrons - Those that mostly undergo elastic scattering events
- Secondary Electrons - Electrons generated from the material, most commonly due to collisions from the main beam.
- Auger Electrons - The energy of these electrons is characteristic of the element from where they were generated.
- Bremsstrahlung x-rays - These photons are generated due to the deceleration of the electrons as they enter the specimen.
- Characteristic x-rays - These x-rays are generated as electrons that were "knocked out" of their orbitals are replaced by cascading of other electrons in the atom. The energy of these x-rays is characteristic of the element from where it was generated.

*The Monte Carlo simulations shown in this chapter were generated using Public Domain code NISTMonte available from the National Institute of Standards and Technology. For details see appendix C.

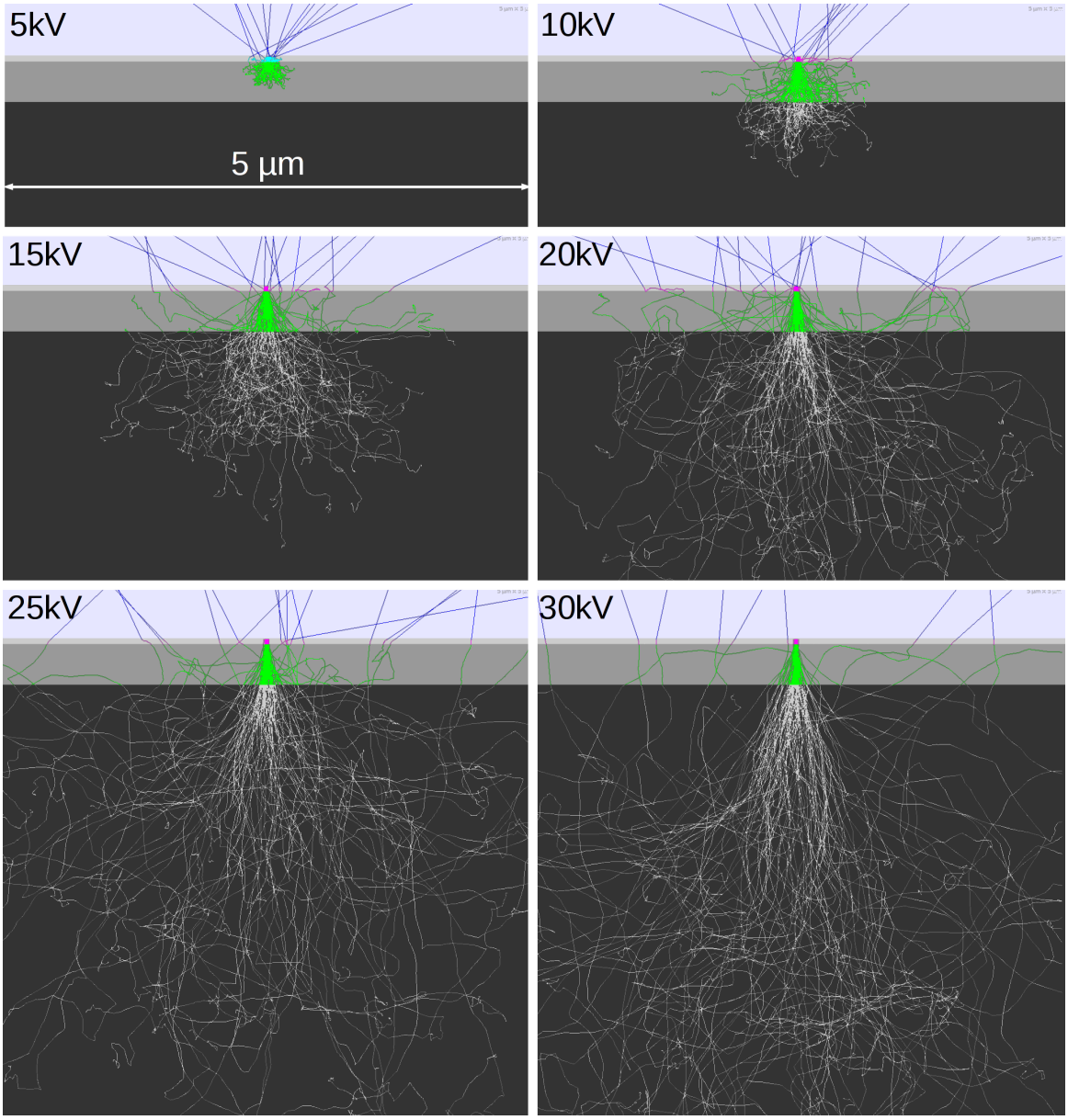

Figure 3.1 Monte Carlo simulations of the interaction volumes of electron beams with energies of 5, 10, 15, 20, 25, and 30 kV, through a sample comprising of a 50 nm VO_2 film (light gray) on top a 380 nm SiO_2 (medium gray) layer on a Si substrate (dark gray).

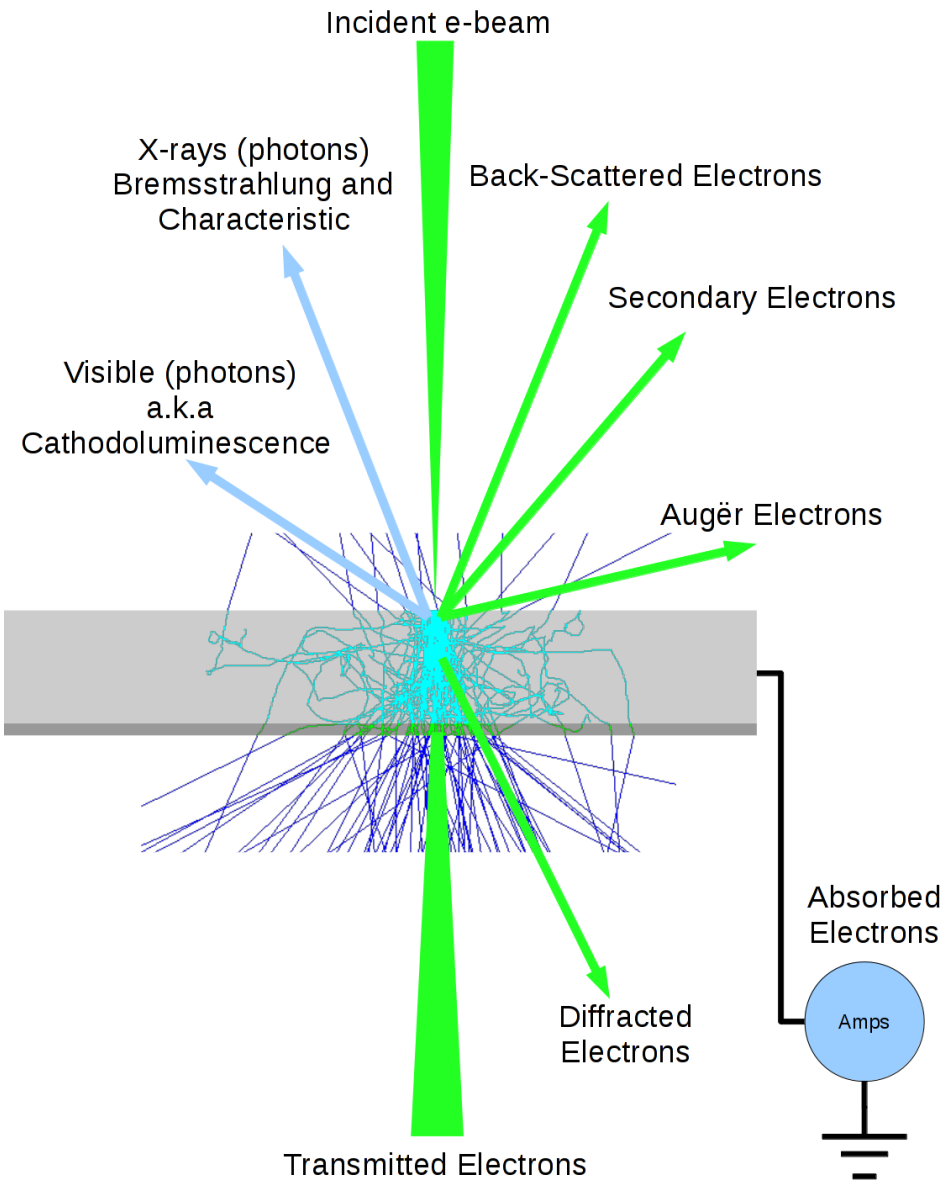

Figure 3.2 Some of the signals that can be detected from an electron beam interacting with a specimen.

- Cathodoluminescence - The generation of photons is not limited to the x-rays, but visible light is also generated as electrons interact with the specimen

3.2 Scanning Electron Microscopy

The Scanning Electron Microscope (SEM) is a tool that allows for the imaging of small specimens with the use of an electron beam. The creation of the electron beam in the Scanning Electron Microscope is usually achieved in the following manner: 1) Electrons are extracted from a tip either thermally (thermionic emission) or by field emission; 2) These electrons are then accelerated towards an anode at a set potential difference from the tip; 3) The beam of electrons is then focused using magnetic lenses in order to make a fine probe.

In order to form an image, the electron beam passes through a set of scanning or deflector coils that shift or raster the beam so that it may scan the sample (thus the name *Scanning Electron Microscope*). The beam is then allowed to interact with the sample and an image is formed by the interactions that take place between the electron-beam and the sample as the beam is scanned.

The interactions between the electrons and the sample allow for a rich amount of information that might be obtained in the Scanning Electron Microscope. Secondary Electrons, Backscattered Electrons, Characteristic X-rays, Auger Electrons, and Visible Light are among some of the "by-products" that take place during the scanning process. Depending on the detectors available, the SEM can be used to obtain a wealth of information regarding the specimen. Typically, the image is formed by using a Secondary Electron Detector[†]. Nonetheless, there is more information that can be extracted from the Scanning Electron Microscope, and this information depends on the type of detector being used.

Under a typical imaging mode (secondary electron detector), the surface of the specimen is imaged without any other data collected. A useful aspect of the SEM under imaging mode is the ability to tilt the specimen. Imaging a surface where the electron beam is normal to the thin film is commonly called a "plan-view." Imaging where the sample is placed so that beam is parallel to the films is commonly referred to as a "cross-sectional view." Tilts in the specimen anywhere

[†]The scanning electron micrographs obtained for this work were acquired using the Secondary Electron Detector.

between a plan and a cross-sectional view will be referred in this work as tilted views. For a thin film, imaging the surface at different angles can give information regarding the morphology of the thin film, as well as give a rough estimate regarding the roughness of the surface.

The resolution available under a particular imaging mode is limited by the size of the probe achieved. The size of the probe depends on the "spot size" which determines the number of electrons used (current), the electron energy (determines the wavelength of the electron beam), and the focus of the beam (adjusted by the magnetic lenses). Contrast under this imaging mode depends on the angle between the electron beam and the features in the surface. In this manner, edges and corners are enhanced in the composed image. Figure 3.3 shows a rough schematic on how contrast is obtained in the Scanning Electron Microscope using the Secondary Electron Detector. As the figure shows, the amount of secondary electrons that reach the detector is greatly determined by the the surface topography. The edges and facets facing the detector will scatter more secondary electrons toward the detector than those edges and facets facing away from it. Thus the contrast is therefore created in a manner analogous to an object illuminated with light, thus the topographical image created by the secondary electron detector can be easily recognized.

3.2.1 Tilted View Surface Imaging

While plan-views allow for an initial view of the surface, a tilted view can give a rough estimate on the roughness of the film. Though it is not as quantitative as a roughness measurement in an Atomic Force Microscope, an estimated height profile for particles might be calculated. Further, a tilted sample is required in order to obtain Electron Back-Scattered Diffraction (EBSD) patterns,[98] and to perform Orientation Imaging Microscopy (OIM) analysis.

A monte carlo simulation showing he effects of sample tilt is presented in figure 3.4. This figure models the interaction of a 25 keV electron beam with a 50nm VO_2 film on top a 380 nm SiO_2 layer on a Si substrate at angles varying from 0° with respect to the normal to 80° (in steps

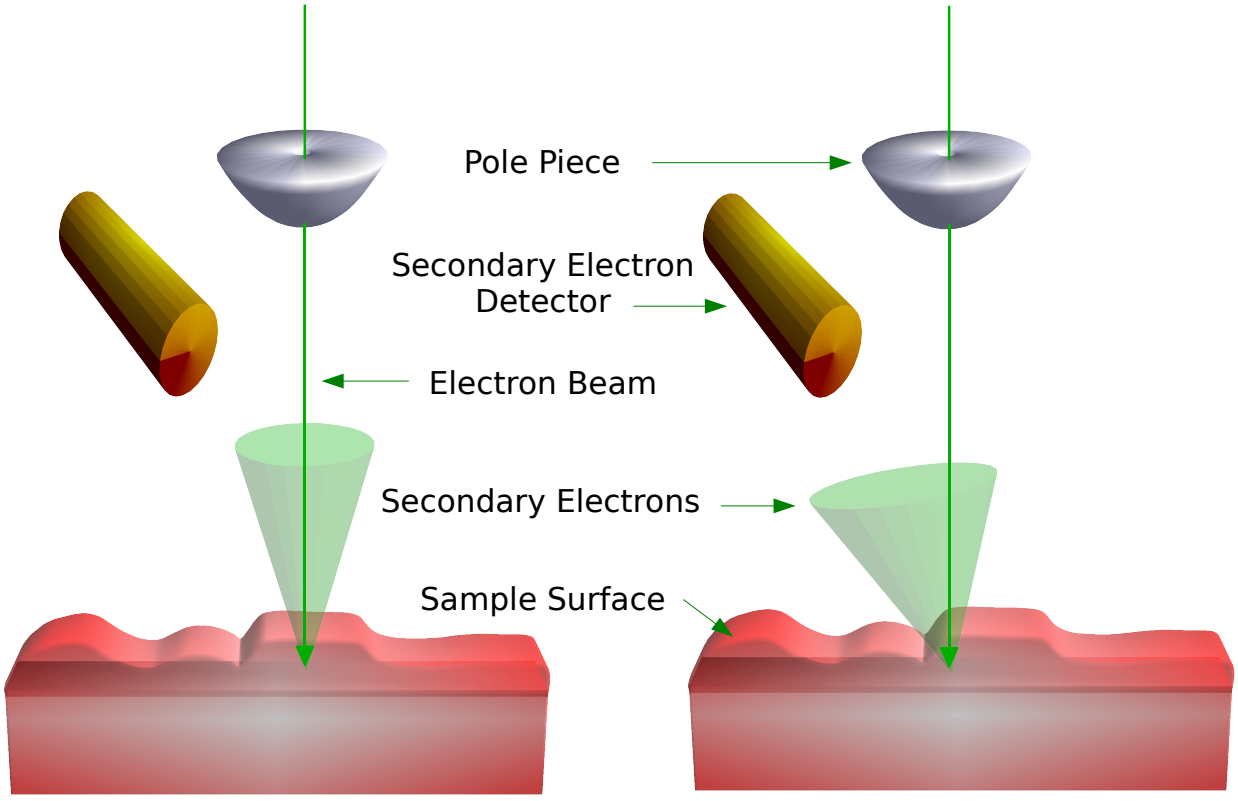

Figure 3.3 Using the Secondary Electron Detector in the Scanning Electron Microscope, contrast is obtained by the number of secondary electrons detected. The number of secondary electrons that "leave" the surface of the sample depends on the the angle between the main beam and the surface

of 10°). As seen int he figure, the interaction volume remains in the preferred direction of the incident electron beam, nonetheless, due to the sample tilt, the interaction with each one of the layers varies. Thus, a benefit of sample tilt is being able to probe the material closer to the surface.

Furthermore, as evident in the figure 3.4, the number of back-scattered electrons able to leave the sample increases with increased angle. At an angle of $\sim 70°$, there is enough current leaving the surface of the sample, that electron back-scattered diffraction patterns may be obtained.

3.2.2 Electron Back-Scattered Diffraction and Orientation Imaging Microscopy

As the electron beam interacts with the sample, the electrons in the beam scatter in all directions (but mainly in the direction of the beam). This will provide a virtually endless supply of electrons traveling in all directions (see figure 3.5). If the sample is crystalline, then several of the scattered electrons inside the sample will find themselves in the Bragg condition. These electrons will scatter multiple times while remaining in the Bragg condition. This creates a "channeling" effect that allows electrons to escape the sample creating observable contrast. (See figure 3.6) These multiple scattering events (along with the radial symmetry rising from having electrons scattered in all directions) creates Kossel Cones. Since most of the electrons that enter the sample scatter in the forward direction (figure 3.5) a tilted sample provides the benefit of having a larger number of the scattered electrons close to the surface and able to exit the sample[99–102] (see figure 3.4).

The intersection of the Kossel Cone with the Ewald Sphere creates the condition necessary to observe a set of Kikuchi lines. Figure 3.7 shows a diagram of the Kossel cones, the (*hkl*) plane they represent, and the observed Kikuchi lines. Since the Kikuchi lines are formed by the intersection of a plane with a cone, they are conic sections (in this case, hyperbolas). However, since the angle between the plane and the Kossel cone is small, these Kikuchi bands will look like parallel lines.

A full Electron Back-Scattered Diffraction (EBSD) pattern is formed by all the Kikuchi lines

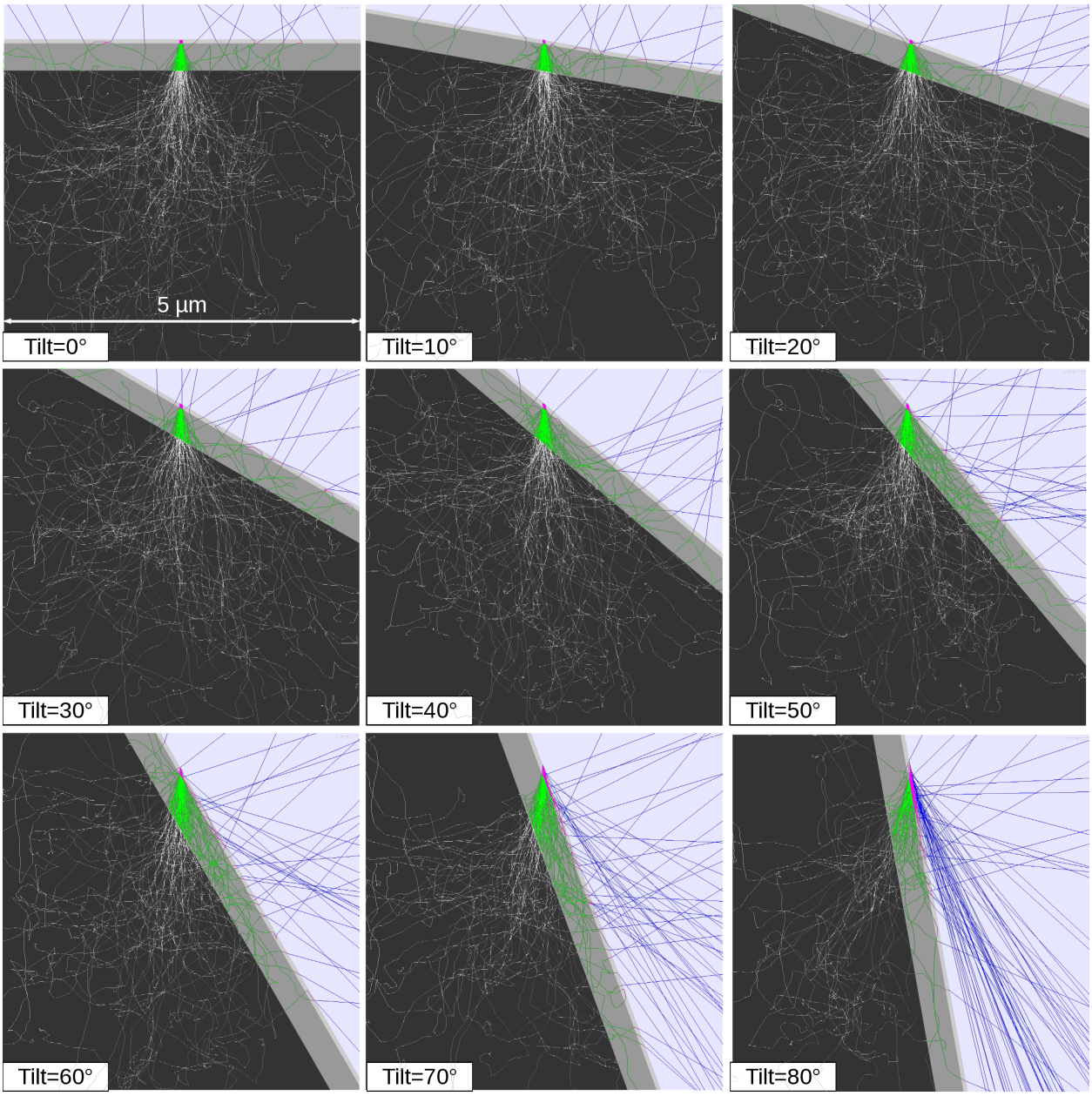

Figure 3.4 Monte Carlo simulation of a 25 keV electron beam interacting with a sample comprised of a 50 nm VO_2 film (light gray) on top a 380 nm SiO_2 (medium gray) layer on a Si substrate (dark gray). The tilt angles vary from 0° with respect to the normal to 80° in steps of 10°.

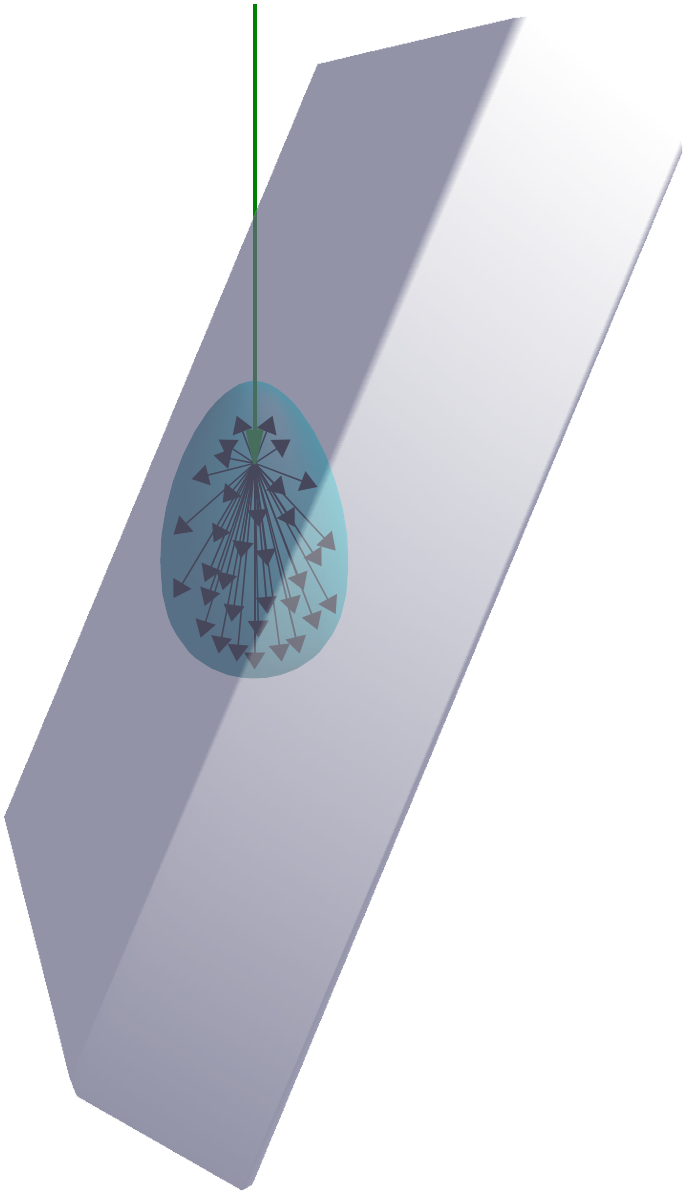

Figure 3.5 As the electron beam interacts with the sample, electrons will scatter in all directions (but with a preferential scattering direction following the direction of the beam).

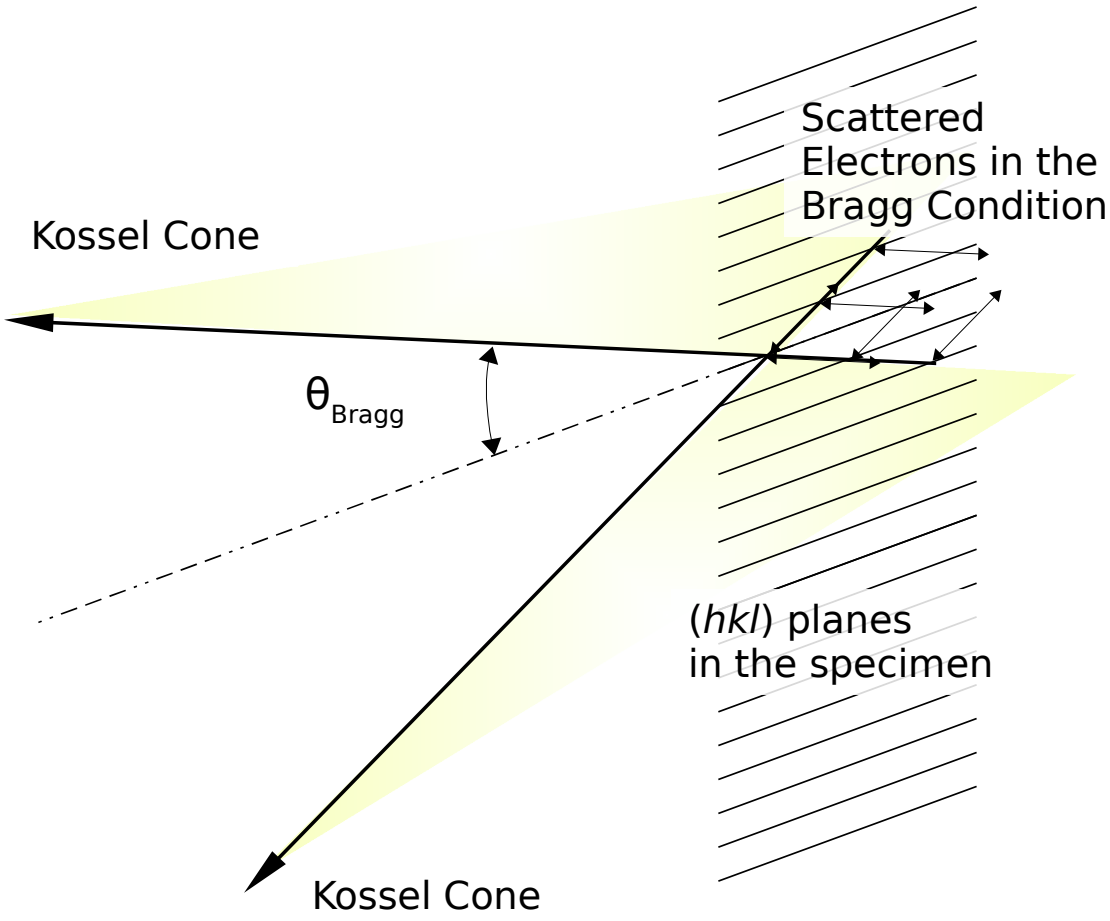

Figure 3.6 Since the electrons from the main beam scatter in all directions, a number of them will find themselves in the Bragg condition. Kossel cones are created from all the electrons scattering in the Bragg condition.

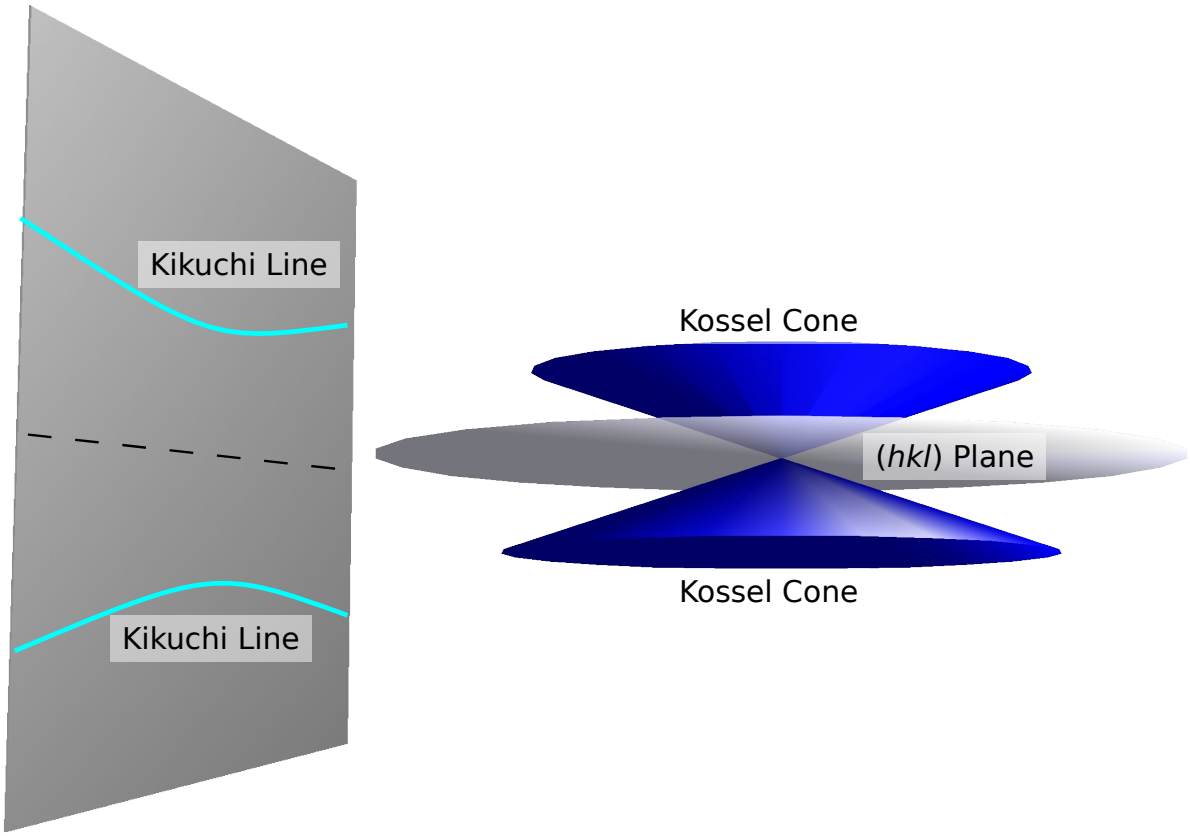

Figure 3.7 Kikuchi lines are the intersections of Kossel cones with the phosphor screen. (The bands are actually hyperbolic not parallel. However, due to the small angle between the plane and the cone, they look like parallel lines in practice.)

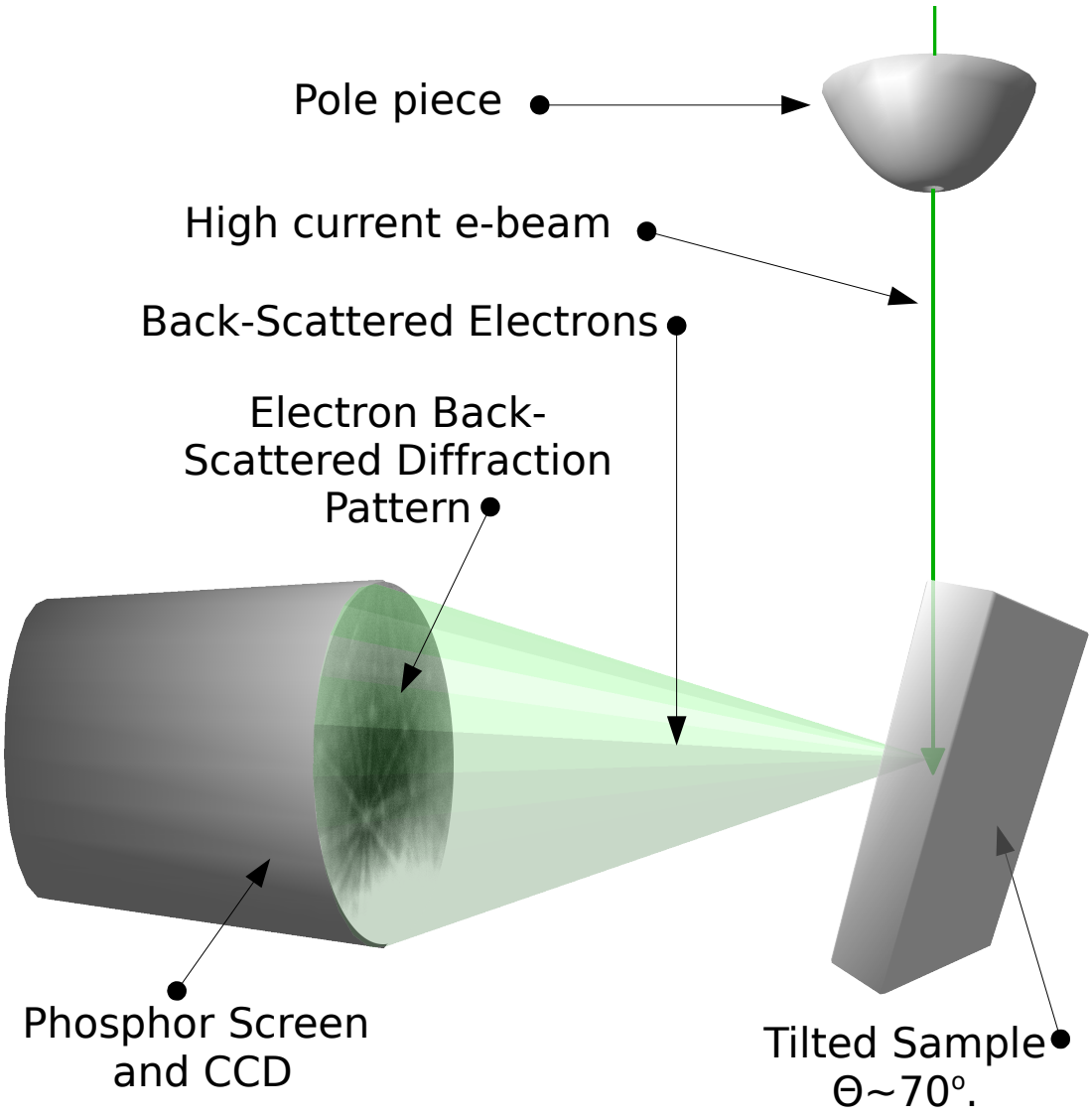

Figure 3.8 As the electron beam interacts with the sample, some of the electrons will be "back-scattered" in the Bragg Condition. These electrons will form Kikuchi patterns that can be detected with a phosphor screen and a camera. In Orientation Imaging Microscopy, Kikuchi patterns are recorded and indexed as a scan takes place in the Scanning Electron Microscope.

that intersect the phosphor screen (See fig. 3.8). A full Orientation Imaging Micrograph can then be performed. This is done by letting the software be in charge of collecting EBSD patterns while a scan of the surface takes place. The software then indexes each of the patterns collected, keeping them referenced to the position where they belong. By this method, a map of the surface may be created where individual grains are selected by sections of the scan having the same orientation. This method helps determine orientation of the grains in the surface, misorientations between grains, and grain sizes (see figure 3.9). The attainable resolution depends on factors such as the beam size, scan parameters, and quality of the sample. Figure 3.10 shows a typical OIM scan, the particle sizes observed in the scanning electron micrograph can be used to determine how fine of a scan to perform for OIM. In the case of figure 3.10, EBSD patterns were obtained every 50 nm in a hexagonal grid, thus about 6 EBSD patterns could be obtained while scanning across a 300 nm long particle.

3.2.3 Simulated Electron Back-Scattered Diffraction Patterns

Electron Back-Scattered Diffraction (EBSD) patterns may be simulated as they depend on the structure of the material observed. Since EBSD is a diffraction technique,[101] it can be used to index different crystallographic structures. Further, since the crystal structures among the different vanadium oxides varies considerably[‡], EBSD is a good candidate for characterizing resulting vanadium dioxide thin films. Crystal structures, such as the ones mentioned in sections 2.1 and 2.2.1, may be used to generate possible EBSD patterns. Figure 3.11 shows some calculated diffraction patterns for several vanadium oxide stoichiometries, including two phases for vanadium dioxide, along with the orientation that would yield such patterns. The software available for OIM uses these calculated diffraction patterns to compare them against obtained EBSD patterns. Some of the characteristics that are used for indexing the patterns obtained include the angle between bands,

[‡]see sections 2.1 and 2.2.1

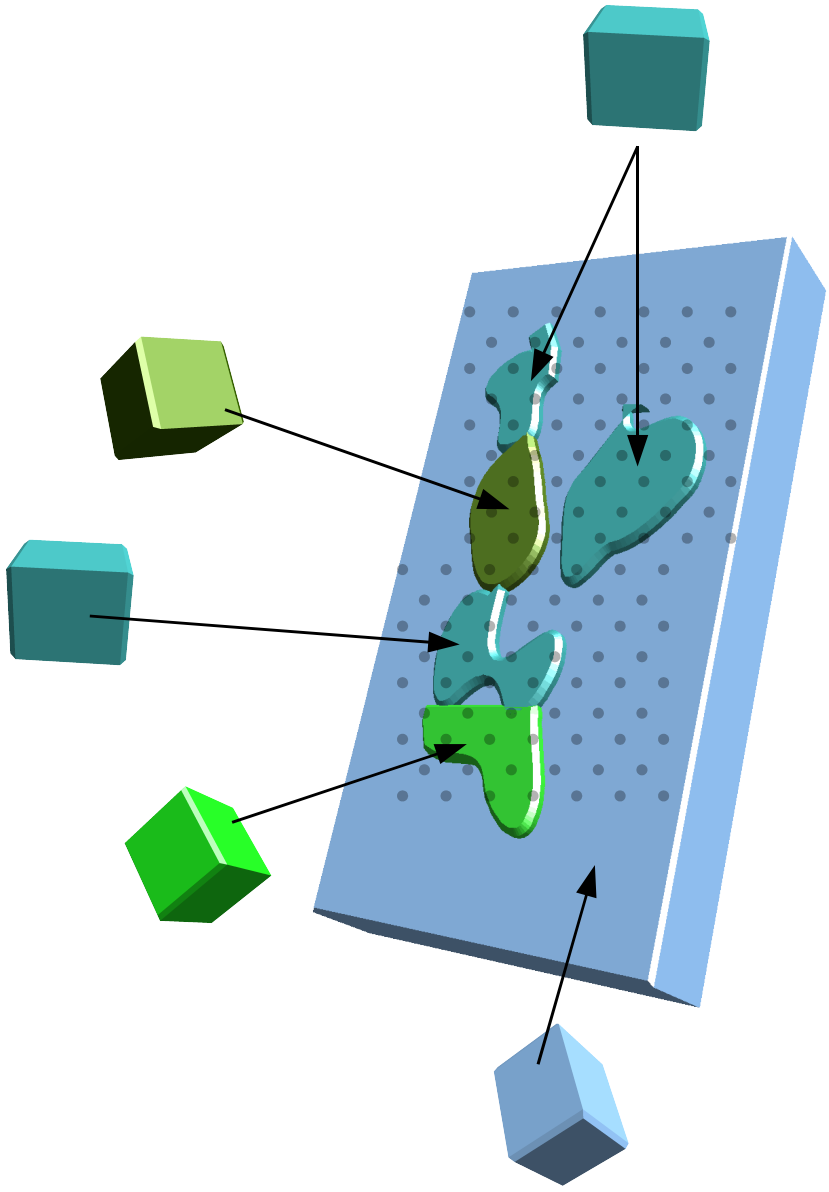

Figure 3.9 In an Orientation Image Micrograph the features, such as grain shapes and sizes, are determined by the crystal orientation. Resolution of this technique is determined by the beam size, scan parameters, and quality of the sample.

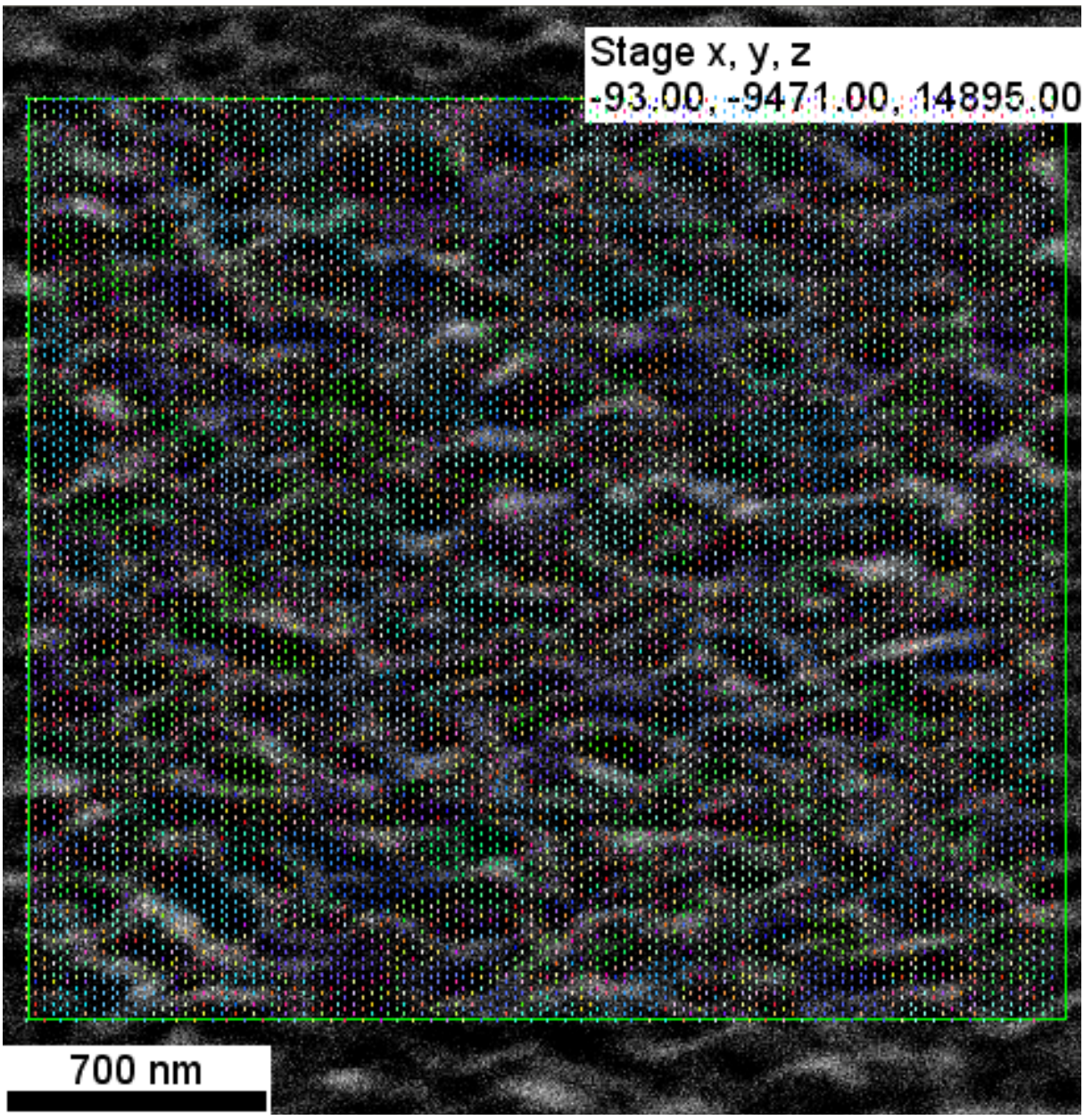

Figure 3.10 (color) During an OIM scan two important factors to consider are the grain size, and the scan size. In this sample image, the grain size is approximately 300 nm across and the distance between sampling points is about 50nm.

distance among zones, and number of zones seen in the pattern. As observed from the calculations in figure 3.11, the change in symmetry of VO_2 yields some missing bands, but otherwise, the VO_{2-R} and VO_{2-M1} patterns are rather similar.

3.3 Transmission Electron Microscopy

Just like with the Scanning Electron Microscope, the Transmission Electron Microscopes (TEMs) take advantage of the wave-particle duality of electrons, except that they rely more on the wave-like properties of the electrons for imaging. Another benefit of the use of the TEM is the resolution that arises from using highly accelerated electrons for imaging. Louis de Broglie related a particle's momentum (p) to its wavelength (λ) though his well-known equation:

$$\lambda = \frac{h}{p} \tag{3.1}$$

where h is Plank's constant. For a electrons with energy higher than $100keV$, like it is the case with these TEMs, the relativistic momentum should be the one to be used for equation 3.1. This substitution yields

$$\lambda = \frac{h}{\left[2m_0eV\left(1+\frac{eV}{2m_0c^2}\right)\right]^{\frac{1}{2}}} \tag{3.2}$$

where m_0 is the rest mass of the electron, c is the speed of light and eV is the energy of the accelerated electron. As examples: For a 300 kV electron, the associated relativistic wavelength (using equation 3.2) is 0.019 Å; and for a 200 kV electron, the relativistic wavelength is 0.025Å. Nonetheless, in practice this resolution is not achieved due to lens aberration effects.[§]

Imaging in the TEM is obtained through the forward scattering of electrons through the sample. Furthermore, as shown in figure 3.2, due to the electron-sample interactions that take place

[§]The resolutions reported by the manufacturer for the instruments currently at BYU are: 2.4 Å for the TF30, and 1.7 Å for the TF20.

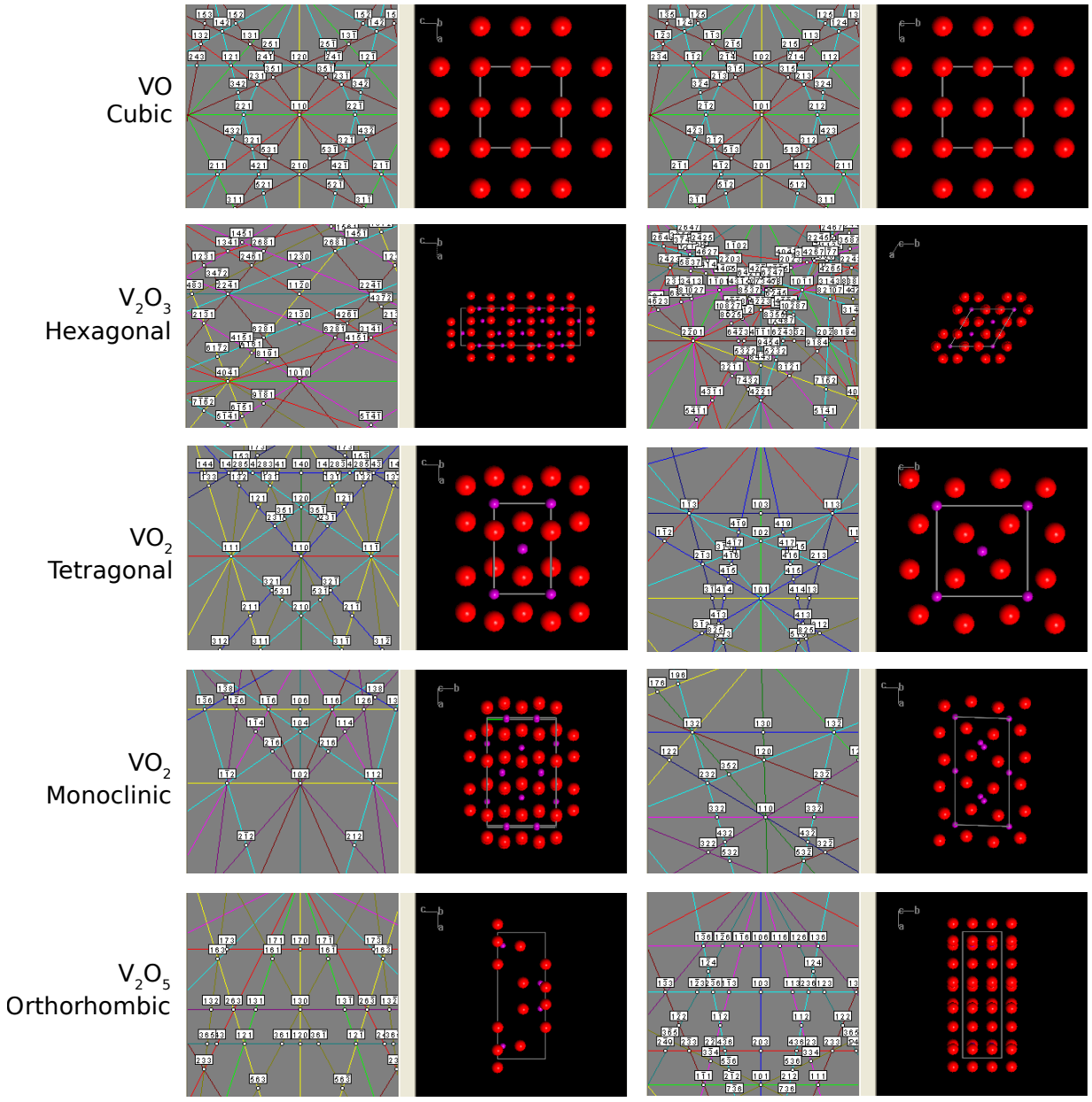

Figure 3.11 Calculated EBSD patterns for VO, V_2O_3, VO_2 tetragonal, VO_2 monoclinic, and V_2 O_5. The patterns calculated from the VO, V_2O_3, VO_2, and V_2 O_5 are distinctive enough to distinguish between them.

during the TEM imaging process, it is possible to obtain a higher wealth of information regarding the specimen. For example, the generated signals visible to a SEM (in fig. 3.2 characteristic X-rays, visible light, Auger electrons, back-scattered electrons, secondary electrons) are still generated during the TEM imaging process and can be collected trough the use of an analytic TEM. Moreover, in addition to the generated signals already mentioned, the transmitted electrons also carry with them information gathered as they interact with the sample. As examples: Transmitted electrons carry with them phase information which changes as they go through different materials, thus electrons with different phases interfere with each other and high-resolution images of columns of atoms may be formed; electron may get scattered away from the main beam due to the crystallinity of the sample or from the atomic nuclei of the material, giving the ability to generate diffraction contrast or z-contrast in the image; also, electrons may loose energy that can be used to characterize the materials they go through.

3.3.1 Imaging with the Transmission Electron Microscope

Akin to an optical microscope, the TEM is equipped with an illumination source, focusing lenses, a sample stage, and means of viewing the magnified image. The main differences being of course that it employs electrons instead of photons, and thus uses electromagnetic lenses instead of optical lenses. Figure 3.12 shows a rough, and very simplified, schematic of the illumination and imaging system in the TEM. The figure also displays two of the modes commonly used to obtain information from the sample.

Part of the illumination system of the TEM consists of an electron emitter or electron gun which may be thermionic or field-emission (FEG). One of the advantages of the FEG is the narrower energy spread of the electrons extracted from it (compared with thermionic). The lenses and aperture above the sample allow for the control of the probe used to illuminate the sample. This is necessary as different imaging conditions require different currents in order to obtain usable images. As

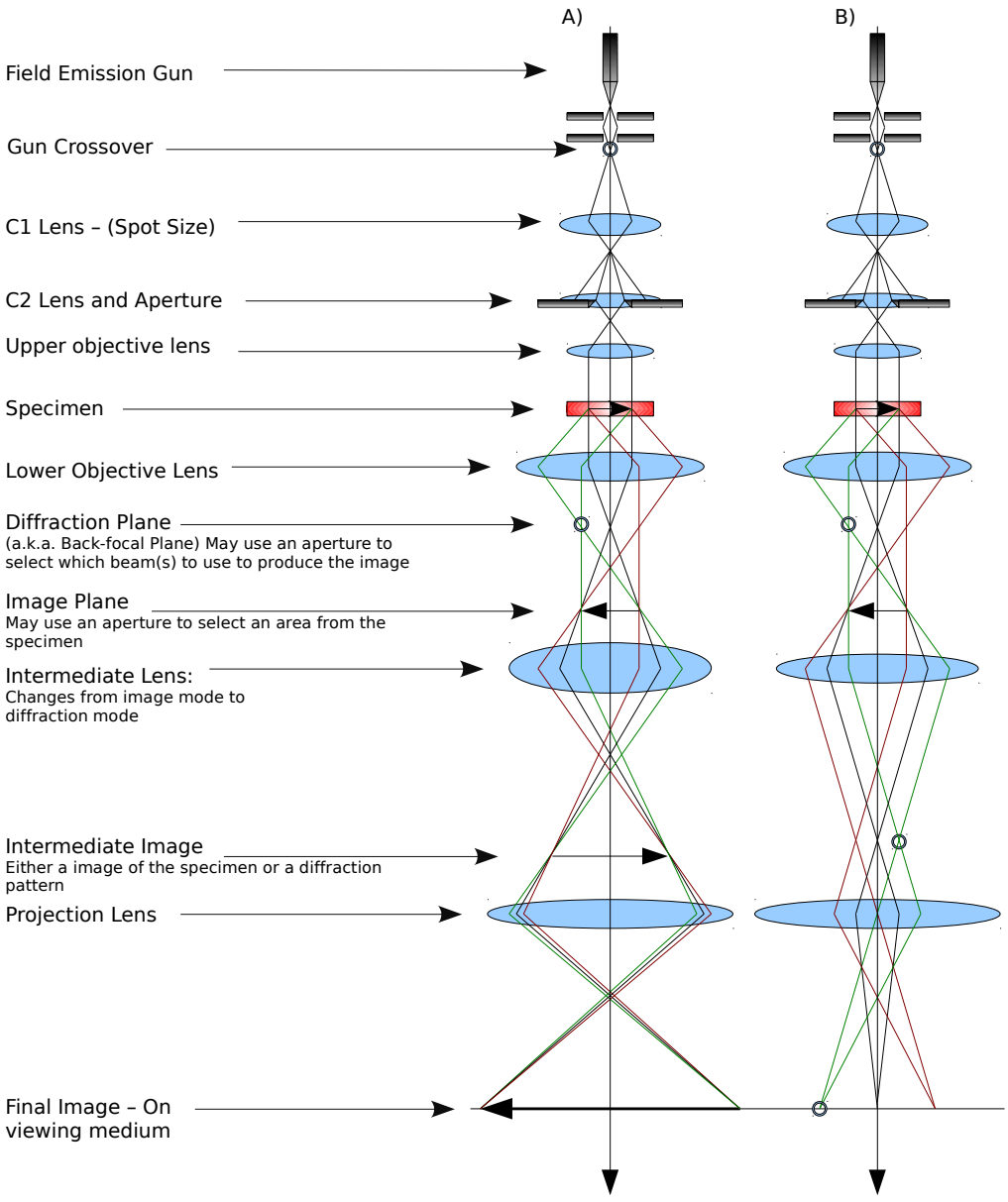

Figure 3.12 Rough schematic of the TEM's illumination and imaging system as set for obtaining A) an image of the specimen or B) electron diffraction from the specimen

illustrated in figure 3.12 when the electrons from the beam interact with the specimen, they scatter and diffract. The transmitted electron beam that remains in the optic axis will be referred to as the *main beam*, while electrons deflected off the optic axis (by any scattering events) will be referred to as *diffracted beams*.

Since it is required for the electron beam to pass through the sample, the thickness of the sample plays an important role in the quality of the acquired image. The effects of sample thickness are qualitatively displayed in figure 3.13

The objective lens serves to form both a diffraction plane and an image plane. Apertures may be placed in these planes in order to select what information can be collected from the specimen. For example, an aperture may be placed in the diffraction plane in order to only let one of the diffracted beams through, and thus image the sample with the electrons that satisfy that particular diffraction condition. Also, an aperture may be placed in the image plane and isolate a specific selected area of the sample from which to obtain diffraction information. The intermediate lens can then be used to select which of the two planes to use to create the final image. Finally the projector lens will project the final image onto a screen or recording medium.

The use of apertures (or lack thereof) determines the image of the sample on the recording medium. For transmission electron microscopy there are several common methods to achieve contrast in the sample image, some of them include *mass-thickness contrast*, *bright field*, *dark field*, and *phase contrast*.

Imaging: Mass–Thickness, Bright–Field, and Dark–Field

Figure 3.12a shows a ray diagram of the imaging process in the TEM. As it is observed from the diagram, the diffracted rays, as well as the main beam are all combined in the final image. This often results in an image of little contrast due to the interference between the main beam and the diffracted beams. Under these conditions, any contrast that appears in the image is usually achieved

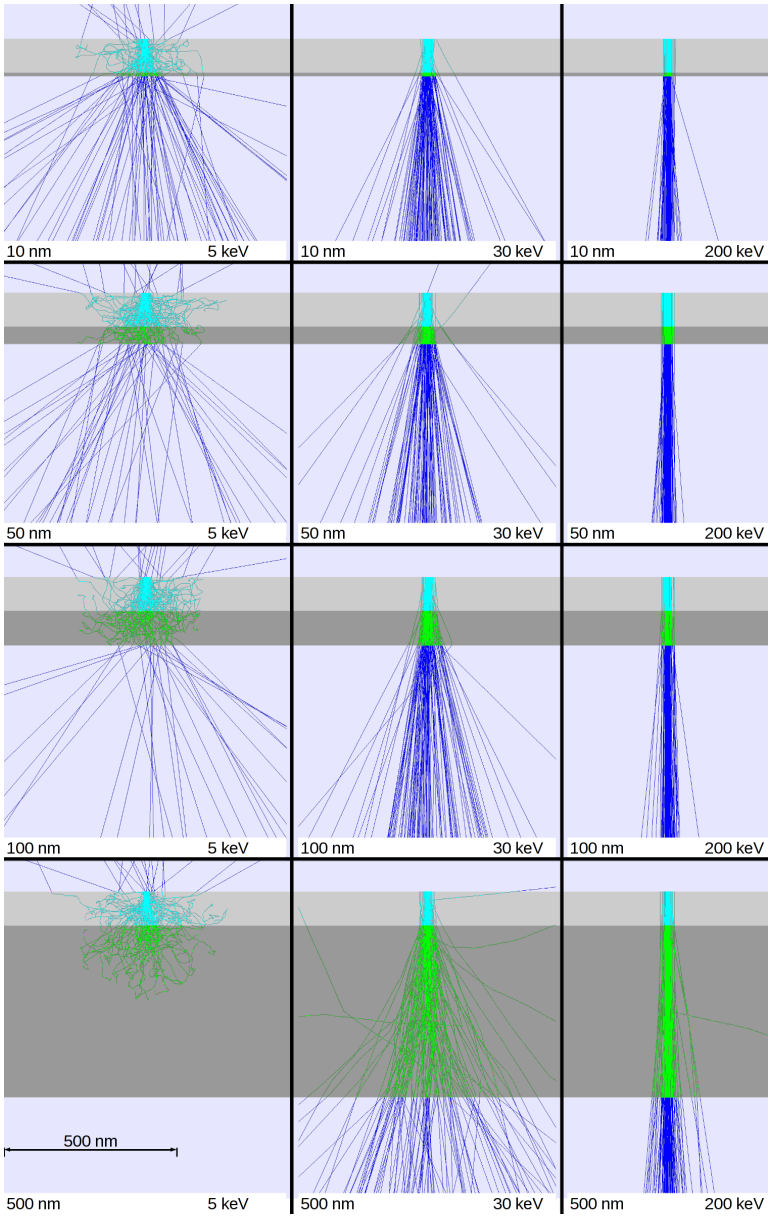

Figure 3.13 Array of Monte Carlo simulations depicting the electron interactions through a sample consisting of a 50 nm VO_2 film (light gray) on top of a supporting SiO_2 layer of various thickness. The energy of the incident electron beam is also varied.

due to variations in thickness or differences in mass in the sample. (This is commonly known as Mass-Thickness contrast as it is non-trivial to differentiate between the two.) Added contrast might be achieved while imaging by "blocking" or "selecting" the desired beams that will allow for the image to be formed. In this manner, the interference of the blocked beams is eliminated, and the image from the selected beam(s) is enhanced. This selection process is achieved by placing "apertures," (a thin sheet of metal with a hole drilled through it) that allow the user to "select" or "block" information to form the desired image. Some of these apertures are located in the diffraction plane[¶] and the image plane (see fig 3.12) and these are varied in size.

A Bright-Field (BF) condition is created by using an aperture in the diffraction plane to select the main beam while blocking the diffracted beams.[‖] Under these conditions, the main beam is used to create the image and contrast is enhanced since the interference of the diffracted beams is eliminated. Since the main beam carries most of the electrons the image looks bright (hence, Bright-Field). This seems to be a very common and one of the easiest ways to obtain contrast in TEM images, specially since the sample needs not be crystalline.

On the other hand, a Dark-Field (DF) condition is created by using the aperture to block the main beam and selecting instead a diffracted beam to form the image.[**] In this case, the main beam (which carries most of the electrons) is blocked, and the image is formed only by those electrons that satisfy the Bragg condition necessary to diffract to that chosen spot. Since most the electrons are blocked, the image tends to be darker (hence Dark-Field). However, intensity might be increased by tilting the sample in such a way that the selected diffraction spot shares a comparable amount of electrons to the main beam (a two-beam condition).

[¶]Also known as the *back focal plane*.

[‖]Known as the Objective Aperture

[**]To get better images, in practice it is preferred to tilt the main beam in such a way that the selected diffracted beam is placed where the main beam used to be. This allows for the aperture to remain in place, and for the rest of the optics to use a centered beam.

A Dark-Field imaging mode is peculiar as it forms an image only from those crystals in the sample that are aligned in such a way as to meet the required diffraction condition. As such, the image will show brightness in areas where the orientation of the crystals meets the specified diffraction condition.

Electron Diffraction in the Transmission Electron Microscope

As the electron beam interacts with the sample electrons will undergo scattering events (for example collisions due to atomic nuclei or Bragg diffraction). Figure 3.12B shows a ray diagram for the case when the intermediate lens images the diffraction plane instead of the image plane. In this case the image in the recording medium is not of the sample, but rather of the location of the diffracted beams. There is ample information that can be obtained from diffraction data, information such as the level of crystallinity of the sample (from amorphous, to polycrystalline, to single-crystal). In the case of an amorphous sample, an electron diffraction patter will show diffuse ring(s) that correlate to the average inter-atomic distance(s). Similarly, in the case of a polycrystalline sample, the electron diffraction pattern will show definite diffraction rings that correlate to the inter-atomic plane distances. Single crystal electron diffraction patterns correlate directly with the crystal structure of the sample.

3.4 Scanning Transmission Electron Microscopy – STEM

The scanning transmission electron microscope (STEM) is an interesting "combination" of the advantages of SEM and TEM to the point that it merits its own section. In a (S)TEM, in addition to the upper lenses there is also a set of scanning coils that will help raster the beam across the sample (the "S" in STEM). By using the lenses above the sample, the electron beam in a (S)TEM can be condensed into a fine probe. By recalling equation 3.1 and figure 3.13, a higher accelerating

voltage corresponds to a higher spatial resolution and transmission through a sample, thus a 200 kV electron beam has a much higher spatial resolution than a 5 kV beam. It is worthwhile to note that, while a (S)TEM may be used as either a TEM or a STEM, that is not the case for a dedicated TEM or a dedicated STEM.

3.4.1 STEM imaging

Imaging in a STEM is accomplished by scanning the sample with a fine electron probe. The main transmitted beam is often to strong to image directly with, so in practice, an annular dark-field (ADF) detector is employed. In an ADF detector, the main beam passes through the center of the detector and the signal is generated by the scattered electrons. By comparing the 200 kV beam simulations in figure 3.13, it can be observed that a thicker region of a sample will scatter the beam more, generating a greater signal in the ADF and, thus, a brighter spot in the generated image.

During STEM operation, the intermediate lens is used to image the diffraction plane (see figure 3.12. In this manner, while the scanning coils scan trough the sample, the signal can be obtained in the ADF. Figure 3.14 shows a rather simplified diagram of the use of annular dark-field detectors in STEM mode. As displayed in the figure, different information can be obtained by imaging using different scattering angles. The angles collected by the ADF can be selected by "changing the camera length" between the sample and the detectors [†].

One benefit of imaging through scattering comes at higher scattering angles. Heavier elements (high Z) will scatter electrons at a higher angle than lighter (lower Z) elements due to Rutherford scattering. Thus, with the STEM and a high-angle ADF (HAADF) detector, a z-contrast image may be generated, while minimizing the low-angle scattering signals that arise from Bragg diffraction or due to the mass/density/thickness[††] of the sample.

[†]Since the sample and the detectors have a fixed z-position, in practice the camera length is determined by the projection lenses in the STEM.

[††]See figure 3.13

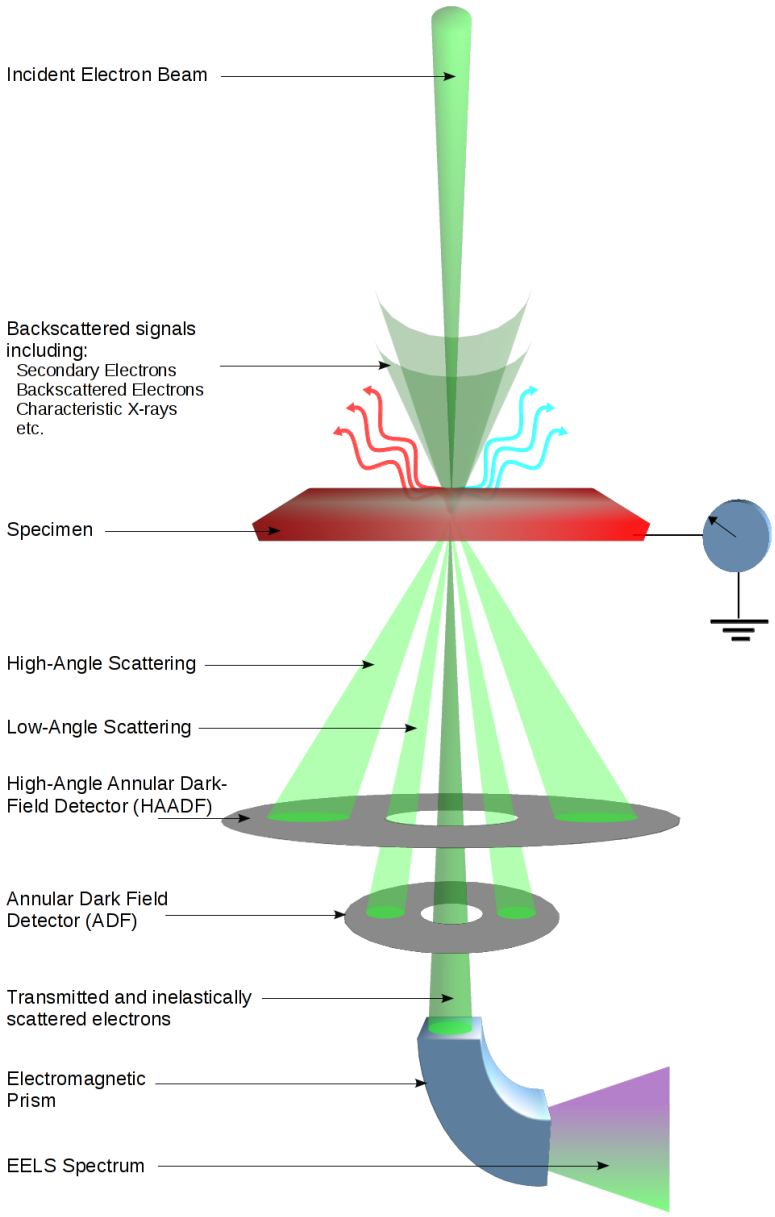

Figure 3.14 Diagram showing signal acquisition to image in a scanning transmission electron microscope (STEM). Imaging is often acquired through annular dark field detectors leaving the main beam available for other analytical tools. In this diagram the main beam is directed to an electromagnetic prism in order to generate an electron energy-loss spectrum.

3.4.2 STEM analysis

Having the electron beam focused onto the sample provides an electron probe through which the sample may be analyzed. Recalling figures 3.2 and 3.14, all the electron-generated signals mentioned in those figures are available in a STEM. Naturally, the detection of those signals depends on the detectors available[‡]. In the case of BYU, some of the detectors with which the TF20 is equipped include:

- An energy-dispersive x-ray (EDX) spectrometer for characterizing materials based on the characteriztic x-rays generated,
- a Gatan imaging filter (GIF) used for EELS or energy-filtered TEM (EFTEM),
- a CCD camera to collect convergent-beam electron diffraction (CBED) patterns.

While the signals mentioned in figure 3.2 are generated simultaneously, their collection is not necessary simultaneous. This difficulty arises from the placement and/or requirements of the detectors. As an example, in the diagram shown in figure 3.14, the STEM is set up to collect an electron energy-loss spectrum from the main transmitted beam, while simultaneously acquiring the amplitude of the beams scattered at low and high angles using two ADF detectors. This set up thus now excludes the ability to collect CBED patterns using the CCD.

In practice, the rate at which a detector is able to collect information may also limit which signals are taken concurrently. For example, in practice a STEM image is first obtained using the ADF detectors (due to their fast collection speed, and the high available signal), and after the image is obtained, EDX or EELS scans are performed (due to the slow collection speed or low signal available). In cases such as this, analysis of the sample is susceptible to artifacts where the

[‡]TEMs equipped with a variety of detectors for sample analysis are referred as analytical electron microscopes (AEMs).

analytical data collected may/(may not) correlate directly to the previously attained STEM image. A common artifact may be elongated/shortened chemical profiles due to sample drift.

3.5 TEM Sample Preparation: TEM's dirty little secret

In order to be able to image the samples using the Transmission Electron Microscope, the sample must be thin enough to become "electron transparent." This means that the thickness of a good TEM sample is smaller than the mean-free path of the electrons. "Electron transparency" varies from material to material. As shown in figure 3.13, for TEM sample preparation, thinner is better. It is often the goal to achieve samples where there is a region thinner than 100 nm. For many materials, achieving the required thickness for electron transparency is non trivial. Some of the techniques that allow the polishing of TEM samples include:

- Mechanical polishing methods – progressively use abrasives to remove unwanted material leaving regions of the desired thickness. Examples of this type of TEM sample preparation include the "Wedge Technique" or "Dimpling"
- Chemical etching methods – Chemically dissolve unwanted material while selectively leaving material of the desired thickness. Examples of this TEM sample preparation method include "JET polishing" and "Selective back-etching"
- Ion-based polishing methods – Use ion beams to erode material until the desired thickness is reached. Examples of this polishing method include "ion milling" and "focused ion beam" TEM sample preparation

While no one method is applicable to all materials, each of these sample preparation methods comes with its own strengths within its applications. These strengths may vary from sample preparation time, imageable area, cost, probability of success, etc. Furthermore, some of these

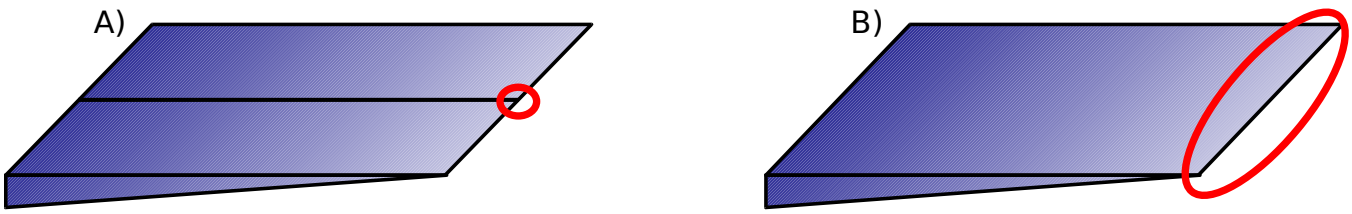

Figure 3.15 TEM "wedge" samples for A) a cross-sectional view, where the film is "sandwiched" between two silicon pieces in order to view its thickness; and B) a plan-view where the substrate is polished thin leaving the film undisturbed along the edge

techniques may be more adequate depending whether you are interested in imaging the surface (plan-view) or in the cross-section.

3.5.1 Wedge Technique

As mentioned earlier, this is a mechanical polishing TEM sample preparation method. The polishing is usually performed with abrasive lapping films with grit sizes down to less than 0.3 μm. In order to aid with the polishing of the sample, a polishing wheel and a tripod sample mount may be used.

For a cross-sectional sample, the film is "sandwiched" together, and both sides of the sample polished, leaving a small, thin area of interest where the film may be observed. On the other hand, with plan-view samples, the film is left untouched while the substrate is polished from underneath in order to create a wedge. Figure 3.15 shows the areas of interest for cross-sectional and plan view wedge samples after they have been thinned.

For both, cross-section and plan-view samples, the wedge is polished so that the angle in the wedge is approximately 1°, in that manner, the area that is 50 nm or thinner may extend close to 2.5 μm from the polished edge. This gives a substantial region of interest to analyze the film and particles. These wedges are finally secured to a 3 *mm*-diameter copper washer for support (see figures 3.16 B and C).

3.5.2 Chemical back-etching

This chemical etching method works to produce plan-view samples of thin films where there is a chemically selective etchant that will dissolve the substrate and leave the film intact. In our case, (see section 2.5.1) the samples obtained from Kevin Coffey at UCF are composed of a silicon wafer with a thermally grown thin SiO_2 layer upon which the VO_2 films were deposited. Selective etchants such as an HF/NHO_3, KOH, or TMAH can be used to etch away the silicon underneath[103–105] while selectively leaving the SiO_2 layer to protect the VO_2 film on top. Though TEM sample preparation time with this method is limited by etch rates, the time can be lowered by a previous mechanical polish of the substrate (with either a dimpler or a tripod polisher) and by the increasing the concentration of the etchants.

The chemical back-etching method is suited for preparing plan-view TEM samples and not cross-section samples. While cross-section samples are not prepared with this method, some benefits of this method include (1) the use of the sample itself as its own "TEM support grid" and (2) large viewing area(s) (in the order of tens of microns) that arise from the substrate being etched up to the protective layer. However, due to the formation of "bubbles" and irregular etching the viewable areas vary in size and location throughout the sample (see figure 3.16 D)

3.5.3 Focussed ion beam (FIB) TEM sample preparation

As far as the cost of the equipment required for TEM sample preparation is concerned, the cost a FIB system far exceeds that of the required equipment for mechanical polishing or chemical etching. However a FIB system is not limited to TEM sample preparation [‡‡], furthermore, this cost brings with it several noteworthy advantages for TEM sample preparation such as the ability for site-specific TEM sample preparation.[106–111] Furthermore, recent developments with computer-controlled FIB devices allows for scripted automatic cross-section TEM sample preparation of

[‡‡] Section 3.6 covers in a little more detail some uses/applications for the focused ion beam.

multiple areas in a specimen. The viewing areas of the FIB TEM samples may measure in length from a few microns to tens of microns. These samples may then be placed on a grid by either welding them *in–situ* or lifting them out *ex–situ*. At BYU an Omniprobe™micromanipulator is employed to place for welding up to 8 FIB TEM samples onto a copper support grid (see figure 3.16 E).

To emphasize, while the viewing window of the FIB TEM sample may only be a few tens of microns long, the imageable area is extracted directly from the region of interest. The other TEM sample preparation methods mentioned thus far lack the feature of site–specificity.

3.6 Focussed Ion Beam – imaging and patterning

A focused ion beam (FIB) instrument is not exclusively limited to the preparation of TEM samples.[112–114] The FIB also allows for the imaging of small specimens, but in contrast to the SEM, it uses ions instead of electrons. At BYU the FIB system is a Helios Nanolab 600 Dual Beam from FEI. This "dual beam" setup has an electron column and a focused ion beam column.

3.6.1 Ions – The other charged particles

The use of ions for microscopy is quite analogous to the use of electrons, and much of the explanations described in this chapter relating to electron microscopy carry over to ion microscopy. This analogy is because ions, just like electrons, are charged particles, therefore, electrostatic and electromagnetic fields may be employed to accelerate, focus, and raster an ion beam onto and across a sample.[115]

Ion microscopes can use ions varying from He^+ ions up to Xe^+ ions and, theoretically, any element may be used as an ion source. One of the most common elements used for FIB microscopy is Ga in a source often referred to as a liquid-metal ion source (LMIS).[116] One distinguishing

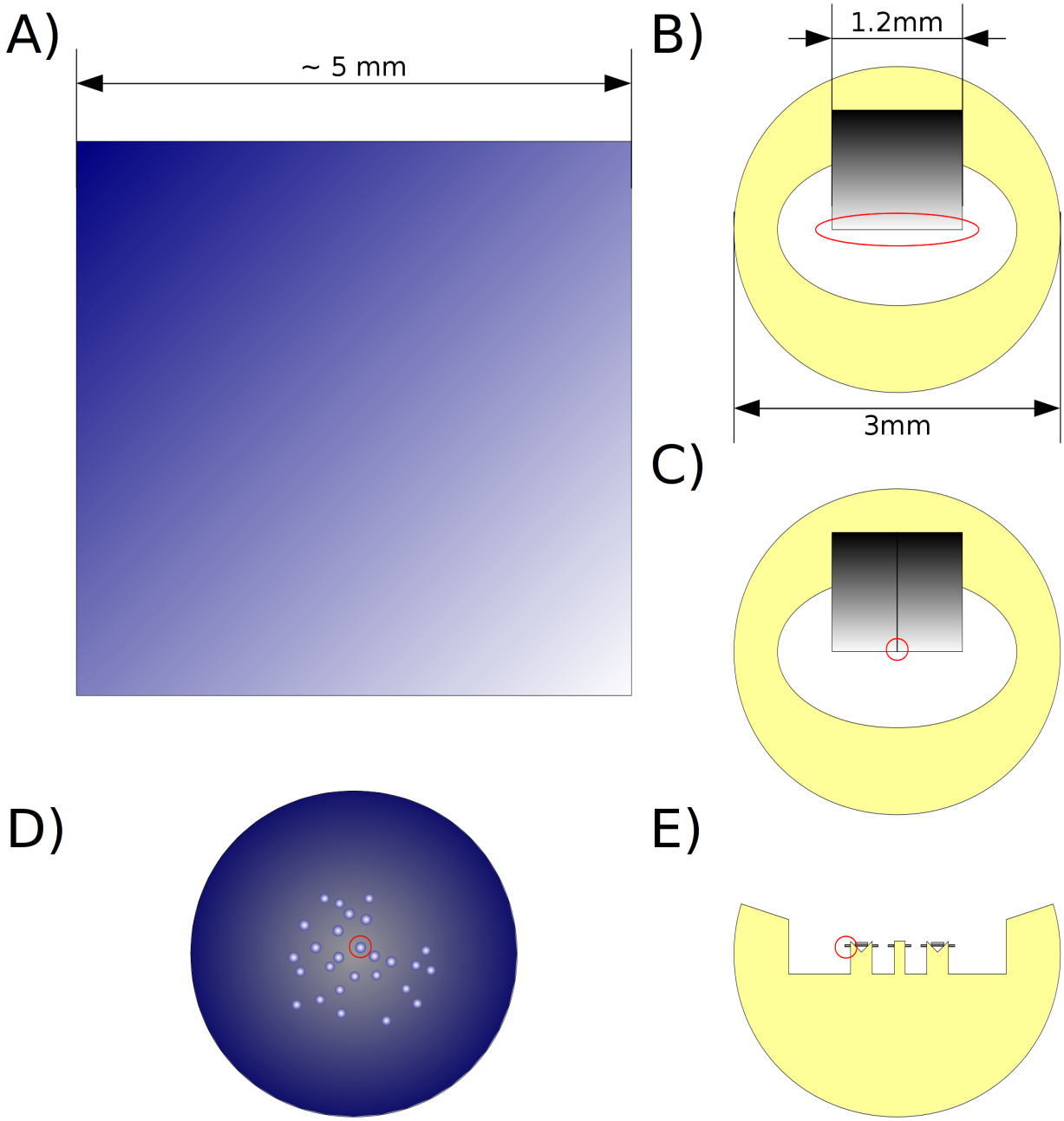

Figure 3.16 Diagram showing a relative comparison among TEM samples prepared by various sample preparation techniques. A) A 5 mm by 5 mm die typical sample size used in the SEM. B) Plan-view and C) cross-section samples prepared by the wedge technique mounted onto 3 mm support copper grids. D) Plan-view sample prepared by the chemical back-etched method on a 3 mm dimpled disk. E) 6 individual cross-section TEM samples prepared by FIB welded onto a support copper TEM grid. For comparison, some imageable areas are circled in red.

feature between electrons and ions is the wide range of element-dependent ion masses and sizes. As comparison, a Ga^+ ion is over 127,000 times more massive than an electron ($He^+ > 7{,}200\ m_e$ and $Xe^+ > 239{,}000\ m_e$). This difference in mass gives the accelerated ions enough momentum to erode the surface of the sample and reveal information not available to the electron beam, and the inherent size of the ion also determines the penetration depth.

3.6.2 Imaging

FIB imaging is analogous to that of the SEM (described in section 3.2) wherein a focused beam of ions is rastered (scanned) onto a surface and the image is dependent upon the ion-sample interactions.[117] In the most common manner, the ion impact onto a surface does generate a secondary electron signal which may be then used for imaging. Furthermore, other signals that may be used for imaging or sample analysis are generated from the ablated sample surface material.[118]

As well as with electrons, positively charged ions may also charge up the surface being imaged.[119] However an advantage presents with ion microscopy as these charged ions may be neutralized before they strike the surface by means of an electron flood gun. Thus, imaging of an insulating surface becomes now easier.

3.6.3 Patterning

As previously mentioned, the added mass of the ions gives these accelerated particles enough momentum to ablate the surface of the sample. This eroding process allows for the use of a focused ion beam to be used for the patterning of a sample.[118,120–128] As mentioned in section 3.5.3, it is through this eroding process that TEM samples are milled out of the specimen.

Deposition of materials is also performed in a FIB with the addition of a gas carying the material desired for deposition.[128,129] Thanks to the added momentum of the accelerated ions in a FIB, the rate of deposition os materials is increased.[130] One of the commonly used materials for FIB

deposition is Pt due to its conductive properties.

Some issues that arises due to the ablating nature of FIB patterning is that of re-deposition of the milled material[131] and ion damage on the surfaces of the material. Often these issues are addressed by controlling the current and spot size of the incident ion beam.[111, 132]

Chapter 4

Solid-phase crystallization of vanadium dioxide thin films deposited on amorphous silicon dioxide and their morphology -SEM imaging-

Though there are several methods that are successful for depositing $VO_{x,x\approx2}$ thin films onto various substrates (see section 2.5), one characteristic that they all share is the need to crystallize the $VO_{x,x\approx2}$ films. This can be accomplished by depositing directly onto a heated substrate, or by carrying out a post-deposition annealing in order to crystallize the deposited film.

Here we explore the annealing parameters and the resulting morphology achieved by solid-phase crystallization of VO_2 thin films deposited onto amorphous SiO_2. As mentioned in section 2.5.1 these samples were obtained from Kevin Coffey at UCF and comprised of amorphous $VO_{x,x\approx2}$ films (of 50, 10, and 5 nm nominal thickness) on an amorphous SiO_2 layer thermally

grown on a Si wafer.*

4.1 Introduction to Solid Phase Crystallization

Solid phase crystallization (SPC) has been extensively studied due to its application to the silicon industry.[133–135] The main goal of SPC is to give enough mobility to the atoms in an amorphous solid so that they may nucleate and allow those crystal nucleae to grow and form single crystals. This crystallization usually takes place by means of a "thermodynamic-driving-force," which may be accomplished by use of a furnace during an annealing process.[134]

The kinetics of the transition from amorphous material to crystalline material can be described by the "classical nucleation theory."† which is based on the capillarity effects at the crystal-amorphous interface.[134] The nucleation rate and the velocity of grain growth are explained by conventional thermodynamics. The energy required for nucleation carries two important factors: 1) The energy difference between amorphous and crystalline phases, ΔG_{ac} (proportional to volume); and 2) The energy required to maintain the amorphous-crystal interface (proportional to surface area).[134]

Figure 4.1 shows an energy diagram that helps explain the process of solid phase crystallization. In the energy diagram, the energies for the crystalline phase and the amorphous states are both local minima (labeled G_c and G_a respectively). Solid phase crystallization can take place as long as the crystalline state remains more "energy favorable" than the amorphous state. This means that free energy for the crystalline state is lower than the free energy for the amorphous state. The local minima between the crystalline state and the amorphous state are separated by an energy barrier. This energy barrier is due to the amorphous-crystal interface. In order to achieve solid phase

*Refer to appendix A.1 for details on the deposition of these films.

†For more details and references regarding this topic, the reader is encouraged to turn to "Thin Film Transistors: Materials and Processes" by Yue Kuo, 2003

crystallization, energy must be introduced into the system such that atoms found in the amorphous state (G_a) can overcome the barrier (G_1). The *rate* at which solid phase crystallization takes place depends, in part, on the size of the barrier (G_1), and how much more favorable the crystalline state is (ΔG_{ab}).[‡]

4.1.1 Thermodynamic rationale for solid phase crystallization

Based on classical thermodynamics, there should be an exchange of atoms at the amorphous-crystalline interface. The "jumps" that the atoms take to either make a crystal nucleus grow or shrink can be expressed by equations 4.1 and 4.2 respectively.[134]

$$\gamma^{+} = P\nu n_a f_c \exp\left(-\frac{\Delta G_1}{kT}\right) \tag{4.1}$$

$$\gamma^{-} = P\nu n_c f_a \exp\left(-\frac{\Delta G_2}{kT}\right) \tag{4.2}$$

Where P is the probability for an atom to make the "jump" in the interface; ν is the vibrational frequency; n is the atomic density at the amorphous-crystal interface; f_a and f_c represent the filling fraction of atoms; ΔG the height of the energy barrier; k is Boltzmann's constant; and T is temperature in Kelvin. The subscripts a and c refer to either amorphous or crystalline.

The net effect in the nucleation site is found by $\gamma = \gamma^{+} - \gamma^{-}$. The growth rate of the nucleation site can be found by

$$r_g = fV\gamma = fV\left(\gamma^{+} - \gamma^{-}\right) \tag{4.3}$$

where V is an atomic volume. Now, by assuming that $f_a \cong f_c \equiv f$, and that $n_a \cong n_c \equiv n$, then equation 4.3 can be written as[134]

[‡]Other factors that affect the rate of solid phase crystallization also include: The probability of an atom to overcome the barrier, temperature, the atom's vibrational frequency, and the number of atoms at the amorphous-solid interface

$$r_g = PnVf^2\nu \exp\left(-\frac{\Delta G_1}{kT}\right)\left[1-\exp\left(-\frac{\Delta G_{ac}}{kT}\right)\right] \tag{4.4}$$

where now the parameter ΔG_{ac} (The energy difference between amorphous and crystalline phases) is used. Figure 4.1 shows a schematic representation of the free energy of amorphous and crystalline states to help clarify the relationships between the amorphous state, the crystalline state and the energies G_a, G_c, ΔG_1, ΔG_2, and ΔG_{ac}.

As a summary, Solid Phase Crystallization through thermal methods involves giving enough thermal energy to the atoms in the film to overcome the energy barrier (ΔG_1 in the figure) between the amorphous and crystalline states. In this manner, the atoms can find a more energetically preferred position in crystalline form. Annealing post-processing, (as mentioned in section 2.5) is a common technique for vanadium dioxide thin films.

4.2 Methods – Sample Annealing and SEM Characterization

200 mm wafers used for this study were provided by Kevin Coffey[§] at the University of Central Florida. The characteristics of these wafers are described in section 2.5.1[¶]. Pieces of these wafers were cleaved to squares approximately 5 mm on the side. These individual squares were then subject to the following process:

1. Samples were annealed with temperatures ranging from 200°C up to 1000°C and times ranging from 17 hrs down to 5 min.

2. Samples were imaged in the Scanning Electron Microscope in order to observe any noticeable changes.

3. Electron Back-Scattered Diffraction patterns were attempted to test for crystallinity.

[§]To whom the author would like to express his sincerest gratitude.

[¶]Refer to appendix A.1 for further details on the deposition parameters for these samples.

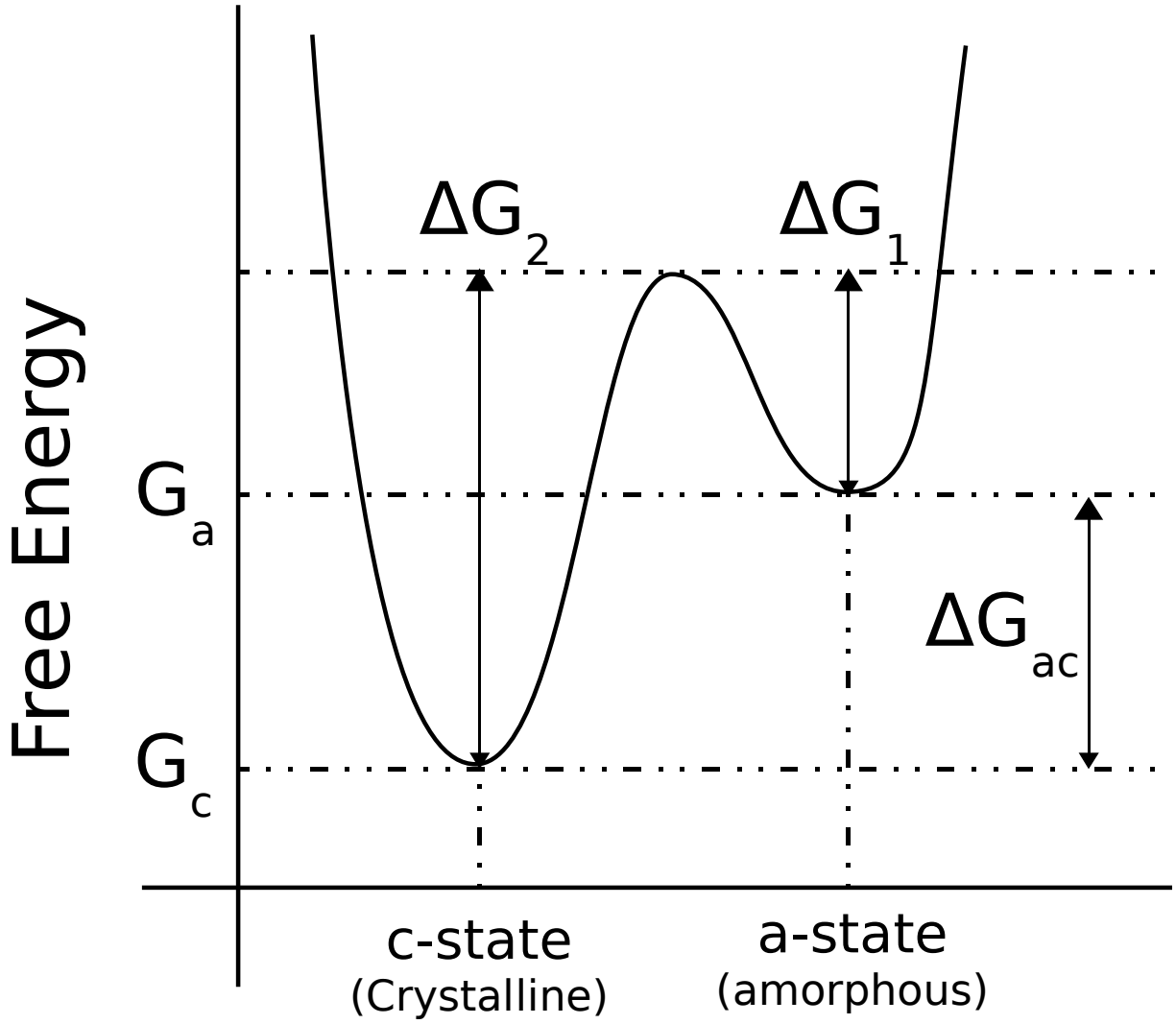

Figure 4.1 Schematic diagram of the free energy of amorphous and crystalline states. Kuo(2003).[134]

4.2.1 Solid Phase Crystallization - Annealing Procedure

Annealing conditions ranged from 200°C for more than 15 hrs up to 1000°C for 5 min. Depending on the environment or the time, annealing process varied slightly. The two environments chosen to anneal in were air and argon. In both cases, the temperature quoted was that reported by the temperature controller, and it was noticed to "ring" within 2°C upon reaching the set temperature.

Air Environment

For the anneals performed in air the furnace in figure 4.3 was used. The sample was placed inside the furnace, allowing it to be as close to the center of the tube as possible. The temperature controller was then programmed to ramp up to the selected temperature at the rate set by the controller. The temperature was held there for a specified amount of time and then allowed to cool down. Figure 4.2a shows a diagram of a typical annealing program.

Argon Environment

The furnace for this annealing process was manufactured by "Lindberg-Blue." (See Figure 4.4) The furnace uses a quartz tube to hold the sample in, while being able to control the environment in which the annealing takes place. Individual pieces are placed inside of the tube as close to the center of the tube (radially) and as close to the the thermocouple as possible (length-wise) (see figure 4.5). Samples were initially placed inside the quartz tube as close to the thermocouple as possible, with a few exceptions described below. The argon environment was controlled by flowing argon gas through the quartz tube. The argon used was 99.9% purity. Rubber seals were used in the inlet and outlet of the tube to prevent air from the surroundings to enter into the tube (see figure 4.6). A positive pressure was kept inside the quartz tube by using a vacuum oil bubbler gas outlet and a constant flow of argon into the tube. The flow rate used for these anneals was a constant 600 sccm as controlled by a Mass Flow Controller (see figure 4.7).

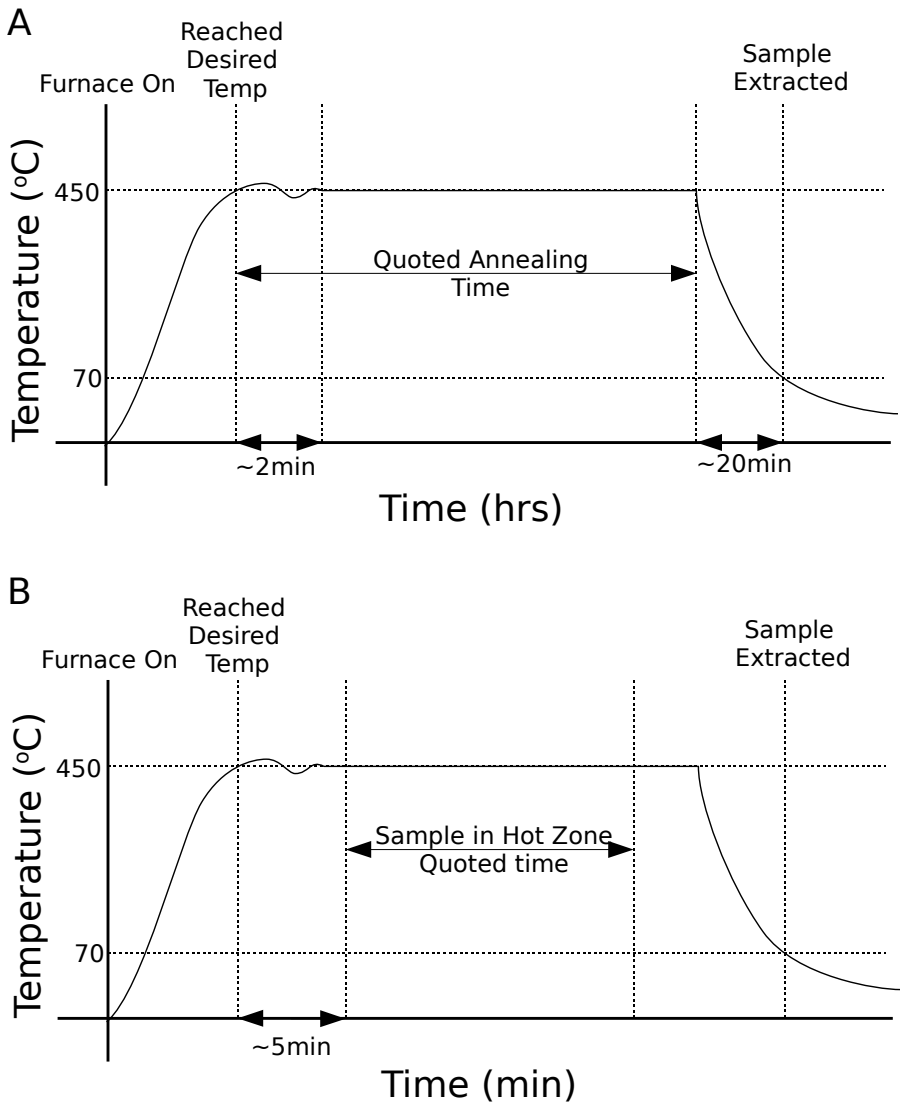

Figure 4.2 Temperature vs. time diagram depicting a typical annealing cycle. The temperature controller was allowed to ramp up at its default rate to the set temperature. There was a slight "ringing" once the set temperature was reached of (at most) 2°C. The annealing time ranged from about 5 min to 17 hrs before the furnace was allowed to cool down. Long term anneals ($>$ 1 hr) followed program A, where the sample was placed in the hotzone for the whole process. Short term anneals ($<$ 1 hr) followed process B where the sample was inside the furnace, but away from the "hot-zone" and was brought into the "hot-zone" only for the specified annealing time.

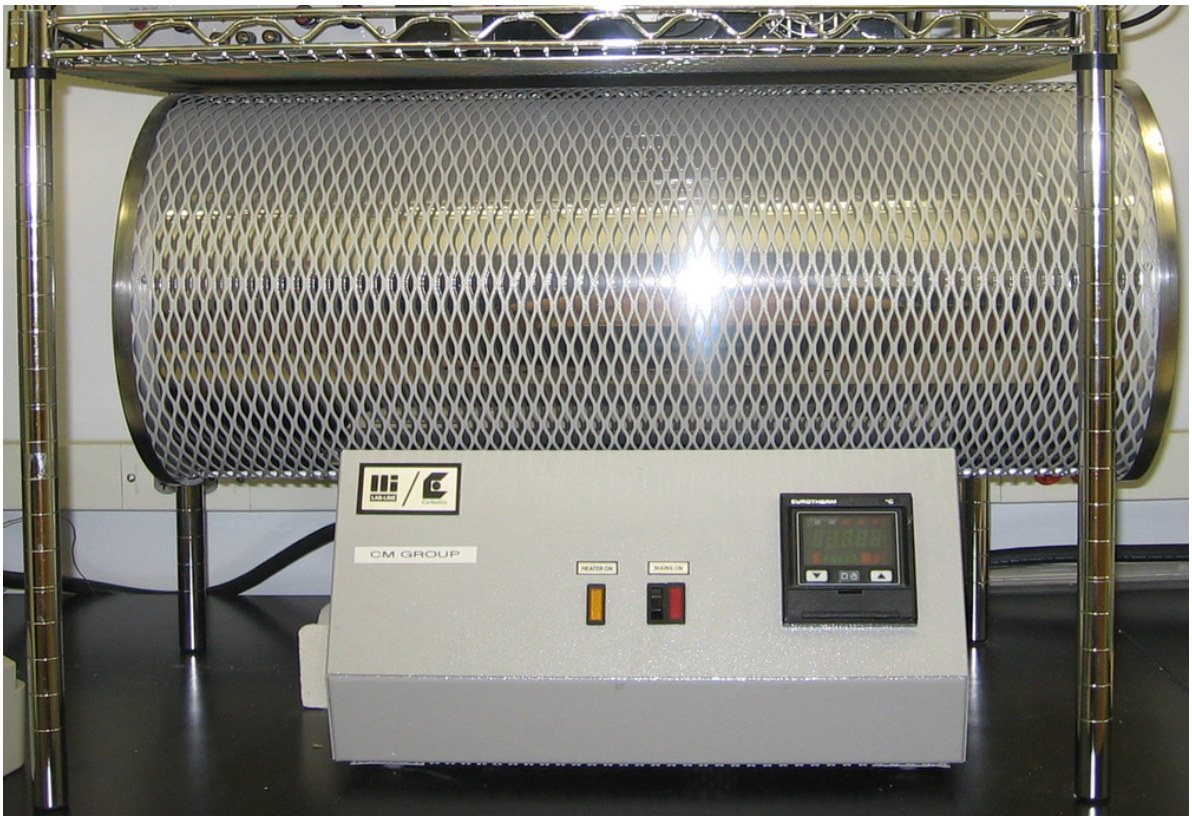

Figure 4.3 Furnace used for the anneals done in air.

Figure 4.4 Furnace used to perform the argon anneals in.

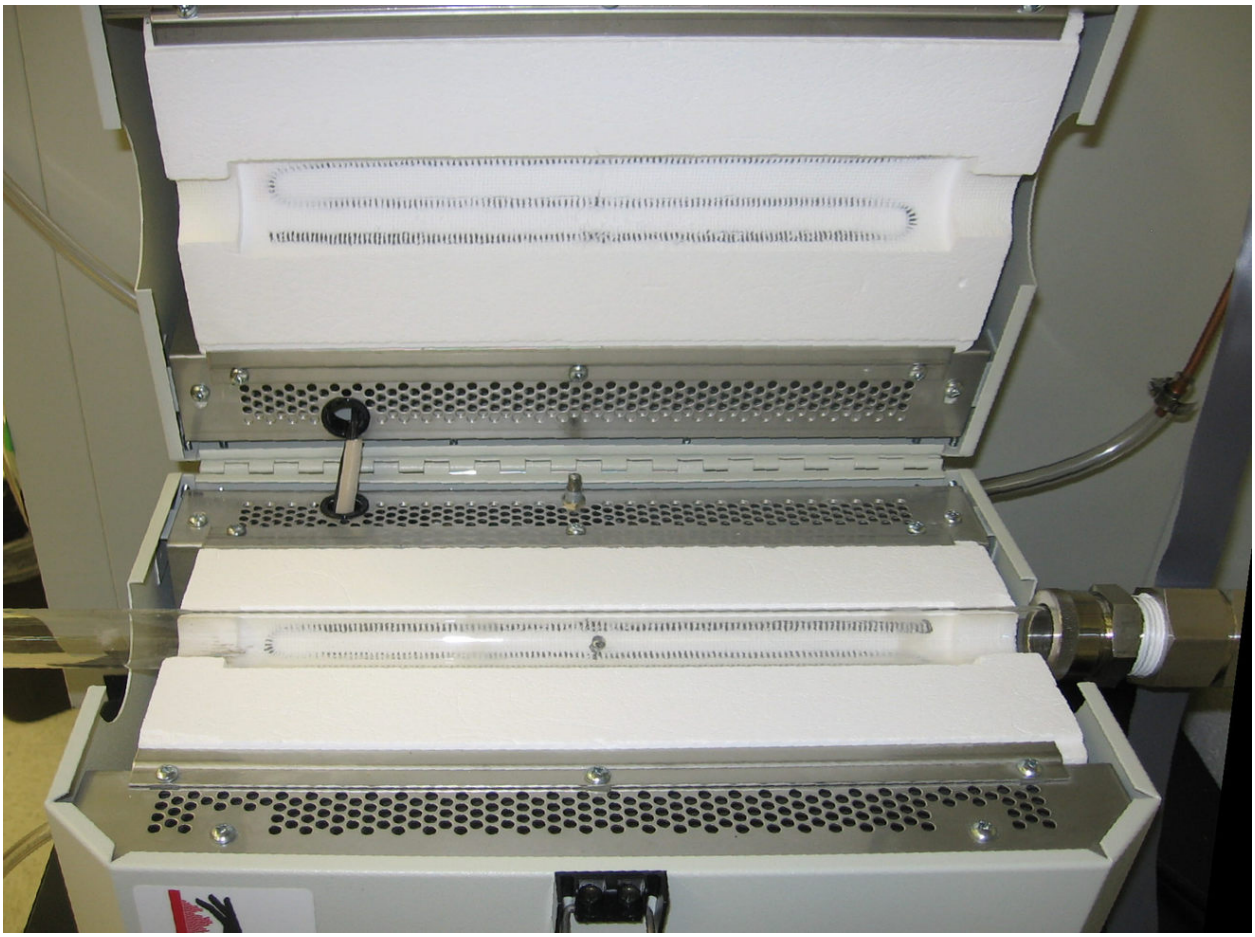

Figure 4.5 Furnace used to perform the argon anneals. The ability to open the furnace allows for easy placement of the sample close to the thermocouple (located in the middle).

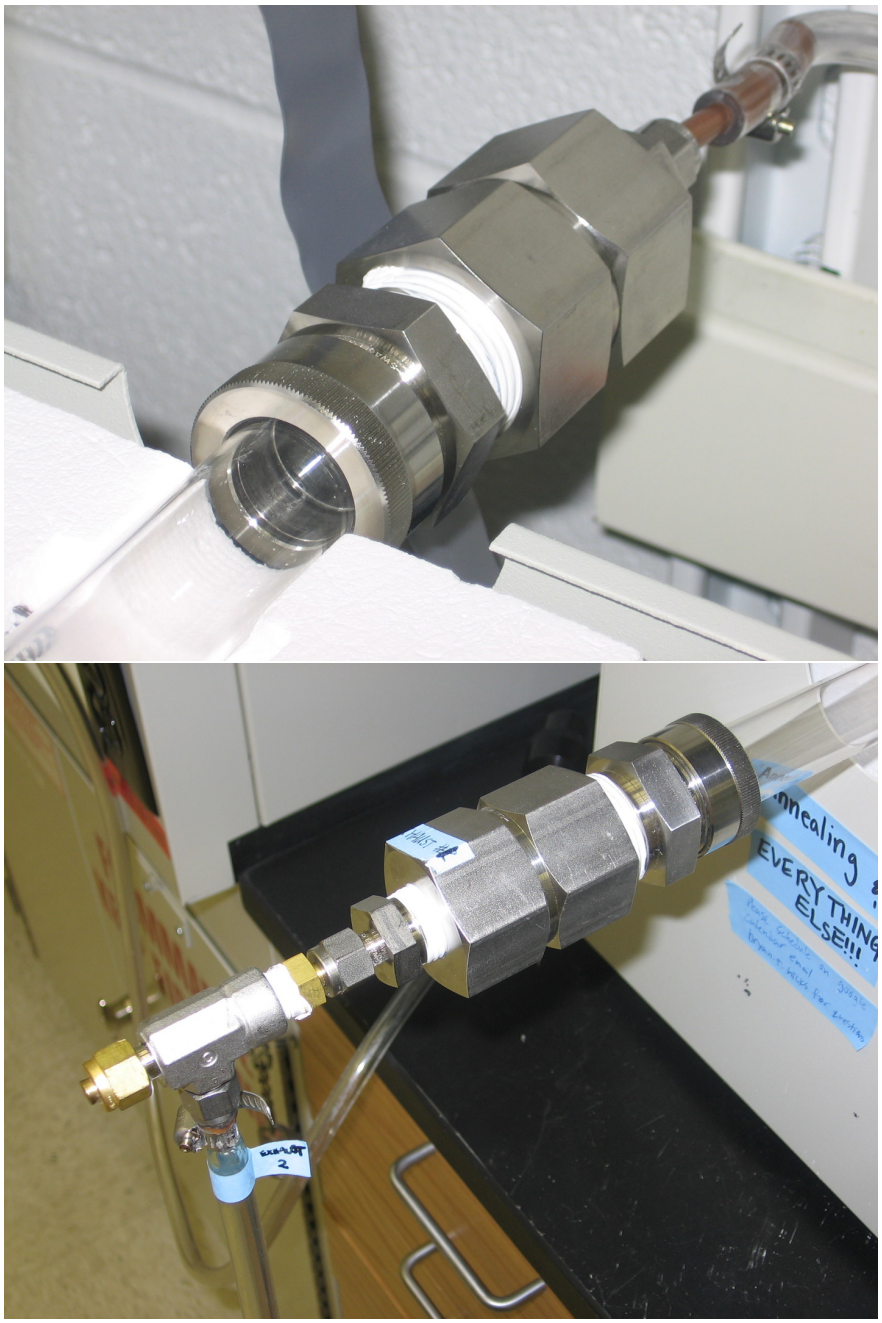

Figure 4.6 Both inlet and outlet to the quartz tube are fitted with a rubber "O"-ring to form an air-tight seal. Further, the outlet was outfitted with a "T" joint to allow a guiding rod to move the sample into and out of the "hot-zone." (Here, the "T" joint is plugged as it is not being used)

Figure 4.7 Mass Flow Controller used to control the argon flow.

For the cases where the anneals were on the order of one hour or longer, the sample was placed inside the furnace and the conditions mentioned above were set before any annealing took place inside the furnace. Upon ensuring that the setup was correct, the furnace was allowed to purge (at room temperature) for 10 minutes in order to eliminate the air inside the quartz tube. The furnace's temperature controller was then programmed to ramp up to the selected temperature at the rate set by the controller. The temperature was held there for a specified amount of time and then allowed to cool down (see figure 4.2A). This whole process was completed maintaining the argon flow until the sample cooled down to below 100°C. At that point, the annealing chamber was opened and the sample extracted.

For the cases where the anneals were 30 min or less, the process in figure 2.1b was followed. In this process, the sample was initially placed inside the furnace, however it was placed away from the "hot-zone." The outlet in the argon furnace was outfitted with a "T" joint to allow for a guiding rod to move the sample into and out of the "hot-zone" (See figure 4.6). This technique allowed the placement of the sample to within 2 mm of the zone. The conditions mentioned above were set before any annealing took place just like mentioned previously. Upon ensuring that the setup was correct, the furnace was again allowed to purge (at room temperature) for 10 minutes in order to eliminate the air inside the quartz tube. The furnace's temperature controller was then

programmed to ramp up to the selected temperature at the rate set by the controller. The furnace was then given a 5 min window of time to stabilize. After the furnace was thermally stable, the sample was moved into the "hot-zone," the sample kept there the specified amount of time, and then moved out of the "hot-zone." The furnace was then allowed to cool down. This whole process was completed while maintaining the argon flow until the furnace cooled down to below 100°C. At that point, the furnace was opened and the sample extracted.

4.2.2 Surface Imaging Through Scanning Electron Microscopy

The Physics and Astronomy Department at Brigham Young University is equipped with a Phillips XL30 Scanning Electron Microscope (figure 4.8). This particular microscope is equipped with several detectors, including a detector for Orientation Imaging Microscopy. Further, this instrument has an "Ultra High Resolution" (UHR) mode that gives the ability to obtain spatial resolution in the nanometer range.

After the annealing process took place, the samples were mounted onto an aluminum SEM stub. Adhesion to the stub was accomplished by means of colloidal graphite in order to ensure a conductive path from the sample onto the SEM stub (see figure 4.9). The colloidal graphite was diluted using isopropanol (allows for quicker drying) It was of great importance to ensure the complete drying of the colloidal graphite to prevent contamination from hydrocarbons inside the SEM vacuum.

Both "plan-views" and "tilted-views" were acquired through the SEM. The conditions under

Figure 4.8 Phillips XL30 Scanning Electron Microscope. Shown in the picture are also the SE, the XEDS, and the EBSD detectors

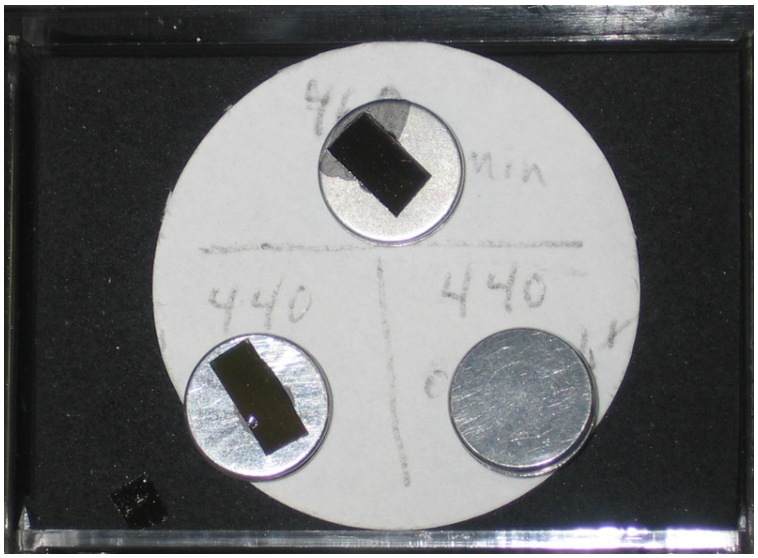

Figure 4.9 Samples were mounted onto a SEM stub by means of colloidal graphite in order to ensure a conductive path from the sample onto the stub.

which the images were acquired depended upon the type of image desired.[‖] The specific conditions of the beam, such as spot size, accelerating voltage,as well as the detector used, were recorded with each image taken. It was imperative to be able to find a distinguishable feature (any feature) in order to be able to properly focus the image and correct for astigmatism. As the image is magnified, the focus and stigmators are manually corrected. The image was usually magnified as high as the spot size and voltage permit, while ensuring that the focus and astigmatism were corrected. Most images were then taken at a lower magnification, while the maintaining the probe as finely focused as possible and thus better detail might be extracted from the image at a lower magnification.

[‖]The accelerating voltage can be as low as 1 kV and as high as 30 kV. Spot sizes are labeled from 1 to 7 where a smaller number indicates a finer probe. Usual imaging under this mode is best achieved with a spot size of 3, a 5 kV accelerating voltage, and placing the sample at a working distance of 5 mm. UHR mode can also be used under these settings.

Plan-View Surface Imaging

In order to obtain a plan-view image, the sample sits perpendicular to the beam. Figure 4.10 shows the inside of the SEM as the sample sits ready to be imaged in plan-view. This condition allowed for a "top-down" view of the sample. Grain sizes were observed and their length and width measured. Unfortunately, height information and roughness are not accessible with this view.

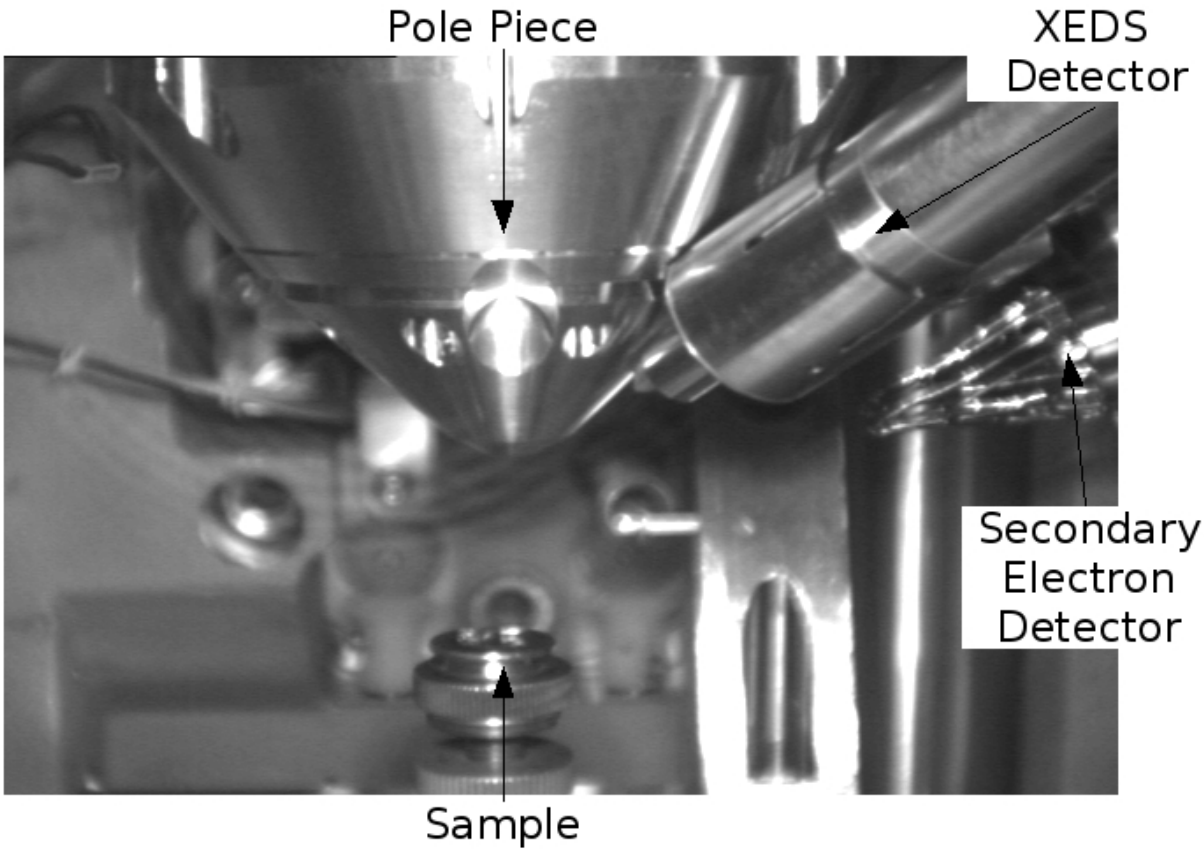

Figure 4.10 Interior of the Phillips XL30 SEM set for a plan-view image. The sample sits perpendicular to the beam.

Tilted-View Surface Imaging

The XL30-SEM allows for the sample to be tilted. The tilt allows for an estimate of the height and roughness of a surface. Although the height information cannot be quantified as well as an atomic

force microscope (AFM) would, qualitative roughness may be seen. In order to tilt the stage, the sample was moved further away from the pole piece as a safety precaution.** In order to carry out Orientation Imaging Microscopy (OIM) the sample was tilted at 70°. Figure 4.11 shows the inside of the XL30-SEM with the sample tilted ready to acquire an EBSD pattern.

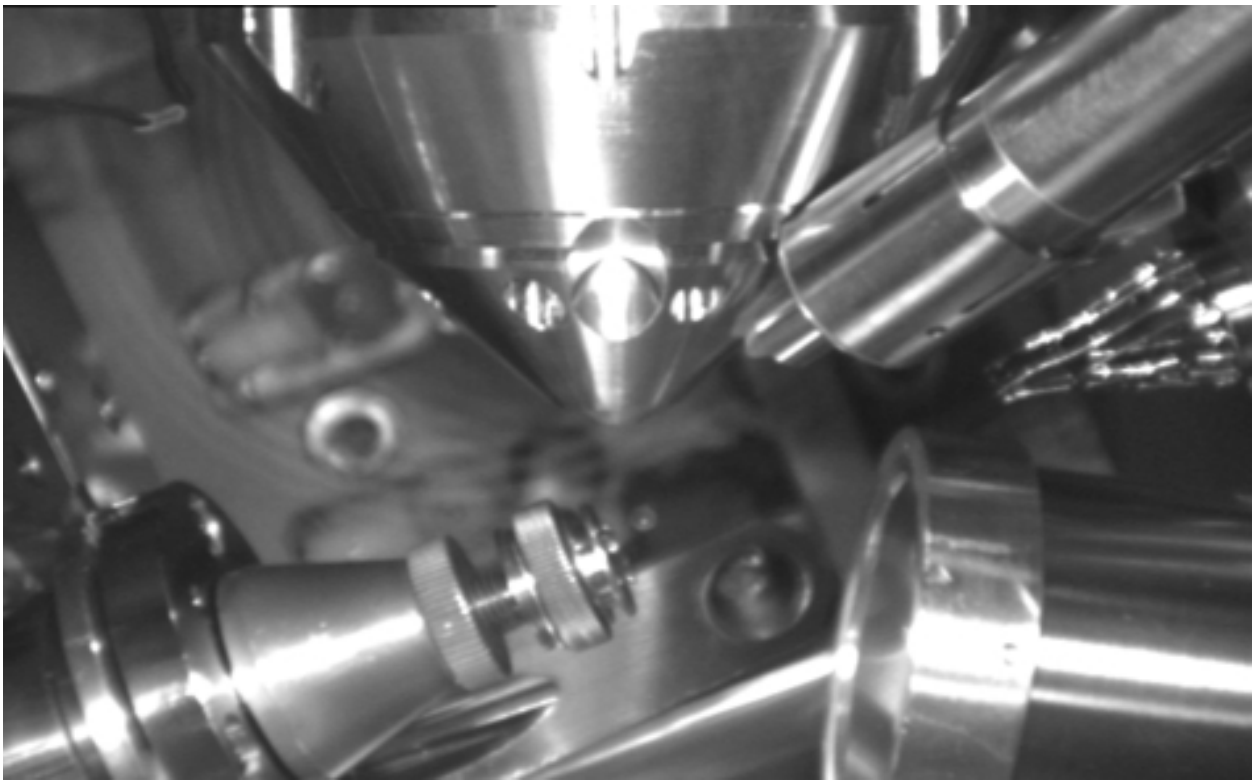

Figure 4.11 Interior of the Phillips XL30 SEM set for a tilted-view. The normal to the sample is 70° away from the beam. These conditions are necessary to perform an OIM scan. The EBSD detector has been inserted into the SEM.

4.2.3 Electron Back-Scattered Diffration Characterization

With the sample tilted so that the normal of the plane is 70° away from the electron beam, EBSD patterns were obtained. The working distance of the sample was such that the back-scattered

**Due to the tilting, the sample itself moves, so if it is desired to image the same area with a plan-view and a tilted-view, the working distance of the sample should be taken into account.

electrons hit the phosphor screen (see figure 3.8). The sample's x, y, and z, coordinates were taken with respect to the stage itself, not with the beam. Thus, in order to change the working distance (distance to the pole piece) the y and z coordinates of the sample were manually adjusted.[††] The EBSD detector and the SE detector were used simultaneously in some instances. In this manner, the working distance was adjusted so that the highest signal was detected in the EBSD detector, while keeping the area of interest imaged. Typically, a working distance of 12 mm was optimal. (see figure 4.11)

In order to achieve an indexable pattern, enough electrons must hit the phosphor screen so that an image is formed. This requirement in current limited the available beam conditions and it was usually achieved with an accelerating voltage of 25 kV and a spot size of 6[†]. With this beam condition, the spatial resolution in the SEM was greatly diminished.[‡]

The technique of OIM is based on collecting EBSD patterns from different areas in the sample and forming an image based on the orientation of the grains (see section 3.2.2.

Electron Back-Scattered Diffraction on VO_x

Crystallinity of the annealed VO_2 samples was tested by EBSD. The SEM was set as described previously and shown in figure 4.11. Even though the EBSD detector and the SE detector can be used simultaneously as described before, individual patterns are collected from spots in the surface. Thus, the imaging of the surface is "frozen" so that the beam can be placed in a specific spot and the pattern collected.

If, and only if, the beam is placed in a large enough crystal, a EBSD pattern will be formed.

[††]The SEM software does not seem to provide an automated process that can achieve this

[†]The label "spot size" is a term used related to the electron beam current wherein a spot size of 1 is the lowest current (thus finer focused beam) and 7 is the highest current (thus harder to focus the beam).

[‡]Finer scans may be attempted with smaller spot sizes, but at the expense of longer collection time, danger of sample drift, and possible contamination to the sample.

If not, no line patterns will be observed. Since there is the possibility of crystals in different orientations, individual patterns may be difficult to observe. Some steps were taken in order to enhance the EBSD patterns collected:[§]

1. A background image was obtained while a SEM image is being obtained. This way, the background image was an average of the patterns in all the area within the SEM view.

2. When a EBSD pattern was collected from a specific spot, the background image was subtracted in order to help enhance the image.

By doing these steps, crystallinity of the sample may be observed. The software was used to index the pattern obtained and compared with a list of pre-loaded calculated EBSD patterns for indexing (see section 3.2.3). Identification of the crystals observed was carried out at this time. It is also during this stage where the average exposure time was determined in order to obtain indexable patterns.

As show in figure 4.21 indexing of the acquired EBSD patterns was based in several criteria:

1. Observed crystallographic zones

2. Observed Kikuchi bands

3. Angles between Kikuchi bands

4. Kikuchi band widths

These parameters were compared with the calculated EBSD patterns. Using these parameters, each obtained EBSD pattern received a number of "votes" as well as a confidence index as to what material offers the best match.

[§]The software offers several tools to digitally enhance the EBSD patterns collected. It was found that a simple background subtraction was more than adequate.

4.3 Results of Annealing Amorphous $VO_{x,x\approx2}$ Thin Films in an Argon Atmosphere

As described in section 4.2: The films were subjected to an annealing process in order to achieve Solid Phase Crystallization; then the morphology of the resulting films were studied through scanning electron microscopy (to characterize the average grain size and film continuity) and the crystallinity of the grains through electron back-scattered diffraction. The results for the annealed films performed in an argon atmosphere are presented in the following subsections.

4.3.1 Morphology of Solid Phase Crystallization Observed in the SEM

Three sets of wafers were used to study the annealing time-temperature parameter space. A wafer with a 50 nm thick VO_2 amorphous film was used to probe the overall parameter space by ranging in temperature from 200°C up to 1000°C and times from 10 min to more than 10 hrs. Based on the results from this wafer, the parameter space was narrowed for wafers VO_2 films 10 nm and 5 nm in thickness.

50 nm thick amorphous $VO_{x,x\approx2}$ films

Table 4.1 summarizes the annealing conditions for individual samples, as well as the average grain sizes obtained. Changes in the surface are evident from the micrographs shown in Figure 4.12. Higher surface mobility was observed for higher temperatures. At 1000°C, grain growth was limited by the amount of material available. This was evident from the formation of grain sizes up to 1 μm in length. Isolated particles decreased in size as temperature decreased. It was observed that 500°C showed the formation of individual grains when given a large time to grow and semi-continuous films for shorter times.

Continuous and semicontinuous crystalline thin films were obtained with anneals between

400°C and 450°C. Again, temperature and time helped determine the size of the grain obtained.

Under argon anneals, no change in the surface was observed for anneals under 300°C.

Temperature °C	~10 min	~30 min	~1 hr	~10 hrs
< 300	–	–	–	NEP
400	–	–	NEP	50 nm*
440	NEP	NEP	IC	100 nm
450	NEP	IC	200 nm	250 nm
500	300 nm	500 nm (IP)	–	–
680	500 nm(IP)	500 nm(IP)	–	–
1000	LIP> $1\mu m$	LIP> $1\mu m$	–	–

Table 4.1 Average particle size resulting from annealing process in argon. The following labels are used: — NEP - "No EBSD Patterns" Observed; — IC - "Inconclusive" - There was evidence of EBSD, however the acquired patterns could not be adequately indexed; — IP - "Isolated Particles"; — LIP - "Large Isolated Particles"; — finally, a "dash" (−) is placed for those conditions not tested. *The films annealed at 400°C for over 10 hrs yielded distinct particles that produced EBSD patterns, but the quality of the EBSD patterns obtained was quite faint and not easily indexable.

10 nm thick amorphous $VO_{x,x\approx 2}$ films

As observed from the results in the 50 nm $VO_{x,x\approx 2}$ crystallization occurs above 300°C and they stop being continuous above 500°C for an hour. Therefore, the annealing parameter space for the 10 and 5 nm $VO_{x,x\approx 2}$ films was set using these limiting conditions. These 10 nm samples were annealed under an argon atmosphere using the method described in section 4.2.1 (page 68) with annealing temperatures of 380°C, 400°C, 450°C and 500°C. The annealing times chosen for these

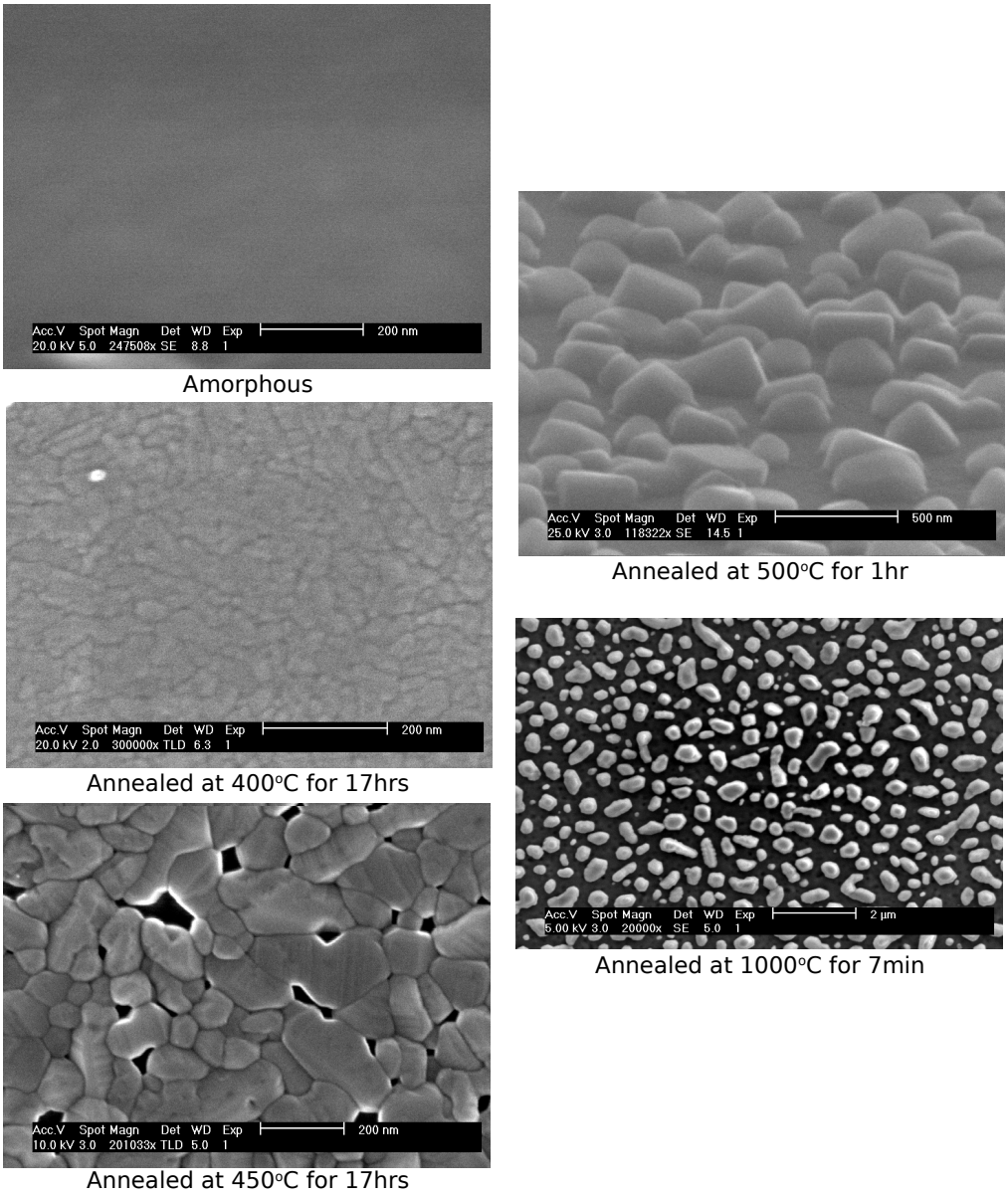

Figure 4.12 Scanning electron micrographs of the resulting 50 nm VO_2 films annealed under various conditions. Scale bars vary from 2 μm in the 1000°C anneal down to 200 nm in the 450°C anneal. Grain growth is evident as a function of temperature. Higher temperatures showed higher mobility as larger and isolated grains are formed.

films included 10 min, 30 min, and 60 min[‡‡]. Since the annealing times were 60 minutes or less, the reported time inside the annealing furnace followed that of figure 4.2B.

Figure 4.13 shows box plots of the measured particle sizes for films annealed for 10 min at 400°C, 450°C and 500°C. For a relatively constant annealing time, the plots show an evident particle size dependence on temperature. The average particle size increases with increasing temperature. Furthermore, as the plot shows, there is also a wider distribution of particle sizes with increasing temperatures.

Scanning electron micrographs of the 10 nm $VO_{x,x\approx2}$ films annealed for constant time are shown in figures 4.14 (10 min anneals) and 4.15 (60 min anneals). The temperature dependent growth is qualitative evident in both figures. The scanning electron micrographs for the 10 min anneals also show the increased surface mobility (with increased temperature) of the VO_2 films on the SiO_2 layer. This surface mobility is evident due to the larger voids between grains as temperature increases. This same effect of surface mobility is evident in the 60 min anneals shown in figure 4.15.

[‡‡]Not all combinations of temperatures and times were attempted. For a summary of temperatures and times see figure 4.18

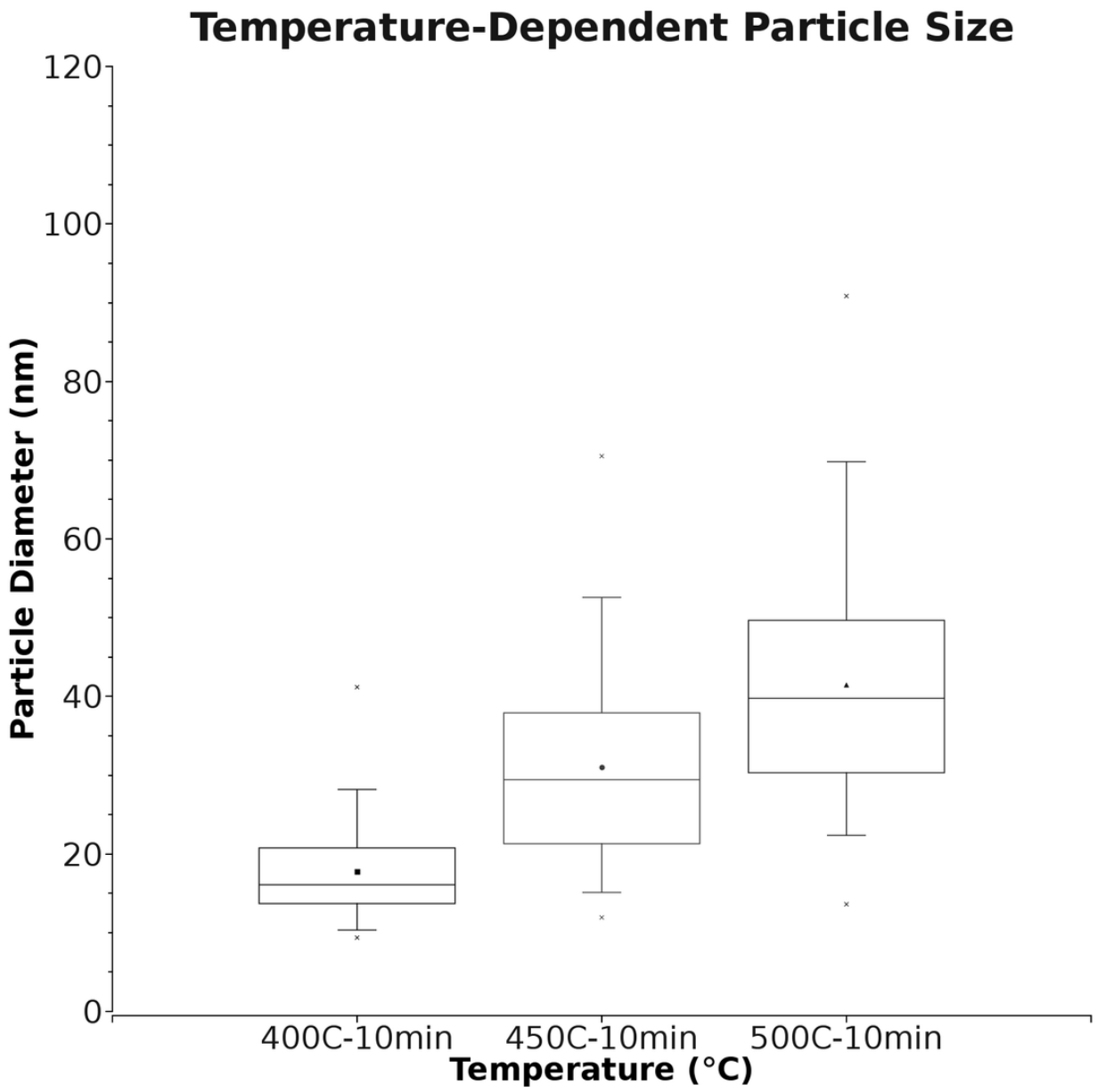

Figure 4.13 Box plots (with outliers) for the particle size distribution for 10 nm thick $VO_{x,x\approx2}$ samples annealed for 10 min. The dependence in annealing temperature of the particle size and distribution is evident.

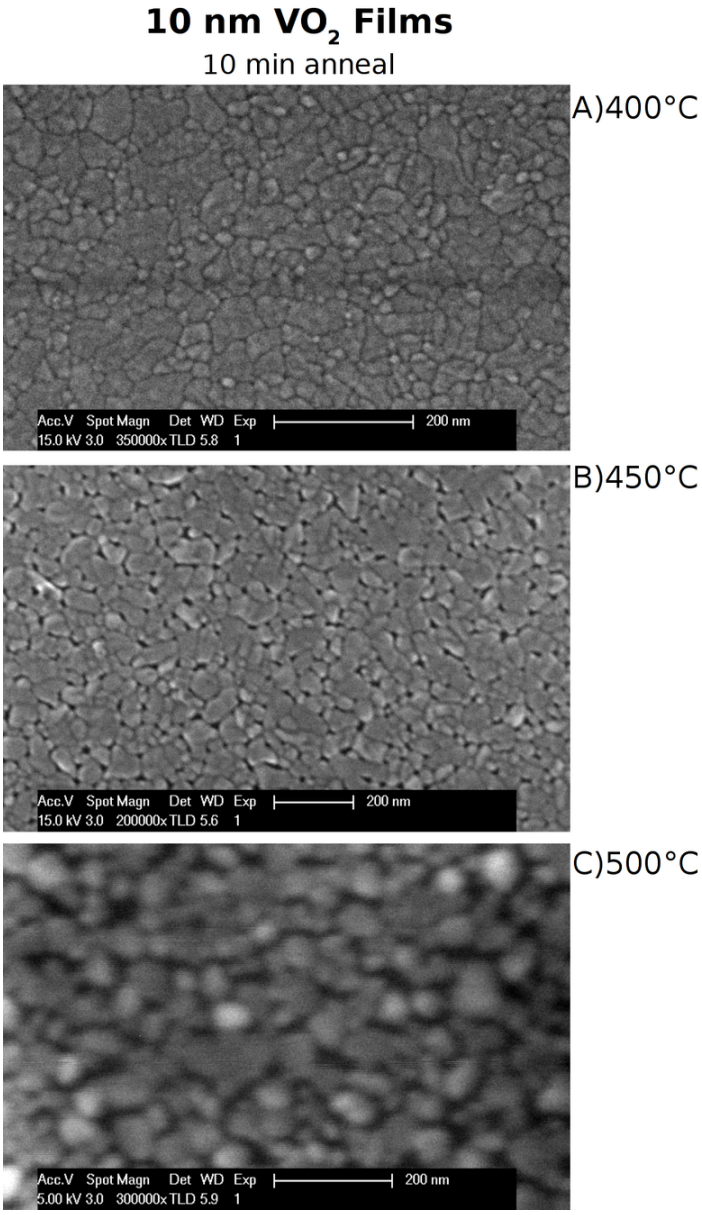

Figure 4.14 Scanning electron micrographs showing the particle size temperature dependence for 10 nm thick $VO_{x,x\approx2}$ film annealed for 10 minutes. Grain growth is evident as a function of temperature. Higher temperatures showed higher mobility as larger and isolated grains are formed.

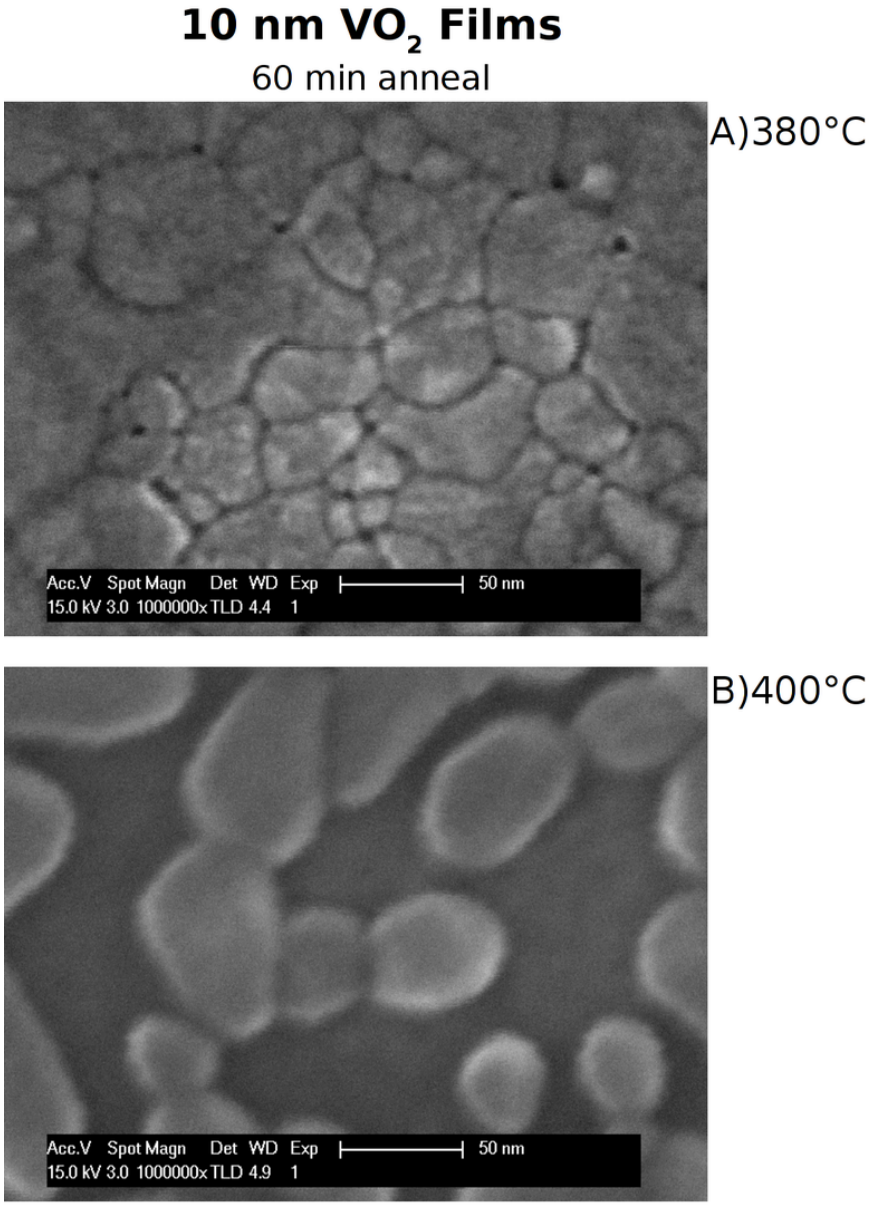

Figure 4.15 Scanning electron micrographs showing the particle size temperature dependence for 10 nm thick $VO_{x,x\approx2}$ film annealed for 60 minutes. Grain growth is evident as a function of temperature. Higher temperatures showed higher mobility as larger and isolated grains are formed.

Figure 4.16 shows box plots of measured particle sizes for 10 mn $VO_{x,x\approx2}$ films annealed at 400∘C for 10 min, 30 min, and 60 min. For a relatively constant annealing temperature, the plot shows evident grain growth as a function of time. Furthermore, as the plot shows, there is also a wider distribution of particle sizes with increasing annealing times. A qualitative view of grain growth as a function of time from these three films is shown on the micrographs in figure 4.17. The grain growth is evident in the micrographs of the 10 min and 30 min anneals (fig. 4.17 A and B). In the 10 min anneal the area comprised of smaller particles in larger than in the 30 min anneal. Furthermore, as the sequence of figures 4.17A, B, and C hint, grain growth continues at the expense of the smaller particles.

To summarize the annealing parameters for the 10 nm VO_2 films, figure 4.18 plots the average particle size as a function of time for films annealed at 380°C, 400°C, 450°C, and 500°C. As shown in the plot, anneals at 500°C for 10 min and 380°C for 60 min were used as limits in the parameter space. For constant times, the temperature dependence is shown as higher temperatures yield (on average) larger particles. Similarly, for constant temperatures, longer times yield (on average) larger particles. To note, recalling the box plots in figures 4.13 and 4.16, there is also a distribution of particle sizes associated with each anneal[†].

[†]For clarity, the distribution of sizes was not plotted in figure 4.18

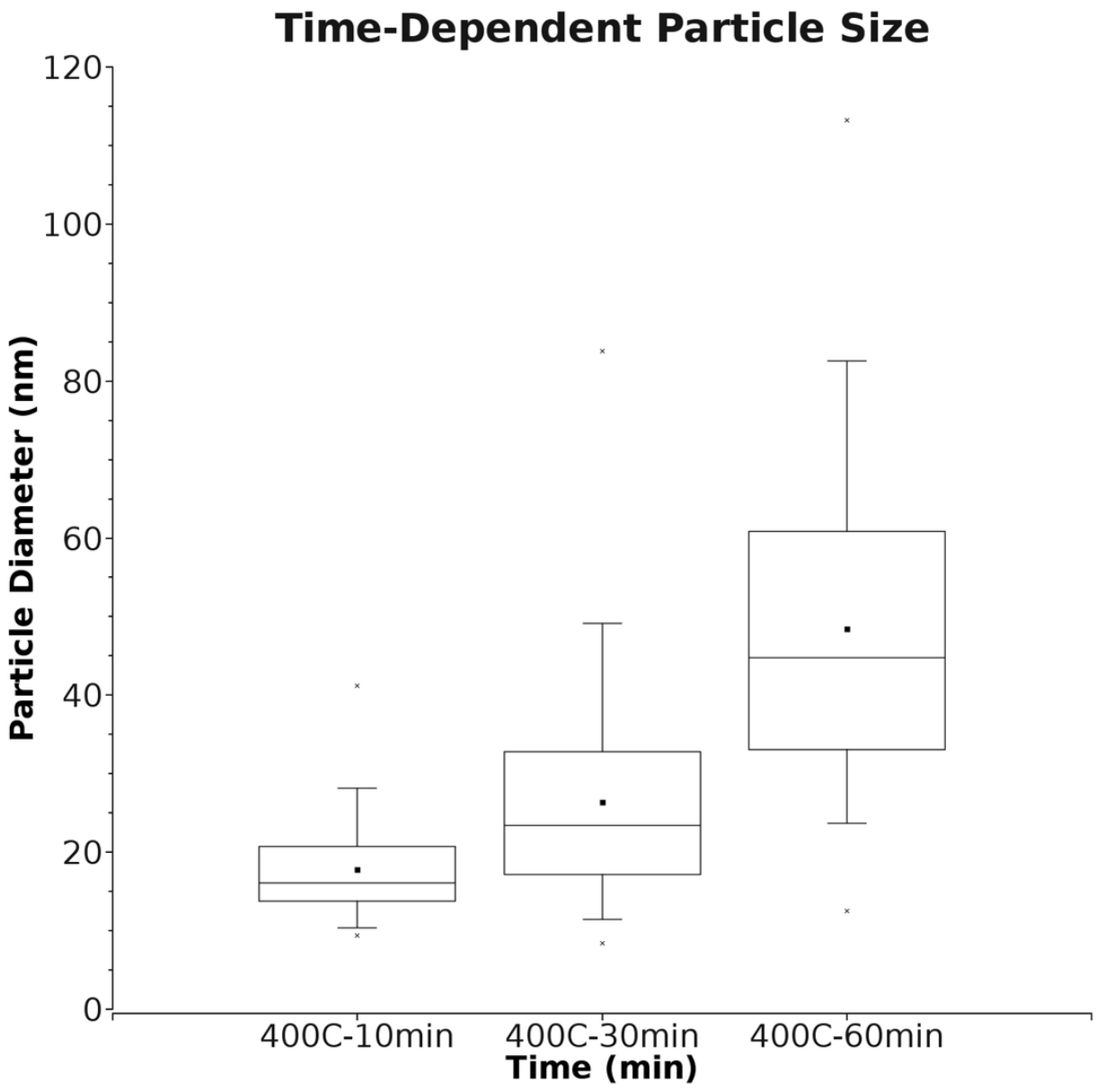

Figure 4.16 Box plots (with outliers) for the particle size distribution for 10 nm thick VO_2 samples annealed at 400°C. The dependence in annealing time of the particle size and distribution is evident.

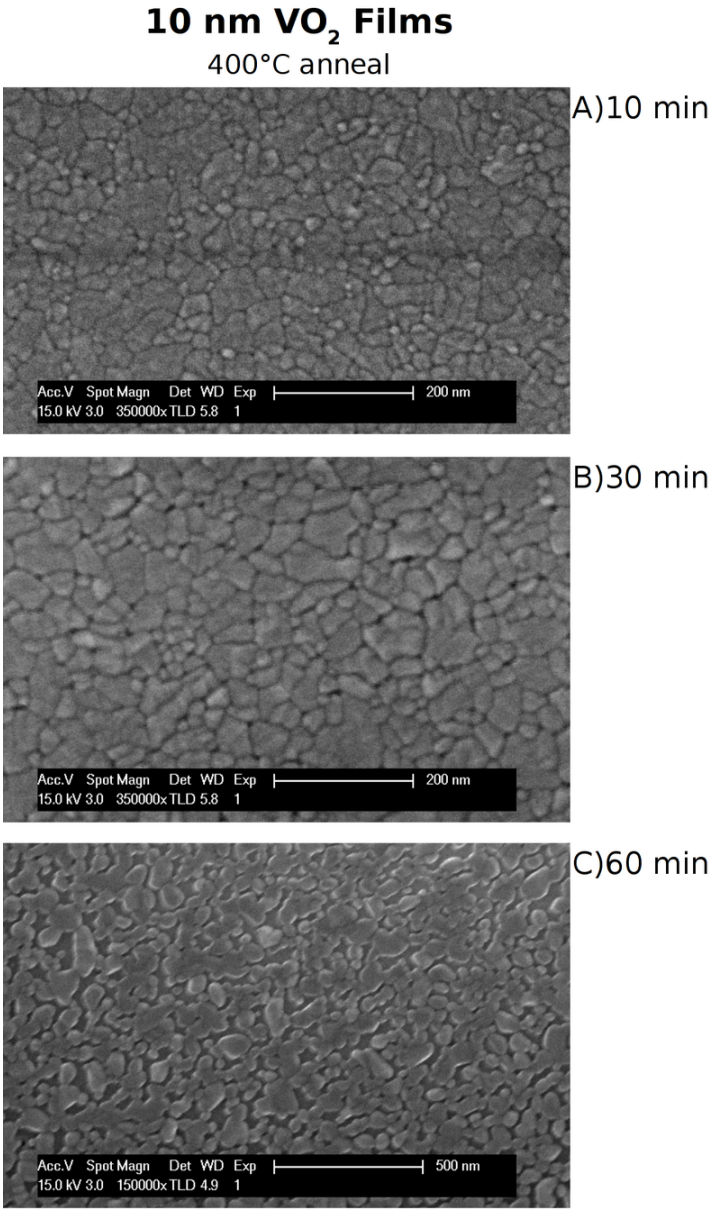

Figure 4.17 Scanning electron micrographs showing the particle size temperature dependence for 10 nm thich $VO_{x,x\approx2}$ film annealed for 10 minutes. Grain growth is evident as a function of temperature. Higher temperatures showed higher mobility as larger and isolated grains are formed.

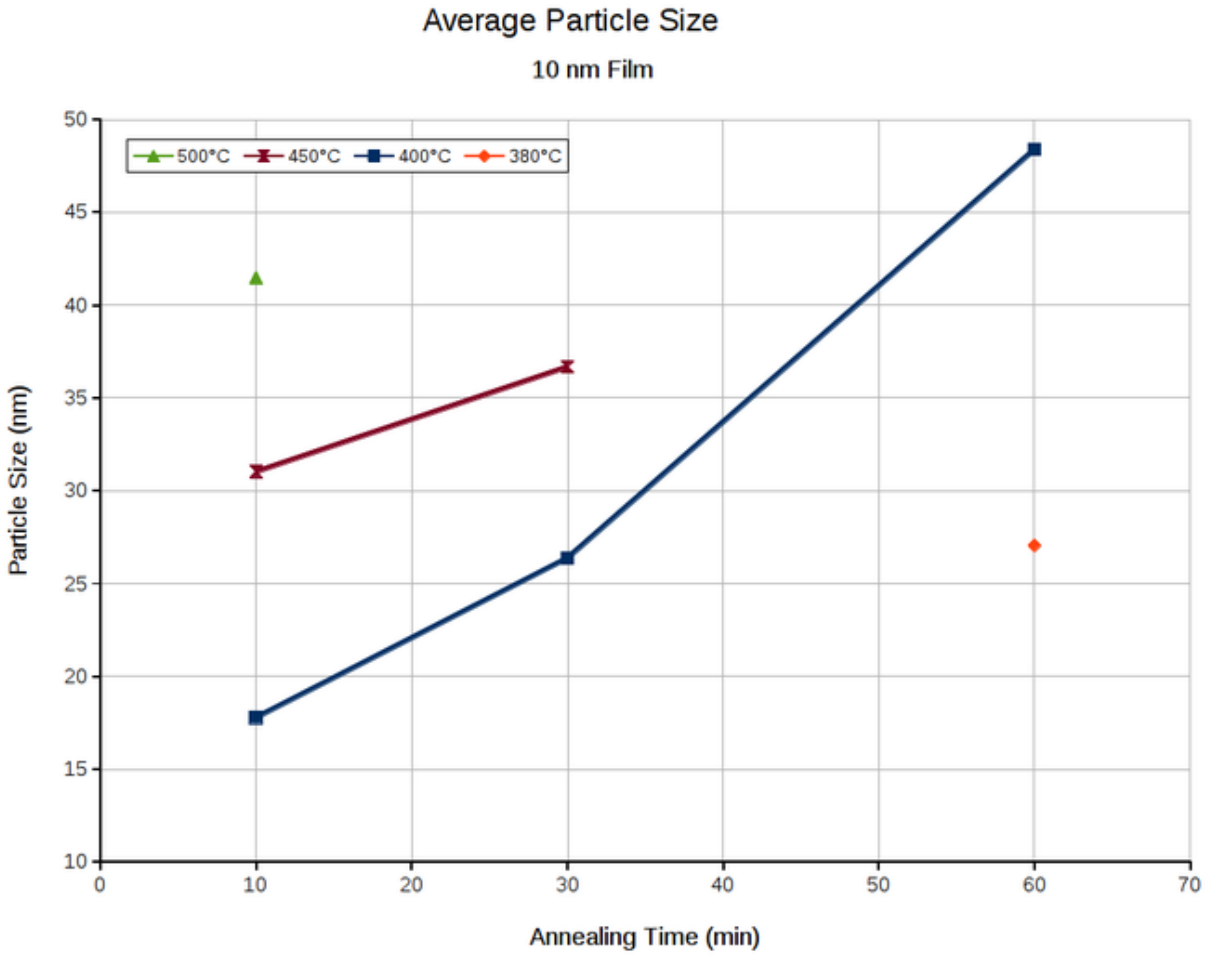

Figure 4.18 Summary of the average particle size for 10 nm thick $VO_{x,x\approx2}$ films annealed under different conditions. The dependence in annealing time and temperature of the particle size and distribution is evident.

5 nm thick amorphous $VO_{x,x\approx 2}$ films

As mentioned with the 10 nm $VO_{x,x\approx 2}$ film anneals (page 83), these $VO_{x,x\approx 2}$ 5 nm-thin films were annealed under an argon atmosphere for times 60 min and less. The temperature dependence of grain size in these films is depicted in figures 4.19 and 4.20.

Figure 4.19 shows box plots for the measured particle sizes in the 5 nm $VO_{x,x\approx 2}$ annealed for 30 min at 400°C and 450°C. Similar to the 50 nm and 10 nm $VO_{x,x\approx 2}$ annealed films, there is a wider spread in particle sizes as well as a larger average particle size for the higher temperature anneal. Figure 4.20 shows scanning electron micrographs of 5 nm $VO_{x,x\approx 2}$ annealed for 60 min at 380°C, 400°C, and 450°C. While the same trend in average particle size is qualitatively observed in the micrographs in figure 4.20, it is noteworthy to mention the fine particles seen in the 60 min anneal at 380°C. These fine particles indicate that at 380°C there is enough thermal energy to overcome the amorphous energy barrier (Labeled ΔG_1 in figure 4.1) but at a very low solid phase crystallization rate (see equation 4.4)[‡].

[‡]A back-of-the-envelope calculation using equation 4.4 and data from the 50 nm, 10 nm and 5 nm $VO_{x,x\approx 2}$ annealed films puts ΔG_1 between 1.25 and 1.75 eV and $\Delta G_{ac} \approx (1/8)\Delta G_1$

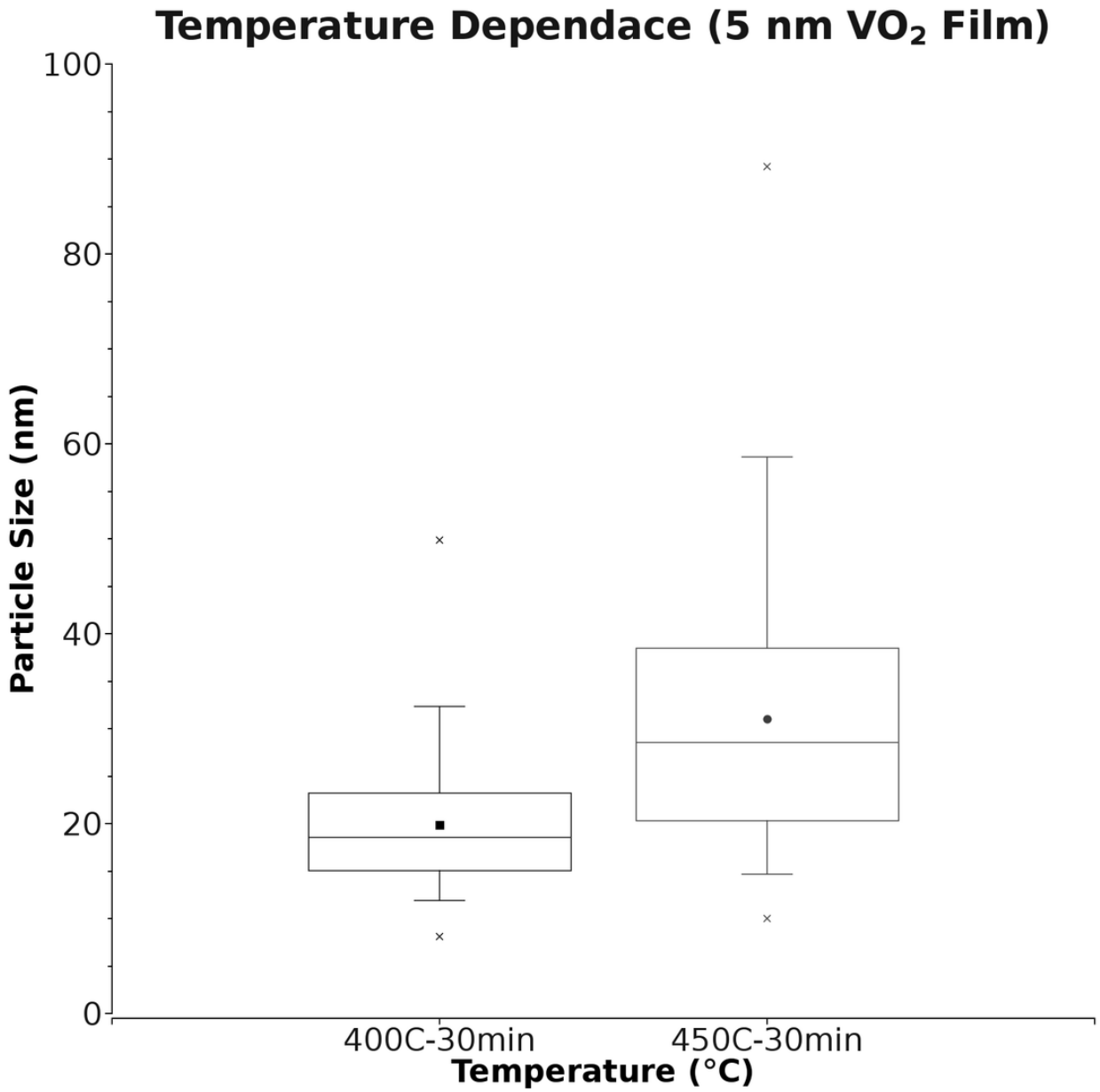

Figure 4.19 Box plots (with outliers) for the particle size distribution for 5 nm thick $VO_{x,x\approx2}$ samples annealed for 30 min. The dependence in annealing temperature of the particle size and distribution is evident.

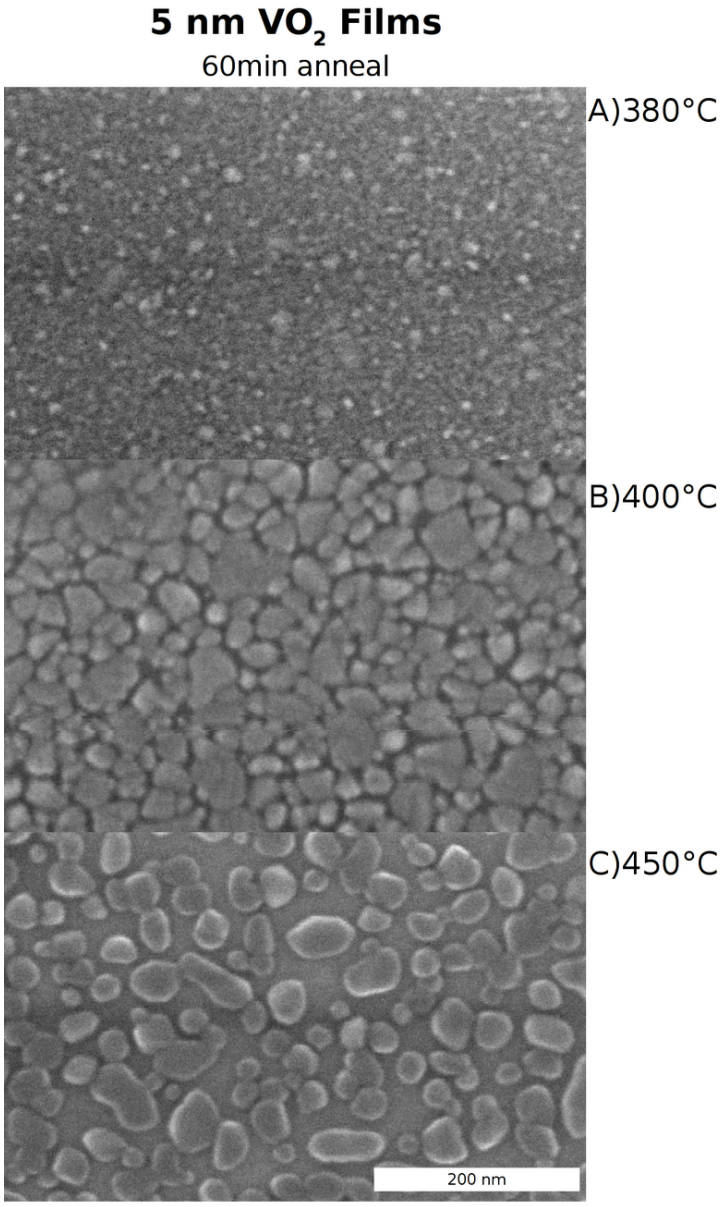

Figure 4.20 Scanning electron micrographs showing the particle size temperature dependence for 5 nm thick $VO_{x,x\approx2}$ film annealed for 60 minutes. Grain growth is evident as a function of temperature. Higher temperatures showed higher mobility as larger and isolated grains are formed.

4.4 Electron Back-Scattered Diffraction Characterization

As mentioned in sections 4.2.3 and 3.2.3, the annealed samples were identified and differentiated using electron back-scatter diffraction. The EBSD system consisted of a TSL/OIM detector with a 1024 by 1024 pixel CCD camera. The patterns acquired by the CCD are automatically indexed with the OIM software (TSL OIM Data Collection V. 4.6). The EBSD patterns corresponding to the crystal structures of different vanadium oxide stoichiometries (VO, V_2O_3, VO_{2-M1} (monoclinic), VO_{2-R} (tetragonal), and V_2O_5) were calculated by the OIM software from the material's known structural parameters (see section 3.2.3). Differentiation among the different vanadium oxides was initially performed as a test of this technique. Commercial powder samples of VO_2 and V_2O_5, obtained from Alfa Aesar, were used as control samples. EBSD patterns were acquired from these control samples and compared to calculated patterns. The OIM software correctly indexed and identified the structures for the commercial powders. This was performed to verify that the patterns calculated from the known materials' structures would match those patterns acquired from the actual samples. EBSD accurately discerned among the different commercial powders.

Using a scanning electron microscope, with an accelerating voltage of 25 kV, and a 70° incident angle, EBSD patterns were obtained from the individual particles of the thin films produced from the annealed samples described in the previous sections. Figures 4.21 and 4.22 show representative EBSD patterns obtained from samples annealed at 450°C for 17 hrs. The indexing shown in figure 4.21 indicates a match for vanadium dioxide (VO_{2-R}). The zones, lines, and band widths are a good match for the structure files provided. From the EBSD patterns obtained from the annealed films in Argon the vanadium dioxide structure files received the highest number of votes from the automated EBSD indexing. Furthermore, there was no evidence of any other vanadium oxide stoichiometries present in $VO_{x,x\approx 2}$ samples annealed in argon where EBSD patterns were successfully acquired.

The EBSD pattern shown in figure 4.22 is characteristic of patterns obtained from the anneals

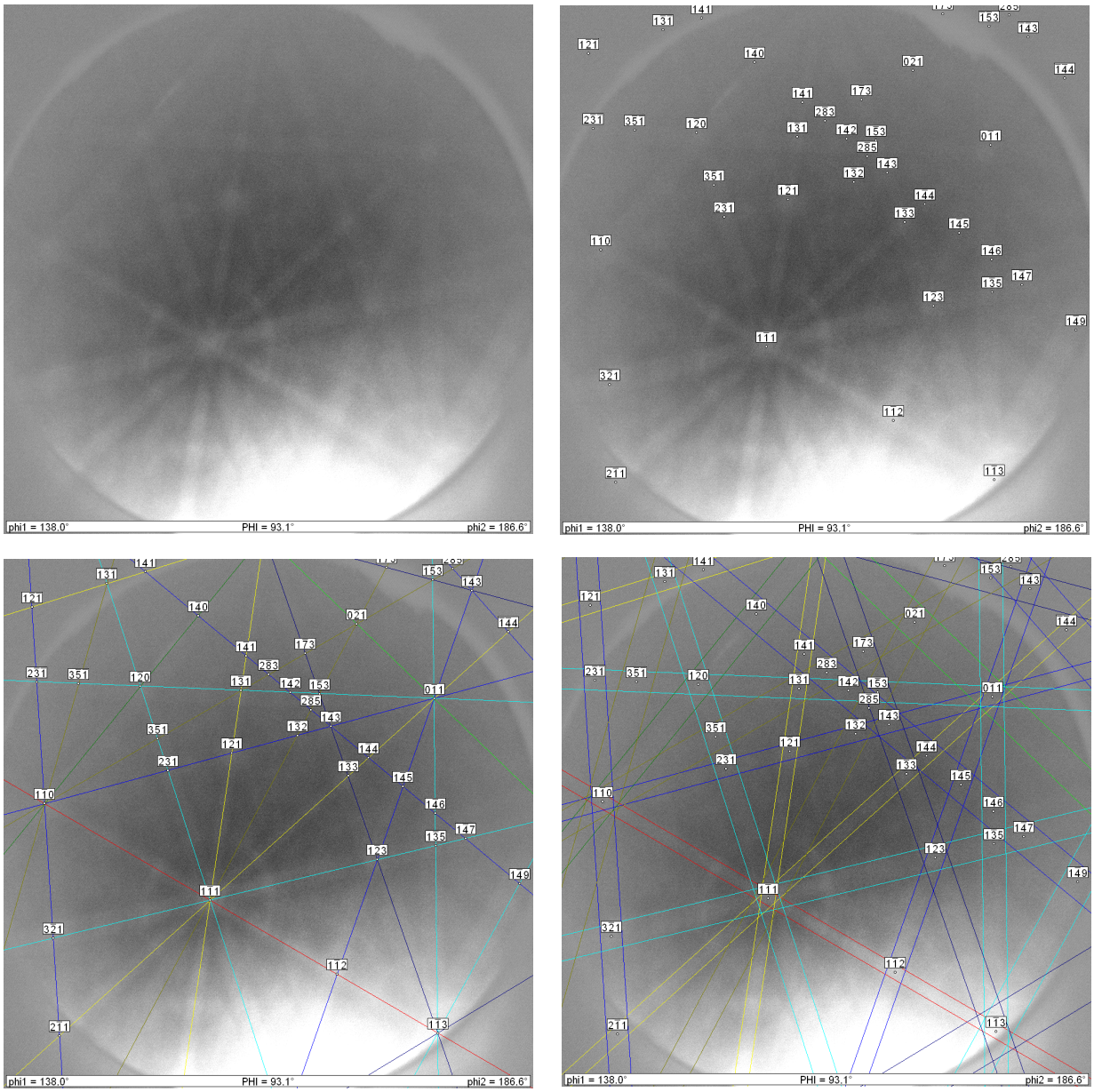

Figure 4.21 (Top Left) Electron Back-Scattered Diffraction Pattern obtained from a 300 nm-long VO_2 grain in the sample annealed at 450°C for 17 hrs. Indexing of the EBSD pattern takes place by 1) identifying the acquired crystallographic zones (top right); 2) location of the observed bands and the angles between them (bottom left); and 3) the band widths (bottom right). This pattern is characteristic to the patterns obtained from produced large particles in $VO_{x,x\approx2}$ films under an argon anneal, indicating crystalline vanadium dioxide.

of the 50 nm $VO_{x,x\approx 2}$ thin films performed at 440°C and above. The diffuse bands shown in the pattern indicate the crystallinity of the spot being probed and the symmetry of those bands reveal the structure and orientation of the crystal. The degraded aspect of the EBSD pattern shown in figure 4.22 can be attributed to the low signal to noise ratio from probing a small grain (approximately 300 nm long, and 60nm deep), and with it, associated problems such as grain boundaries, twinning, sub-grain boundaries, and other various strains in the lattice.[98, 136, 137]

Also, as seen in figure 4.22, it was observed that the monoclinic and tetragonal EBSD patterns are too symmetrically similar for the software to distinguish between them. Figures 4.22b-d show the same diffraction pattern overlaid with the calculated patterns from the tetragonal (VO_{2-R}) and two (VO_{2-M1} and VO_{2-M3}) of the monoclinic phases of vanadium dioxide. As observed from figures 4.22a-d, the bands shown in the acquired EBSD pattern are present in all three phases (tetragonal, M1, and M3) of VO2. The locations of the calculated bands, their widths, and the angles between these three phases of VO_2, are too close to the acquired EBSD pattern that the OIM software cannot accurately differentiate among them. Furthermore, the monoclinic phases of vanadium dioxide (M1 and M3 shown in figures 4.22c and 4.22d respectively) "suffer" from a pesudo-symmetry to which the OIM software invariably gives a "confidence index" of zero since it cannot determine the orientation of the crystal of the monoclinic phases. This inability to discern between the phases of vanadium dioxide occurred in the observations made from both the commercial powder samples and the crystalline thin film samples. Nonetheless, EBSD quite accurately differentiated between the structures of different stoichiometries in the vanadium oxides as their crystal structures are remarkably different. It was found that the post anneal in an argon environment at temperatures above 400°C consistently produced crystalline vanadium dioxide, as determined by EBSD patterns.

The clarity of the patterns obtained played a big role in the ability of the software to reliably index the films. For the samples annealed at 400°C the quality of the EBSD patterns was so low

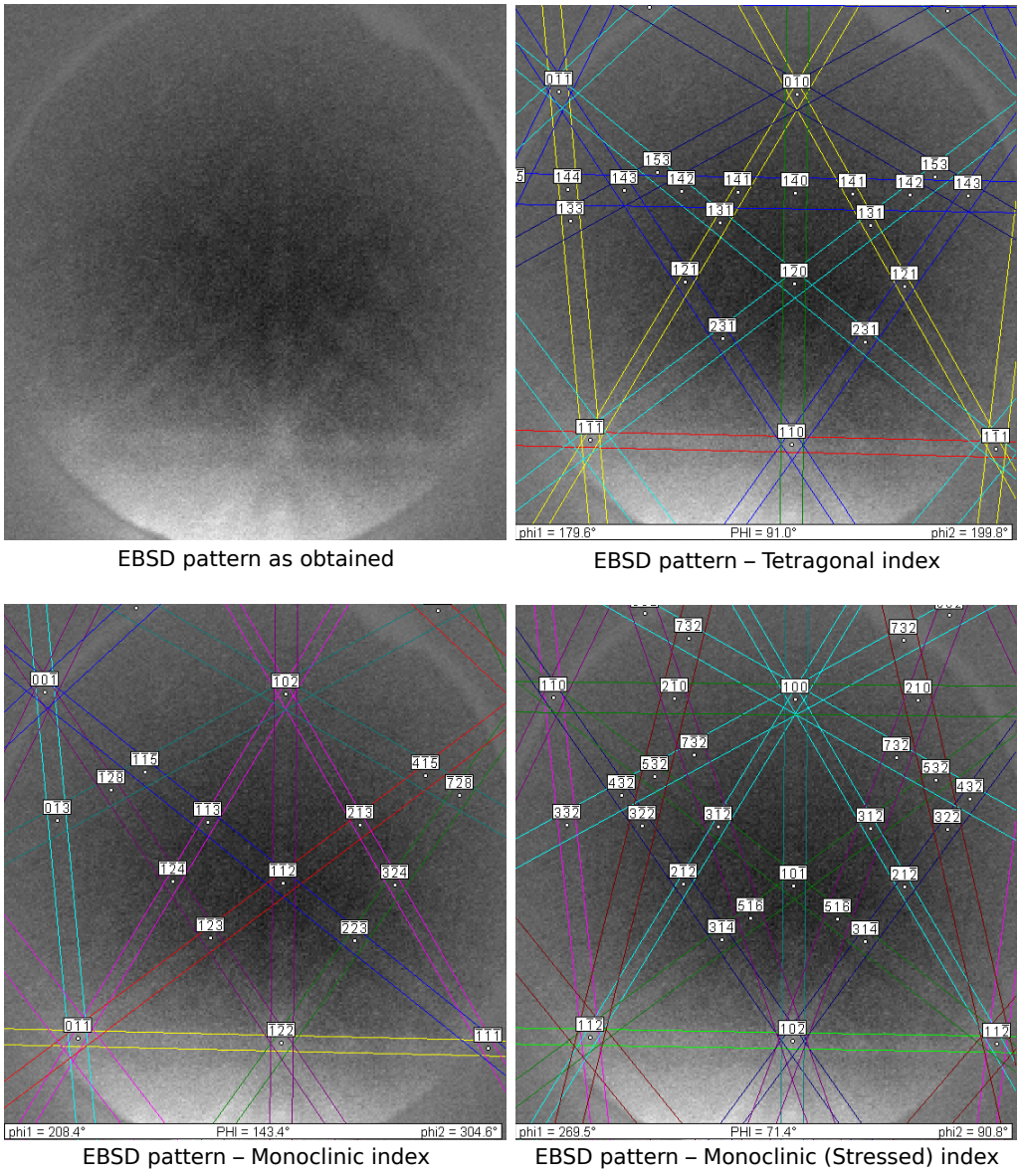

Figure 4.22 Electron Back-Scattered Diffraction Pattern obtained from the sample annealed at 450°C for 17 hrs. Due to the many similarities between the calculated EBSD patterns for the three known vanadium dioxide phases, the software is unable to distinguish between them. The tetragonal index is the most readily recognized and, because of its symmetry, more easily indexed. Also, the grain formation and orientation took place during the annealing at $T > 300°C$ where the structure formed was tetragonal.This pattern is characteristic to most patterns obtained from the produced films under an argon anneal, indicating crystalline vanadium dioxide.

that the software could not index the patterns automatically (thus an OIM scan was not performed). However, several indexable patterns were manually obtained in different areas of the film and the software indexed them as VO_{2-R}. Despite the observed morphology shown in the previous section, samples with grains smaller than 100 nm in length and width with 50 nm thickness did not produce indexable EBSD patterns. This includes all the 10 nm and 5 nm $VO_{x,x\approx 2}$ thin films as well as the 50 nm $VO_{x,x\approx 2}$ samples annealed at temperatures near 400°C and below.

The inability to acquire EBSD patterns from these finer-grained films was attributed to a combination of surface roughness, small grain size, and specimen drift rather than lack of crystallinity. In this study, crystals greater than 100 nm in length and width with 50 nm thickness produced indexable EBSD patterns. This last observation indicates that the use of the EBSD technique for determining crystallinity of VO2 thin films is limited to films with particles larger than a 50 nm radius and covering the thickness of the film.

This need in clarity of EBSD was seen as a limit in this characterization technique to determine the presence of crystallinity and stoichiometric determination from fine-grained samples.

4.5 Annealing in an Air Atmosphere

As described in section 4.2.1 annealing under an air atmosphere took place. Similar to the anneals done in argon, no crystallization was observed under 300°C and high mobility was observed at temperatures above 600°C. Figure 4.23 summarizes the results. It was observed that the crystals obtained indexed to the V_2O_5 structure with the anneals as early as 300°C. The presence of air allowed for further oxidation of the VO_2 thin films and readily formed V_2O_5.

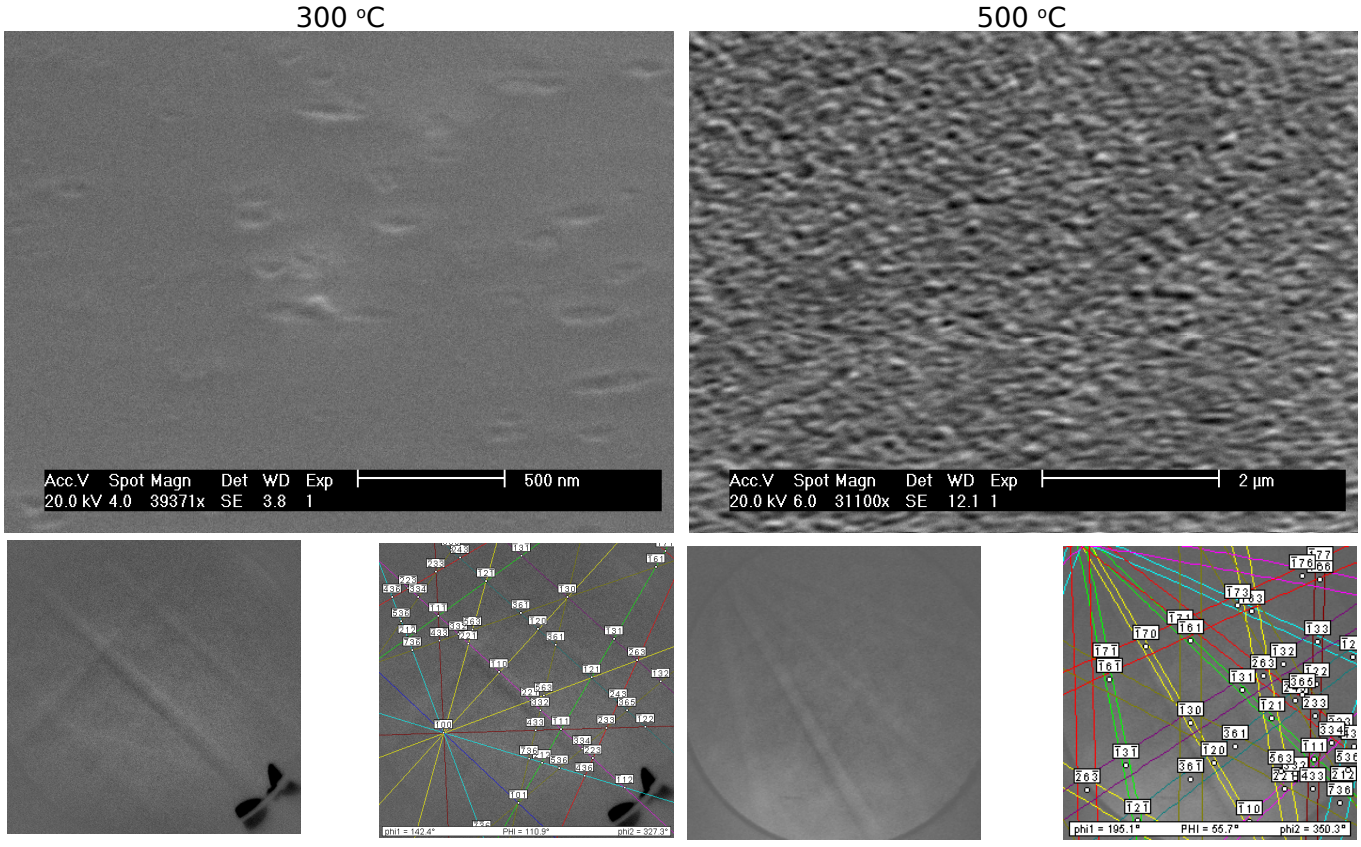

Figure 4.23 Scanning electron micrographs and EBSD patterns collected of two characteristic air anneals. The EBSD patterns show that the resulting films, though crystalline, formed V_2O_5 instead of VO_2.

4.6 Conclusions on the Solid Phase Crystallization of $VO_{x,x\approx2}$ thin films

There are several significant results obtained from the study in the solid phase crystallization of $VO_{x,x\approx2}$ thin films. Among those results:

- For amorphous $VO_{x,x\approx2}$ thin films deposited on amorphous SiO_2 there is a narrow set of parameters that will yield continuous thin films.
- A change in morphology indicating beginning nucleation and crystallite growth is observed as early as 380°C for amorphous $VO_{x,x\approx2}$ thin films.
- Electron back-scattered diffraction was successfully used to accurately distinguish among different stoichiometries for films with crystalline VO_2 grains larger than 100 nm in diameter and 50 nm thick.
- Due to the close crystallographic symmetry in the different phases of VO_2, EBSD cannot discern among them in thin films.
- A limit on the use of EBSD as a characterization tool for crystallinity and stoichiometric identification was reached in annealed thin films with crystallites smaller than 100 nm.
- Oxygen control in the annealing environment plays an important role since amorphous $VO_{x,x\approx2}$ thin films readily oxidized in an air anneals.

Chapter 5

Orientation of VO_2 Grains on Different Substrates: - Use of Electron Back-Stattered Diffraction and Oriantation Imaging Microscopy -

In addition to the samples described in the previous chapter, where VO_2 was crystallized atop amorphous SiO_2, crystalline vanadium dioxide (VO_2) thin films were deposited by pulsed laser deposition (PLD) onto a variety of substrates including different cuts of sapphire, and titanium dioxide (see 2.5.1 in page 27, and appendix A.2). Electron back-scattered diffraction (EBSD) was used to study the orientation of the crystalline grains obtained. Automated indexing of EBSD patterns used the tetragonal phase of vanadium dioxide since EBSD patterns for the monoclinic (M1) and tetragonal (R) phases of vanadium dioxide are indistinguishable by computer-automated-indexing. EBSD showed epitaxial relationships between the different single-crystal substrates. Sapphire substrates show a predominant family of crystallographic relationships present in all cuts

of sapphire wherein the rutile VO_2 {001} planes tend to lie parallel to the substrate's {10-10} and the rutile VO_2 {100} planes lie parallel to the substrate's {1-210} and {0001}. While this family of relationships accounts for the majority of the VO_2 grains observed, due to the sapphire substrate's geometry there were variations within these rules that changed the orientation of VO_2 grains with respect to the substrate's normal direction. Transmission electron diffraction patterns taken from cross-section of particles of the A and R cut sapphire substrates not only solidified the predominant family mentioned, but also helped lift the ambiguity present in the rutile {100} axes (see section 6.1.1). Furthermore, the C and R cut of sapphire showed additional families of crystallographic relationships found in the EBSD analysis, most starting from the aforementioned predominant family. Finally for the TiO_2, a substrate lower lattice mismatch, we observe the expected relationship where the rutile VO_2 [100], [110], and [001] crystal directions lie parallel to the TiO_2 substrate's [100], [110], and [001] crystal directions respectively.

5.1 Introduction

As mentioned in previous chapters, vanadium dioxide has become a material of particular interest. This interest has arisen because crystalline vanadium dioxide (VO_2) exhibits a first-order semiconductor to metal phase transition (SMT) near 68°C.[2,3,22,30,45] Due to its phase transition, vanadium dioxide undergoes a reversible structural change from a low temperature semi-conducting monoclinic phase to a high-temperature tetragonal metallic phase. This structural and reversible metal to insulator phase transition is accompanied with a change in the band structure of VO_2 which, in turn, exhibits several drastic optical and electronic changes such as a resistivity change of several orders of magnitude and a sharp change in optical transmittance in the infrared region faster than 200 fs.[64,66,138] These changes in its optical and electronic properties hint at its use for several technical applications.[46–49,51,52,139]

As of the year of this writing, the nature of the phase transition and its mechanism are still under debate.[11,23–28,64,140,141] Variations in transition temperature, hysteresis, and sharpness of the transition in VO_2 thin films are seen and attributed to particle size, stress, misorientations between grains, morphological faults, and other "imperfections." One way to manipulate these properties is to vary the substrate upon which these films are deposited. Therefore, we have studied how the microstructure of vanadium dioxide thin films is affected by different substrates.[49,63,65,94]

As mentioned in chapter 2, in the high temperature phase, above 68°C, vanadium dioxide crystals (VO_{2-R}) are arranged in a tetragonal (rutile) structure (#136 *P 42/mnm*)[44,142] with lattice parameters $a = b = 4.554$Å and $c = 2.849$Å where vanadium atoms lie collinear along these directions with equal spacings. As the material cools down below its transition temperature, the atoms suffer subtle changes in their position. There is a break in the symmetry of the unit cell and a low temperature monoclinic (VO_{2-M1}) phase is formed with structure (#14 $P2_{1/c}$) and lattice parameters a=5.7529 Å, b=4.5263 Å, c=5.3825 Å, and beta=122.6° (Recall figures 2.7 and 2.9).[44,54,143] The tetragonal symmetry of the high-temperature phase poses an ambiguity in the $VO_2[100]_R$ and $VO_2[010]_R$ axis when the transition is drawn schematically and, thus, there are various mappings from the VO_{2-R} phase to the VO_{2-M1} phase.[44,54,142–144] As mentioned in section 2.3.1, the mapping between these two structures as shown in figure 2.9 wherein the shown origin and the $VO_2[010]_{R,M1}$ axes of both structures are kept fixed throughout the structural transition. This mapping is preferred and used as the author feels it is somewhat simpler to have the $VO_2[010]_R$ matching to $VO_2[010]_{M1}$ and it also makes the matching of atomic positions clearer.* Still, it is noteworthy to point out that, due to the symmetry of a tetragonal unit cell, there is an ambiguity between the VO_{2-R} a- and b- axes that becomes important when mapping between the VO_{2-R} and VO_{2-M1} crystal structures.

*Though equivalent, in the Andersson mapping the $VO_2[001]_R$ and $VO_2[100]_{M1}$ axes do not appear to be a good mapping until the rutile unit cell is shifted to the VO_{2-R} body centered position.

As the structural phase transition takes place (going from high temperature to low temperature) there is an 0.94% expansion along the VO_{2-R} c-axis accompanied with an VO_{2-R} a- and b-axes contraction of 0.42% and 0.59% respectively. The break in symmetry takes place along the VO_{2-R} a- and c-axes where the atoms move from being collinear along these axes to being staggered along these directions (recall figure 2.7). Further, the spacing between the vanadium atoms along the rutile a-axis now alternates between 4.836 Å and 4.258 Å, while the atoms along the rutile c-axis alternate between 2.602 Å and 3.190 Å. This staggering doubles the unit cell along these directions.

Even though the nature of the SMT is still under debate,[11,23–28] stresses on crystal grains can significantly affect the properties of the transition.[17,59,60,145,146] For thin films, the crystalline orientation of the grains, as well as interactions between them and the substrate, may give a preference for either the conductive phase or the insulating phase, and thus locally affect the transition temperature. In order for vanadium dioxide to undergo its structural phase change, any hindrance in either the contraction or expansion of the axes may affect the phase transition and desired properties.

Because of the differences in either lattice constants or angle of the lattice vectors between the substrate and grown film (lattice mismatch), the substrate plays an important role in the quality of the epitaxial films and their microstructure. Usually a crystal with the same crystallography is chosen as the substrate, as that reduces the angle mismatch to zero. This largely reduces the lattice misfit which is then only determined by the difference in lattice constants between the substrate and epitaxial film. However, sometimes it is hard to choose a same crystallographic crystal for the substrate, as is the case for the monoclinic VO_{2-M1} crystal system.

Among the different substrates used for the deposition of vanadium dioxide thin films, sapphire is considered specially useful due to its close lattice match to vanadium dioxide's monoclinic structure. VO_2 is monoclinic at room temperature, with lattice angles of $\alpha = \gamma = 90^\circ$ and $\beta = 122.6^\circ$, making it pseudohexagonal, rendering hexagonal sapphire a preferred substrate for

epitaxial thin film growth. Sapphire, the single-crystal form of Al_2O_3, especially the R-cut plane $(01\bar{1}2)$ and the C-cut plane (0001) of Al_2O_3, has been the preferred substrate for epitaxial growth of VO_2 due to its easy availability, stability at high temperatures, and less reactivity with the oxides.[52,84,87,96,97,147–149]

In this chapter, electron backscattered diffraction (EBSD)[98,137] is used to study the crystallographic orientation relationship between the deposited VO_2 thin films and these substrates:

- A-cut sapphire – Al_2O_3 $(1\bar{2}10)$
- C-cut sapphire – Al_2O_3 (0001)
- R-cut sapphire – Al_2O_3 $(1\bar{1}02)$
- C-cut rutile – $TiO_2(001)$

5.2 VO_2 Thin Film Sample preparation by Pulsed Laser Deposition.

This set of samples were obtained from Joyeeta Nag and Richard Haglund at Vanderbilt University. More details about the deposition and initial characterization done at Vanderbilt are found on appendix 5.2. As a manner of description, epitaxial VO_2 films of 80 nm nominal thickness were deposited onto c-, r-, a-cut sapphire, and $TiO_2(001)$ substrates using pulsed laser ablation of 99.99% pure vanadium metal target in a background of 50 mTorr of oxygen, with a target-substrate distance of 5 cm, at a temperature of $\sim$500°C.

Figure 5.1 shows the acquired infrared transmission for the VO_2 films deposited on a-cut Al_2O_3, c-cut Al_2O_3, r-cut Al_2O_3, and $TiO_2(001)$ substrates (respectively from top to bottom). There is an evident difference in the SMT between the films, as well as the hysteresis. As a reference, the accepted transition temperature is labeled across all graphs by a solid black line pointing

Substrate	Transition (°C)	Hysteresis (°C)
A-cut Al_2O_3 $(1\bar{2}10)$	67.7	5.4
C-cut Al_2O_3 (0001)	68.1	4.8
R-cut Al_2O_3 $(1\bar{1}02)$	58.7	1.4
C-cut $TiO_2(001)$	52.4	5.4

Table 5.1 Transition temperatures and measured hysteresis width for VO_2 thin films deposited onto different substrates. (All measurements in °C.)

to 68°C. Table 5.1 shows the measured transition temperature and hysteresis width for the VO_2 thin films on the different substrates. The transition temperature is reported at the midpoint of the hysteresis, and the hysteresis was the measured full width at half maximum.

The transition temperature, width and shape of the observed hysteresis in these deposited films show variation despite having the same deposition and growth parameters. For example, the VO_2 films on $TiO_2(001)$ and r-cut Al_2O_3 have considerably lower transition temperatures when compared to the VO_2 films deposited on c-cut and a-cut Al_2O_3.

5.3 Sample Characterization Through EBSD and OIM -The Technique-

Sections of these specimens were imaged and analyzed with a Helios Nanolab 600 dual-beam from FEI equipped with EBSD capabilities. The EBSD system used comprised a TSL/OIM detector with a 1 mega-pixel (1024 by 1024 pixel) CCD camera. EBSD patterns were obtained from each the samples using an accelerating voltage of 30kV and an incident beam at a 70° tilt from the normal. Due to the geometry of the Helios Nanolab 600 and the limitations of the stage, it was necessary to mount the samples on a 45° pre-tilted SEM stub. To ensure an angle as close to the

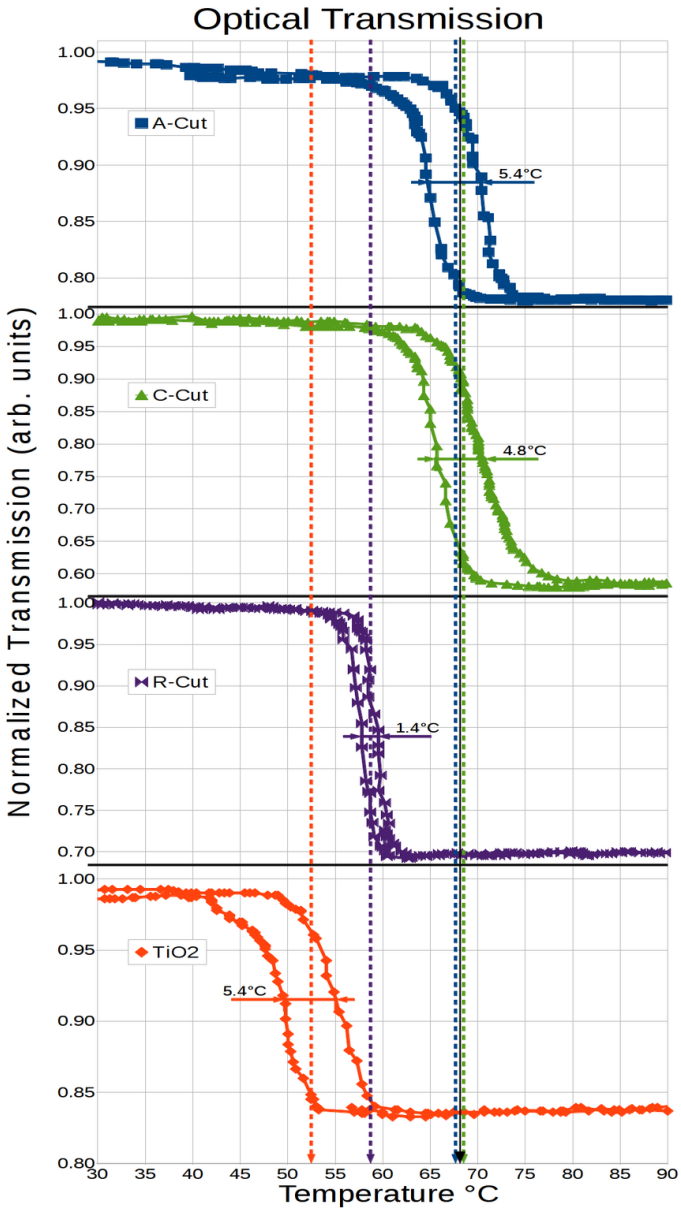

Figure 5.1 Normalized infrared transmission acquired from the VO_2 epitaxial films deposited on the following substrates (from top to bottom): a-cut sapphire, c-cut sapphire, r-cut sapphire, and c-cut TiO_2. As reference, the accepted transition temperature for bulk VO_2 is 68°C. (Data courtesy of Joyeeta Nag and Richard Haglund at Vanderbilt University.)

desired 70° tilt, and to compensate for any "mis-mounting," the stage of the Helios was tilted to ∼45° in order to find the angle at which the beam was parallel to the surface of the specimen, and then, the sample was tilted ∼20° back from there.

In order to mitigate the electrostatic charging that occurs due to the insulating nature of the substrates, the edges of the samples were coated with colloidal graphite paint, further a thin amorphous carbon layer was deposited onto the surfaces for imaging. Scanning electron micrographs were obtained from the tilted surface of the samples and scans of no less than 6 μm wide by 1.5 μm tall were selected to collect EBSD patterns every 50 nm in a hexagonal grid (See fig. 5.2b). Figure 5.2a shows a scanning electron micrograph obtained from the surface of a-cut sapphire. Rows of VO_2 particles are evident. It is worth noting that, even though electrostatic charging artifacts were minimized by the measures described above, artifacts were not completely suppressed. The change in brightness at the bottom of figure 5.2a, and a slight drift in figure 5.2b, are examples of charging artifacts still present.

The EBSD patterns acquired by the CCD were automatically indexed with the OIM data collection software.

As mentioned in chapter 4, EBSD can correctly identify, differentiate, and index crystalline vanadium dioxide grains. In order to ease the software indexing, only the crystal structure for the substrate and of VO_{2-R} were given as choices for indexing. The justification for using only the tetragonal VO_2 crystal structure (instead of that for monoclinic) arose due to the following reasons:

1) Formation of the vanadium dioxide grains occurred at a temperature above that of the phase transition, thus any crystallographic relationship between the film and the substrate occurred while VO_2 was found in the rutile structure. Hence, it makes sense to discuss and compare how the rutile crystalline vanadium dioxide grains arrange themselves as deposited.

2) The VO_2 structural phase change from tetragonal to monoclinic is due to a very slight relocation of the vanadium atoms, with their position remaining quite close to the original VO_{2-R}. As

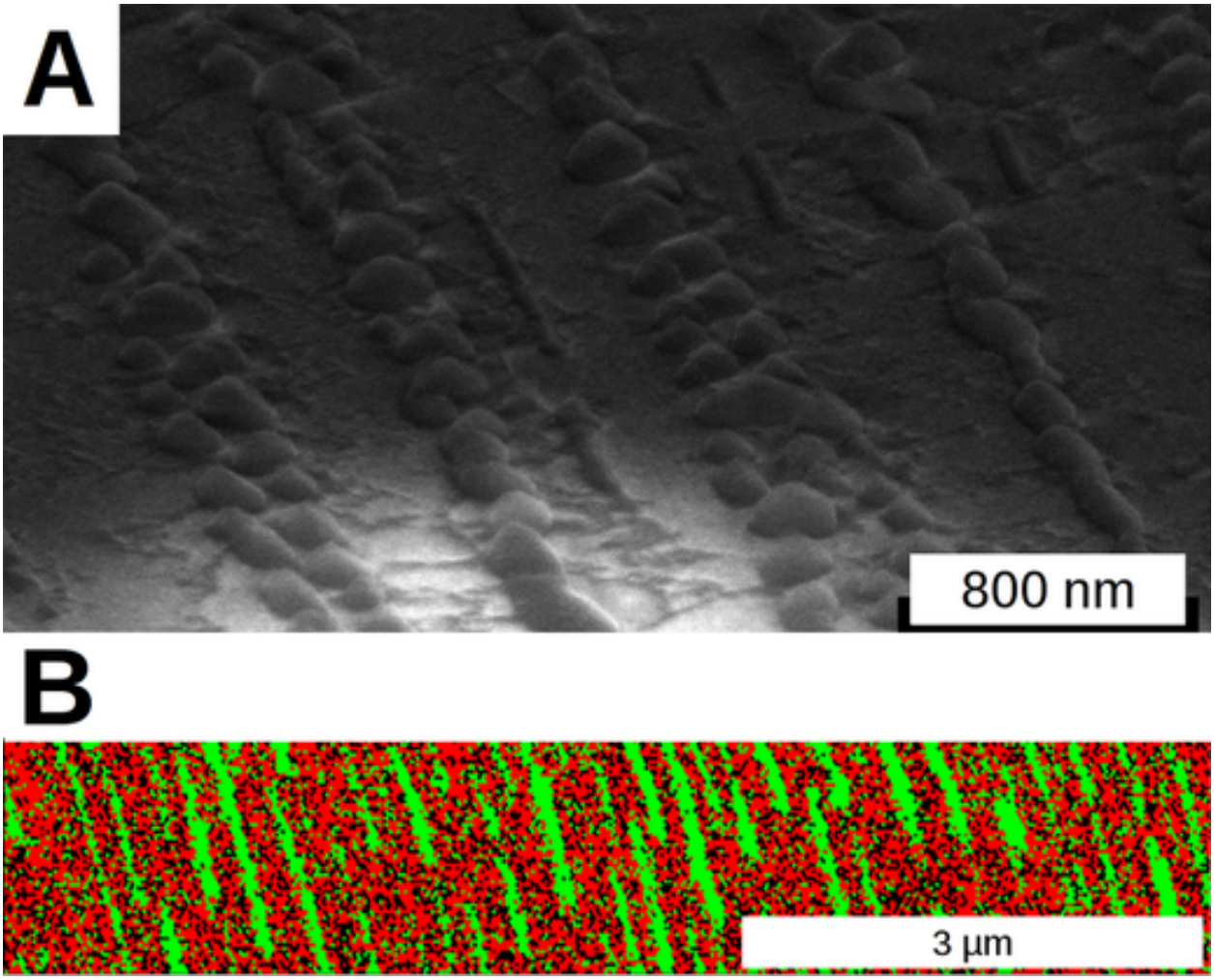

Figure 5.2 (A) Scanning electron micrograph of the surface of crystalline vanadium dioxide grains deposited on an a-cut sapphire substrate. Image taken at a 70° tilt. (B) EBSD map taken from the surface of the sample mentioned above. Red indicates an EBSD pattern indexed to sapphire, green to VO_2.

a consequence, the electron back-scattered diffraction patterns of VO_{2-M1} and VO_{2-R} nanograins are indistinguishable by computer-automated-indexing.

3) The EBSD indexing software invariably attributes the VO_{2-M1} indexed patterns a value of "zero confidence" to the matches found when using this structure, thus making the data from the VO_{2-M1} structure inadequate for computerized analysis. This "zero-confidence" vote is due to: a) the pseudosymmetry in the VO_{2-M1} structure that arises from close similarity between the VO_{2-M1} and VO_{2-R} structures, and b) because the EBSD indexing software determines and indexes the structure based on the matches found in the number and location of crystallographic zones present, visible bands, and the band's width between the calculated structure and the acquired pattern. Thus, the VO_{2-M1} structure is inadequate for EBSD automated computerized analysis when it is compared with other similar structures.

Figure 5.3 shows representative EBSD patterns taken from the samples as well as examples of the best-fit automated indexing for each material (Al_2O_3 and VO_{2-R}). The substrate alone shows a clear and indexable EBSD pattern. The expected crystallographic relationship can be inferred by the similarity of the calculated EBSD patterns for sapphire and VO_2 (figs 5.3bcef). Nonetheless, with the use of the crystal structure of the tetragonal phase, the automated computer indexing correctly and confidently differentiated between the substrate (figs 5.3a-c) and a VO_2 crystalline grain (figs 5.3d-e) by giving the substrate (fig 5.3a) a preferred match to sapphire (fig 5.3b). Similarly, with the background subtracted, an EBSD pattern taken from one of the grains (fig 5.3d) was also correctly indexed as VO_2 (fig 5.3f).

A sample map of indexed EBSD patterns is shown in figure 5.2b. As the map shows, the software was able to differentiate between the structure of the substrate (color-coded in red) and the vanadium dioxide rows (color-coded in green). Each pixel in the map is an indexed EBSD pattern taken every 50 nm in a hexagonal grid. The brightness of the color represents the "confidence" given to each indexed pattern. Notice that even when there was variation in the confidence indices

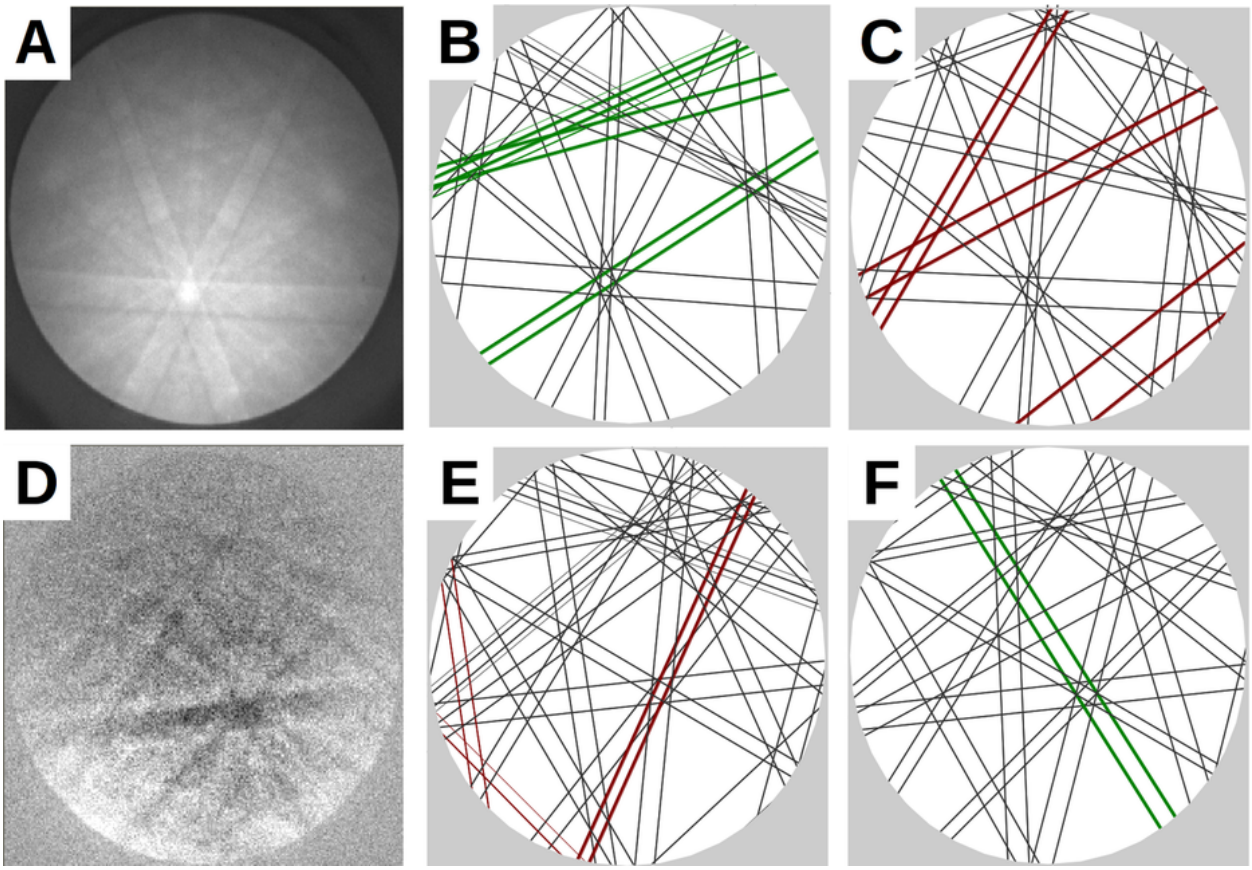

Figure 5.3 Acquired and indexed electron back-scattered diffraction (EBSD) patterns of (A) The A-cut sapphire substrate (raw) with best fit indexing as (B) sapphire and as (C) VO_2. (D) VO_2 grain (background subtracted) with best-fit indexing as (E) sapphire and as (F) VO_2. Despite the similarity in the EBSD patterns, automated software indexing can correctly discern between the substrate and the vanadium dioxide grains.

within VO_2 and the substrate, the overall presence of the rows of vanadium dioxide particles shown in figure 5.2a are still evident in figure 5.2b. Furthermore, those rows are indeed characterized as vanadium dioxide based solely by their EBSD patterns.

The orientation information obtained from each of the EBSD scans was then compiled and analyzed by an automatic generation of orientation density functions (ODFs). The analysis software automatically expanded the ODF into a series of generalized spherical harmonics and plotted on pole figures. For this work, each ODF expansion has a series rank of 32 using a Gaussian smoothing of 2°. Due to the finite limit and truncation in the series expansion, the plots show the main orientation peaks while allowing numerical artifacts that appear as ringing emanating from such peaks. These ODFs will be shown in figures 5.4, 5.5, 5.6, and 5.7

The pole figures map the directions where specific crystal planes point in the in the upper hemisphere of the sample. The peaks in the ODF represent a distribution of the acquired points that have a crystal plane oriented in that direction. In order to ease interpretation, and as a form of reference, the orientation density functions for each substrate were plotted in pole figures and used to correct any physical tilting and rotation misalignments in the microscope. These corrections were done so that the plane-cut of the substrate was placed at the center pole and orthogonal in-plane directions matched major plot axes. In this way, the data was plotted such that specific crystal directions of the substrate line-up with the major axes in the pole figure, and then these directions were used to label the axes of the pole figures accordingly. As an example the plots in figure 5.4 are lined up such that the $Al_2O_3(1\bar{2}10)$ plane direction is normal to the substrate (center pole), the $Al_2O_3(10\bar{1}0)$ direction is in-plane along the vertical axis of the plot, and the $Al_2O_3(0001)$ direction runs along the horizontal axis.

The following sections show the results of the orientation studies. The results are presented in the following order:

- Single-crystal sapphire A-cut Al_2O_3 $(1\bar{2}10)$

- Single-crystal sapphire C-cut Al_2O_3 (0001)
- Single-crystal sapphire R-cut Al_2O_3 $(1\bar{1}02)$
- Single-crystal C-cut $TiO_2(001)$
- Results on amorphous SiO_2 (from samples described in chapter 4)

5.4 Crystal Orientation of Vanadium Dioxide Crystalline Grains Deposited on A-Cut Sapphire.

Figures 5.4a and 5.4b, show the ODFs for the single-crystal a-cut Al_2O_3 substrate wherein the $\{1\bar{2}10\}$ and $\{10\bar{1}0\}$ directions are plotted (5.4a and 5.4b respectively). For this single-crystal a-cut Al_2O_3 substrate, the $Al_2O_3(1\bar{2}10)$ plane direction is normal to the substrate (center peak in figure 5.4a). As expected, there are two equivalent $\{1\bar{2}10\}$ directions 60° from the normal (remaining two peaks in fig. 5.4a). Also, for this substrate the $Al_2O_3(10\bar{1}0)$ direction is found in-plane (peaks at the edge of the pole figure 5.4b) with two equivalent $\{10\bar{1}0\}$ directions found 60° from the surface (peaks located 30° from the normal in fig. 5.4b). The presence and locations for the peaks plotted in figures 5.4a and 5.4b are consistent for single-crystal a-cut Al_2O_3.

The orientation density distribution for rutile vanadium dioxide on a-cut Al_2O_3 is presented as pole figures 5.4c and 5.4d. In contrast to the substrate, the peaks plotted in figures 5.4c and 5.4d do not correspond to a single VO_{2-R} orientation, but rather three individual orientations with a common axis. Considering that the locations of the plotted VO_{2-R} peaks are closely match to those of the a-cut Al_2O_3 substrate indicate a set of crystallographic relationships between the substrate and the deposited VO_2 film.

In order to ease interpretation for these and future pole figures, individual VO_{2-R} peaks are labeled in each VO_{2-R} pole figure according to families of VO_2–substrate crystallographic rela-

tionships.

In the case of figure 5.4, there is one "family" of relationships, but three different manifestations (or variants) of that same crystallographic family. The first number of the label represents the overall crystallographic family, thus all the pole figure peaks where the label begins with the numeral 1 follow the same crystallographic relationships. To differentiate between the variants, the numeral following the decimal will enumerate the variant within the family of rules, and the letter at the end will represent the axis of the VO_{2-R} structure.

Based on the locations of the VO_{2-R} peaks in figure 5.4, the following family of relationships can be inferred:

– FAMILY 1 –

$$VO_2\{100\}_R \parallel Al_2O_3\{1\bar{2}10\}; Label(1a) \tag{5.1}$$

$$VO_2\{010\}_R \parallel Al_2O_3\{0001\}; Label(1b) \tag{5.2}$$

$$VO_2(001)_R \parallel Al_2O_3\{10\bar{1}0\}; Label(1c) \tag{5.3}$$

Relationship (1a) is based on figures 5.4a and 5.4c; relationship (1b) is based on figure 5.4c; and relationship (1c) is based on figures 5.4b,and 5.4d.

As mentioned earlier, due to the tetragonal symmetry of the VO_{2-R} unit cell, the VO_2100_R and VO_2010_R directions are ambiguous, hence, they will be labeled as general directions in this family.

Though there is one underlying family of relationships relating the crystal structures of the VO_{2-R} film and the underlying Al_2O_3 substrate, the peaks in figures 5.4c and 5.4d indicate that there is more than one orientation for the grains in the VO_{2-R} film.

– Variations within FAMILY 1 – In figure 5.4, the peaks labeled 1-b, 1.1a, and 1.1c form a set that corresponds to the orthogonal symmetry of the VO_{2-R} unit cell. The VO_{2-R} grains that are represented by these peaks are oriented such that:

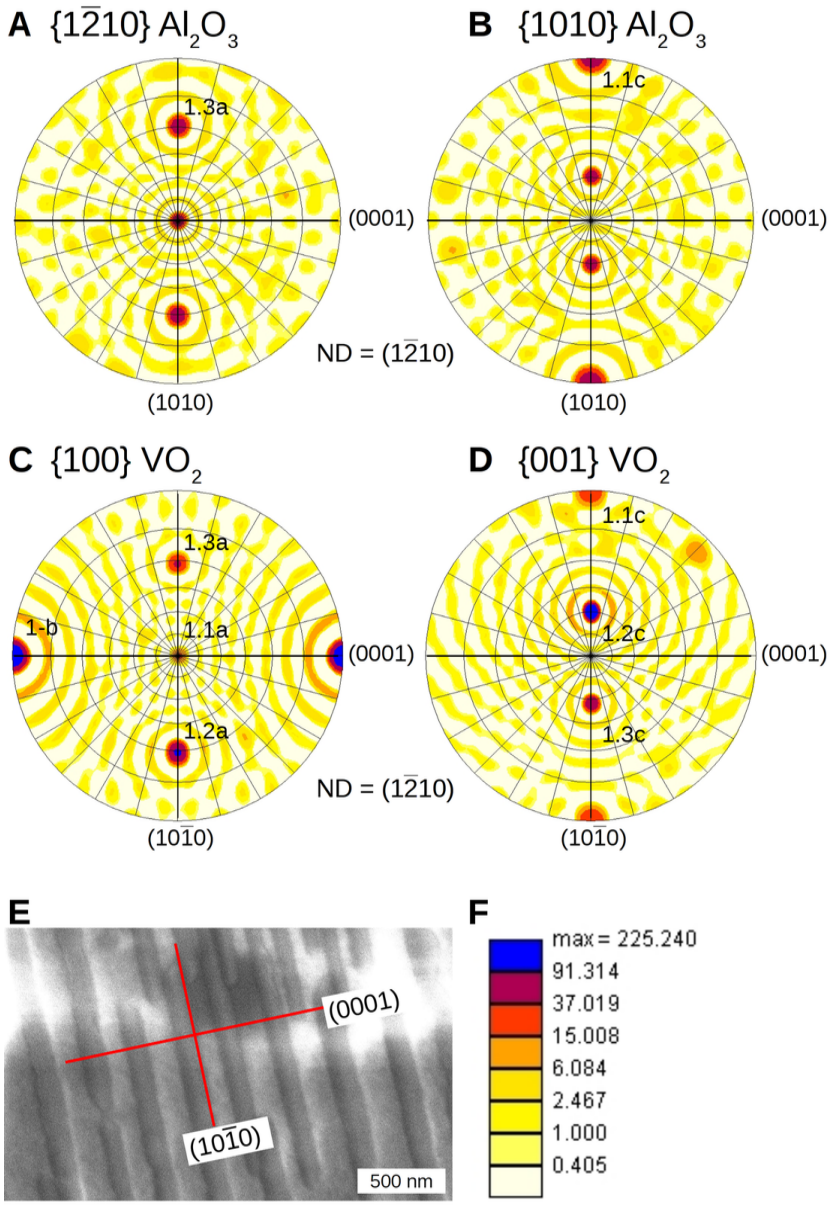

Figure 5.4 Orientation density distribution of crystalline vanadium dioxide grains deposited on a-cut sapphire with directions related to the underlying substrate. (As reference, the (A) {1-210} and (B) {10-10} crystal directions in an a-cut Al_2O_3 substrate are plotted) (C) Pole figure plot of the {001} VO_2 direction. (D) Pole figure plot of the {100} VO_2 direction. (E) Scanning electron micrograph of the surface with an overlay showing the labeled directions for the substrate. F) Scale for plots C and D where the maximum (blue color) is over 200 times the background (white). (Grid lines in pole figures every 15°)

- (1.1a) $VO_2\{100\}_R \parallel Al_2O_3\{1\bar{2}10\}$ (Normal to surface);
- (1b) $VO_2\{010\}_R \parallel Al_2O_3\{0001\}$ (in-plane);
- (1.1c) $VO_2(001)_R \parallel Al_2O_3\{10\bar{1}0\}$ (in-plane);

Thus, following the stated nomenclature, this set of peaks all correspond to **Family 1** of relationships mentioned earlier. For brevity, future labels in the variants will forgo re-stating relationships such that instead of writing "(1.1a) $VO_2\{100\}R \parallel Al_2O_3\{1-210\}$" only (1.1a) will be used (To be read as: **Family 1, variant 1, a-axis**).

A second set of peaks in figures 5.4c and 5.4d that form the orthogonal symmetry of VO_{2-R} are labeled 1-b, 1.2a, and 1.2c. Again, each of these peaks follow the relationships stated in **Family 1**, however these grains are oriented such that the (1.2a) relationship points $\sim 60^\circ$ away from the normal, and as a consequence, the (1.2c) relationship points $\sim 60^\circ$ from the surface of the a-cut Al_2O_3 substrate.

Finally, in a similar manner, the third set of orthogonal peaks is labeled 1.3a, 1-b, and 1.3c. This set of peaks also corresponds to VO_{2-R} grains that follow the same crystallographic relationships from **family 1** but oriented with VO_{2-R} a-axis $\sim 60^\circ$ from the normal (in the opposite direction than variant labeled 1.2). It is noteworthy to mention that these three labeled variations share relationship (1b) as a common axis and thus it shows up more prominently in the pole figure.

Several scans were taken from this sample, across different areas. Independent of the area scanned, relationship (1b) was always present in-plane. However, while there is also a strong overall preference for relationship (1c), only a fraction ($<50\%$) of the grains lie in-plane (1.1c). Multiple scans showed the (1.2c) and (1.3c) relationships ranging from 10% up to 90%.

The pole figures (5.4cd) also show a few weak ($<5\%$ in intensity) peaks in addition to the ringing mentioned earlier. While these weak peaks are not as appreciable as the labeled ones, and often similar in magnitude to the ringing artifacts, they suggest a low level of non-perfect particles.

Figures 5.2a and 5.4e show scanning electron micrographs of the surface of the vanadium dioxide grains deposited onto the A-cut sapphire. In both images, there is an evident alignment of the grains that form chains of elongated crystals of vanadium dioxide. In figure 5.4c, the axes used for the pole figure are overlaid onto the micrograph. The long axis of the vanadium dioxide chains/grains matches closely with the $Al_2O_3(10\bar{1}0)$ direction of the sapphire substrate, while the chains break along the $Al_2O_3(0001)$ direction.

5.5 Crystal Orientation of Vanadium Dioxide Crystalline Grains Deposited on C-Cut Sapphire.

The crystal orientation for vanadium dioxide grains on a c-cut sapphire substrate is presented in figure 5.5. Again, data for the Al_2O_3 substrate was used to correct any physical tilting and rotation misalignments in the microscope, and to label the axes of the VO_2 pole figures. In the case of this cut of sapphire, the $Al_2O_3(0001)$ plane is normal to the surface of the specimen (center pole in fig. 5.5), and, the $Al_2O_3\{10\bar{1}0\}$ and $Al_2O_3\{1\bar{2}10\}$ diffraction directions are both in plane with a 6 and 3-fold symmetry (respectively). The $Al_2O_3(10\bar{1}0)$ direction is plotted in the lower vertical axis, with the corresponding equivalent directions labeled in the figures with bold tick lines 60° from the vertical. Also, in the figures, the right horizontal axis represents the $Al_2O_3(1\bar{2}10)$ direction, with equivalent directions 120° from there (while not marked in the figure, they would be placed between the bold tick marks of the $Al_2O_3\{10\bar{1}0\}$ directions).

Figures 5.5c and 5.5d show two families of orientations for the deposited VO_{2-R} grains. (labeled by numerals 1 and 2) which share a common axis with crystallographic relationship (1a) stated earlier (peak labeled 1&2a). The family comprised by the peaks labeled 1a, 1.4b, and 1.4c, shares the same rules for Family 1 of crystallographic relationships described for the sapphire a-cut. This particular variant of Family 1 places relationships (1a) and (1c) in-plane and orthogonal

to each other, and relationship (1b) normal to the surface (peaks 1a, 1.4c, and 1.4b respectively).

While the second family shares in common relationship (1a), the other two crystallographic directions are different enough to merit their own label. This second family shows the following crystallographic relationships:

– FAMILY 2 –

$$(2a) : VO_2\{100\}_R \parallel Al_2O_3\{1\bar{2}10\} : (= 1a); \tag{5.4}$$

$$(2b) : VO_2[0\bar{1}1]_R \parallel Al_2O_3\{\bar{1}010\} \tag{5.5}$$

in-plane (which puts the $VO_2\{010\}_R$ $\sim 28^\circ$ off the plane);

$$(2c) VO_2[013]_R \parallel Al_2O_3\{0001\} \tag{5.6}$$

normal to the surface, which puts the $VO_2(001)_R$ $\sim 28^\circ$ off the normal (2c).

(Alternatively, and within the confidence of the measurement, putting the $VO_2[013]_R$ crystal direction normal to the surface puts the $VO_2[0,-7,6]_R$ crystal direction closer to in-plane than $VO_2[0-11]_R$.)

Several independent scans were taken from this sample, and across different areas. In all scans, the aforementioned variant of family 1 was predominantly present. The expected 3-fold symmetry given by the substrate showed in the pole figures by a rotation of 60° from the horizontal axis of the peaks 1a and 1.4c (peak 1.4b remained normal to the surface). Interestingly enough, and despite the expected 3-fold symmetry, the automated indexing software showed preference to mainly one of these three symmetry choices at a time. These relationships are in agreement with the results obtained from the a-cut sapphire sample. Again, the pole figures (8ab) show a few weak reflections suggesting a low level of non-perfect particles.

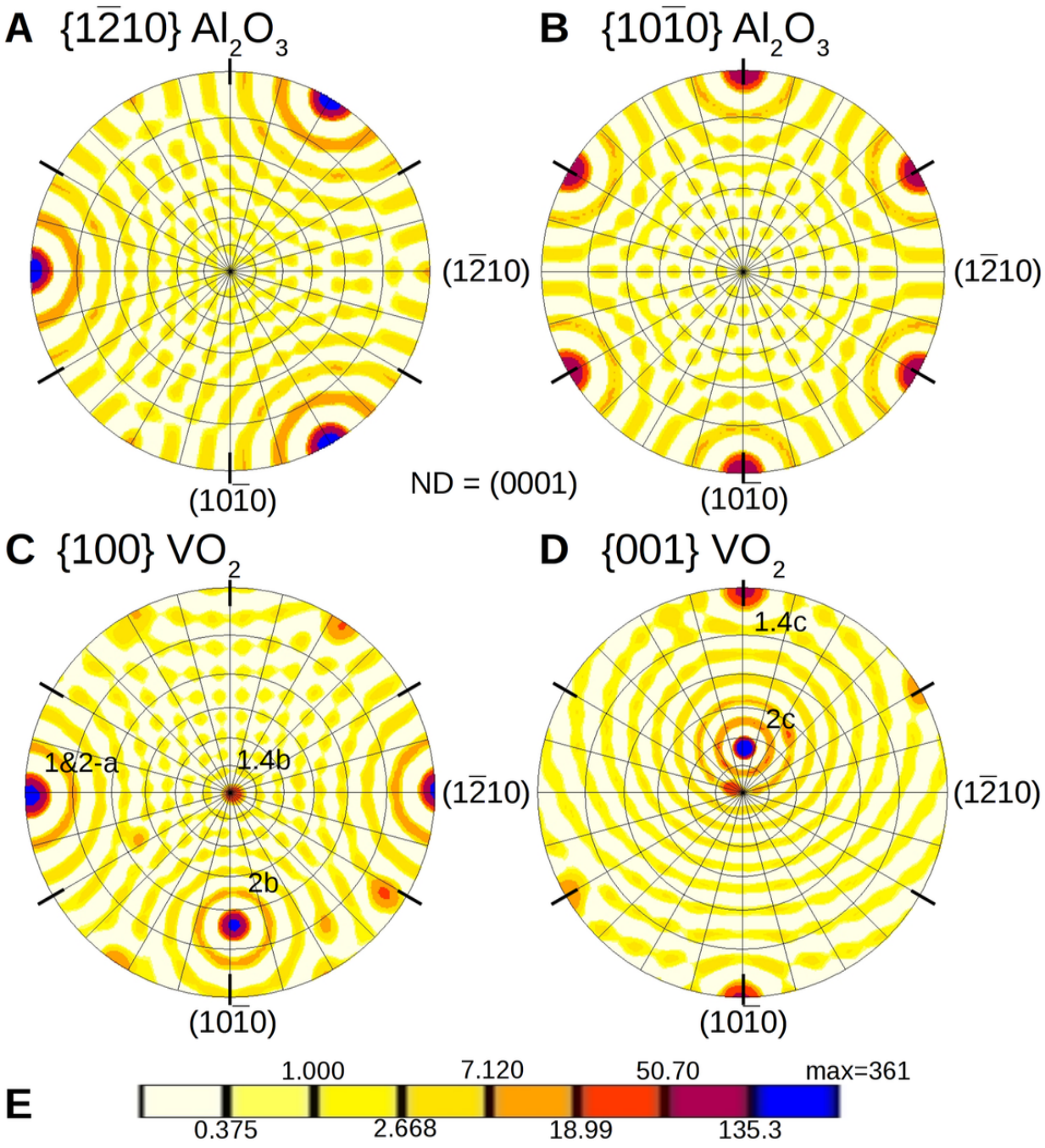

Figure 5.5 Orientation density distribution of crystalline vanadium dioxide grains deposited on c-cut sapphire with directions related to the underlying substrate. (As reference, the (A) {1-210} and (B) {10-10} crystal directions in an a-cut Al_2O_3 substrate are plotted) A) Pole figure plot of the $VO_2\{100\}_R$ direction. B) Pole figure plot of the $VO_2\{001\}_R$ direction. (Grid lines in pole figures every 15°)

5.6 Crystal Orientation of Vanadium Dioxide Crystalline Grains Deposited on R-Cut Sapphire.

Figure 5.6 shows both the pole figures with the orientation density plots for the substrate as well as for the VO_2 grains. Again, data for the Al_2O_3 substrate was used to correct any physical tilting and rotation misalignments, and, for this cut of sapphire, the $Al_2O_3(1\bar{1}02)$ was purposefully placed as the normal direction. There are also equivalent $Al_2O_3\{1\bar{1}02\}$ quasi 4-fold symmetrical directions in plane (fig 5.6a). As a reference, figures 5.6 includes the locations of the poles for $Al_2O_3\{0001\}$, $Al_2O_3\{10\bar{1}0\}$, and $Al_2O_3\{1\bar{2}10\}$ (figs. 5.6a, 5.6b, 5.6c, and 5.6d respectively) in order to be able to compare the $VO_2\{100\}_R$ and $VO_2\{001\}_R$ directions (figs 5.6e and 5.6f respectively).

Figures 5.6e and 5.6f show several peaks that can be separated into three main families of relationships. Following the nomenclature used for the previous samples, two of the sets of peaks can be considered variants of family 1 and a new family (labeled 3) is also observed. Again, these two families share a common axis (1b) where the $VO_2\{010\}_R$ plane tends to lies parallel to the $Al_2O_3\{0001\}$ plane (Figure 5.6e, peak labeled 1&3b), however, for this cut of sapphire, the $Al_2O_3\{0001\}$ direction lies $\sim 58^\circ$ from the normal.

The sets of peaks {1.5a, 1b, 1,5c} and {1.6a, 1b, 1,6c} both correspond to variations of family 1 that were present in both the a-cut and c-cut of sapphire, while the set {3a, 3b, 3c} is a 30° rotation about the $Al_2O_3\{0001\}$ axis and is present only in this cut. The variation labeled 1.5 places the $VO_2\{100\}_R$||$Al_2O_3\{1\text{-}210\}$ directions in plane (peak 1.5a), the $VO_2\{010\}_R$||$Al_2O_3\{0001\}$ directions $\sim 60^\circ$ from the normal (peak 1b), and the $VO_2\{001\}_R$||$Al_2O_3\{10\text{-}10\}$ directions $\sim 30^\circ$ from the normal (peak 1.5c). A rotation of 60° about the $Al_2O_3\{0001\}$ axis, would place this family in equivalent crystallographic relationships, thus yielding variant 1.6. However, doing so puts none of the $VO_2\{010\}_R$ axes in plane. Similarly, starting from family 1.5 and performing a $\sim 30^\circ$ rotation about the $Al_2O_3\{0001\}$ axis yields family labeled 3. This rotation generates a new set of

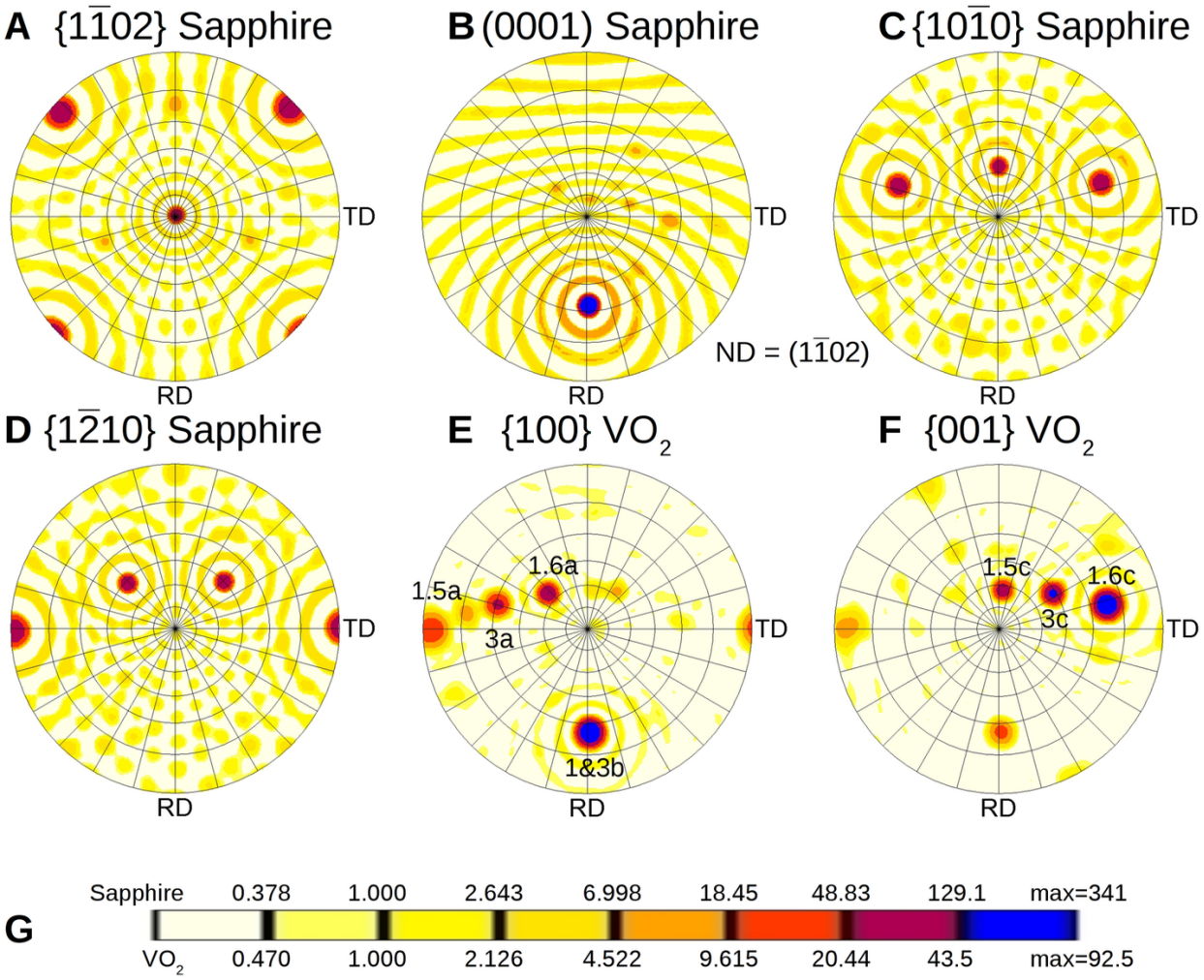

Figure 5.6 Substrate pole figures for (A) {1-102}, (B) (0001), (C) {10-10}, and (D) {1-210}. Orientation density distribution of crystalline vanadium dioxide grains deposited on r-cut sapphire for the (E) $VO_2\{100\}_R$ and (F) $VO_2\{001\}_R$ directions. (G) Scale for figures A-F with the sapphire scale placed above the VO_2 scale. (Grid lines in pole figures every 15°)

crystallographic relationships. Though family 1 and family 3 share the $VO_2\{010\}_R \| Al_2O_3\{0001\}$ relationship in common (peak 1&3b), the new relationships are now:

– FAMILY 3 –

$$(3a) : VO_2\{100\}_R \parallel Al_2O_3 10\bar{1}0 \tag{5.7}$$

$$(3b) : VO_2\{010\}_R \parallel Al_2O_3 0001 \tag{5.8}$$

$$(3c) : VO_2(001)_R \parallel Al_2O_3 1\bar{2}10 \tag{5.9}$$

The pole figures 5.6e-f show other possible variants near the noise level. The strongest of which shows as the reflection $VO_2\{001\}_R \| Al_2O_3\{0001\}$ in figure 5.6f. While these reflections are not as prominent as the labeled reflections, they suggest the existence of non-perfect oriented particles. Furthermore, the labeled families already account for >90% of the particles observed.

5.7 Crystal Orientation of Vanadium Dioxide Crystalline Grains Deposited on Single-Crystal TiO_2 Substrate.

Similar EBSD analysis was performed on vanadium dioxide deposited on a titanium dioxide substrate. Figure 5.7 shows pole figures for both, the substrate (figs 11a-d) and the grains (figs. 5.7e-h). Individual electron back-scattered diffraction patterns for the substrate and the grains were practically identical to the observer, thus indicating a close match between the grains and the substrate. As discussed earlier, the similarities between the EBSD patterns of monoclinic and rutile phases of VO_2 are not different enough for automated software indexing, and in addition, the pseudo-symmetry of the monoclinic phase leads the software to give preference to the rutile phase.

For this sample the difficulties are escalated because the tetragonal phase of VO_2 is indeed close to rutile (TiO_2).

Unlike the samples deposited on the Al_2O_3 substrate, there was no observed difference between individually collected EBSD patterns taken from the TiO_2 substrate or VO_2 grains. The collected background averaged the diffraction patters over the whole scanned area, such that it was dominated by the patterns collected by the underlying substrate. When this background was subtracted form the each data point, very weak patterns remained, insomuch that most patterns were below the threshold needed for automated indexing. (These observations further supported the existence of a very close match between the TiO_2 substrate and the VO_2 particles.)

Under these conditions, and despite the software's inability to differentiate between the grains and the substrate, several large area scans were taken from the sample allowing the computer-automated-indexing to take place. These scans differed somewhat from the method described thus far. Since background subtraction also subtracted the VO_{2-R} EBSD patterns, these large scans were intended to look for any different orientations present, and to ensure that enough indexable patterns were collected. Figure 5.7 shows pole figures for both sets of scans, indexed with the TiO_2 structure (figs 5.7a-c) and with the VO_{2-R} structure (figs 5.7d-f). While there are some fluctuations (as in the other pole figures shown before), no other peaks are seen that are statistically significant.

As expected, the relationships between the TiO_2 substrate and VO_2 grains are as follow:

$$VO_2\{100\} \parallel TiO_2\{100\} \tag{5.10}$$

seen in figures 5.7a and 5.7d, and

$$VO_2(001) \parallel TiO_2(001) \tag{5.11}$$

seen in figures figures 5.7c and 5.7f.

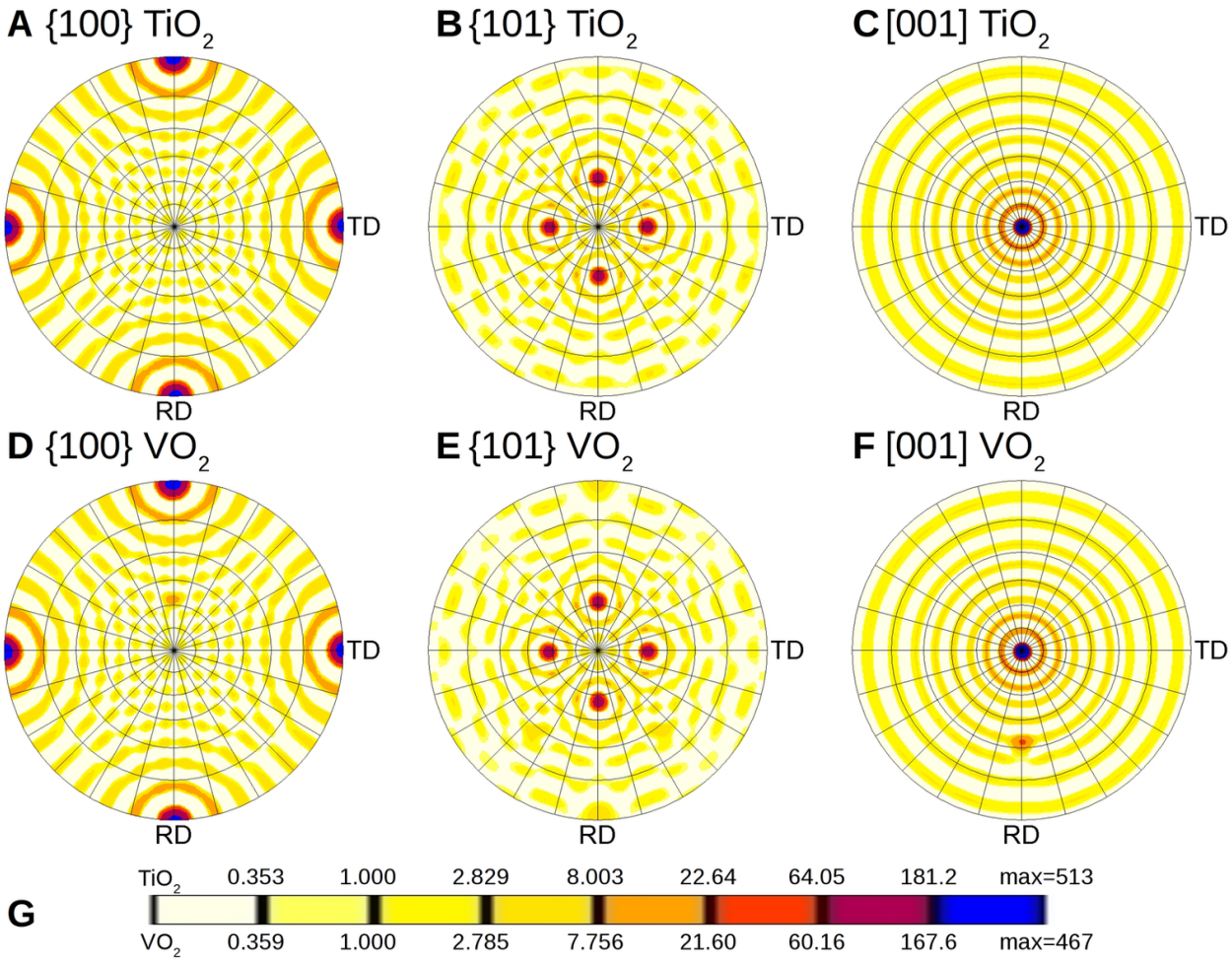

Figure 5.7 Orientation density plots TiO_2 poles (A){100}, (B){101}, (C)(001) and VO_{2R} poles (D){100} (E){101} (F){001} with their corresponding scales (G). (Grid lines in pole figures every 15°)

5.8 Crystal Orientation of Vanadium Dioxide Crystalline Grains Deposited on Amorphous SiO_2

Unlike the previous four substrates mentioned, the samples in this section were obtained from the University of Central Florida. As described in section 2.5.1, the VO_2 films were deposited on an amorphous SiO_2 layer, thus there is no expected epitaxy between the substrate and the film. However, the lack of epitaxy does not rule out the possibility of a preferred orientation for the deposition of VO_2. Thus, in order to study for the possibility of a preferred crystallographic orientation for the VO_2 grains, OIM scans were performed on these samples.

Results of the data obtained from the OIM analysis are summarized in figures 5.8, 5.9, and 5.10. These results were obtained from an OIM scan performed on a sample annealed at 450°C for 17 hrs. They are characteristic of the results obtained from all the anneals performed in argon above 440°C where the grains were allowed to grow to the thickness of the film.

Figure 5.8 shows orientation maps compiled from a scan obtained in the manner described in section 5.3. The horizontal dimension of the scan is approximately 2 μm and EBSD patterns obtained every 50 nm in a hexagonal grid. Two maps of the same data were generated. They display the orientation of the grains with respect to the Normal Direction. Map A uses 3 colors for the fitted data, while map B weighs the colors (in gray-scale) with the pattern's image quality.

This data was sectioned for 3 different orientations:

1. Grains with the C axis $\langle 001 \rangle$ of the tetragonal phase normal to the plane of the specimen. (Red in maps A, and B) [†]

2. Grains with the A axis $\langle 100 \rangle$ of the tetragonal phase[‡] normal to the surface. (Blue in maps A, and B)

[†]The red coloring is up to and including a 60° deviation from the normal.

[‡]in the tetragonal structure, the A and B axes are equivalent

3. The ⟨110⟩ direction of the tetragonal phase normal to the plane of the specimen. (Yellow in map A, and green in map B)

4. Black shows non-indexable patterns (indicative of lack of crystalline material).

The lines separating the grains in Map A are color-coded to indicate the mis-orientation between the grains.

1. Misorientations between 2° and 5° are colored red in map A and yellow in map B.

2. Misorientations between 5° and 15° are colored green in map A and orange in map B.

3. Misorientations between 15° and 180° are colored blue in map A and brown in map B.

Misorientation smaller than 2° are considered part of the same grain.

Figure 5.8 shows in both maps the lack of grains with the ⟨001⟩ normal to the surface of the specimen.

Using this data, the texture of the film can be determined. Figure 5.10 shows pole figures with the texture of a sample annealed at 450°C. The same notation is used as in figure 5.9. This data shows a preferred orientation of the ⟨001⟩ crystal direction of the tetragonal phase parallel to the surface of the specimen

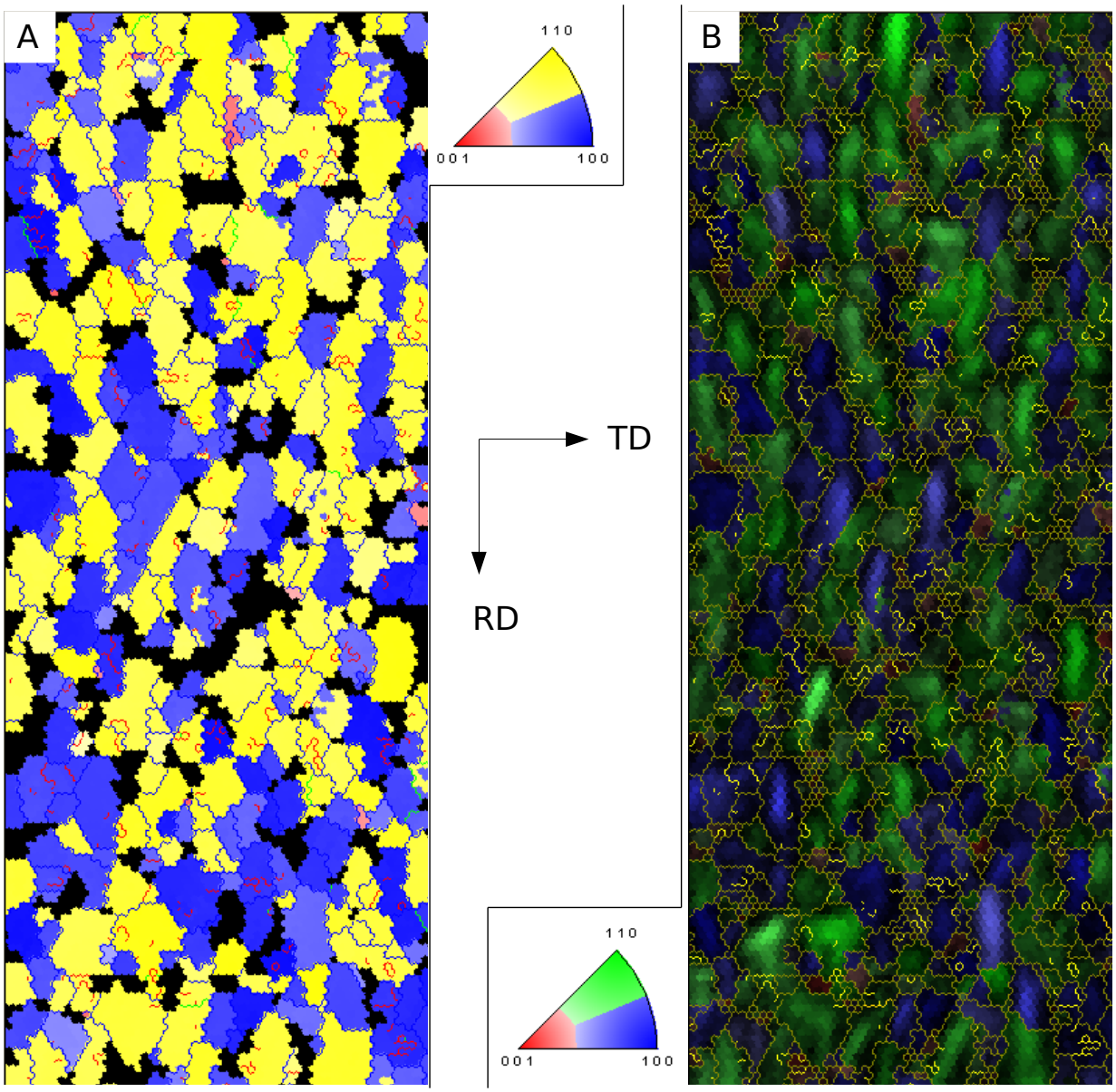

Figure 5.8 [Color] Inverse Pole Figure Map of a scan performed. This image maps out the different crystals scanned and their orientation. Crystal boundaries are determined by the misorientations found within the scan. The boundaries are color-coded depending on the misorientation between data points. Map A shows the overall grains, whereas Map B overlays (in gray-scale) the image quality of each data point obtained.

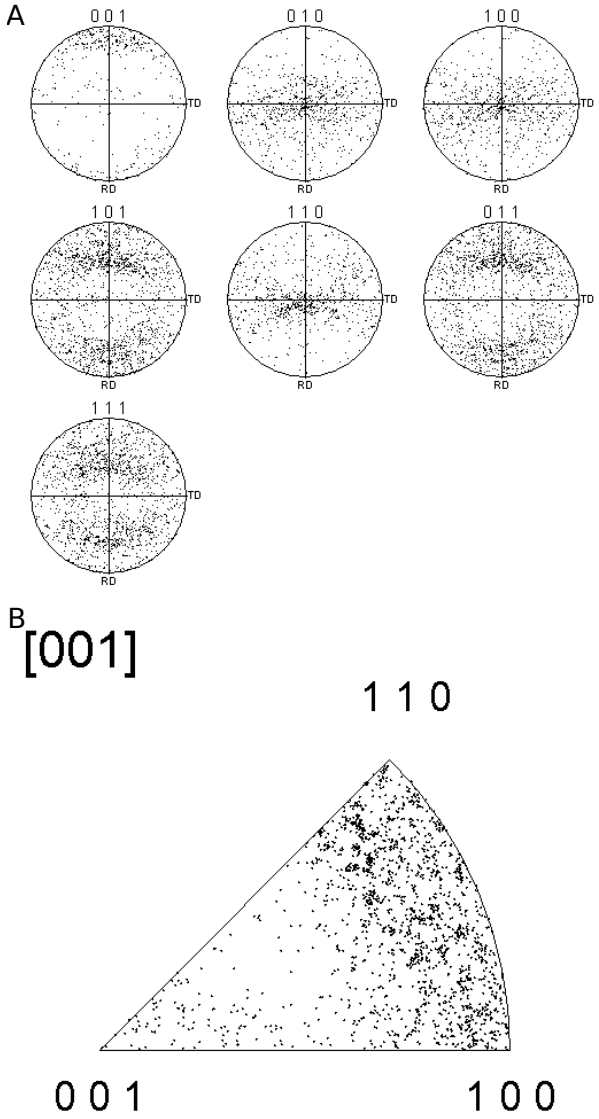

Figure 5.9 Pole Figure (PF) and Inverse Pole Figure (IPF) of an OIM scan obtained from a sample annealed at 450°C. This data is characteristic of the samples annealed above 440°C. Each data point represents the orientation recorded. In the Pole Figure, the Reference Direction (RF) and the Transverse Direction is noted. The index mentioned on top of the pole figure represents the direction normal to the surface of the sample. The Inverse Pole Figure (IPF) shows the orientations normal to the surface. Notice the lack of $\langle 001 \rangle$ crystallographic direction absent from the normal to the plane. (This is plot of the raw data)

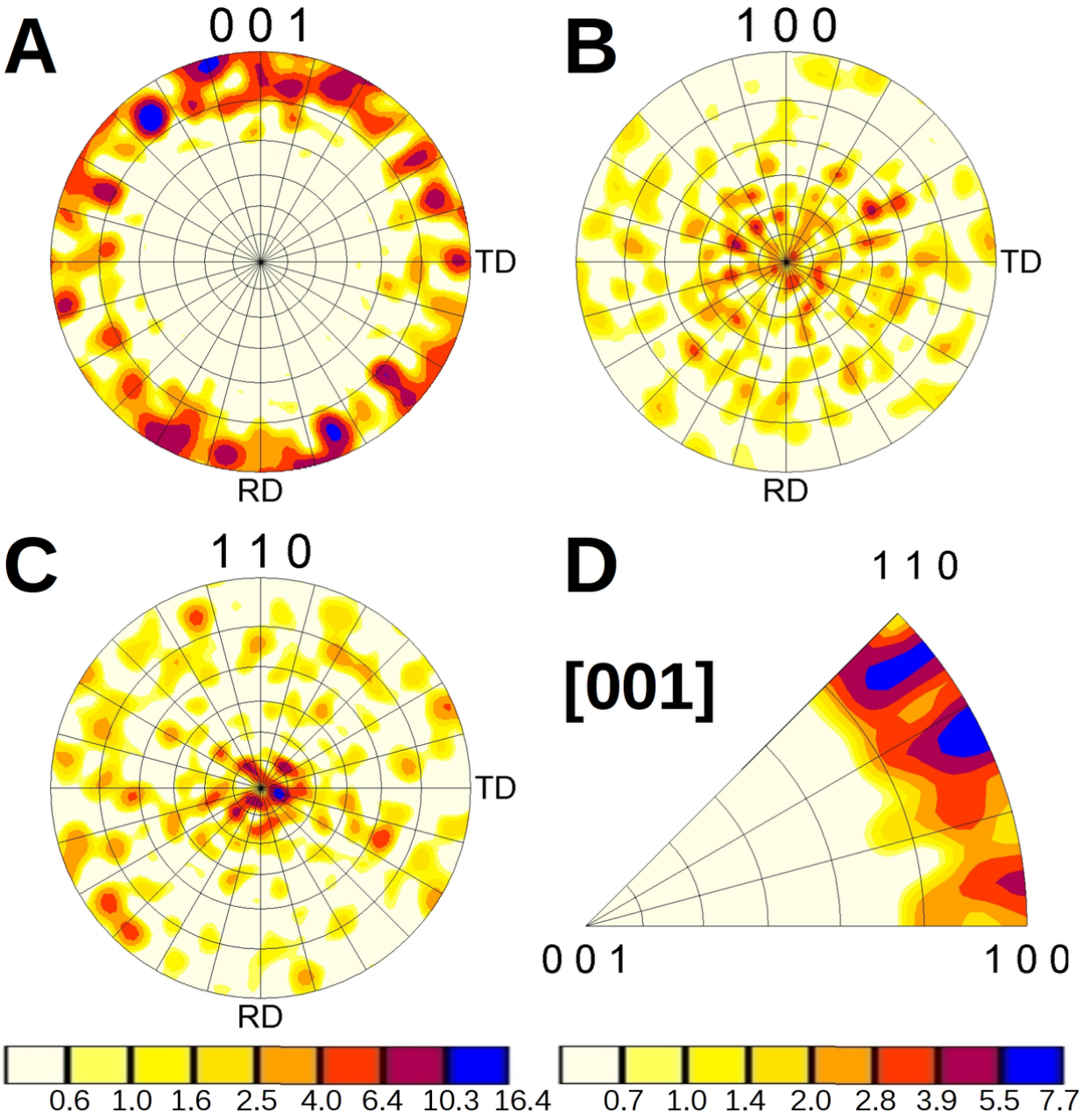

Figure 5.10 Pole Figure (PF) of the texture obtained from a sample annealed at 450°C. In the Pole Figure, the Reference Direction (RF) and the Transverse Direction is noted. The texture shows a preferred orientation of the ⟨001⟩ crystal direction of the tetragonal phase parallel to the surface of the specimen.

5.9 Analysis and Summary of results

For all the vanadium dioxide grains deposited on all different cuts of sapphire, the following crystallographic relationships were observed to some extent:

– FAMILY 1 –

$$VO_2\{100\}_R \parallel Al_2O_3\{1\bar{2}10\}; Label(1a) \tag{5.12}$$

$$VO_2\{010\}_R \parallel Al_2O_3\{0001\}; Label(1b) \tag{5.13}$$

$$VO_2(001)_R \parallel Al_2O_3\{10\bar{1}0\}; Label(1c) \tag{5.14}$$

This set of relationships summarizes the variants identified (1.1 through 1.6) such that specific crystal directions of the $VO_2 - R$ structure âĂIJseek-outâĂİ types of planes in the underlying Al_2O_3 substrate. The additional families (2 and 3) share common axes with family 1 (1a and 1b respectively) through which the VO2 crystal lattice is âĂIJrotatedâĂİ and lower in-plane lattice mismatch. Variants of these same relationships were evident in the different cuts of Al_2O_3. These variants arise from rotations of the VO_{2_R} lattice about one of its axes depending on the sapphire cut. In the case of the TiO_2 substrate, the expected relationship between the rutile phase of VO_2 and the rutile substrate is observed.

– Rutile – Rutile –

$$VO_2\{100\} \parallel TiO_2\{100\} \tag{5.15}$$

$$VO_2(001) \parallel TiO_2(001) \tag{5.16}$$

In the case of amorphous SiO_2, VO_{2-R} grains show this preferred orientation:

$$VO_2(001) \parallel In - Plane \tag{5.17}$$

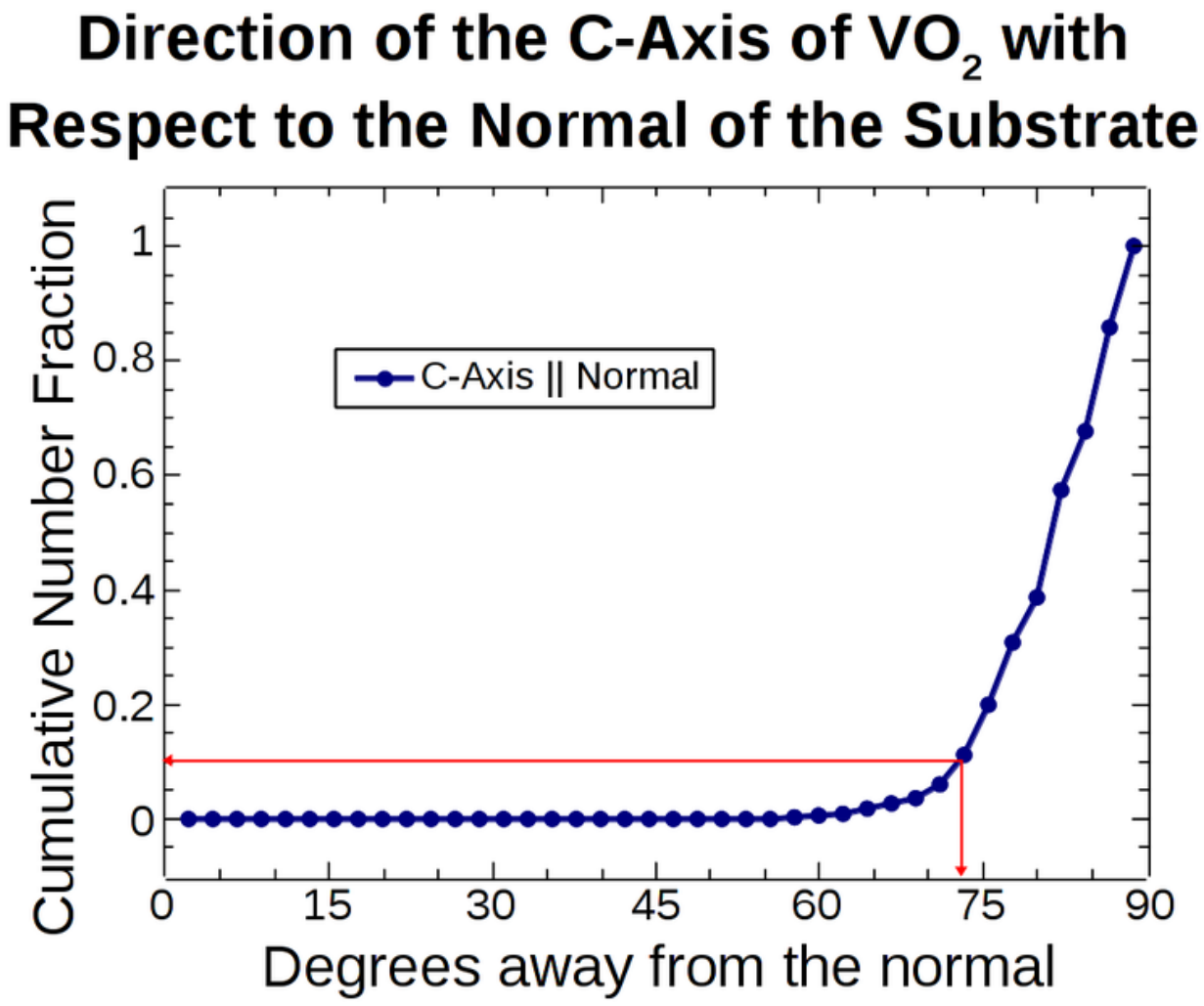

Figure 5.11 Fraction of data points where the $VO_2(001)_R$ is closer to normal than the given angle. Notice that more than 90% of the grains are oriented within 20° from being parallel to the surface.

As expected for an amorphous substrate, this relationship is not perfect. Nonetheless, more than 90% of the observed grains are within 20° of being in parallel. In order to ease this interpretation, figure 5.11 shows a plot of the cumulative fraction of grains that fall within that VO_{2-R} to amorphous SiO_2 relationship.

Table 1 shows a summary of the families of crystallographic relationships for the substrates

Substrate cut	In-plane dir.	VO_{2-R}	% Diff.	VO_{2-M1}	% Diff.	label[s]
Al_2O_3 (1-210)	Al_2O_3{0001}	$[010]_R$	5.490	$[010]_{M1}$	4.857	**1-b**
Al_2O_3 (1-210)	Al_2O_3{10-10}	$[001]_R$	3.549	$[100]_{M1}$	4.537	1.1c
Al_2O_3 (1-210)	Al_2O_3{10-10}	$[101]_R$	-2.392	$[001]_{M1}$	-2.193	**1.2**
Al_2O_3 (1-210)	Al_2O_3{10-10}	$[101]_R$	-2.392	$[303]_{M1}$	-2.653	1.3
Al_2O_3 (0001)	Al_2O_3{1-210}	$[100]_R$	-4.439	$[-10-2]_{M1}$	-4.837	**1&2a**
Al_2O_3 (0001)	Al_2O_3{10-10}	$[001]_R$	3.549	$[100]_{M1}$	4.537	1.4c
Al_2O_3 (0001)	Al_2O_3{10-10}	$[0-76]_R$	-2.782	$[3-70]_{M1}$	-3.024	**2**
Al_2O_3 (1-102)	Al_2O_3[-222]	$[01-1]_R$	4.933	$[-110]_{M1}$	4.767	1.5b
Al_2O_3 (1-102)	Al_2O_3{1-210}	$[100]_R$	-4.439	$[-10-2]_{M1}$	-4.837	1.5a
Al_2O_3 (1-102)	Al_2O_3[-111]	$[1-21]_R$	3.272	$[021]_{M1}$	2.872	**1.6b**
Al_2O_3 (1-102)	Al_2O_3[-308]	$[1-21]_R$	-0.859	$[503]_{M1}$	1.738	**1.6a**
Al_2O_3 (1-102)	Al_2O_3[-111]	$[-27-5]_R$	0.695	$[-27-2]_{M1}$	0.544	**3b**
Al_2O_3 (1-102)	Al_2O_3[-111]	$[-101]_R$	-3.380	$[110]_{M1}$	-3.637	3c
TiO_2 (001)	TiO_2<010>	$[010]_R$	-0.662	$[010]_{M1}$	-1.258	-
TiO_2 (001)	TiO_2<200>	$[200]_R$	-0.662	$[-10-2]_{M1}$	-1.080	-

Table 5.2 Predominant alignments of the VO_2 crystal directions on various substrates. Lattice mismatch uses the substrate as a reference (positive values indicates that the VO_2 lattice value is bigger than that of the substrate). The most prominent alignments for each cut are shown in bold

previously described, as well as the mismatch between the in-plane substrate's directions and the corresponding VO_{2-R} and VO_{2-M1} directions.

The role of the interface between sapphire substrate and the vanadium dioxide grains becomes more evident by looking closer at the variants of the mentioned relationships.

Figures 12(a-d) show diagrams of the atomic positions for the three variants for both phases of VO_2 deposited on the a-cut sapphire, with the most prominent variant (labeled 1.2 in figure 6) being shown in figure 12b.

For case of c-cut sapphire there are two families of relationships present, both sharing the common relationship: $VO_2\{100\}_R \| Al_2O_3\{1\text{-}210\}$ (4.44% mismatch). For this cut, the variant with the lowest mismatch places the $VO_2[0\text{-}76]_R \| Al_2O_3\{\text{-}1010\}$ (-2.78% mismatch) in plane. Diagrams of the relationships present in the sapphire c-cut are shows in figures 12g-k

Similarly, in the case of the r-cut substrate, there is a common axis for all variants,

$$VO_2\{010\}_R \parallel Al_2O_3\{0001\}, \tag{5.18}$$

however, this is not in-plane as in the a- and c- cuts of sapphire.

EBSD did not show differences between the the c-cut titanium dioxide substrate and VO_2 grains, indicating the expected close epitaxial relationship between them.

As shown in figure 3, the choice of substrate has an effect on the transition temperature and hysteresis of the phase transition of VO_2. Also, s shown in figure 2, in order for the structural transition from tetragonal to monoclinic to take place, several conditions must be met:

- The c-axis must expand by 0.94% and be allowed to stagger.
- The a-axis must contract by 0.42% and be allowed to stagger.
- The b-axis must contract by 0.59% and remains collinear.
- The angle between the a- and c-axes should change from 90° to ∼89.2°

In order to shed some light into the causality of the changes in the phase transition temperature, table 3 shows some observed relationships between the measured phase transition temperature and the lattice mismatch in the most common variants observed. The data for this table is compiled from tables 1 and 2 shown earlier. The a- and c- cuts of sapphire are closer to the nominal phase transition of bulk VO_2, while the sapphire r-cut and the titanium dioxide cuts have significantly lower transition temperatures.

The TiO_2 substrate has a lattice spacing that has a "tensile strain" on the VO_2 rutile lattice, thus preventing it from contracting even further to allow for the phase transition at the expected temperature. In contrast, the Al_2O_3 A-cut substrate has a "compressive strain" in the b-axis of the tetragonal phase, required to "motivate" the contraction needed in such direction, thus not hindering the transition temperature.

Unfortunately, if the same explanation is used for, the Al_2O_3 C- and R-cut substrates these tensile or compressive stresses are not enough to explain the changes in transition temperature and hysteresis. Other factors may include the symmetry of the surface, for example, the c-cut sapphire substrate has a hexagonal symmetry which may show preference for the monoclinic phase even though the strains seem to show preference for the rutile structure. Therefore, a more detailed analysis is needed to fully explain the observed changes in the transition temperature.

5.10 VI. Conclusions

Vanadium dioxide has recently become a material of particular interest due to its ultra-fast reversible metal to insulator structural phase transition at neat 68°C, as well as for its drastic optical and electronic changes that accompany it. Al_2O_3 and TiO_2 are often chosen as the substrates for the deposition and study of VO_2 due to their close lattice match and expected epitaxy.

Despite the charging artifacts present during the collection of Electron Back-Scattered Diffrac-

tion patterns, the data obtained yielded self-consistent crystallographic relationships for Vanadiuim Dioxide deposited onto various substrates by pulsed laser deposition. It was found that, during deposition onto sapphire substrates, the rutile phase of vanadium dioxide tends to align itself such that:

$$VO_2\{100\}_R \parallel VO_2\{100\}_{M1} \parallel Al_2O_3\{1\bar{2}10\}; \tag{5.19}$$

$$VO_2\{010\}_R \parallel VO_2\{100\}_{M1} \parallel Al_2O_3\{0001\}; \tag{5.20}$$

and

$$VO_2\{001\}_R \parallel VO_2\{100\}_{M1} \parallel Al_2O_3\{\bar{1}010\}. \tag{5.21}$$

This family of crystallographic relationships was found present in all cuts of sapphire in as much as "90%" of the observed grains. The type of sapphire cut added variations to this family of relationships due to the symmetry of the substrate at the surface interface. Nonetheless in all the sapphire cases, one of these mentioned relationships was a common for all the variations. These variations within the families were rotations in the crystal lattice that lowered the strain between the substrate and the vanadium dioxide grains. Even though these relationships hold for a large amount of the observed grains, these variations (or variants) prevent a perfect epitaxy from taking place by allowing different orientations of vanadium dioxide grains to be formed. In the case for the $TiO_2(001)$ substrate, the expected relationship between the $VO_{2R}(001)$ grains and the substrate is observed.

Given the array of substrates presented in this chapter, and the calculated strains between the substrate and the different phases of VO_2, there is evidence to suggest that these strains, along with the overall motif at the film/substrate interface, affect the transition temperature and width of the hysteresis of the VO_2 films deposited.

Chapter 6

Further Characterization of Thin Films Through Transmission Electron Microscopy

The Physics and Astronomy Department at Brigham Young University is equipped with two Transmission Electron Microscopes: The Technai TF30 (a 300kV, Field-Emission, High Resolution, Transmission Electron Microscope), and the Technai TF20 (a 200kV Field-Emission, High Resolution, Scanning, Analytical, Transmission Electron Microscope). With the use of these TEMs it is possible to image and obtain information about the deposited films down to individual nanoparticles. Furthermore, the analytical capabilities of the TF20 allow for further chemical analysis of the samples.

As mentioned in section 3.3, the theoretical resolution arises from the voltage used to accelerate the electrons (see equation 3.2). In practice, however, this theoretical resolution is limited due to lens aberration. Nonetheless, the spatial resolution achievable with the TEM far surpasses that of the SEM. Furthermore, in transmission electron microscopy, the electron-beam signals are not limited to the transmitted electron, but also the e-beam signals generated above the sample are still present and can be used to further analyze the sample (refer to figure 3.2). With these added

analytical capabilities, it is possible to further study the properties of VO_2 thin films' grains and individual nanoparticles. The transmitted electron beams carry with them a wealth of information regarding the inner-structure of the sample (see figure 3.2).

In this chapter, the use of transmission electron microscopy (TEM) is presented as a tool for further characterization studies of this material. Several preliminary results are presented for various TEM techniques employed with the purpose of encouraging further research with these methods, namely:

- Transmission electron diffraction to study the epitaxy of VO_2 thin films on various substrates.
- Transmission electron diffraction, bright field (BF) and dark field (BF) imaging, as well as convergent-beam electron diffraction to study the phase transition of individual nanoparticles
- Electron energy-loss spectroscopy to study the role of the grain boundaries in continuous VO_2 thin films. (An initial study was performed, but will not be included in this work.)

(In the following chapter, a focused-ion beam technique for preparation of cross-sectional TEM samples of metallic thin films deposited on polymer substrates is demonstrated, along with more characterization available for the TEM.)

6.1 Transmission Electron Microscopy of VO_2 Thin Films and Nanoparticles

In order to expand the initial characterization done by scanning electron microscopy, several samples were taken from the specimens described in the previous chapters. Specifically, plan view samples were prepared from the VO_2 films deposited onto amorphous SiO_2 by means of the wedge polishing method described in section 3.5. Furthermore, cross-section TEM samples were also ob-

tained from the VO_2 films deposited on the A-cut and R-cut sapphire substrates by means of a standard focused ion beam sample preparation technique.

6.1.1 Orientation of VO_2 grains on A- and R-cut Al_2O_3

As indicated in chapters 4 and 5, due to particle size and EBSD is unable to discern between the monoclinic and rutile phases of VO_2. Given the added resolution from a TEM, it is possible to obtain crystallographic information from individual grains through selected area electron diffraction (SAED). Cross-sectional TEM samples from the VO_2 films deposited onto the a-cut and r-cut sapphire were prepared using a focused ion beam standard technique.

A-Cut sapphire

To further investigate the crystallographic relationship between the substrate and the VO_2 grains, a TEM cross-section sample from this specimen was milled out and prepared with a focused ion beam in the Helios dual beam mentioned earlier. This cross-section samples was then imaged using a Technai TF20 transmission electron microscope. A selected area electron diffraction (SAED) pattern was obtained from an area that included a VO_2 grain as well as the A-cut substrate (see figs. 6.1b and 6.1a respectively). The strong diamond shaped array (an array unit highlighted on the left of 6.1b, and respectively in 6.1c) corresponds to the sapphire substrate with a weaker array of spots from the VO_2 interlaced within this array. Using the EBSD results as a starting point, a simulated electron diffraction pattern was generated using sapphire (Al_2O_3) and VO_{2M1} lattice parameters (fig. 6.1c). This calculated electron diffraction pattern was then compared with the obtained SAED pattern (fig 6.1b). The SAED pattern shows that the $VO_2\{200\}_{M1}$ is parallel to the $Al_2O_3(1\bar{2}10)$.

Using the VO_{2-R} to VO_{2-M1} mapping shown in figure 2.9, having the $VO_2\{200\}_{M1}$ parallel to $Al_2O_3(1\bar{2}10)$ indicates in real space that the $VO_2[200]_{M1}$ should be $\sim 32^\circ$ from the normal

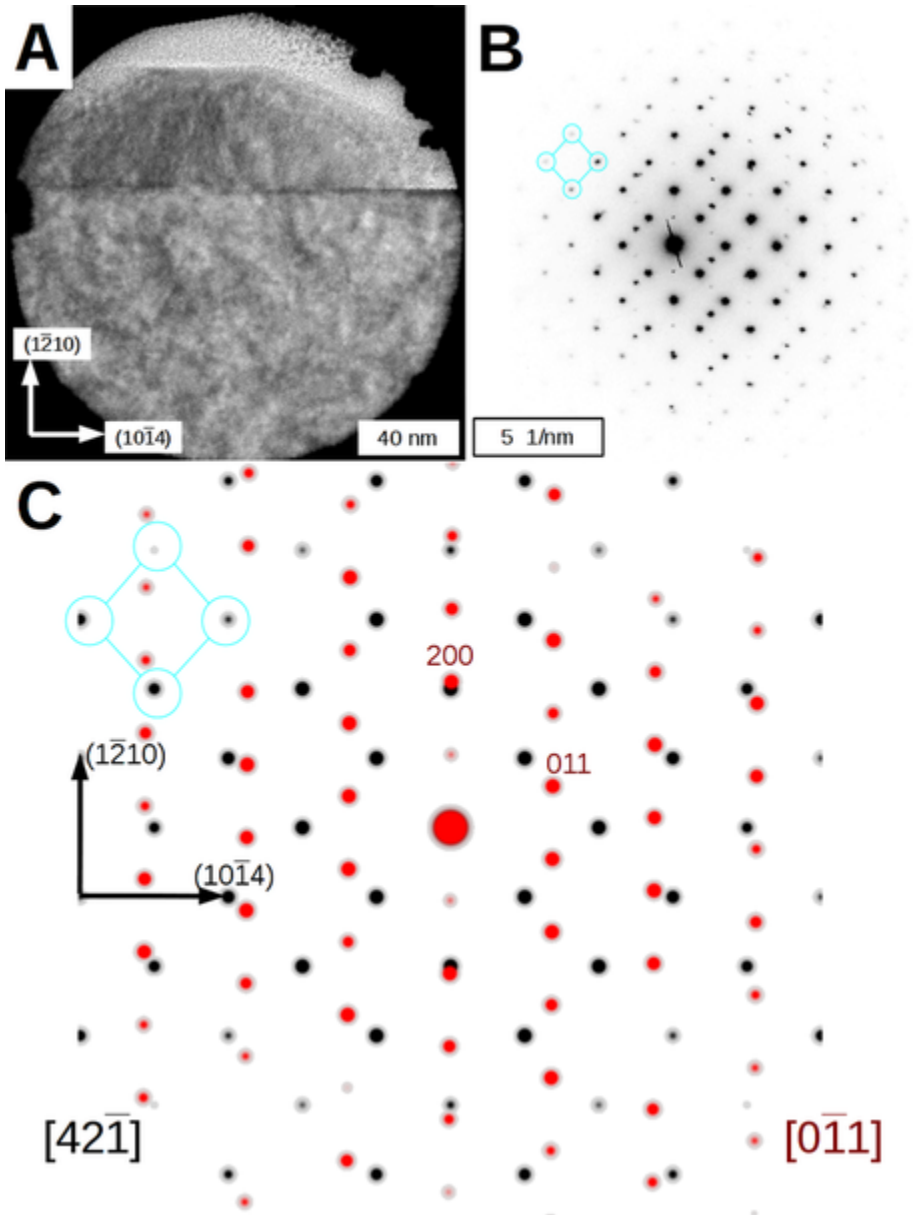

Figure 6.1 A) TEM cross-section image of a vanadium dioxide grain on A-cut sapphire. B) Selected area electron diffraction pattern covering both a VO_2 grain and the A-cut sapphire substrate. C) Matching calculated electron diffraction pattern. Sapphire substrate peaks shown in black, monoclinic VO_2 peaks in red. The sapphire $(1\bar{2}10)$ direction is parallel to the $VO_2\{010\}_{M1}$ direction. The image and diffraction patterns were self-consistently oriented.

direction. Again, using figure 2.9 as a reference, this condition places the $VO_2[001]_R$ $\sim 32^\circ$ from the normal direction, consistent with the two strongest features in figure 5.4b. Furthermore, in the case of the grain imaged by TEM, the zone of the SAED pattern places the $VO_2[010]_{M1}$ and the $VO_2[001]_{M1}$ in plane by virtue of having the $VO_2\{100\}_{M1}$ normal to the surface. This information helps to break the ambiguity in the tetragonal VO_{2-R}a and VO_{2-R}b axes. From figure 5.4a, one of the $VO_2\{100\}_R$ axis lies in plane while the other lies $\sim 60^\circ$ from the normal. For the particle imaged in the TEM, the EBSD and the SAED data are consistent by having the particle oriented with the following rules:

– Variant 1.2 –

$$VO_2\{010\}_R \parallel Al_2O_3(0001) \tag{6.1}$$

in plane;

$$VO_2\{001\}_R \parallel Al_2O_3(10\bar{1}0) \tag{6.2}$$

at $\sim 30^\circ$ off the normal; and

$$VO_2\{100\}_R \parallel Al_2O_3(1\bar{2}10) \tag{6.3}$$

at $\sim 60^\circ$ from the normal. This description is consistent with the strong features in figures 5.4a and 5.4b (peaks 1-b, 1.2c, and 1.2a respectively).

R-Cut sapphire

A TEM cross-section sample was prepared out of this sample in the same manner described for the a-cut sapphire sample. A high-resolution TEM image of a grain deposited in sapphire r-cut showing the epitaxy of the grain on the substrate is shown in figure 10a. Fortuitously, this particular image is oriented such that the substrate is oriented with the $Al_2O_3\{1-102\}$ normal to the surface and the $Al_2O_3\{1\bar{2}10\}$ pointing to the right, thus easing comparisons to the EBSD results in figure 5.6.

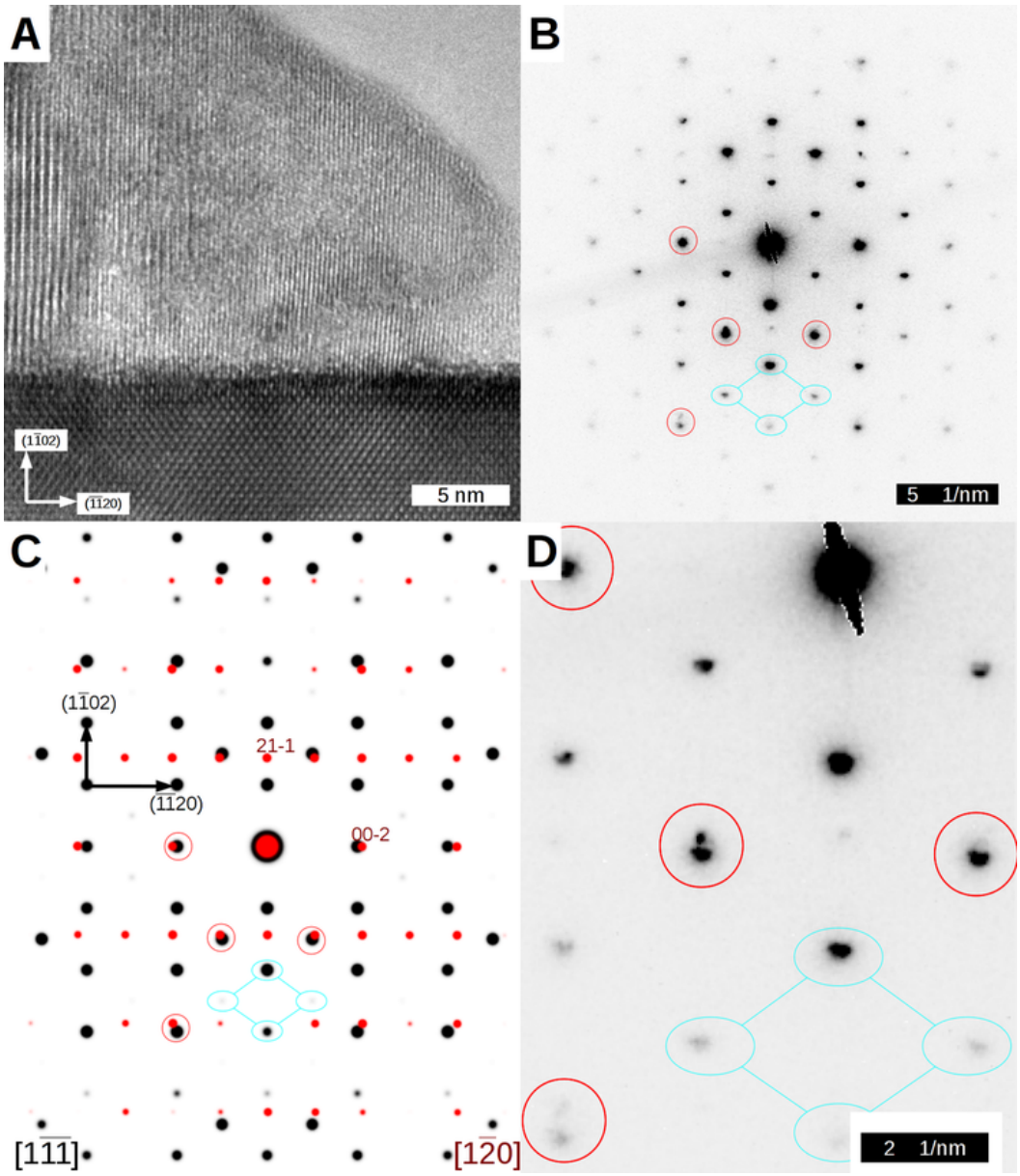

Figure 6.2 A) High-resolution transmission electron micrograph of a cross-section of a vanadium dioxide grain deposited on r-cut sapphire. B) Selected-area electron diffraction of substrate and VO_2 grain. C) Calculated electron diffraction pattern. D) Close-up of the electron diffraction pattern showing the doublets formed by the substrate and grain. The HRTEM image and diffraction patterns were self-consistently oriented.

Figure 6.2b shows an electron diffraction pattern that selected an area covering the particle and the substrate from figure 6.2a. The strong diamond-shaped array of peaks corresponds to the r-cut sapphire substrate (highlighted in the figure) with significantly weaker VO_2 array of peaks interlaced between some of these diamond-shapes. A simulated electron diffraction pattern was generated in a manner similar to the pattern generated for the a-cut sapphire substrate (fig. 6.2c). Peaks prominently present in the SAED yet weak in the simulation are attributed to multiple scattering events from electron diffraction in the substrate. The highlighted diamond-shape in the calculated diffraction pattern (fig 10c) corresponds to the peaks highlighted in the acquired SAED (fig 6.2b), however the calculated diffraction pattern shows two strong and two weak peaks while the acquired SAED shows the weak peaks stronger.

The following crystallographic relationships were extracted from the SAED pattern:

$$VO_2\{002\}_{M1} \parallel Al_2O_3\{-1-120\} \tag{6.4}$$

in plane and

$$VO_2\{21-1\}_{M1} \parallel Al_2O_3\{1-102\} \tag{6.5}$$

normal to the surface.

According to the mapping shown in figure 2.9, these translate to the following relationships for the rutile VO_2 phase:

$$VO_2\{100\}_R \parallel Al_2O_3\{1\bar{2}10\} \tag{6.6}$$

in plane, and

$$VO_2\{115\}_R \parallel Al_2O_3\{1-102\}. \tag{6.7}$$

Fixing these two VO_{2-R} vectors, places the

$$VO_2\{010\}_R \parallel Al_2O_3(0001) \tag{6.8}$$

at $\sim 60^\circ$ off the normal, and the

$$VO_2\{001\}_R \parallel Al_2O_3(10\bar{1}0) \tag{6.9}$$

at $\sim 30^\circ$ off the normal, which correspond to the 1.5 family in figure 5.6 (peaks 1b and 1.5c respectively). The information obtained from the SAED helps again to break the ambiguity present between the $VO_2\{100\}_R$ and $VO_2\{010\}_R$ types of planes. Furthermore, these crystallographic relationships found reinforce the relationships found for the a-cut sapphire.

The SAED pattern also indicates the presence of double peaks that arise from the diffraction from the VO_2 grain's lattice overlaid over the diffraction from the substrate's lattice. Four of these expected doublets are circled in the acquired SAED pattern (fig 6.2b) with corresponding circles on the calculated diffraction pattern (fig 6.2c). Figure 6.2d shows a close-up of the circled doublets in order to enhance the detail.

6.2 Summary and Conclusions

Summary and analysis of results For all the VO_{2-R} grains deposited on all different cuts of sapphire, the crystallographic relationships from family 1 were observed to some extent. Variants of these same relationships and additional families were evident in the different cuts of Al_2O_3. As previously mentioned these variations arise from rotations of the VO_{2-R} lattice about one of the axes present in family 1.

In this chapter, electron diffraction patterns from TEM cross-sectional samples confirmed the crystallographic relationships mentioned in family 1, for the a- and r-cut sapphire substrates. Furthermore, the obtained TEM electron diffraction pattens, indexed using the VO_{2-M1} phase, helped

lift the inherent ambiguity between the $VO_2\{100\}_R$ and $VO_2\{010\}_R$ families of planes. Both TEM samples showed these specific and more complete set of crystallographic relationships between the VO_2 films and the Al_2O_3 sapphire substrates:

– Family 1 (more complete) –

$$(1a) : VO_2(100)_R \parallel Al_2O_3\{1\bar{2}10\} \parallel VO2(\bar{1}0\bar{2})_{M1}; \tag{6.10}$$

$$(1b) : VO_2(010)_R \parallel Al_2O_3\{0001\} \parallel VO_2(010)_{M1}; \tag{6.11}$$

$$(1c) : VO_2(001)_R \parallel Al_2O_3\{10\bar{1}0\} \parallel VO_2(100)_{M1}. \tag{6.12}$$

This modified set of relationships (compare to family 1 mentioned in a-cut) summarizes the variants identified (1.1 through 1.6) such that specific crystal directions of the VO_{2-R} structure "seek-out" types of planes in the underlying Al_2O_3 substrate, and also maps those relationships to the low-temperature phase VO_{2-M1}.

Chapter 7

Alternative FIB TEM Sample Preparation Method for Cross-Sections of Thin Metal Films Deposited on Polymer Substrates

The integration of electronic components onto flexible substrates has created many interesting products with increasingly shrinking electronic geometries. Consequently, this integration has also created the need to study the behavior of these materials and devices in the nano-scale. Transmission electron microscopy (TEM) and focused ion beam (FIB) are proven tools in the semiconductor industry to produce site-specific samples in which to study these devices, from the initial processing up to their causes for failure, as well as investigating the quality, defects, interface layers, etc., of these devices. However, the use of polymers in the substrate presents an array of new challenges for site-specific suitable TEM sample preparation such as sample warping, heating, charging, and melting. In addition to the current options that address some of the problems that come with polymer substrate TEM sample preparation, we add an alternative method and FIB sample geometry that address these challenges and produce TEM samples suitable for TEM elemental analysis. In

this chapter, TEM elemental analysis of various thin metallic films deposited on polycarbonate, plastic, lacquer, and PDMS patterned substrates, is shown as a proof-of-concept of the method. The aspect ratios of the patterns in the substrates include low (500 nm wide : 100 nm tall), medium (100 nm wide : 200 nm tall), and high (100 nm wide : 800 nm tall). We further show that this FIB sample preparation method preserved these patterned structures.

7.1 Introduction

The integration of electronic components onto flexible substrates has created many interesting products, from flexible displays and solar cells to wearable electronics. There are many aspects that make polymers attractive for the use as substrates in applications. These aspects range from the inexpensive cost of the raw material and manufacturing, to the ease of production and patterning. These desirable qualities of polymer substrates, in conjunction with increasingly shrinking electronic geometries, have opened the need to study the behavior of these materials and devices in the nano-scale, in a manner parallel to semiconductor manufacturing. Traditionally, semiconductor device manufacturers rely on well-established cross-sectional transmission electron microscopy (TEM) analytical techniques for studying and monitoring the process, observing and investigating defects, as well as interface layers of their devices. Furthermore, current focused ion beam (FIB) TEM sample preparation methods also provide a tool to produce high-quality, site-specific, TEM cross-section samples for the semiconductor industry.[99, 106–108, 112–118, 120, 123, 128, 133, 150, 151]

Sample preparation is one of the critical steps in TEM analysis that significantly determines the quality of the characterization and chemical analysis in the smallest and most critical structures. However, the same qualities that make polymers attractive for use in patterned and/or flexible substrates, present an array of new challenges that must be overcome in order to apply the established analytical techniques (already used for semiconductors) in the study of these polymer-substrate

devices. For example, due to the nature of polymer substrates, as the sample is thinned by the ion beam to a thickness suitable for TEM analysis, the sample begins to warp, heat up, charge, and melt.[110,116,117,120,122,132,152]

Thanks to the use of transmission electron microscopy in the biological sciences, TEM sample preparation methods such as ultramicrotomy and cryo-FIB are currently employed to deal with some of the problems mentioned above.[109,153–155] In the case of ultramicrotomy, a sharp blade is used to mechanically produce sequential thin sections of a hardened sample relatively fast. Cryo-FIB, while slower than microtomy, adds the benefit of being able to produce site-specific TEM samples of a cryogenically hardened sample. These cryogenics also help against sample heating problems, but require the needed cryogenic equipment and handling for the FIB and TEM.[119,132,150,156–162]

In this paper, we would like to present and add an alternative FIB-based cross-sectional TEM sample preparation method and sample geometry. This method has proven reliable and robust in producing TEM samples of metallic thin films deposited onto various polymer substrates, while retaining the benefit of being site specific, and extending the use of FIB instruments without a cryogenic stage. As proof-of-concept for this method several TEM samples were prepared and analyzed by TEM and energy-dispersive x-ray spectroscopy (EDX). Some of these samples included commercial recordable DVDs, BluRay disks, and nanopatterned PDMS and plastic films. The analyzed metallic thin films ranged from a single layer approximately 30 nm thick to multi-layer stacks approximately 200 nm in thickness.

While this method increases the sample preparation time by approximately 50% (compared to a similar sample in a glass substrate[151] the approach presented here has the advantage of extending the use and benefits of FIB instruments (currently without a cryogenic stage) to prepare site-specific TEM samples for the study of materials deposited onto polymer substrates.

7.2 Materials and Methods

The process used for sample preparation took place within a Helios Nanolab 600 dual-beam from FEI equipped with a Ga^+ ion source, a platinum metal-organic gas injection system (GIS), and with an Omniprobe micromanipulator. The analysis of the produced TEM samples was performed in an FEI Technai TF20 analytical (Scanning)TEM equipped with a EDX system.

The various specimens, from which TEM samples were prepared, comprised metallic layers of various thicknesses deposited on top of different polymer substrates patterned with structures of diverse aspect ratios. The polymer-substrates varied from a 500 μm-thick polycarbonate substrate down to a $\sim$100 μm-thin patterned lacquer film, and included softer silicone-based polymer-substrates. The structures patterned ranged in aspect ratio from the size of a BluRay write track ($\sim$50 nm high and $\sim$300 nm wide) up to structures 800 nm tall and 100 nm wide. Finally, the deposited thin film stacks ranged from a single metallic layer $\sim$30 nm thick up to multi-layer stacks $\sim$120 nm thick (with the thinnest layers in the order of 10 nm). Table 7.1 summarizes the specimens from which the TEM samples were extracted using the process that will be described shortly.

Following the sample preparation these TEM samples were then imaged using the TF20. EDX line-scans were then obtained in order to study the deposited metallic thin film stacks. Though EDX line-scans were common among the samples, other TEM analysis and imaging (comprising of bright- and dark-field imaging, high resolution TEM, and selected area electron diffraction) was done depending on the sample.

Polymer Substrate	Thin Film Stack	Aspect Ratio (H:W)
Polycarbonate (DVD and BluRay disks)	Multi-layered (∼120 nm)	Low (800 nm:100 nm)
PDMS (Imprints)	Single Layer (∼30 nm)	High (100 nm : 600 nm)
Flex Plastic Films (Imprints)	Single Layer (∼30 nm)	Medium (150 nm:50 nm)
Lacquer Films (BluRay disks)	Multi-layered (∼120 nm)	Low (400 nm:30 nm)

Table 7.1 Summary and description of the specimen with polymer-substrates from which TEM samples were extracted.

7.2.1 Outline of "Modified Self–Supported H-Bars" TEM Sample Preparation Method.

The use of polymer substrates presents an array of challenges when preparing TEM cross-sectional samples. Some of these include charging, heating, warping, and melting. In order to address many of these challenges, the following steps were used to prepare cross-sectional TEM samples. As a form of reference the following terms are defined as follows: the length of the sample is arbitrary and runs in-plane along the region of interest; the width of the sample is in-plane and perpendicular to the region of interest; the depth goes into the sample, cutting through the thin film into the substrate. (See the diagram in figure 7.1a)

– 1) Ex-situ protective conductive coatings –

Polymer substrates are poor conductors and, as a consequence, they tend to image poorly inside an electron microscope. Furthermore, FIB imaging causes significant damage to the surface of the specimen.[106, 107, 116, 120] Both of these problems can be addressed by depositing a conductive protective layer onto the specimen before inserting the sample into the dual beam microscope (fig. 7.1a). Based on our experience, a protective carbon layer ∼80 nm thick offers the following benefits:

1. Small sputtering cross-section, thus protecting the sample's surface while imaging with the focused ion beam;

2. Conductive, thus minimizing charging issues in the electron microscope;

3. Low Z, providing adequate contrast to differentiate it from the metallic layers, and low electron scattering for EDX profiles.

For our samples, the protective carbon layer was thermally deposited. A gold conductive layer, as common in scanning electron microscopy (SEM) imaging, was done for initial trials. However, the issues mentioned in point 3 arose while performing EDX line-scans.

– 2) In-situ protective platinum pad –

This step goes in-line with "standard" FIB TEM cross-section sample preparation.[121, 130] This platinum deposition provides an additional protective conductive layer for the FIB TEM sample processing (fig. 7.1a). Due to the amount of imaging that takes place during the milling out of the TEM sample, as well as the varied currents required for the milling of the TEM sample, this additional Pt layer becomes invaluable in protecting the deposited metallic films against the energetic incident Ga^+ ions.

A comparison in the micrographs from 7.1a and 7.1b shows how damaging the FIB patterning process can be on the surface of the nearby areas of the sample. Thus, as the micrographs in figures 7.1a and b show, a Pt conductive pad about 3 μm wide and (at least) 0.5 μm tall was used to protect the areas of interest against the eroding process the ion beam has while imaging.

In addition to the protection provided by the Pt pad, further down the sample preparation process this protective Pt layer will also help provide a rough "rule-of-thumb" regarding the final thinning of the sample while still providing protection to the deposited metallic thin film.

– 3) Mill and lift-out of thick supporting block –

In contrast to "standard" FIB TEM cross-section sample preparation, where the milled sample is between 1 μm and 2 μm wide, this process requires that a "block" at least 5 μm wide is milled out (fig. 7.1b). This block will provide the necessary support for the upcoming sample as well as other thermal benefits that are advantageous during sample preparation. With this in mind, the height of the sample needs to be taller than the size of the desired viewing windows. Since the features of interest for our specimens were below 1 μm deep, samples 6 μm deep were prepared (fig. 7.1b).

While this larger sample-milling does increase sample preparation time (when compared to the "standard" technique), these other added benefits help expedite[122] the process, and increase the chance of success:

1. During this mill, most of the ion damage will be confined to the edges of the support structure. As such, a higher milling current can be employed during the rough milling cuts, while preserving the integrity of the region of interest.

2. This rough milling process also embeds Ga^{+} ions into the polymer, thus metalizing the support structure and increasing (however slightly) the electrical and thermal conductivity of the polymer substrate.

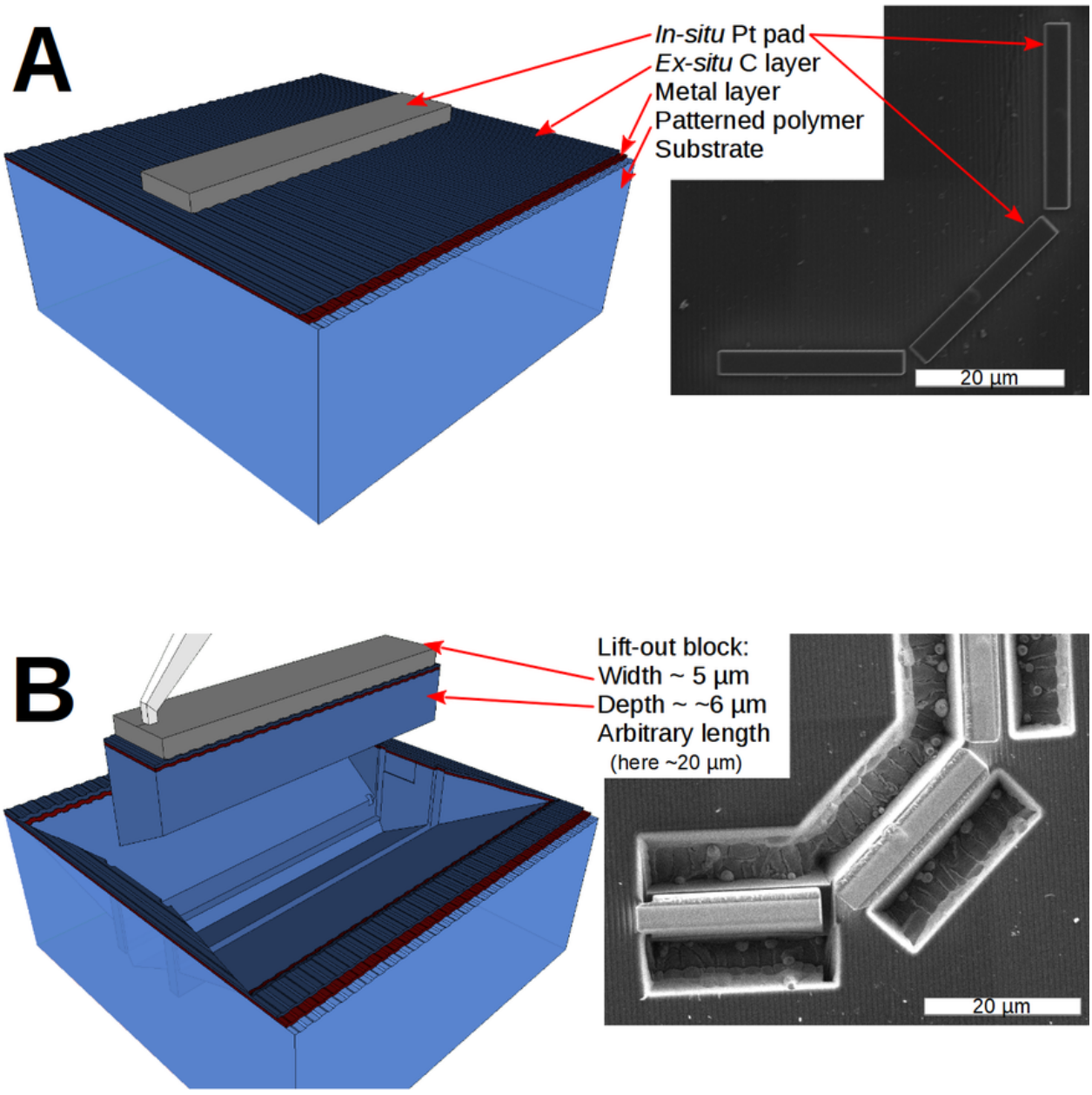

Figure 7.1 (A) Pt and C layers deposited to protect a specimen comprised of a thin metal film deposited onto a patterned polymer substrate. (B) Lift-out of a "thicker-than-usual" support block

3. The size of the block provides room for error (see step 5 and the micrograph in figure 7.2a). While there currently are set parameters for milling into substrates used in the semiconductor industry (and often already pre-set in FIB instruments), such is not the case for varied polymer-substrates. In this case, the bigger support block provides additional "testing" volume in which milling parameters can be fine-tuned.

– 4) Lift-out and weld –

Up to here, this lifted-out block (now gallium-embedded) will help mitigate against the challenges of charging, heating, and warping. This in-situ lift-out technique goes in-line with common standard lift-out techniques and there were no observed difficulties with charging or warping during this step (diagram in fig. 7.1b). For our samples the lift-out was done with an Omniprobe micromanipulator, an accessory added to the FEI dual-beam system. The milled out block was lifted out and welded onto an Omniprobe copper half grid. This welding was done using the platinum GIS. Again, due to the size of the support block, the region of interest is still well protected from lateral ion damage while welding. An observed benefit of welding at this stage of sample preparation is the reduced redeposition during the final thinning.

(The author has not attempted ex-situ lift-out of these samples. However, given the inherent size of these samples, they should be relatively easy to handle and manage with an ex-situ micromanipulator once the sample is finally in-situ thinned.)

– 5) Initial window milling –

In a manner similar to the standard technique, a rough mill is performed on both sides of the sample as to begin the creation of the viewing area (fig. 7.2a). This milling serves as a gauge for the milling parameters needed for the rest of sample preparation. This initial mill should be deep enough to allow a view of the area of interest, yet it must not be too deep that it breaks the

structural integrity of the sample.

For the samples prepared, there were no observed milling parameters that applied to all different polymers. However, at this stage, a trial 500 nm wide by 400 nm deep cut was first attempted along the edge of the sample. Based on the actual milling depth achieved, the milling parameters and the depth of the rest of the cuts were modified accordingly. Since the region of interest is limited to deposited metallic thin films, a viewing window 500 nm deep would be more than sufficient.

Since the lifted out block is approximately 5 μm wide and 5 μm deep, these edge mills can be up to a micron wide and 500 nm deep, leaving the inner 3 μm that contain the region of interest unharmed.

This milling is repeated in the front and rear of the sample (fig. 7.2a). In contrast to common techniques, it is imperative that the milling on both edges remains well below the full depth of the sample in order to preserve the structural integrity of the block. Thus it is recommended to do the initial mill in the edge of the sample that can be imaged with the electron beam after the mill is complete.

Again, in our case, the features of interest for our specimens were within 1 μm from the surface. As such, the initial window mill was set for 2 μm deep. The micrograph in figure 7.2a shows, the following: 1) the first two attempts milled too deep into the block, and 2) the Pt pad provides enough contrast which helps to identify the location of the layer of interest as well as the adequacy of the depth of the milled window.

– 6) Window wells –

As mentioned earlier, the use of polymer substrates present challenges that include charging, heating, warping, and melting. Having the structural support of the thick gallium-embedded block helps mitigate some of the previously mentioned challenges. Nevertheless, as the process to further

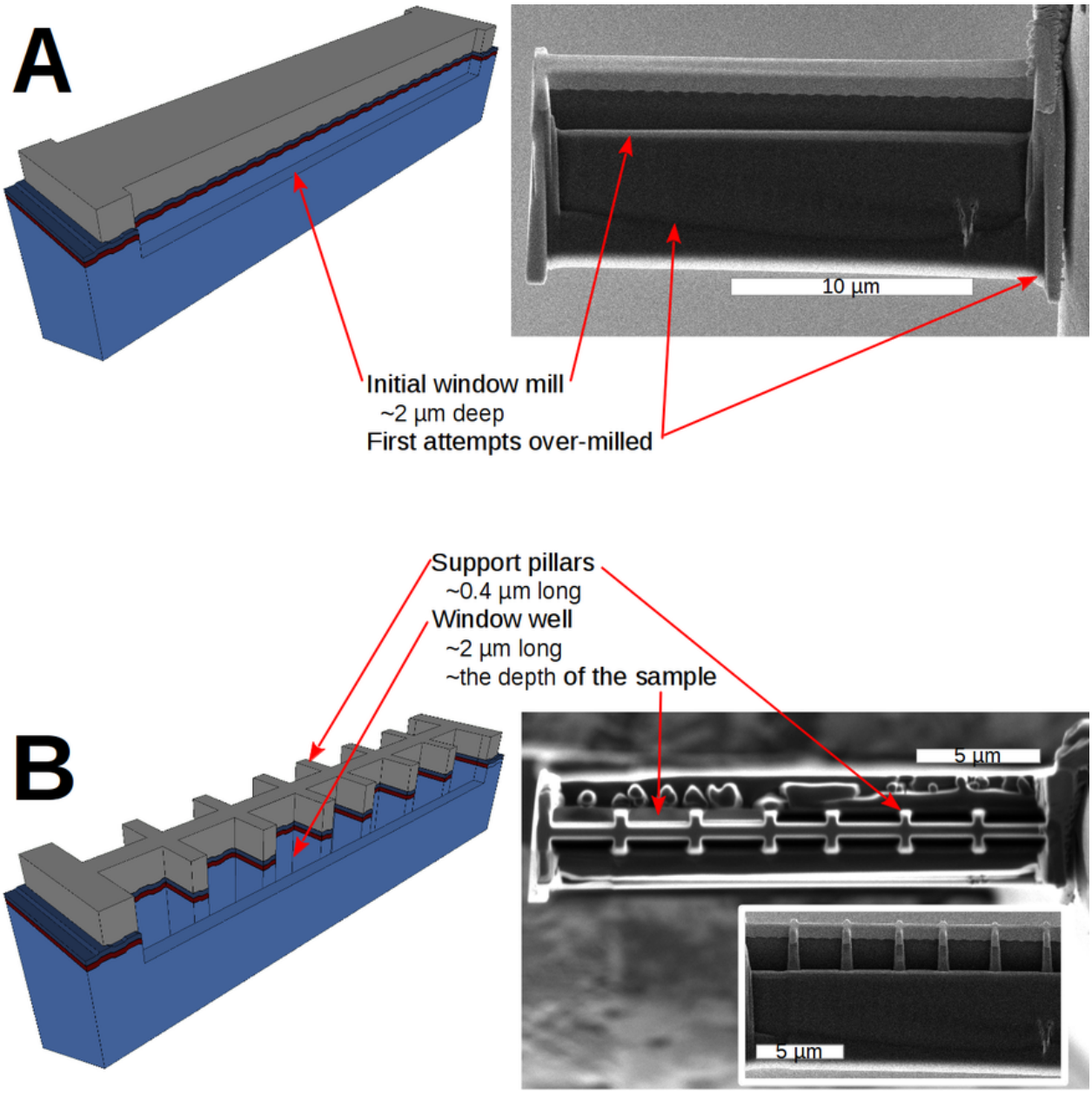

Figure 7.2 (A) Initial "rough" windows milled out in the front and back of the sample to a depth that keeps the bulk of the support block intact. (B) Rough "window wells" milled to the depth of the block, leaving supporting pillars and providing structural and thermal benefits during the final stages of the sample preparation.

thin the windows continues, these challenges remain a cause of concern. As the sample becomes thinner, warping of the lamella becomes much more evident. This particular challenge is enhanced due to the low melting point of many polymers.

For our prepared samples, the length was usually 20 μm in order to have enough "practice room." This length was divided into sections approximately 2 μm wide, each separated by approximately 400 nm. Figure 7.2b illustrates these divisions. The 400 to 750 nm divisions should remain as supporting pillars in order to prevent the warping of the individual 2 μm lamella, which each window will become.

Figure 7.2b shows a diagram, a top-down micrograph, and a side-view (inset) micrograph of the window well milling with the following features:

- – Wide supporting sides (the initial window mill as described in step 5) preserving the structural integrity of the supporting block.
- – Sectioned windows, approximately 2 μm long and 1 μm wide, which are separated by approximately 400 nm-long pillars.
- – The window wells comprised by the section between the region of interest in the middle of the sample and the supporting sides. A close look at the top-down micrograph will show these window wells extend near the depth of the sample.

Milling out all this material near the region of interest brings forth several concerns regarding the quality of the sample preparation, for example 1) redeposition of milled material onto the region of interest, and 2) heat damage from one window to another.

These two concerns are addressed with the geometry formed by the window wells and the supporting pillars. Since the milling takes place within a micron of the region of interest, these mills are performed with a much lower current and milled to the full depth of the sample. At this stage of sample preparation, the supporting pillars now serve additional roles as they significantly

isolate neighboring windows. As the window wells are milled, the supporting pillars act as surfaces that collect some of the redeposition from the mill, and prevent the material from depositing onto neighboring windows. Furthermore, these supporting pillars provide a "cold reservoir" connected to the rest of the block, mitigating heating effects onto neighboring windows.

These window wells, milled to the depth of the sample, further prevent redeposition of material onto the region of interest by providing a path for the forward momentum of the ion beam to carry some of the material away from the region of interest during the final thinning. This effect works in a manner similar to that of regular lift-out TEM cross-section sample preparation.

Finally, these window wells should be milled as to leave the middle 200 nm to 400 nm of the region of interest intact, thus minimizing the damage to the region of interest. The final thinning of each window should be done individually and with much care.

– 7) Final window thinning and low kV clean –

For our polymer substrates, a window length of 2 μm gave a large enough TEM viewing area. Also, the 400 nm long support pillars gave no noticeable warping of the lamella (fig. 7.3). In order to expedite the sample preparation process, the rough milling cuts described in steps 1-6 can be easily scripted using the Helios scripting capability. Ensuring that the middle region of interest remains at least 200 nm wide provides a high success rate ($> 80\%$) in automation.

By the end of "step 6" the windows are already near 200 nm wide. The final thinning was done for each window individually at a lower Ga^+ beam current. This step will further thin the viewing windows, clean any damage on the surface of the metallic films, and thin the windows to an electron-transparent thickness.[106, 111, 132]

Figure 7.3 shows diagrams and scanning electron micrographs of the final thinning process. Some features worth pointing out include the following:

- – The sample and substrate are not charging under the electron-beam.

- – Individual windows are already electron "translucent" at a 5 kV acceleration voltage even before the final thinning (micrograph in fig. 7.3a).
- – In figure 7.3a there are various lamella thicknesses and not all windows were given a final thinning.
- – Figure 7.3b shows how the deposited protective platinum pad served as a guide for the final thinning. As the window becomes thinner, the Pt pad erodes down to near the metallic layer of interest.

For our samples, after the final thinning all lamella were thinned to less than 80 nm without any noticeable warping.

7.3 Principles and Guidelines

In order to deal with the challenges posed by the use of polymer substrates when preparing TEM cross-section samples, these guidelines were followed in designing the sample geometry:

1) Ga^+ ion implantation:

This is a common issue with FIB sample preparation. Work by Lucille Giannuzzi characterized ion beam damage and concluded that this damage is proportional to the acceleration voltage of the ion beam.[106] Fortuitously, in the case of these polymer substrates, the level of gallium implantation helps deal with the electrical and thermal conductivity problems of the substrate. Furthermore, with wider samples, the region of interest remains largely protected from the overall damage. Naturally, the bigger the sample, the longer the sample preparation time.[124, 126]

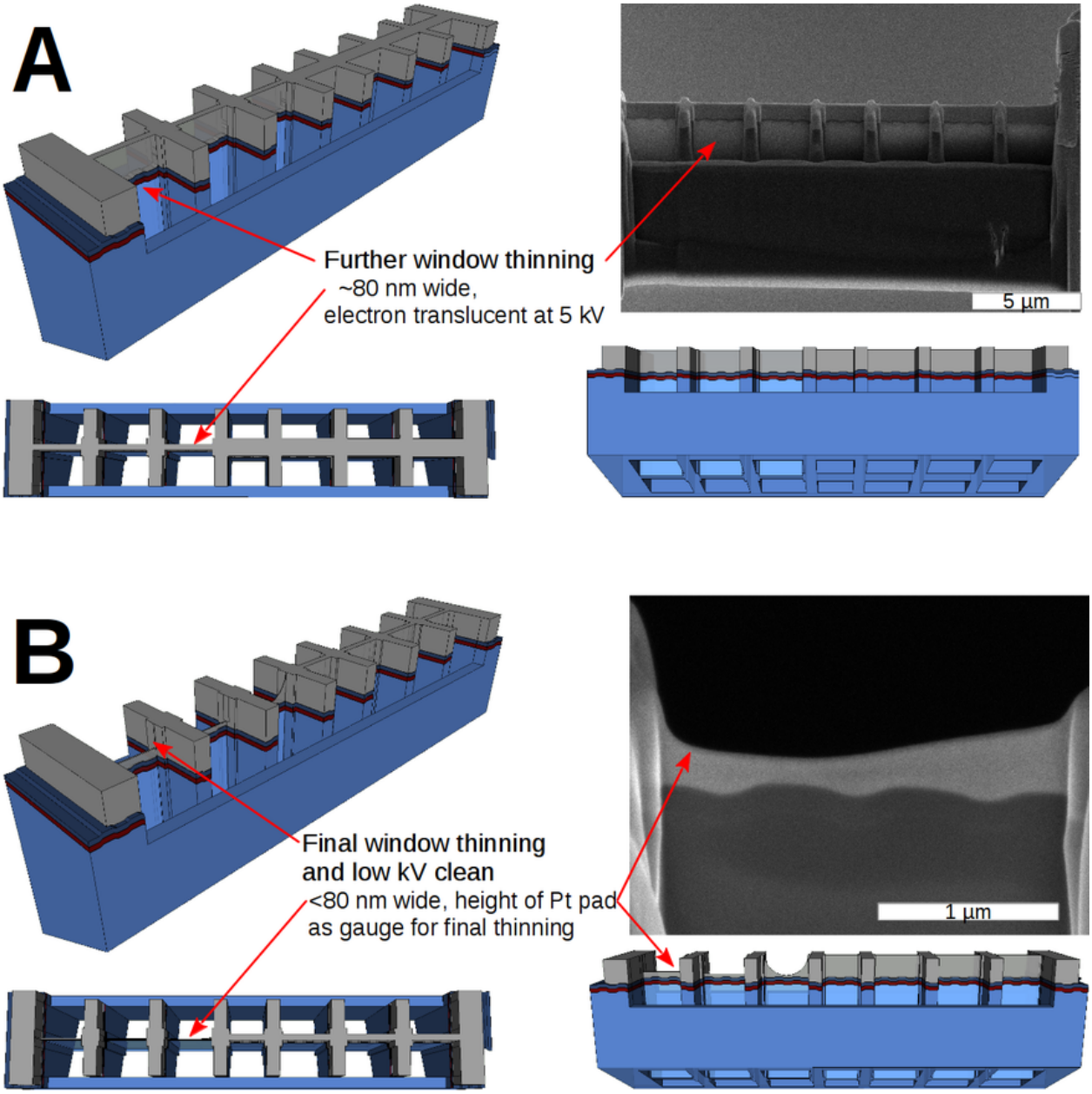

Figure 7.3 Manual (A) and final (B) thinning of the individual windows down to a thickness that is electron-transparent.

2) Thermal management:

This was one of the first identified issues when dealing with warping of the lamella. Though evident in many materials as they become thinner, this was especially problematic with polymer substrates. When the standard TEM cross-section sample preparation was utilized, it was observed that the sample began to warp well before the sample was ready for use in the TEM. This larger block also works as a "cold reservoir" and helps mitigate the damage. However, the need in TEM is thin samples, not wide blocks. Long, thin samples are common for FIB-based TEM preparation in many semiconductor materials. However, this becomes an issue with thermal management in polymer substrates. Due to their (comparatively) low melting temperature, as the sample warms up, it also softens and warps.

3) Structural support:

The other issue with the warping of the lamella deals with adequate support. One manner of dealing with the problems of long-thin samples is to make short-thin samples. The method presented essentially creates a serial array of short-thin samples with a common supporting structure.

4) Redeposition:

One final difficulty with serially preparing adjacent samples is the problem with the redeposition of milled material from one thin area into neighboring, previously thinned areas. The width to which the supporting pillars stretch away from the region of interest impacts the amount of re-deposited material. In addition to providing structural support to help with thermal management, these pillars also help isolate each window from neighboring contamination.[131]

With these principles in mind, several geometries can be attempted. One of such is a pseudo depth profile that can be made by staggering the final location of the thin region (see fig. 7.4). Also, individual parameters can be modified to suit the large array of properties that polymer substrates

have.[108, 109, 114, 122, 124, 125, 127, 129, 155, 163]

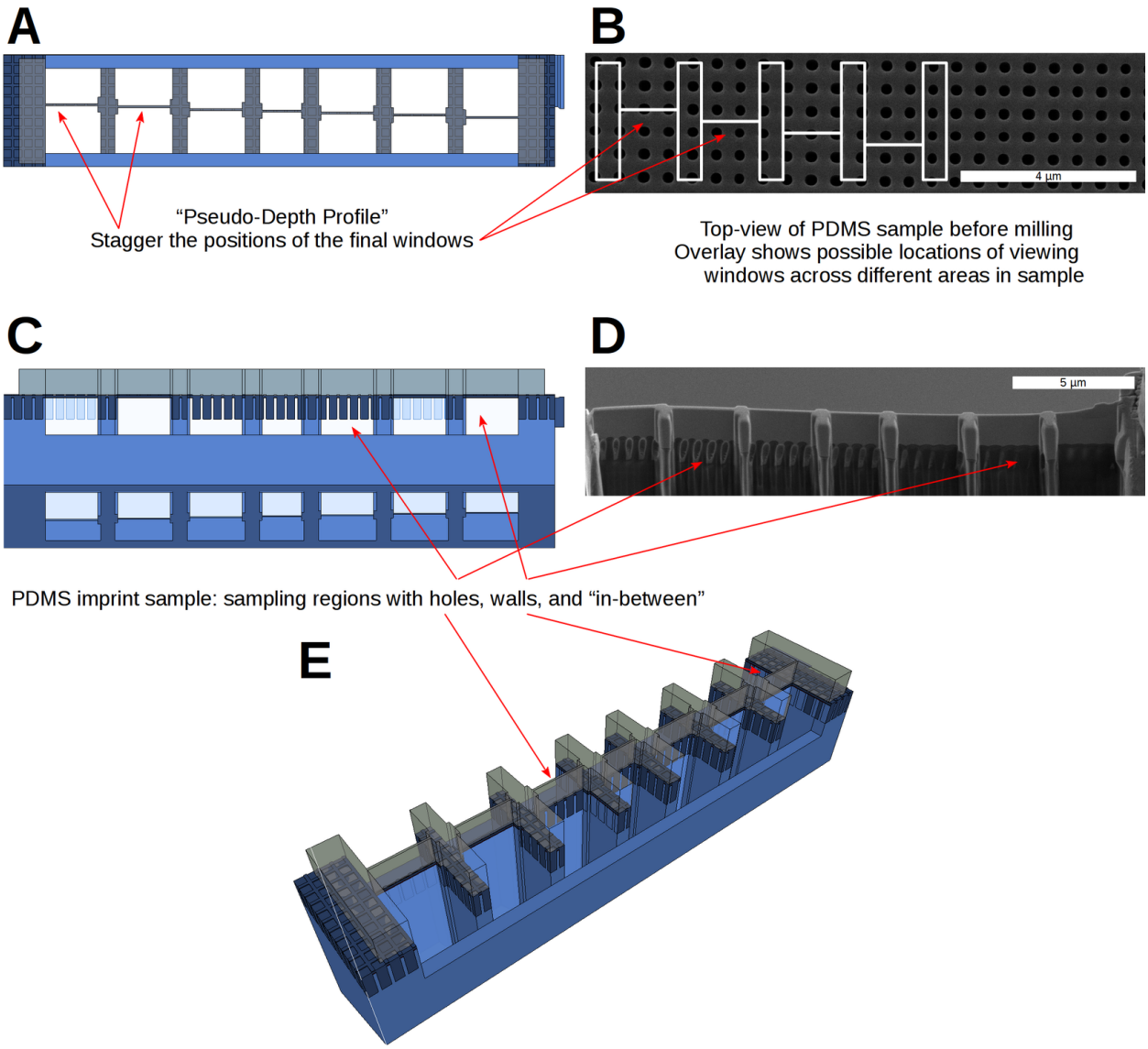

Figure 7.4 Diagrams of a "pseudo-depth profile" sample prepared by staggering the viewing windows across different "depth" locations in a patterned PDMS sample with high aspect-ratio structures. (A) Diagram and (B) surface top views. "Front" views of the (C) diagram and (D) TEM micrograph showing the staggered locations of the viewing windows and the different features of the sample depending on the "depth". (E) Isometric diagram of the sample.

7.4 Results of the Proof-of-Concept TEM Analysis

Using the sample preparation method as described in the previous sections, several TEM cross-section samples were prepared in order to illustrate the versatility and robustness of this method. The substrates varied from polycarbonate, thin plastic films, thin lacquer layer, and PDMS; the patterned structures on these substrates had aspect ratios that varied from low (500 nm wide : 100 nm tall), medium (100 nm wide : 200 nm tall), and high (100 nm wide : 800 nm tall); finally, the deposited metallic films varied from single thin ($\sim$30 nm) metallic layers up to deposited multi-layer stacks ($\sim$120 nm thick stack, with thinnest layer of $\sim$10 nm, refer to table 1).

For most of these samples a STEM/EDX line profile was generated in order to attain a qualitative measure of the electron probe size as well as metrology of the metallic layers of interest.

The extracted TEM samples were prepared from the following specimens:

1) Archival DVD reflective metal films. These DVDs were coated with a reflective silver layer. It was observed that a thin gold film was subsequently deposited on top, presumably to prevent oxidation of the silver layer. We show a comparison of the metals present in the reflective layers of the write track and the metal in the inner ring of the disk.

2) High-aspect ratio structures (100 nm wide : 800 nm tall), imprinted in PDMS, and coated with a thin metallic film. A "pseudo depth-profile" is formed by staggering the viewing windows (see figure 7.4). A comparison is shown among regions at different "depths," as well as the thicknesses of the deposited metal layer.

3a) The active and reflective metallic layers of a commercial writable BluRay disk. In contrast to DVDs, BluRay optics must be placed much closer to the write media (a layered stack of deposited thin metallic and non-metallic films). As such, the write media is deposited onto a thick polymer substrate for support and then covered with a thin ($\sim$100 μm) lacquer film. An EDX chemical analysis of the layers is presented from the write stack.

3b) Same layers as 3a, but taken from the side of the thin ($\sim$100 μm) lacquer film. This is

included to demonstrate the use of this sample preparation method on a different polymer.

Figures 7.5, 7.7, 7.9, and 7.10 show an array of selected cross-sectional TEM samples prepared by the "modified H-bar" method, with corresponding TEM images of the metallic films deposited (shown in the order previously described). Selected STEM/EDX scans from some of these samples are presented in figures 7.6, 7.8, 7.11.

(In addition to the specimens mentioned, additional TEM samples were also prepared from nano-structures imprinted onto a flexible plastic film and coated with a 30 nm metal film: The plastic film was less than 1 mm thick, the film was initially patterned with structures 100 nm wide and 200 nm tall, and subsequently a thin metallic film was deposited. The conformity of the deposition is observed.)

7.4.1 Reflective Metallic Multi-Layer in a Commercial Archival-Grade Recordable DVD.

The geometry of current archival-grade DVDs consists of a patterned polycarbonate substrate where a photosensitive dye is spun on and then coated with a metallic reflective layer deposited on top. An additional polycarbonate disk is then glued on top of the reflective layer in order to protect the deposited active and reflective layered stack. For this particular commercial archival-grade DVD, the write region was silvery while the backside of it was golden colored, thus indicating the use of several metals to protect the recording dye of the DVD.

In order to access the reflective metallic layer, the DVD was forcefully split at the glue layer. This splitting process yielded regions where the reflective metallic film remained either attached to the patterned substrate or to the glue. Small sections from the specimen were taken such that the whole metallic layer remained intact. Samples were taken from the write regions and (for comparison) from the golden inner-ring of the disk. Figure 7.5a shows the top and side views of a milled sample before its final thinning as prepared by the method described here. A side-by-side

TEM comparison between the patterning of the write track (left) and the "inner ring" (right) is shown in figures 7.5b and c. Under electron transmission, the depth of the window wells and the initial window mill are both evident (figs. 7.5b and c). Furthermore, the TEM view of the pillars in figures 7.5b and 7.5c are indicative of the quality of the milled walls. Under transmission mode, the protection provided by the "high-Z" Pt on the pad is shown by the vertically parallel posts (fig. 7.5b) and slight undercut in the polymer substrate below. As expected for FIB samples, there is a widening of the pillars deeper into the window well. Given the symmetry of the milling process, the profile shown by the pillars can be used as to estimate the profile of the viewing windows themselves.

Details of the reflective stack in this DVD can be seen in the bright-field micrographs 7.5d and 7.5e. The thin region of the metallic film shown in figure 7.5e shows the conformity of the deposition over the polymer substrate. This figure also displays one of the benefits of the initial ex-situ C depositions described earlier. As the micrograph shows, there is a thin layer with a low-Z that makes easier to discern between the metal foil of interest and the protective Pt pad.

The granular structure of the reflective layer stack is shown in better detail in figure 7.5e. The grain sizes in the metallic film are in the order of 100 nm. Given the randomized grain size and orientation it can be inferred that these are features inherently preserved in the film rather than caused by the TEM sample preparation process. Though the granular nature is shown throughout the film, the bright-field transmission electron micrograph in figure 7.5e shows a band approximately 50 nm thick with a darker contrast which indicates higher scattering in that region.

Scanning transmission micrographs and EDX line-scans from the write track and the golden inner-ring are shown in figure 7.6. The higher scattering band shown in figure 7.5e is also evident in 7.6a. The EDX elemental analysis (inset in figure 7.6b) shows the deposition of a $\sim$30 nm Au layer intermixing with a previously deposited Ag layer $\sim$120 nm thick.

As a form of reference, the sample preparation method described here allowed for the study of

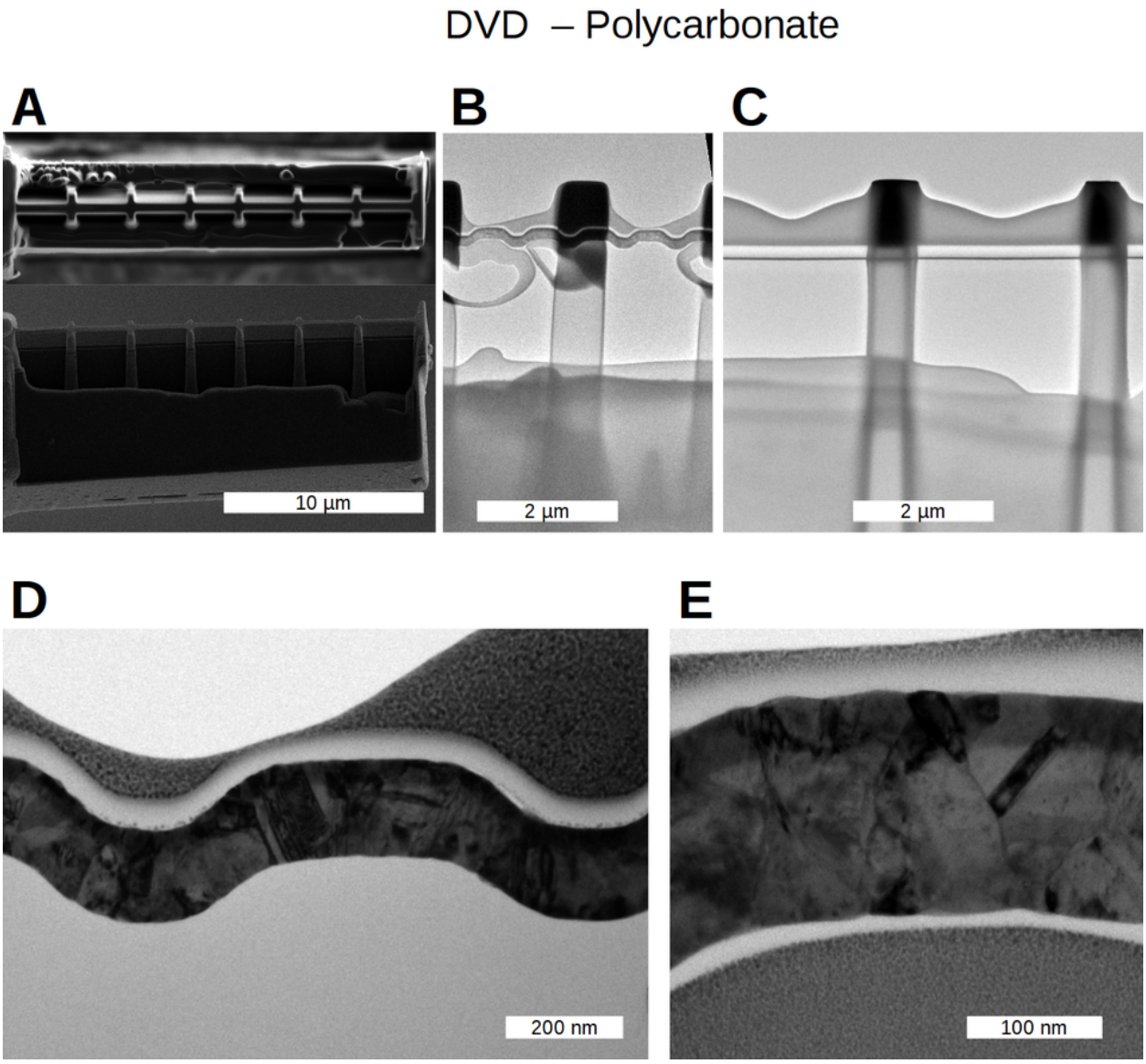

Figure 7.5 Cross-sectional TEM samples prepared from an archival-grage DVD using the "modified-H-bar" method. (A)Top and side views of the prepared TEM sample before its final thinning. Comparison between the (B) reflective write track and (C) the golden inner-ring of the DVD. Close-ups of the (D) pitch of the write track and (E) the granular nature of the reflective layer.

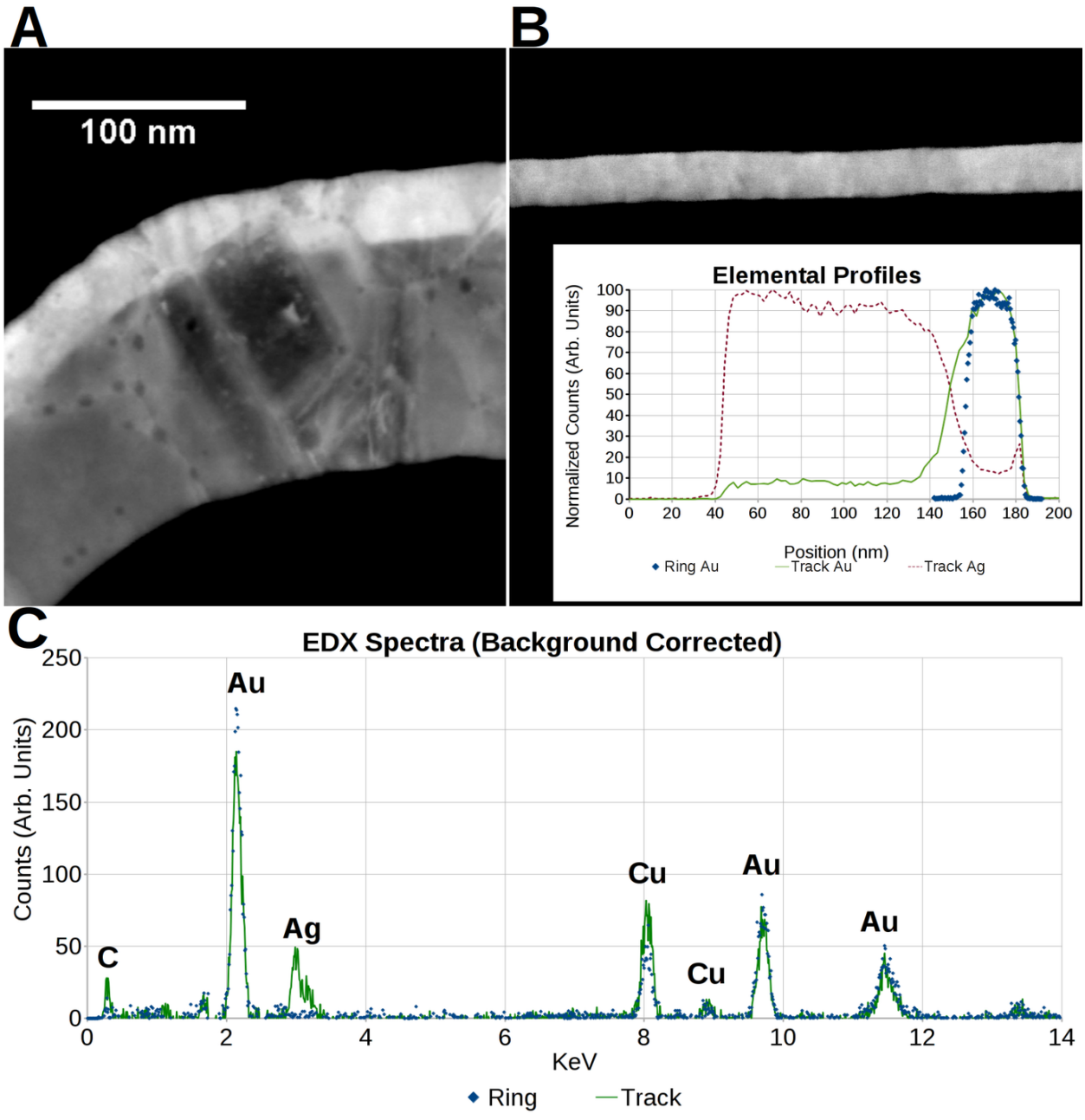

Figure 7.6 Comparison of the metal layers from an archival-grade DVD found in the (A) write track and (B) inner golden ring. (B inset) EDX line-scan showing normalized counts for Au and Ag for the micrographs in (A) and (B). (C) EDX spectrum taken from the write track's intermixed layer and compared with the gold-colored inner ring.

the metal layers deposited in the reflective layer of a DVD, with an EDX mapping resolution better than 5 nm. This resolution is indicated by the transition edge from the polymer-substrate onto the metal layer(s) and onto the ex-situ C film (EDX line-scan inset in figure 7.6b). A results of a more in-depth analysis of the reflective layers, the dye, and the glue from this and other archival-grade DVDs were published previously.[20,21]

7.4.2 Thin Metallic Layers Deposited on Nanostructured PDMS Films.

The staggered sample shown in figure 7.4 was subjected to similar TEM analysis as the aforementioned DVDs (figs 7.7 and 7.8 show the results from the PDMS sample). In contrast to the DVD specimen, this particular PDMS sample features a softer polymer substrate, a higher aspect ratio patterning of the substrate, and a single metallic thin layer deposited film.

The transmission micrograph in figure 7.7a shows two areas within the same sample showing the top wall (left) and the bottom of the holes (right) of the same sample. Unlike the DVD sample, this PDMS imprint exhibits a curtaining artifact common in FIB sample preparation (fig 7.7a, bottom). Figure 7.7b shows another artifact present due to the sample preparation technique, the volume within the holes of the PDMS pattern are partially filled with material milled during the sample preparation. This issue may be of concern when conducting porosity studies.

Despite the mentioned artifacts, this sample preparation method was gentle enough to preserve the high-aspect ratio structures imprinted in the substrate (fig. 7.7b) while still allowing for the imaging of the ~30 nm film deposited on top (figs. 7.7c and 7.7d). Again, the benefits of a carbon deposition are evident in figure 7.7d as the carbon film allows for a low-Z layer that separates the Pt pad from the metal film.

The metallic layer deposited in this imprint was not conformal to the pattern, rather, it was intentionally limited to the top surface of the patterned substrate (fig. 7.7c). The plot of the EDX line-scan presented in figure 7.8b was taken across the ~30 nm Al film.

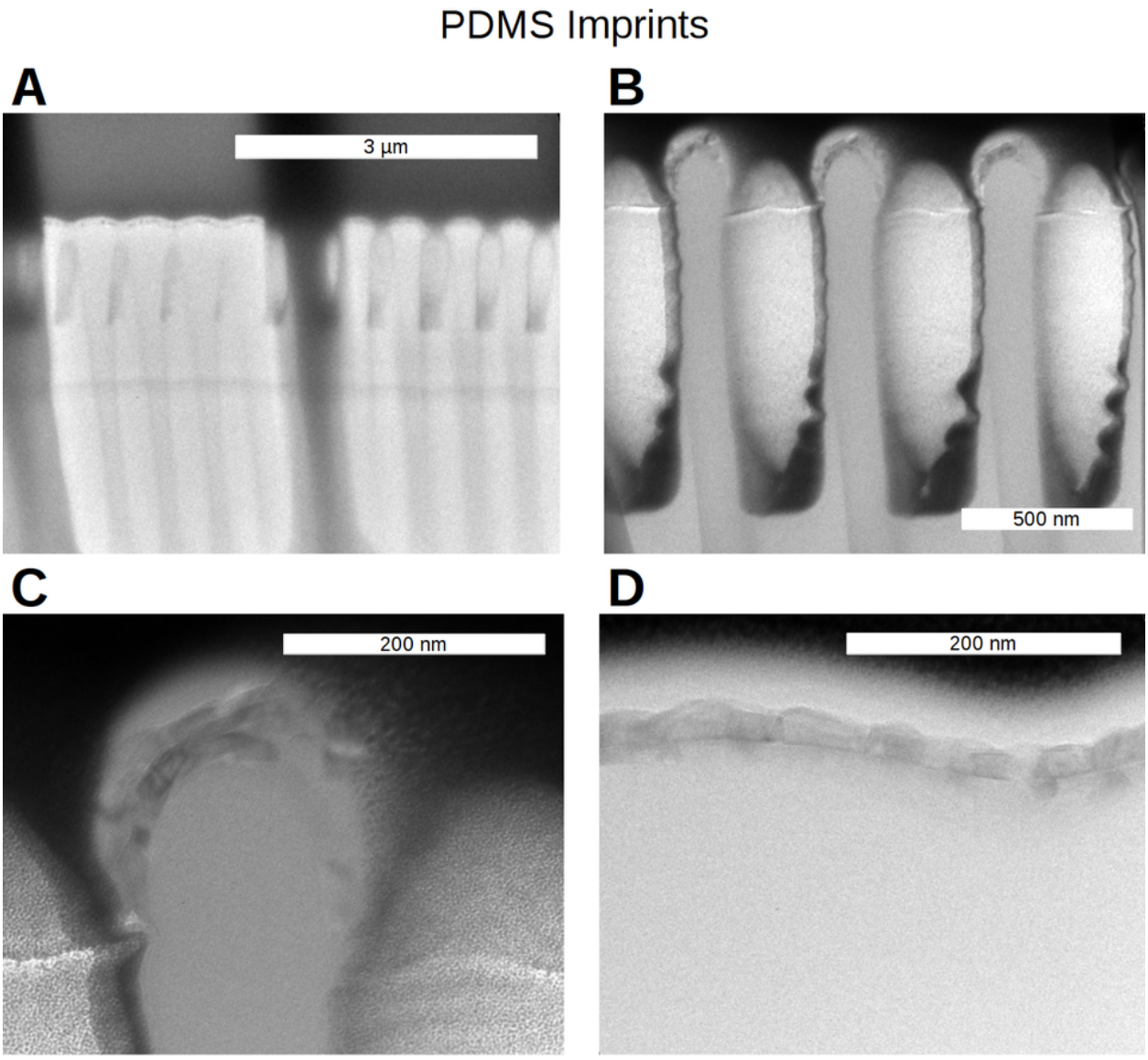

Figure 7.7 Cross-sectional TEM samples prepared using the "modified-H-bar" method from a PDSM sample patterned with high aspect-ratio structures. (A) Comparison between two regions in the sample, one along the wall edge (left) and one through the holes (right). (B) Preservation of the high aspect-ratio structures with a thin film deposited along the top of the structures. Details of the thin metallic film deposited on the patterned sample viewed from the (C) regions through a hole and (D) along the wall.

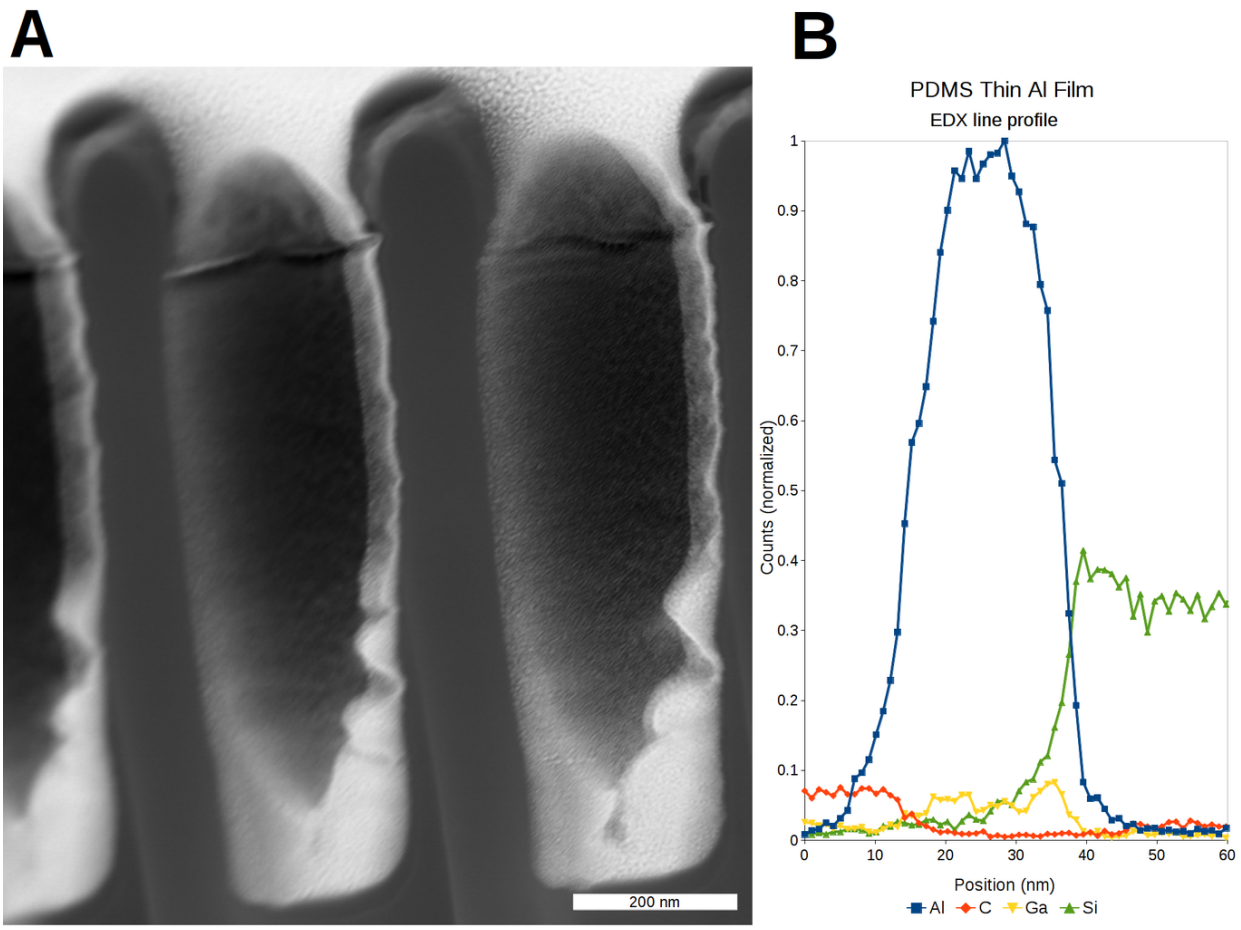

Figure 7.8 (A) STEM micrograph from a cross-section of a PDMS sample patterned with high aspect-ratio structures with a deposited thin metal layer. (B) EDX line-scan showing normalized counts for Al, C, Ga, and Si across the ∼30 nm Al film.

7.4.3 Reflective Layers of a Commercial Recordable BluRay Disk.

As previously mentioned, this specimen is similar to that of a DVD with the notable difference that, instead of using polycarbonate for both faces of the disk, the data layer faces a thin lacquer film. The BluRay disk was split in a manner similar to that of the DVD but with much more ease as the lacquer film easily delaminated from the polycarbonate substrate carrying with it parts of the reflective stack. TEM samples were extracted from both, the polycarbonate side (fig 7.9a, top) and also from the lacquer side (fig. 7.9c, top) in order to ensure that information about the "full stack" was obtained. Despite the different polymers that contained the metalized stack, the method presented here proved to be robust in obtaining viable TEM samples. A comparison between the transmission micrographs obtained from the polycarbonate substrate and the lacquer substrate (figures 7.9 and 7.10 top vs bottom) shows the same individual layers within the stack (though clearly inverted).

Figures 7.9b and 7.9d show the overall conformity of the deposited metal stack as well as the presence of various layers comprised of different materials (mass-thickness contrast images). Similar to the DVD samples, figures 7.10a and 7.10b show the pitch and features of the track in this BluRay disk. Finally Figures 7.10b and 7.10d show in better detail at least 6 individual layers that comprise the BluRay metallic stack.

As with the other samples shown, an EDX line-scan was obtained across the metal stack (fig 7.11).

7.5 Summary and Discussion

Polymer substrates present an array of challenges for TEM sample preparation due to their comparatively low conductivity, low melting temperature, and softness. In order to deal with those challenges, a sample preparation geometry was introduced, which provided structural support,

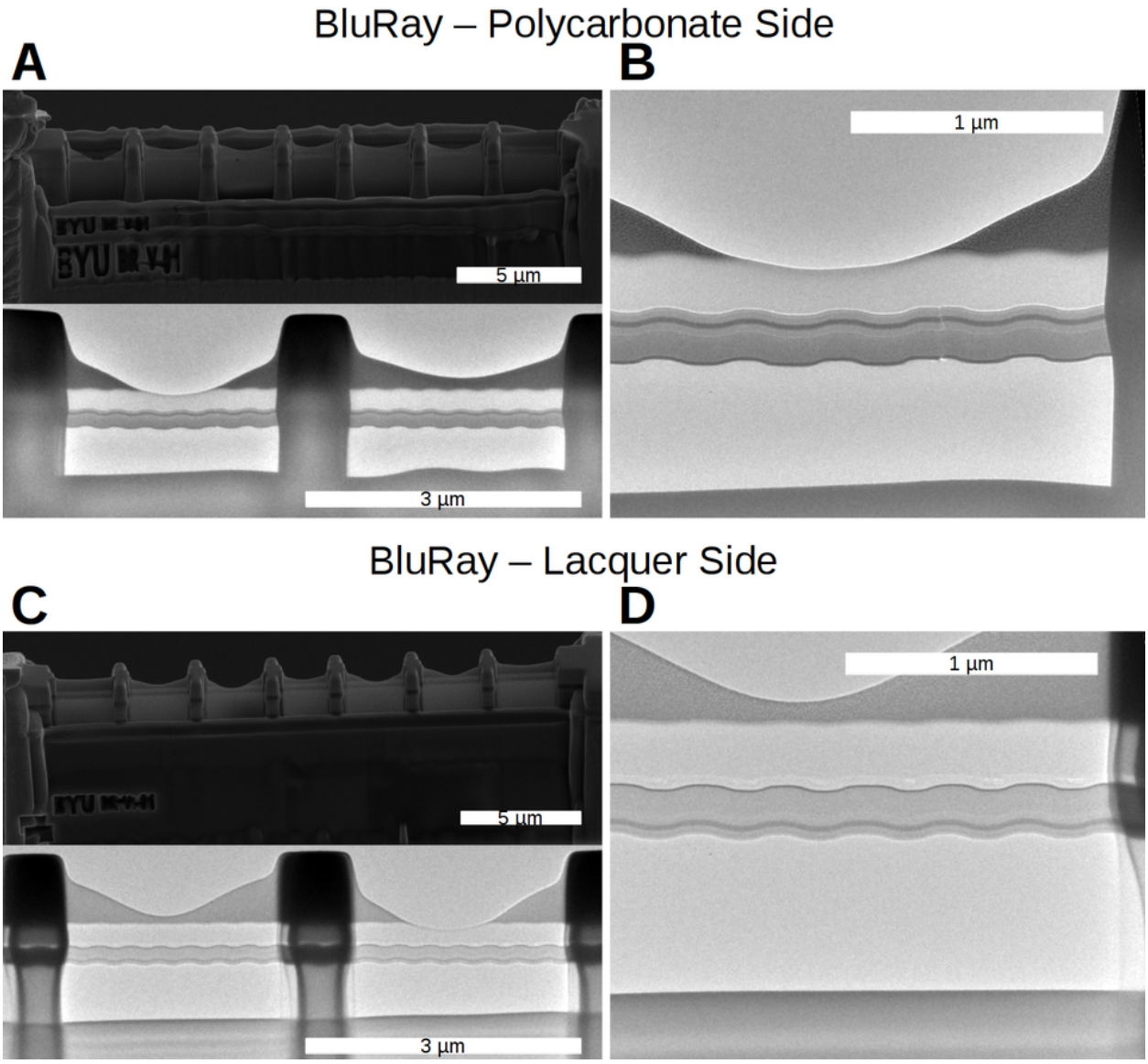

Figure 7.9 Cross-sectional TEM samples prepared using the "modified-H-bar" method from the (A) polycarbonate side and (C) lacquer layer of a BluRay disk. (B) and (D) TEM micrographs showing the metallic BluRay stack.

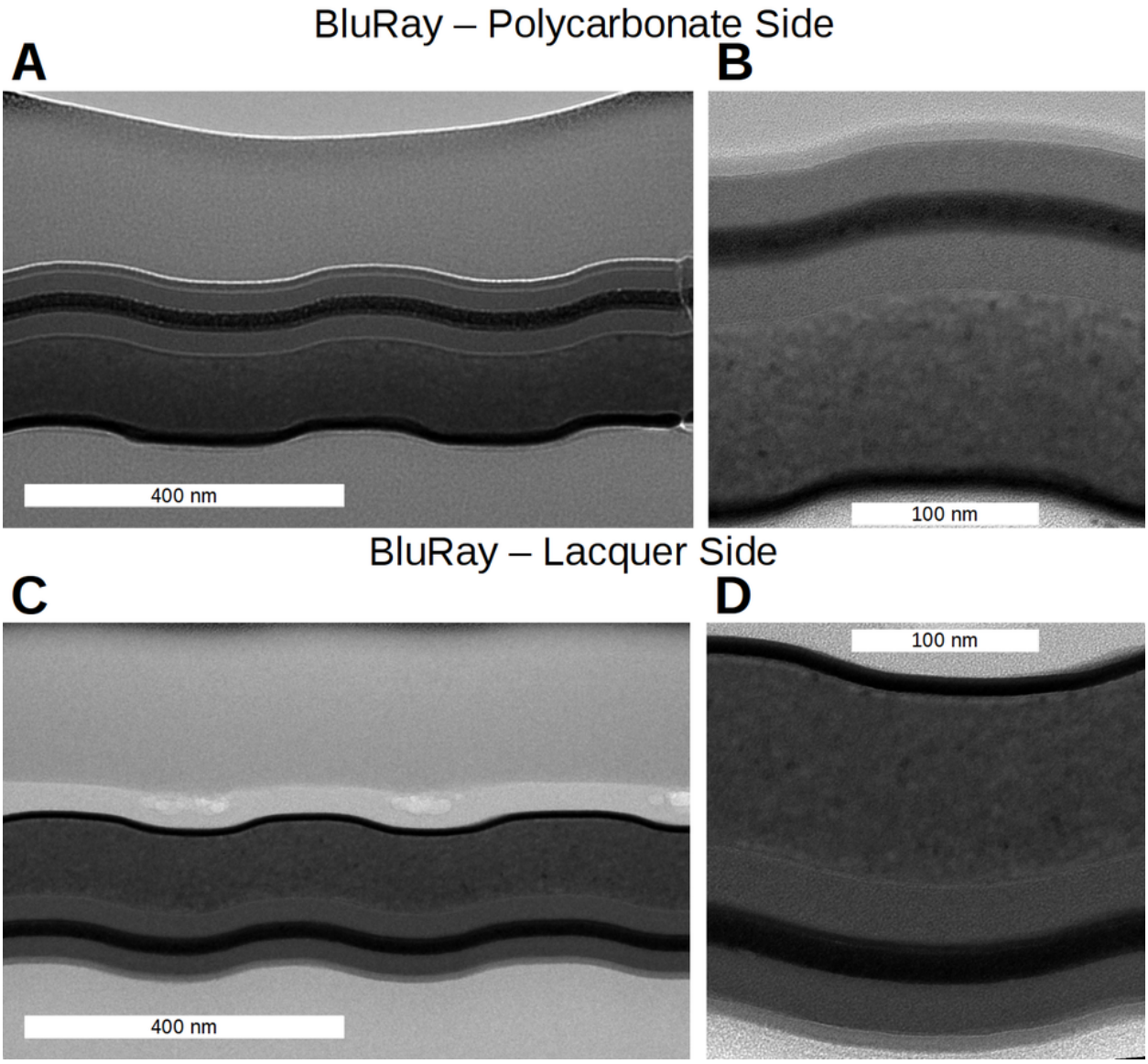

Figure 7.10 Cross-sectional TEM micrographs showing details of the metallic stack of a BluRay disk taken from the (A,B) polycarbonate substrate and the (C,D) thin lacquer protective film. (A,C) pitch of the write track and thickness of metallic layer. (B,D) detail of the individual layers in the metallic BluRay stack.

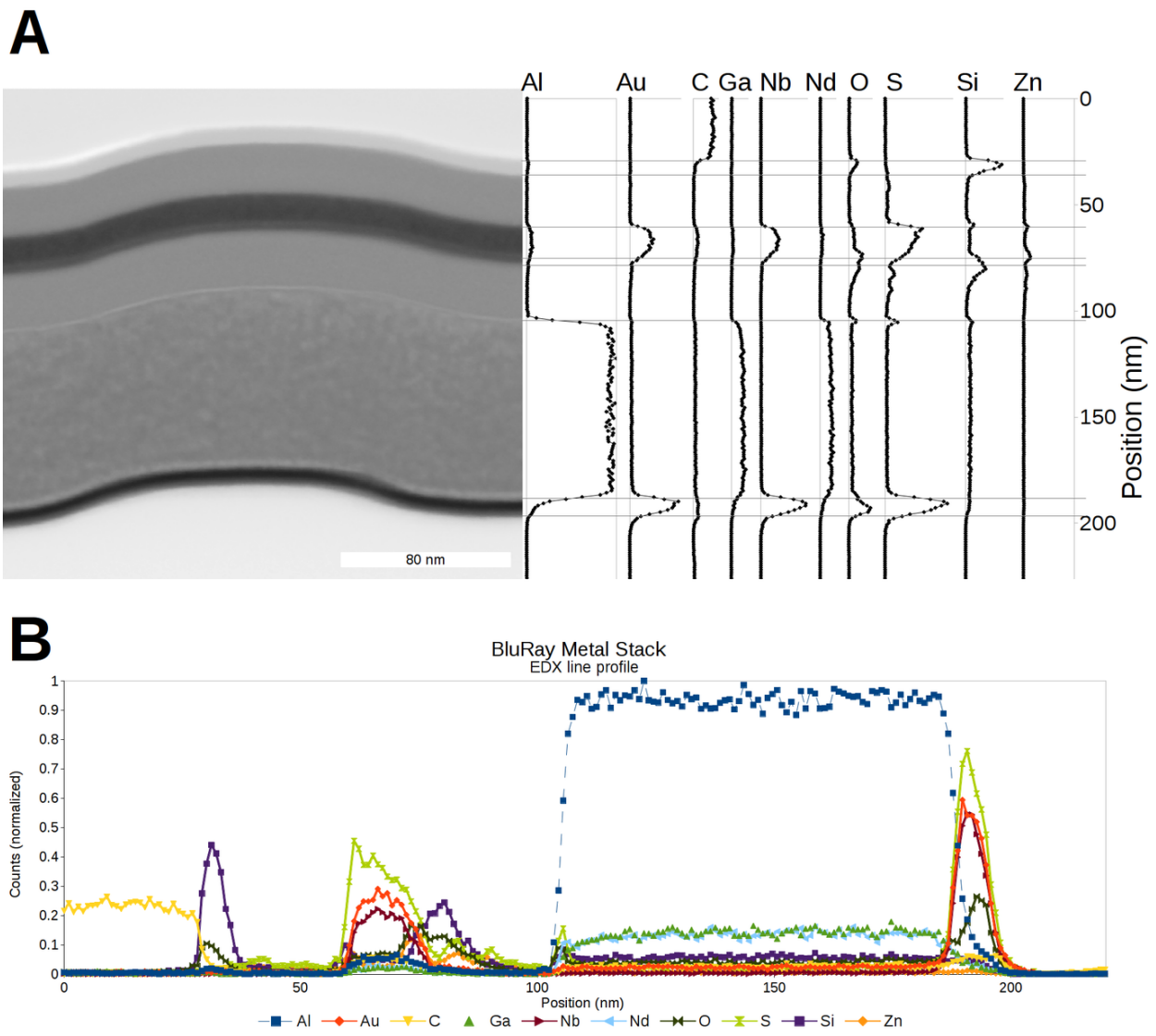

Figure 7.11 (A) STEM micrograph from a cross-section of the metallic layered stack of a BluRay disk (right) with individual EDX line-scans mapping several elements found in the individual layers of the stack. (B) overlaid EDX line-scan showing normalized counts for Al, Au, C, Ga, Nb, Nd, O, S, Si, and Zn across the ∼200 nm BluRay stack.

thermal management, and consistently yielded viable cross-section TEM samples from thin metallic films deposited on patterned polymer-substrates. Table 7.2 shows a summary of the specimens from which TEM samples prepared by the method described in this chapter.

In order to show the robustness of this FIB-based cross-section TEM sample preparation method, various TEM were prepared which allowed the characterization of metallic films deposited on patterned polymer substrates. These samples varied from films as thin as 30 nm deposited on a softer PDMS substrate patterned with high-aspect ratio nanostructures up to multi-layered stacks $\sim$120 nm thick with individual layers as thin as 10 nm deposited on a harder polycarbonate patterned substrate.

TEM imaging of the PDMS samples (fig. 7.7) showed the preservation of the high-aspect ratio structures during the milling process as well as the preparation of TEM samples thin enough for

Sample / Substrate	(W:H) (nm)	EDX Resolution	Stack Observed	Thinnest Layer	Reproduced
DVD – Polycarbonate	800:100	Better than 5 nm	2 layers Ag, Au, Mixed	30 nm Au	yes automated
Tall patterns PDMS	100:600	Better than 15 nm	1 layer Al	30 nm Al	yes manual
BluRay Polycarbonate and Lacquer	400:30	Better than 6 nm	7 layers various elements	10 nm Zn, O	yes automated

Table 7.2 Summary of results from the "modified H–bar" cross-sectional sample preparation method highlighting the various patterned polymer-substrates, the pattern's aspect ratio, the EDX resolution observed, and the layers observed. Dozens of TEM samples were prepared utilizing this method, with a success rate higher than 80% when automated

adequate TEM imaging of a granular Al film 30 nm thick. Given a pitch of ∼100 nm between walls, a thickness of the viewing windows can be estimated to be within that order.

Automated scripts (based on the method herein described) were utilized to prepare several of the low aspect-ratio patterned samples. While the final thinning of each viewing window remained a manual process, the automation decreased the overall sample preparation time. TEM imaging of the patterned polycarbonate substrates in the DVD and BluRay specimens (figs. 7.5, 7.9, and 7.10) also showed the preservation of the underlying structures and metallic layered stacks.

Due to the variability in the milling properties and hardness of the polymer-substrates used, the method and geometries presented here are not fully optimized. Nonetheless, they present a starting point for the polymers milled here. The TEM sample of the BluRay stack, obtained from the lacquer layer, was prepared in an automated manner similar to that of its polycarbonate counterpart. The milling times for the lacquer substrate were adjusted in order to yield samples similar to its polycarbonate counterpart (fig. 7.9).

Sample preparation artifacts are common causes of concern in TEM analysis. As the Ga^+ beam erodes the specimen during the final thinning, sample damage is to be expected. Artifacts such as curtaining and Ga implantation.

Curtaining was observed in the high-aspect ratio PDMS sample (fig. 7.7) but not on the low aspect-ration samples. This type of artifact may be explained by the differing volumes of material the Ga^+ beam milled through. For example, in the regions where there were holes present, the Ga^+ beam lost less energy than filled regions, thus causing uneven milling.

Implantation of Ga was monitored through the use of EDX line profiles. Figures 7.8b and 7.11 both have profiles mapping the location of Ga down the metalized layers. The Ga signature was found near background level nearly throughout the whole EDX profile. A notable exception where the amount of Ga was non-trivial occurred in the Al layers imaged and mapped in figures 7.8 and 7.11. Further, Ga was not observed in any measurable quantity within the polymer substrates.

7.6 Conclusions

Polymers have many aspects that make them attractive substrates, such as inexpensive raw materials, high flexibility, and ease of patterning. The integration of electronic components onto this type of substrates, in conjunction with shrinking electronic geometries, not only has created many interesting products, but it has also created the need to study these materials and devices at the nano-scale. At a basic level, this type of study requires imaging and characterization of thin conductive layers deposited onto these pattered polymer substrates. While cross-sectional TEM has been shown to be an invaluable analytical tool for nano-scale characterization, the same aspects that make polymers attractive as substrates also pose several challenges for current, well-established, nano-scale characterization tools.

In this paper, an additional FIB-based cross-section TEM sample preparation method was presented, which addresses several of these challenges. It also extends the sample preparation capabilities to some soft materials for FIB instruments without a cryogenic system. As proof-of-concept on how this sample preparation method may help in the characterization of materials and devices on polymer substrates at the nano-scale, TEM samples were prepared and analyzed. These samples were comprised of thin metallic films and layered metallic stacks (thinner than 150 nm), and were deposited on a variety of patterned polymer substrates.

Some of the benefits observed for this sample preparation method include:

- FIB-based, thus retains site specificity
- Depending on the hardness of substrate, there may not be a need to fixate the sample into a harder polymer
- Method gentle enough to preserve high-aspect ratio structures on a PDMS substrate
- Geometry provides structural support to thin and flexible lamella

- Supporting pillars help provide thermal management and a barrier against redeposition from the thinning of adjacent windows
- Block provides thermal management benefits to the polymer window
- Pt pad provides adequate protection against Ga implantation onto the underlying substrate during final thinning
- Though not optimized, samples allowed for the characterization of layers as thin as 10 nm in the active reflective layer of a BluRay disk
- Final thinning of the metal layers to less than 80 nm in thickness

In our case, the benefits mentioned above, outweigh some of the shortcomings that arise from FIB-based TEM sample preparation. Artifacts such as curtaining and Ga implantation were still observed. Also, compared to glass substrates, this sample preparation method increases sample preparation time by approximately 50%.

Considering the rise of polymer substrates integrated onto electronic devices, this method provides an additional tool that may help in the characterization, study, and quality control of current and future devices.

Chapter 8

Conclusions and Possible Extensions

Vanadium dioxide (VO_2) is a material of particular interest due to its exhibited metal to insulator phase transition at 68 °C that is accompanied by an abrupt and significant change in its electronic and optical properties and holds promise in several tecnological applications. Electron microscopy techniques from SEM and TEM were utilized to characterize VO_2 thin films and nanoparticles deposited onto various substrates.

8.1 Morphology of the solid phase crystallization of VO_2 thin films deposited on amorphous SiO_2

Solid phase crystallization of VO_2 thin films was obtained by a post-deposition annealing process of a $VO_x, x \approx 2$ amorphous film sputtered on an amorphous silicon dioxide (SiO_2) layer. The specimens, obtained from Dr. Kevin Coffey at the University of Central Florida, consisted of amorphous $VO_{x,x\approx 2}$ films 50nm and 10nm thick. Samples taken from these specimens were annealed in temperatures that ranged from 300°C up to 1000°C and in times ranging from 5 minutes up to 12 hours. Scanning electron microscopy (SEM) and electron-backscattered diffraction (EBSD)

were utilized to study the morphology of the solid phase crystallization that resulted from this post-deposition annealing process.

Depending on the annealing parameters, scanning electron micrographs showed the formation of grains ranging from $\sim$20 nm in the thinner films upto 400nm in the thicker films

EBSD showed that this process yielded polycrystalline vanadium dioxide thin films, semi-continuous thin films, and films of isolated single-crystal particles for the thicker set of samples. However, while EBSD accuratelly distinguished between the different stoichiometries of vanadium oxides, it was unable to accuratelly distinguish between the monoclinic and tetragonal structures of VO_2. Further, EBSD showed a limit in the size of indexable grains that made this technique unavaliable for the smaller grains of the thinner $V0_2$ films.

8.2 Crystallographic Orientation of VO_2 Nanograins and Thin Films on Various Substrates

In addition to these films on SiO_2 obtained from UCF, other VO_2 thin films were deposited onto a-,c-,and r-cuts of sapphire and on $TiO_2(001)$ heated single-crystal substrates by pulsed-laser deposition (PLD) and provided by Dr. Richard haglund at Vanderbilt University. Unlike the UCF samples, the VO_2 films were crystallized *in-situ* by keeping the temperature of the substrates was at $\sim$500°C during deposition. Again, EBSD was used to study the crystallinity of the films. EBSD maps and orientation imaging microscopy were used to study the epitaxy and orientation of the VO_2 grains deposited on the sigle crystal substrates, as well as on the amorphous SiO_2 layer. The EBSD/OIM results showed that: 1) For all the sapphire substrates analyzed, there is a predominant family of crystallographic relationships wherein the rutile $VO_2\{001\}$ planes tend to lie parallel to the sapphire's $\{10-10\}$ and the rutile $VO_2\{100\}$ planes lie parallel to the sapphire's $\{1-210\}$ and $\{0001\}$. Furthermore, while this family of relationships accounts for the majority of the VO_2

grains observed, due to the sapphire substrate's geometry there were variations within these rules that changed the orientation of VO_2 grains with respect to the substrate's normal direction. 2) For the TiO_2, a substrate with a lower lattice mismatch, we observe the expected relationship where the rutile VO_2 [100], [110], and [001] crystal directions lie parallel to the TiO_2 substrate's [100], [110], and [001] crystal directions respectively. 3) For the amorphous SiO_2 layer, all VO_2 crystals that were measurable (those that grew to the thickness of the deposited film) had a preferred orientation with the the rutile VO_2 [001] crystal direction tending to lie parallel to the plane of the specimen.

8.3 Extensions for Tranmission Electron Microscopy of Thin Films

Further work in the characterization of these films is possible with the use of transmission electron microscopy. It was shown that tranmission electron diffraction patterns taken from cross-sections of particles of the A and R cut sapphire substrates not only solidified the predominant family mentioned, but also helped lift the ambiguity present in the rutile 100 axes, thus giving added information that the EBSD method used above did not provide.

Furthermore, electron energy-loss spectroscopy (EELS) was employed to differentiate between VO_2 and V_2O_3, giving the opportunity to study the role of the grain boundaries in continous VO_2 thin films.

Finally, a focussed-ion beam technique for preparation of cross-sectional TEM samples of metallic thin films deposited on polymer substrates is demonstrated. While this technique did not use VO_2, it opened the possibility to study the properties of this material if deposited on polymer substrates.

Appendix A

Deposition Parameters for the Various VO_x Samples Obtained

A.1 Samples obtained from the University of Central Florida

The VO_x films on amorphous SiO_2 obtained for this work were obtained from Kevin Coffey at the University of Central Florida. These films were deposited by means of Reactive RF Magnetron Sputtering.

50nm thick VO_x film on Amorphous SiO_2:

- Sample#050506
- 0.5% oxygen partial pressure.
- 8 min deposition time
- RF power: 260 V and 40 W
- DC power: 200 W

- DC voltage: 334 V
- DC current: 0.595 amps

The substrate was a silicon wafer with a thermally grown amorphous silicon dioxide layer approximately 380 nm in thickness, and the resulting VO_x film was approximately 50 nm

10nm and 5nm thick VO_x film on Amorphous SiO_2: For this sample, the parameters were similar to the sample described above. In this case, the substrate was a silicon wafer with a thermally grown amorphous silicon dioxide layer approximately 90 nm in thickness, and the resulting VO_x films were approximately 10 nm and 5nm nominal thickness.

A.2 Samples obtained from Vanderbilt University

Epitaxial VO_2 films of 80 nm nominal thickness were deposited onto c-, r-, a-cut single-crystal Al_2O_3, and TiO_2(001) substrates using pulsed laser ablation of 99.99% pure vanadium metal target in a background of 50 mTorr of oxygen, with a target-substrate distance of 5 cm, at a high temperature of $\sim$500 °C.

The epitaxial character of the films was confirmed by reciprocal space mapping using a PANalytical X'pert Pro MRD and images acquired in the HF3300 transmission electron microscope (TEM).

The metal-insulator transition (in both heating from room temperature and cooling from high temperature) of the acquired VO_2 thin films was observed by measuring the infrared transmission using a mechanically chopped white light source (3000 K blackbody) and an InGaAs detector; the chopped signal (frequency 190 Hz) was fed as the reference to a lock-in amplifier that recorded the signal from the detector. The films were heated and cooled during optical characterization by a Peltier thermoelectric element. The temperature was measured with a precision thermocouple in

thermal contact with the VO_2 surface.

Figure A.1 shows the acquired infrared transmission for the VO2 films deposited on a-, c-, r-cut sapphire, and TiO2(001) substrates (respectively from top to bottom). There is an evident difference in the SMT between the films, as well as the hysteresis. As a reference, the accepted transition temperature is labeled across all graphs by a solid black line pointing to 68°C. Table 1 shows the measured transition temperature and hysteresis width for the VO2 thin films on the different substrates. The transition temperature is reported at the midpoint of the hysteresis, and the hysteresis was the measured full width at half maximum.

The transition temperatures of VO2 films on TiO2 and c-cut sapphire show a considerable difference based on the strain associated with the epitaxial film grown on the respective substrates. In fact, the hysteresis parameters like transition temperature, width of hysteresis, contrast of switching and slope of transition are all dependent on the substrate and the strain in the epitaxial film grown on top of it.

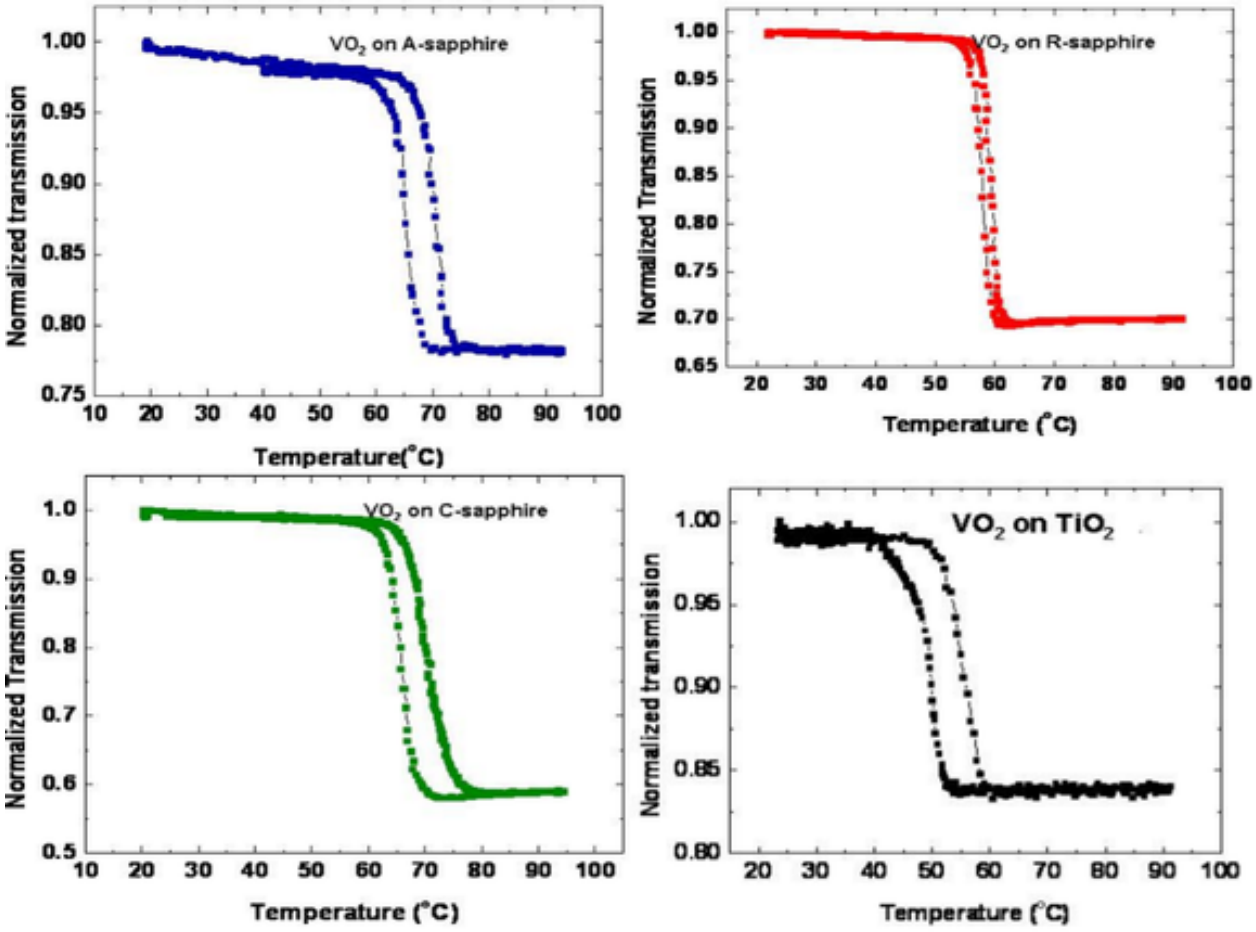

Figure A.1 Normalized infrared transmission acquired from the VO_2 epitaxial films deposited on the following substrates (from top to bottom): a-cut sapphire, c-cut sapphire, r-cut sapphire, and c-cut TiO_2. As reference, the accepted transition temperature for bulk VO_2 is 68°C. (Courtesy of Joyeeta Nag and Richard Haglund at Vanderbilt University.)

Appendix B

Use of ISODISTORT to Model the Phase Transition

ISODISTORT is a web-based tool that enables the study of structural phase transitions. It can be used via a web-browser and allows the user to visualize and manipulate the transition. *ISODISTORT* uses subroutines available in the *ISOTROPY*[*] software package and wraps an easy to use graphical user interface.[62]

In order to use *ISODISTORT* the two phases must be introduced. Then, the software decomposes the phase transition by:

1. Determining the distortion symmetry
2. Identifying the distortion modes
3. Determining the individual mode amplitudes
4. Expressing the distorted structure in terms of the familiar xyz basis

[*]This software package is available at http://stokes.byu.edu/isotropy.html[164]

Once a distortion has been computed, an interactive Java applet shows a three-dimensional image of how the two structures match. These representations shows how the shapes of the structures, lattice parameters, atomic bonds, and atom positions change during the phase transition. Futher, the applet also allows for:

1. Specific viewing directions
2. Rotations of the structures
3. Zooming
4. Animating the phase transition
5. Adjusting each distortion individually

Thus making it easier to visualize how the phase transition takes place. *ISODISTORT* is currently available at http://stokes.byu.edu/isodisplace.html[62]

B.1 Phase Transition of Vanadium Dioxide Between the Rutile (R) phase and the Monoclinic (M3) Phase

Figure B.1 shows the rutile structure (in pink) and the monoclinic $M3$ structure (in blue) as well as each of the atom positions. The $M3$ structure is four times as big as the R structure due to the doubling of two of the basis vectors of the R structure.

Figure B.2. shows the changes observed looking down the a, b, and c axis of the tetragonal phase. The displacement of the vanadium atoms is evident in views A and C by looking at the

vanadium-oxygen bonds. View B shows a "bowing" that takes place in the *M*3 phase. *ISODISTORT* shows that the phase transition between the *R* and the *M*3 phase produces a slight change in the angle (seen in view C) from 90° to 91.8°.

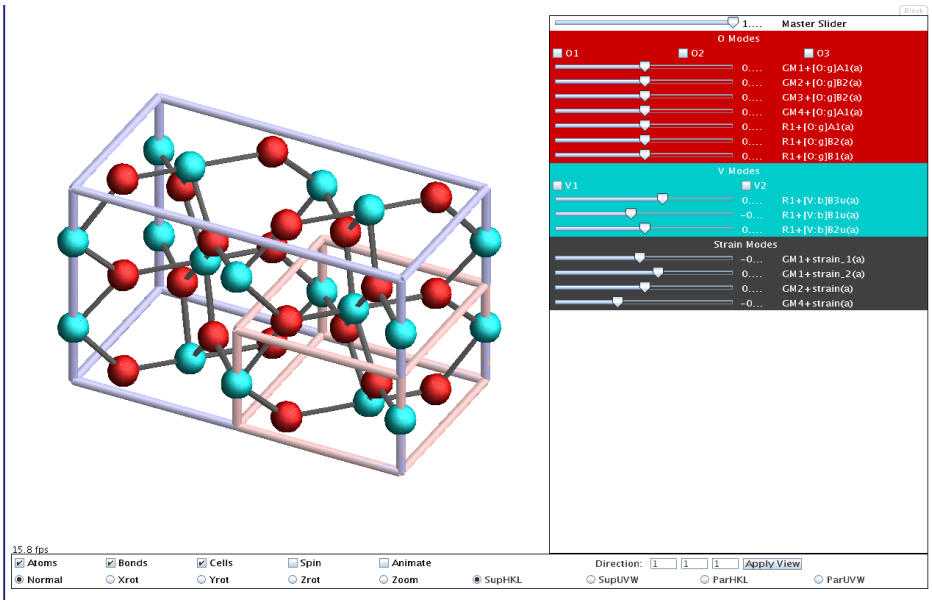

Figure B.1 *ISODISTORT* showing the monoclinic, *M*3 (blue), and the tetragonal, *R* (pink), structures for vanadium dioxide. The doubling of two basis vectors is evident from the diagram. Vanadium atoms are shown in cyan while the oxygen atoms are shown in red.

B.2 Distortion File for the Phase Transition of Vanadium Dioxide Between the Rutile (R) phase and the Monoclinic (M3) Phase

The following file is generated by *ISODISTORT* saving the required information that the Java applet needs to show the phase transition. Some of the code saved is intended to be displayed as choices in the web browser, and options that will be passed on to applet itself. However, the

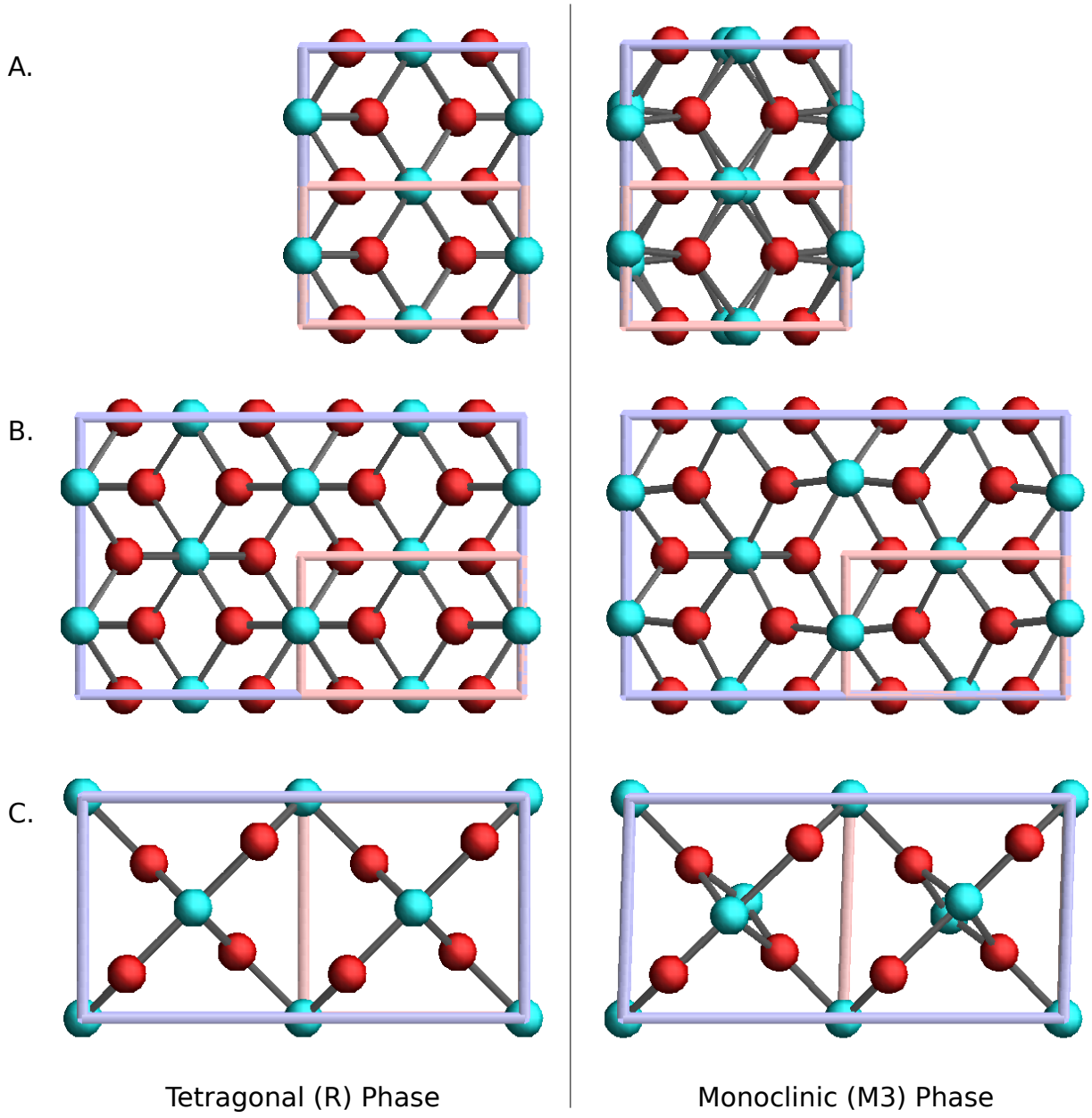

Figure B.2 The changes observed with *ISODISTORT* showing the changes between the *M*3 and the *R* structures for vanadium dioxide. The three views in A, B, and C correspond to viewing down the *a*, *b*, and *c* axis of the tetragonal phase (respectively). The displacement of the vanadium atoms is evident in A and C from the vanadium-oxygen bonds. C also shows a change in angle that takes place during the phase transition. Vanadium atoms are shown in cyan while the oxygen atoms are shown in red.

changes that take place during the transition are also stored in the file itself. Some of the information stored which regards to the phase transition includes:

1. The "high-symmetry" rutile structure [†] (including the lattice parameters, space-group, and the atom positions)

2. Specific changes to the unit cell (including the magnitude of each change)

3. Specific changes to the atom positions (also including the magnitude of the change)

4. Whether the transition is first order or continuous.

This text may be copied into a ".txt" file and uploaded into *ISODISTORT* in order to view the model of the transition.

```
Space Group: 136 P4_2/mnm   D4h-14,
Lattice parameters: a=4.55460, b=4.55460, c=2.85140, alpha=90.00000, beta=90.00000, gamma=90.00000<br>
Space-group preferences: monoclinic axes a(b)c, monoclinic cell choice 1, orthorhombic axes abc, origin choice 1, hexagonal axes<br>
O 4f   (x,x,0), x= 0.30000,
V 2a   (0,0,0)<br>
Subgroup:  12 C2/m, basis={(0,2,0),(0,0,2),(1,0,0)}, origin=(0,0,1/2), s=2, i=8<br>
<FORM ACTION="isodisplace2.cgi" METHOD="POST" target="_blank">
<INPUT TYPE="hidden" NAME="input" VALUE="displaydistort">
<INPUT TYPE="hidden" NAME="spacegroup" VALUE="136 P4_2/mnm   D4h-14">
<INPUT TYPE="hidden" NAME="settingaxesm" VALUE="a(b)c               ">
<INPUT TYPE="hidden" NAME="settingcell" VALUE="1">
<INPUT TYPE="hidden" NAME="settingorigin" VALUE="1">
<INPUT TYPE="hidden" NAME="settingaxesh" VALUE="h">
<INPUT TYPE="hidden" NAME="settingaxeso" VALUE="abc                 ">
<INPUT TYPE="hidden" NAME="lattparam" VALUE="a=4.55460, b=4.55460, c=2.85140, alpha=90.00000, beta=90.00000, gamma=90.00000">
<INPUT TYPE="hidden" NAME="dlattparam" VALUE="   4.5546        4.5546        2.8514        90.00        90.00        90.00">
<INPUT TYPE="hidden" NAME="wycount" VALUE="  2">
<INPUT TYPE="hidden" NAME="wypointer001" VALUE="1004">
<INPUT TYPE="hidden" NAME="wynumber001" VALUE=" 6">
<INPUT TYPE="hidden" NAME="wyckoff001" VALUE="4f   (x,x,0), x= 0.30000">
<INPUT TYPE="hidden" NAME="wyatom001" VALUE="O">
<INPUT TYPE="hidden" NAME="wyparam001" VALUE="  0.300000000000000       0.000000000000000E+000  0.000000000000000E+000">
<INPUT TYPE="hidden" NAME="wypointer002" VALUE=" 999">
<INPUT TYPE="hidden" NAME="wynumber002" VALUE=" 1">
<INPUT TYPE="hidden" NAME="wyckoff002" VALUE="2a   (0,0,0)">
<INPUT TYPE="hidden" NAME="wyatom002" VALUE="V">
<INPUT TYPE="hidden" NAME="wyparam002" VALUE="  0.000000000000000E+000  0.000000000000000E+000  0.000000000000000E+000">
<INPUT TYPE="hidden" NAME="irrepcount" VALUE="0">
<INPUT TYPE="hidden" NAME="basisorigin" VALUE="   1   0   0   0   1   1   0  -1   1   0   0   1   2">
<INPUT TYPE="hidden" NAME="isofilename" VALUE="           ">
<INPUT TYPE="hidden" NAME="orderparam" VALUE="Subgroup:  12 C2/m, basis={(0,2,0),(0,0,2),(1,0,0)}, origin=(0,0,1/2), s=2, i=8">
<INPUT TYPE="hidden" NAME="isosubgroup" VALUE="    0">
<INPUT TYPE="hidden" NAME="subgroupsym" VALUE="  12">
<INPUT TYPE="hidden" NAME="distortfilename" VALUE="isodisplac3_16707.iso">
<INPUT TYPE="hidden" NAME="atomsfilename" VALUE="isodisplace_55267.iso">
<p><INPUT TYPE="radio" NAME="origintype" VALUE="viewdistortion" CHECKED> View distortion
<a href="/iso/isodisplacehelp.html#viewdist" target="_blank">(help)</a>
<INPUT TYPE="radio" NAME="origintype" VALUE="viewdiffraction"> View diffraction
<a href="/iso/isodisplacehelp.html#viewdiff" target="_blank">(help)</a>
<INPUT TYPE="radio" NAME="origintype" VALUE="structurefile"> CIF file
<a href="/iso/isodisplacehelp.html#cifsub" target="_blank">(help)</a>
<INPUT TYPE="radio" NAME="origintype" VALUE="distortionfile"> Distortion file
<a href="/iso/isodisplacehelp.html#dfile" target="_blank">(help)</a>
<INPUT TYPE="radio" NAME="origintype" VALUE="domains"> Domains
```

[†]This structure is also known as the "parent" structure.

```
<a href="/iso/isodisplacehelp.html#domains" target="_blank">(help)</a>
<INPUT TYPE="radio" NAME="origintype" VALUE="primary"> Primary order parameters
<a href="/iso/isodisplacehelp.html#setsprimary" target="_blank">(help)</a>
<INPUT TYPE="submit" VALUE="OK"><p>
Enter mode and strain amplitudes:
<a href="/iso/isodisplacehelp.html#modeamp" target="_blank">(help)</a><br>
<p>
P4_2/mnm[0,0,0]GM1+(a) 136 P4_2/mnm, basis={(1,0,0),(0,1,0),(0,0,1)}, origin=(0,0,0), s=1 i=1<br>
<input type="text" name="mode001001" value="  -0.02834" size=5>[O:f]A1(a)<br>
<input type="text" name="strain1" value="  -0.00554" size=5>strain_1(a)<br>
<input type="text" name="strain2" value="   0.01652" size=5>strain_2(a)<br>
<p>
P4_2/mnm[0,0,0]GM2+(a) 58 Pnnm, basis={(1,0,0),(0,1,0),(0,0,1)}, origin=(0,0,0), s=1 i=2<br>
<input type="text" name="mode001002" value="  -0.00676" size=5>[O:f]B1(a)<br>
<input type="text" name="strain3" value="  -0.00085" size=5>strain(a)<br>
<p>
P4_2/mnm[0,0,0]GM3+(a) 84 P4_2/m, basis={(0,1,0),(-1,0,0),(0,0,1)}, origin=(0,1/2,0), s=1 i=2<br>
<input type="text" name="mode001003" value="  -0.00032" size=5>[O:f]B1(a)<br>
<p>
P4_2/mnm[0,0,0]GM4+(a) 65 Cmmm, basis={(-1,1,0),(-1,-1,0),(0,0,1)}, origin=(0,0,0), s=1 i=2<br>
<input type="text" name="mode001004" value="  -0.00193" size=5>[O:f]A1(a)<br>
<input type="text" name="scalar001001" value="   0.00000" size=5>[O:f]order(a)<br>
<input type="text" name="scalar002001" value="   0.00000" size=5>[V:a]order(a)<br>
<input type="text" name="strain4" value="  -0.03281" size=5>strain(a)<br>
<p>
P4_2/mnm[0,1/2,1/2]R1-(0,a,0,0) 12 C2/m, basis={(0,2,0),(0,0,2),(1,0,0)}, origin=(0,0,1/2), s=2 i=8<br>
<input type="text" name="mode001005" value="  -0.02222" size=5>[O:f]A1(a)<br>
<input type="text" name="mode001006" value="   0.01426" size=5>[O:f]B2(a)<br>
<input type="text" name="mode001007" value="   0.00225" size=5>[O:f]B1(a)<br>
<input type="text" name="mode002001" value="  -0.22029" size=5>[V:a]B3u(a)<br>
<input type="text" name="mode002002" value="  -0.17736" size=5>[V:a]B1u(a)<br>
<input type="text" name="mode002003" value="  -0.01932" size=5>[V:a]B2u(a)<br>
<input type="text" name="scalar001002" value="   0.00000" size=5>[O:f]order(a)<br>
<p>Parameters:
<a href="/iso/isodisplacehelp.html#modeparams" target="_blank">(help)</a><br>
"View distortion":<br>
Atomic radius:
<input type="text" name="atomicradius" value="     0.400" size=5> Angstroms<br>
Maximum bond length:
<input type="text" name="bondlength" value="     2.114" size=5> Angstroms<br>
Applet width:
<input type="text" name="appletwidth" value="1024" size=5> pixels<br>
"View distortion" and "View diffraction":<br>
Maximum mode amplitudes:
<input type="text" name="modeamplitude" value="     1.000" size=5> Angstroms<br>
Maximum strain amplitudes:
<input type="text" name="strainamplitude" value="     0.100" size=5><p>
</FORM><p>
<A href="/iso/isodisplacehelp.html" target="_blank"><B>Complete help file</B></A><P>
distortfilename=isodisplac3_16707.iso
          20           7           2           5          16           8
          20          18           7           3           2           1
           3           2           4
        6454        6455        6456        6457        6490           0
           0           0           0           0           0           0
           0           0           0           0           0           0
           0           0           0           0           0           0
           0         136          58          84          65          12
           1           1           1           1           2           1
           2           2           2           8           1           2
           3           4           5           5           5           5
           5           5         396         399         399         396
         396         398         399         781         780         782
           4           5           4         396         396         775
           1           1           2           4           1           1
           1           1           4           1           1           1
           1           1
           1           0           0           0           1           0
           0           0           1           0           0           0
           1
           1           0           0           0           1           0
           0           0           1           0           0           0
           1
           0           1           0          -1           0           0
           0           0           1           0           1           0
           2
           0           1           0          -1           0           0
           0           0           1           0           0           0
           1
           1           0           0           0           1           1
           0          -1           1           0           0           1
           2
   9.10920000   5.70280000   4.55460000  90.00000000  90.00000000  90.00000000
   0.50000000   0.25000000   0.00000000   0.00000000   0.00000000   1.00000000
   0.50000000   0.00000000   0.00000000   0.00000000   0.50000000   0.00000000
   1.92150227
```

```
 1.00000000   1.00000000   0.00000000   0.00000000   0.00000000   0.00000000
 0.00000000   0.00000000   1.00000000   0.00000000   0.00000000   0.00000000
 1.00000000  -1.00000000   0.00000000   0.00000000   0.00000000   0.00000000
 0.00000000   0.00000000   0.00000000   0.00000000   0.00000000   1.00000000
 1.00000000   1.00000000   1.00000000   1.00000000   0.00000000   1.00000000
 0.00000000   0.00000000
1    0.150000000000   0.750000000000   0.300000000000   0.077625563297
     0.000000000000   0.155251126594  -0.077625563297   0.000000000000
     0.155251126594  -0.077625563297   0.000000000000   0.155251126594
     0.077625563297   0.000000000000   0.155251126594   0.000000000000
     0.000000000000   0.000000000000   0.000000000000   0.175352458441
     0.000000000000   0.000000000000   0.000000000000   0.000000000000
     1.000000000000   0.000000000000
1    0.150000000000   0.250000000000   0.300000000000   0.077625563297
     0.000000000000   0.155251126594  -0.077625563297   0.000000000000
     0.155251126594  -0.077625563297   0.000000000000   0.155251126594
     0.077625563297   0.000000000000   0.155251126594   0.000000000000
     0.000000000000   0.000000000000   0.000000000000  -0.175352458441
     0.000000000000   0.000000000000   0.000000000000   0.000000000000
     1.000000000000   0.000000000000
1    0.650000000000   0.750000000000   0.300000000000   0.077625563297
     0.000000000000   0.155251126594  -0.077625563297   0.000000000000
     0.155251126594  -0.077625563297   0.000000000000   0.155251126594
     0.077625563297   0.000000000000   0.155251126594   0.000000000000
     0.000000000000   0.000000000000   0.000000000000  -0.175352458441
     0.000000000000   0.000000000000   0.000000000000   0.000000000000
     1.000000000000   0.000000000000
1    0.650000000000   0.250000000000   0.300000000000   0.077625563297
     0.000000000000   0.155251126594  -0.077625563297   0.000000000000
     0.155251126594  -0.077625563297   0.000000000000   0.155251126594
     0.077625563297   0.000000000000   0.155251126594   0.000000000000
     0.000000000000   0.000000000000   0.000000000000   0.175352458441
     0.000000000000   0.000000000000   0.000000000000   0.000000000000
     1.000000000000   0.000000000000
2    0.100000000000   0.000000000000   0.800000000000  -0.077625563297
     0.000000000000   0.155251126594   0.077625563297   0.000000000000
     0.155251126594  -0.077625563297   0.000000000000  -0.155251126594
     0.077625563297   0.000000000000  -0.155251126594   0.077625563297
     0.000000000000  -0.155251126594   0.000000000000   0.000000000000
     0.000000000000   0.077625563297   0.000000000000   0.155251126594
    -1.000000000000  -1.000000000000
3    0.100000000000   0.500000000000   0.800000000000  -0.077625563297
     0.000000000000   0.155251126594   0.077625563297   0.000000000000
     0.155251126594  -0.077625563297   0.000000000000  -0.155251126594
     0.077625563297   0.000000000000  -0.155251126594  -0.077625563297
     0.000000000000   0.155251126594   0.000000000000   0.000000000000
     0.000000000000  -0.077625563297   0.000000000000  -0.155251126594
    -1.000000000000   1.000000000000
3    0.600000000000   0.000000000000   0.800000000000  -0.077625563297
     0.000000000000   0.155251126594   0.077625563297   0.000000000000
     0.155251126594  -0.077625563297   0.000000000000  -0.155251126594
     0.077625563297   0.000000000000  -0.155251126594  -0.077625563297
     0.000000000000   0.155251126594   0.000000000000   0.000000000000
     0.000000000000  -0.077625563297   0.000000000000  -0.155251126594
    -1.000000000000   1.000000000000
2    0.600000000000   0.500000000000   0.800000000000  -0.077625563297
     0.000000000000   0.155251126594   0.077625563297   0.000000000000
     0.155251126594  -0.077625563297   0.000000000000  -0.155251126594
     0.077625563297   0.000000000000  -0.155251126594   0.077625563297
     0.000000000000  -0.155251126594   0.000000000000   0.000000000000
     0.000000000000   0.077625563297   0.000000000000   0.155251126594
    -1.000000000000  -1.000000000000
3    0.400000000000   0.000000000000   0.200000000000   0.077625563297
     0.000000000000  -0.155251126594  -0.077625563297   0.000000000000
    -0.155251126594   0.077625563297   0.000000000000   0.155251126594
    -0.077625563297   0.000000000000   0.155251126594   0.077625563297
     0.000000000000  -0.155251126594   0.000000000000   0.000000000000
     0.000000000000   0.077625563297   0.000000000000   0.155251126594
    -1.000000000000   1.000000000000
2    0.400000000000   0.500000000000   0.200000000000   0.077625563297
     0.000000000000  -0.155251126594  -0.077625563297   0.000000000000
    -0.155251126594   0.077625563297   0.000000000000   0.155251126594
    -0.077625563297   0.000000000000   0.155251126594  -0.077625563297
     0.000000000000   0.155251126594   0.000000000000   0.000000000000
     0.000000000000  -0.077625563297   0.000000000000  -0.155251126594
    -1.000000000000  -1.000000000000
2    0.900000000000   0.000000000000   0.200000000000   0.077625563297
     0.000000000000  -0.155251126594  -0.077625563297   0.000000000000
    -0.155251126594   0.077625563297   0.000000000000   0.155251126594
    -0.077625563297   0.000000000000   0.155251126594  -0.077625563297
     0.000000000000   0.155251126594   0.000000000000   0.000000000000
     0.000000000000  -0.077625563297   0.000000000000  -0.155251126594
    -1.000000000000  -1.000000000000
3    0.900000000000   0.500000000000   0.200000000000   0.077625563297
     0.000000000000  -0.155251126594  -0.077625563297   0.000000000000
    -0.155251126594   0.077625563297   0.000000000000   0.155251126594
```

```
   -0.077625563297   0.000000000000   0.155251126594   0.077625563297
    0.000000000000  -0.155251126594   0.000000000000   0.000000000000
    0.000000000000   0.077625563297   0.000000000000   0.155251126594
   -1.000000000000   1.000000000000
1   0.850000000000   0.750000000000   0.700000000000  -0.077625563297
    0.000000000000  -0.155251126594   0.077625563297   0.000000000000
   -0.155251126594   0.077625563297   0.000000000000  -0.155251126594
   -0.077625563297   0.000000000000  -0.155251126594   0.000000000000
    0.000000000000   0.000000000000   0.000000000000   0.175352458441
    0.000000000000   0.000000000000   0.000000000000   0.000000000000
    1.000000000000   0.000000000000
1   0.850000000000   0.250000000000   0.700000000000  -0.077625563297
    0.000000000000  -0.155251126594   0.077625563297   0.000000000000
   -0.155251126594   0.077625563297   0.000000000000  -0.155251126594
   -0.077625563297   0.000000000000  -0.155251126594   0.000000000000
    0.000000000000   0.000000000000   0.000000000000  -0.175352458441
    0.000000000000   0.000000000000   0.000000000000   0.000000000000
    1.000000000000   0.000000000000
1   0.350000000000   0.750000000000   0.700000000000  -0.077625563297
    0.000000000000  -0.155251126594   0.077625563297   0.000000000000
   -0.155251126594   0.077625563297   0.000000000000  -0.155251126594
   -0.077625563297   0.000000000000  -0.155251126594   0.000000000000
    0.000000000000   0.000000000000   0.000000000000  -0.175352458441
    0.000000000000   0.000000000000   0.000000000000   0.000000000000
    1.000000000000   0.000000000000
1   0.350000000000   0.250000000000   0.700000000000  -0.077625563297
    0.000000000000  -0.155251126594   0.077625563297   0.000000000000
   -0.155251126594   0.077625563297   0.000000000000  -0.155251126594
   -0.077625563297   0.000000000000  -0.155251126594   0.000000000000
    0.000000000000   0.000000000000   0.000000000000   0.175352458441
    0.000000000000   0.000000000000   0.000000000000   0.000000000000
    1.000000000000   0.000000000000
2   0.100000000000   1.000000000000   0.800000000000  -0.077625563297
    0.000000000000   0.155251126594   0.077625563297   0.000000000000
    0.155251126594  -0.077625563297   0.000000000000  -0.155251126594
    0.077625563297   0.000000000000  -0.155251126594   0.077625563297
    0.000000000000  -0.155251126594   0.000000000000   0.000000000000
    0.000000000000   0.077625563297   0.000000000000   0.155251126594
   -1.000000000000  -1.000000000000
3   0.600000000000   1.000000000000   0.800000000000  -0.077625563297
    0.000000000000   0.155251126594   0.077625563297   0.000000000000
    0.155251126594  -0.077625563297   0.000000000000  -0.155251126594
    0.077625563297   0.000000000000  -0.155251126594  -0.077625563297
    0.000000000000   0.155251126594   0.000000000000   0.000000000000
    0.000000000000  -0.077625563297   0.000000000000  -0.155251126594
   -1.000000000000   1.000000000000
3   0.400000000000   1.000000000000   0.200000000000   0.077625563297
    0.000000000000  -0.155251126594  -0.077625563297   0.000000000000
   -0.155251126594   0.077625563297   0.000000000000   0.155251126594
   -0.077625563297   0.000000000000   0.155251126594   0.077625563297
    0.000000000000  -0.155251126594   0.000000000000   0.000000000000
    0.000000000000   0.077625563297   0.000000000000   0.155251126594
   -1.000000000000   1.000000000000
2   0.900000000000   1.000000000000   0.200000000000   0.077625563297
    0.000000000000  -0.155251126594  -0.077625563297   0.000000000000
   -0.155251126594   0.077625563297   0.000000000000   0.155251126594
   -0.077625563297   0.000000000000   0.155251126594  -0.077625563297
    0.000000000000   0.155251126594   0.000000000000   0.000000000000
    0.000000000000  -0.077625563297   0.000000000000  -0.155251126594
   -1.000000000000  -1.000000000000
1   0.000000000000   0.750000000000   0.000000000000   0.000000000000
    0.000000000000   0.000000000000   0.000000000000   0.175352458441
    0.000000000000   0.000000000000   0.000000000000   0.000000000000
    1.000000000000
1   0.000000000000   0.250000000000   0.000000000000   0.000000000000
    0.000000000000   0.000000000000   0.000000000000  -0.175352458441
    0.000000000000   0.000000000000   0.000000000000   0.000000000000
    1.000000000000
1   0.500000000000   0.750000000000   0.000000000000   0.000000000000
    0.000000000000   0.000000000000   0.000000000000  -0.175352458441
    0.000000000000   0.000000000000   0.000000000000   0.000000000000
    1.000000000000
1   0.500000000000   0.250000000000   0.000000000000   0.000000000000
    0.000000000000   0.000000000000   0.000000000000   0.175352458441
    0.000000000000   0.000000000000   0.000000000000   0.000000000000
    1.000000000000
2   0.250000000000   0.000000000000   0.500000000000   0.077625563297
    0.000000000000  -0.155251126594   0.000000000000   0.000000000000
    0.000000000000   0.077625563297   0.000000000000   0.155251126594
   -1.000000000000
2   0.250000000000   0.500000000000   0.500000000000  -0.077625563297
    0.000000000000   0.155251126594   0.000000000000   0.000000000000
    0.000000000000  -0.077625563297   0.000000000000  -0.155251126594
   -1.000000000000
2   0.750000000000   0.000000000000   0.500000000000  -0.077625563297
    0.000000000000   0.155251126594   0.000000000000   0.000000000000
```

```
      0.000000000000  -0.077625563297   0.000000000000  -0.155251126594
     -1.000000000000
  2   0.750000000000   0.500000000000   0.500000000000   0.077625563297
      0.000000000000  -0.155251126594   0.000000000000   0.000000000000
      0.000000000000   0.077625563297   0.000000000000   0.155251126594
     -1.000000000000
  1   0.000000000000   0.750000000000   1.000000000000   0.000000000000
      0.000000000000   0.000000000000   0.000000000000   0.175352458441
      0.000000000000   0.000000000000   0.000000000000   0.000000000000
      1.000000000000
  1   1.000000000000   0.750000000000   0.000000000000   0.000000000000
      0.000000000000   0.000000000000   0.000000000000   0.175352458441
      0.000000000000   0.000000000000   0.000000000000   0.000000000000
      1.000000000000
  1   1.000000000000   0.750000000000   1.000000000000   0.000000000000
      0.000000000000   0.000000000000   0.000000000000   0.175352458441
      0.000000000000   0.000000000000   0.000000000000   0.000000000000
      1.000000000000
  1   0.000000000000   0.250000000000   1.000000000000   0.000000000000
      0.000000000000   0.000000000000   0.000000000000  -0.175352458441
      0.000000000000   0.000000000000   0.000000000000   0.000000000000
      1.000000000000
  1   1.000000000000   0.250000000000   0.000000000000   0.000000000000
      0.000000000000   0.000000000000   0.000000000000  -0.175352458441
      0.000000000000   0.000000000000   0.000000000000   0.000000000000
      1.000000000000
  1   1.000000000000   0.250000000000   1.000000000000   0.000000000000
      0.000000000000   0.000000000000   0.000000000000  -0.175352458441
      0.000000000000   0.000000000000   0.000000000000   0.000000000000
      1.000000000000
  1   0.500000000000   0.750000000000   1.000000000000   0.000000000000
      0.000000000000   0.000000000000   0.000000000000  -0.175352458441
      0.000000000000   0.000000000000   0.000000000000   0.000000000000
      1.000000000000
  1   0.500000000000   0.250000000000   1.000000000000   0.000000000000
      0.000000000000   0.000000000000   0.000000000000   0.175352458441
      0.000000000000   0.000000000000   0.000000000000   0.000000000000
      1.000000000000
  2   0.250000000000   1.000000000000   0.500000000000   0.077625563297
      0.000000000000  -0.155251126594   0.000000000000   0.000000000000
      0.000000000000   0.077625563297   0.000000000000   0.155251126594
     -1.000000000000
  2   0.750000000000   1.000000000000   0.500000000000  -0.077625563297
      0.000000000000   0.155251126594   0.000000000000   0.000000000000
      0.000000000000  -0.077625563297   0.000000000000  -0.155251126594
     -1.000000000000
done
atomsfilename=isodisplace_55267.iso
   9.06640   5.79700   4.52550  90.00000  91.88000  90.00000
   0.00000   0.00000   0.00000   0.00000   0.00000   0.00000
O1
   0.14820   0.24750   0.29420
   0.00000   0.00000   0.00000
O2
   0.39690   0.00000   0.20890
   0.00000   0.00000   0.00000
O3
   0.10000   0.00000   0.79870
   0.00000   0.00000   0.00000
V1
   0.00000   0.71890   0.00000
   0.00000   0.00000   0.00000
V2
   0.23140   0.00000   0.53120
   0.00000   0.00000   0.00000
   0.00000   0.00000   0.00000
done
```

Appendix C

Sample Scripts Used in *NISTMonte* to Simulate Electron Trajectories Through Various Thin Films

NISTMonte is a Monte Carlo simulation tool for electron and x-ray transport in solid materials, developed at the National Institute of Standards and Technology. It contains a series of libraries useful for the simulation of electron trajectories through materials using the Monte Carlo method, as well as for the simulation of generated x-rays. Though its main purpose is to ease the simulation of electron trajectories and generated x-ray spectra, the simulations presented do not take into account any effects generated by the crystallinity of the irradiated materials.

The two main libraries used are:

1. Electron Probe Quantitation [sic] (*gov.nist.microanalysis.EPQLibrary*) - Contains the tools needed for the "characterization" of the different materials, thus, it is used to set the appropriate material properties.

2. NISTMonte (*gov.nist.microanalysis.NISTMonte*) - Contains the tools for the Monte Carlo

Simulation of electron trajectories. Thus, it also contains the necessary tools for setting the appropriate parameters (including location) for the electron beam, chamber, detectors, sample.

NISTMonte is not subject to copyright protection and is in the public domain.

Though *NISTMonte*'s libraries are JAVA based, an effective way to write scripts for the *NISTMonte* is through the Jython scripting language. Jython is a JAVA implementation of the Python scripting language, thus, it allows to use the Python syntax to call and access the JAVA *NISTMonte* libraries.

The scripts presented here are written in Jython to use with the *NISTMonte* libraries.

C.1 Generate Electron Trajectories for an Electron Beam with Normal Incidence for Various Electron Energies

This script will generate a series of cross-section images (electron trajectories and intensity of x-ray) and x-ray spectra for a 50 nm thick VO_2 film deposited onto a 380 nm thick SiO_2 layer with a Si substrate. Sets of images are generated for electron energies of 5, 10, 15, 20, 25, and 30 keV. Each generated image represents a $5\mu m \times 5\mu m$ cross-section of the electron interactions.

```
# A simple script for various electron energies
import gov.nist.microanalysis.EPQLibrary as epq
import gov.nist.microanalysis.NISTMonte as nm
import java.io as io
import javax.imageio as imgio
print "Start...";
for e in [5.0, 10.0, 15.0, 20.0, 25.0, 30.0]:
   # create an instance of the model
   monte=nm.MonteCarloSS()
   monte.setBeamEnergy(epq.ToSI.keV(e))
   #
   # create the VO2 thin film, shape and region
   VO2=epq.Material()
   VO2.defineByMoleFraction([epq.Element.V,epq.Element.O],[1.0,2.0])
   VO2.setDensity(epq.ToSI.gPerCC(3.06))
   VO2.setName("VO2")
   # create a film of VO2 on the top most surface
   VO2Film = nm.MultiPlaneShape.createSubstrate([0.0, 0.0, -1.0],[0.0, 0.0, 0.0])
```

```
   r1=nm.MonteCarloSS.Region(monte, monte.getChamber(), VO2, VO2Film)
   #
   # create the SiO2 layer, shape and region
   SiO2=epq.Material()
   SiO2.defineByMoleFraction([epq.Element.Si,epq.Element.O],[1.0,2.0])
   SiO2.setDensity(epq.ToSI.gPerCC(2.65))
   SiO2.setName("SiO2")
   # create a layer of SiO2 50nm from the surface
   SiO2plane = nm.MultiPlaneShape.createSubstrate([0.0, 0.0, -1.0],[0.0, 0.0, 0.05e-6])
   r2=nm.MonteCarloSS.Region(monte, r1, SiO2, SiO2plane)
   #
   # create a matrix of Si 430nm from the surface
   mat=epq.MaterialFactory.createPureElement(epq.Element.Si)
   subs = nm.MultiPlaneShape.createSubstrate([0.0, 0.0, -1.0],[0.0, 0.0, 0.43e-6])
   nm.MonteCarloSS.Region(monte, r2, mat, subs)
   #
   # add event listeners
   xrel=nm.XRayEventListener(monte,monte.computeDetectorPosition(40*(3.1415926/180),0.0))
   monte.addActionListener(xrel)
   przs=nm.PhiRhoStats.watchDefaultTransitions(xrel,-1.0e-6,9.0e-6)
   #
   # add a trajectory image
   img=nm.TrajectoryImage(1024,1024,5.0e-6)
   monte.addActionListener(img)
   #
   # add generation images
   imgs=nm.EmissionImage.watchDefaultTransitions(xrel,512,5.0e-6)
   #
   # run the simulation
   monte.runMultipleTrajectories(1000)
   #
   # determine where to save the results
   dest=DefaultOutput+PathSep+"E0=%5.1f keV" % (e)+PathSep
   #
   # output the phi-rho-z stats
   nm.PhiRhoStats.dumpToFiles(przs,dest)
   #
   # output the trajectory image
   img.dumpToFile(dest)
   #
   # output the transition image
   nm.EmissionImage.dumpToFiles(imgs,dest)
print "Done!"
```

C.2 Generate Electron Trajectories for a 25 keV Electron Beam at Various Sample Tilts

This script will generate a series of cross-section images (electron trajectories and intensity of x-ray) and x-ray spectra for a 50 nm thick VO_2 film deposited onto a 380 nm thick SiO_2 layer with a Si substrate. Sets of images are generated for a 25keV electron energy and for sample tilts of 0°,

10°, 20°, 30°, 40°, 50°, 60°, 70°, and 80° with respect to the incident beam. Again, each generated image represents a $5\mu m \times 5\mu m$ cross-section of the electron interactions.

```
# A simple script for various sample tilts
import gov.nist.microanalysis.EPQLibrary as epq
import gov.nist.microanalysis.NISTMonte as nm
import java.io as io
import javax.imageio as imgio
print "Start...";
for phi in [0.0, -10.0, -20.0, -30.0, -40.0, -50.0, -60.0, -70.0, -80.0]:
   # create an instance of the model
   monte=nm.MonteCarloSS()
   monte.setBeamEnergy(epq.ToSI.keV(25.0))
   #
   # create the VO2 thin film, shape and region
   VO2=epq.Material()
   VO2.defineByMoleFraction([epq.Element.V,epq.Element.O],[1.0,2.0])
   VO2.setDensity(epq.ToSI.gPerCC(3.06))
   VO2.setName("VO2")
   # create a film of VO2 on the top most surface
   VO2Film = nm.MultiPlaneShape.createSubstrate([0.0, 0.0, -1.0],[0.0, 0.0, 0.0])
   r1=nm.MonteCarloSS.Region(monte, monte.getChamber(), VO2, VO2Film)
   #
   # create the SiO2 layer, shape and region
   SiO2=epq.Material()
   SiO2.defineByMoleFraction([epq.Element.Si,epq.Element.O],[1.0,2.0])
   SiO2.setDensity(epq.ToSI.gPerCC(2.65))
   SiO2.setName("SiO2")
   # create a layer of SiO2 50nm from the surface
   SiO2plane = nm.MultiPlaneShape.createSubstrate([0.0, 0.0, -1.0],[0.0, 0.0, 0.05e-6])
   r2=nm.MonteCarloSS.Region(monte, r1, SiO2, SiO2plane)
   #
   # create a matrix of Si 430nm from the surface
   mat=epq.MaterialFactory.createPureElement(epq.Element.Si)
   subs = nm.MultiPlaneShape.createSubstrate([0.0, 0.0, -1.0],[0.0, 0.0, 0.43e-6])
   nm.MonteCarloSS.Region(monte, r2, mat, subs)
   #
   # rotate the sample
   monte.getChamber().rotate([0.0,0.0,0.0],0.0,phi*1.74533e-2,0.0)
   #
   # add event listeners
   xrel=nm.XRayEventListener(monte,monte.computeDetectorPosition(40*(3.1415926/180),0.0))
   monte.addActionListener(xrel)
   przs=nm.PhiRhoStats.watchDefaultTransitions(xrel,-1.0e-6,9.0e-6)
   #
   # add a trajectory image
   img=nm.TrajectoryImage(1024,1024,5.0e-6)
   monte.addActionListener(img)
   #
   # add generation images
   imgs=nm.EmissionImage.watchDefaultTransitions(xrel,512,5.0e-6)
   #
   # run the simulation
   monte.runMultipleTrajectories(1000)
   #
   # determine where to save the results
   dest=DefaultOutput+PathSep+"Tilt=%5.1f_deg" % (phi)+PathSep
   #
   # output the phi-rho-z stats
   nm.PhiRhoStats.dumpToFiles(przs,dest)
   #
```

```
   # output the trajectory image
   img.dumpToFile(dest)
   #
   # output the transition image
   nm.EmissionImage.dumpToFiles(imgs,dest)
print "Done!"
```

C.3 Generate Electron Trajectories for a Electron Beams with Various Electron Energies in Transmission Through Samples of Various Thicknesses

This script will generate a series of cross-section images (electron trajectories and intensity of x-ray) and x-ray spectra for a 50 nm thick VO_2 film on a SiO_2 support layer of thicknesses varying from 10, 20, 50, 100, 200, and 500 nm. Electron energies for each thickness vary between 5, 30, and 200 keV.

Each generated image represents a $1\mu m \times 1\mu m$ cross-section of the electron interactions under normal incidence.

```
# A simple script for various thicknesses of a film
import gov.nist.microanalysis.EPQLibrary as epq
import gov.nist.microanalysis.NISTMonte as nm
import java.io as io
import javax.imageio as imgio
print "Start...";

for ev in [5.0, 30.0, 200.0]:
  for thick in [10.0, 20.0, 50.0, 100.0, 200.0, 500.0]:
   # create an instance of the model
   monte=nm.MonteCarloSS()
   monte.setBeamEnergy(epq.ToSI.keV(ev))
   #
   # create the VO2 thin film, shape and region
   VO2=epq.Material()
   VO2.defineByMoleFraction([epq.Element.V,epq.Element.O],[1.0,2.0])
   VO2.setDensity(epq.ToSI.gPerCC(3.06))
   VO2.setName("VO2")
   # create a film of VO2 on the top most surface
   VO2Film = nm.MultiPlaneShape.createFilm([0.0, 0.0, -1.0],[0.0, 0.0, 0.0],0.110e-6)
   r1=nm.MonteCarloSS.Region(monte, monte.getChamber(), VO2, VO2Film)
   #
   # create the SiO2 layer, shape and region
```

```
   SiO2=epq.Material()
   SiO2.defineByMoleFraction([epq.Element.Si,epq.Element.O],[1.0,2.0])
   SiO2.setDensity(epq.ToSI.gPerCC(2.65))
   SiO2.setName("SiO2")
   # create a layer of SiO2 50nm from the surface
   SiO2plane = nm.MultiPlaneShape.createFilm([0.0, 0.0, -1.0],[0.0, 0.0, 0.10e-6],thick*1.0e-9)
   r2=nm.MonteCarloSS.Region(monte, r1, SiO2, SiO2plane)
   #
   # add event listeners
   xrel=nm.XRayEventListener(monte,monte.computeDetectorPosition(40*(3.1415926/180),0.0))
   monte.addActionListener(xrel)
   przs=nm.PhiRhoStats.watchDefaultTransitions(xrel,-1.0e-6,9.0e-6)
   #
   # add a trajectory image
   img=nm.TrajectoryImage(1024,1024,1.0e-6)
   monte.addActionListener(img)
   #
   # add generation images
   imgs=nm.EmissionImage.watchDefaultTransitions(xrel,512,1.0e-6)
   #
   # run the simulation
   monte.runMultipleTrajectories(1000)
   #
   # determine where to save the results
   dest=DefaultOutput+PathSep+"set-%5.1fnm"%(thick)+"_%5.1fkeV"%(ev)+PathSep
   #
   # output the phi-rho-z stats
   nm.PhiRhoStats.dumpToFiles(przs,dest)
   #
   # output the trajectory image
   img.dumpToFile(dest)
   #
   # output the transition image
   nm.EmissionImage.dumpToFiles(imgs,dest)
print "Done!"
```

Bibliography

[1] R. P. Feynman, "There's Plenty of Room at the Bottom," Engineering and Science **23,** 22–36 (1960).

[2] F. Morin, "Oxides Which Show a Metal-to-Insulator Transition at the Neel Temperature," Physical Review Letters **3,** 34–36 (1959).

[3] C. Hébert, M. Willinger, D. Su, P. Pongratz, P. Schattschneider, and R. Schlögl, "Oxygen K-edge in vanadium oxides: simulations and experiments," The European Physical Journal B **28,** 407–414 (2002).

[4] M. Imada, A. Fujimori, and Y. Tokura, "Metal-insulator transitions," Reviews of Modern Physics **70,** 1039–1263 (1998).

[5] H. Liu, V. Avrutin, N. Izyumskaya, U. Özgür, and H. Morkoç, "Transparent conducting oxides for electrode applications in light emitting and absorbing devices," Superlattices and Microstructures **48,** 458–484 (2010).

[6] A. Fujishima, X. Zhang, and D. Tryk, "TiO2 photocatalysis and related surface phenomena," Surface Science Reports **63,** 515–582 (2008).

[7] Y. Wang, "High Resolution Electron Energy Loss Spectroscopy on Perfect and Defective Oxide Surfaces," Zeitschrift für Physikalische Chemie **222,** 927–964 (2008).

[8] Z. Yang, C. Ko, and S. Ramanathan, "Oxide Electronics Utilizing Ultra-Fast Metal-Insulator Transitions," Annual Review of Materials Research **41,** 337–367 (2010).

[9] L. Cario, C. Vaju, B. Corraze, V. Guiot, and E. Janod, "Electric-field-induced resistive switching in a family of mott insulators: Towards a new class of RRAM memories.," Advanced materials (Deerfield Beach, Fla.) **22,** 5193–7 (2010).

[10] S. Asanuma *et al.*, "Tuning of the metal-insulator transition in electrolyte-gated NdNiO[sub 3] thin films," Applied Physics Letters **97,** 142110 (2010).

[11] A. L. Pergament, P. P. Boriskov, A. Velichko, and N. A. Kuldin, "Switching effect and the metal-insulator transition in electric field," Journal of Physics and Chemistry of Solids **71,** 874–879 (2010).

[12] J. Yao, Z. Sun, L. Zhong, D. Natelson, and J. M. Tour, "Resistive switches and memories from silicon oxide.," Nano letters **10,** 4105–10 (2010).

[13] R. M. Briggs, I. M. Pryce, and H. A. Atwater, "Compact silicon photonic waveguide modulator based on the vanadium dioxide metal-insulator phase transition," Optics Express **18,** 11192 (2010).

[14] S. Sengupta, K. Wang, K. Liu, A. K. Bhat, S. Dhara, J. Wu, and M. M. Deshmukh, "Field-effect modulation of conductance in VO2 nanobeam transistors with HfO2 as the gate dielectric," Applied Physics Letters **99,** 062114 (2011).

[15] S. Populoh, P. Auban-Senzier, P. Wzietek, and C. Pasquier, "The power factor of Cr-doped V2O3 near the Mott transition," Applied Physics Letters **99,** 171902 (2011).

[16] Z. Zhang, Y. Gao, H. Luo, L. Kang, Z. Chen, J. Du, M. Kanehira, Y. Zhang, and Z. L. Wang, "Solution-based fabrication of vanadium dioxide on F:SnO2 substrates with largely

enhanced thermochromism and low-emissivity for energy-saving applications," Energy & Environmental Science **4,** 4290 (2011).

[17] A. Tselev, J. D. Budai, E. Strelcov, J. Z. Tischler, A. Kolmakov, and S. V. Kalinin, "Electromechanical Actuation and Current-Induced Metastable States in Suspended Single-Crystalline VO(2) Nanoplatelets.," Nano letters **11,** 3065–73 (2011).

[18] N. Ni, S. Lozano-Perez, J. Sykes, and C. Grovenor, "Quantitative EELS analysis of zirconium alloy metal/oxide interfaces.," Ultramicroscopy **111,** 123–30 (2011).

[19] F. Rivera, L. Burk, R. Davis, and R. Vanfleet, "Electron back-scattered diffraction of crystallized vanadium dioxide thin films on amorphous silicon dioxide," Thin Solid Films **520,** 2466–2461 (2011).

[20] G. Jiang, F. Rivera, S. S. Kanyal, R. C. Davis, R. Vanfleet, B. M. Lunt, and M. R. Linford, "Analysis of the plastic substrates, the reflective layers, and the adhesives of today's archival-grade DVDs," In *SPIE Proceedings Paper*, **7730,** 77301N–77301N–8 (SPIE, 2010).

[21] G. Jiang, F. Rivera, S. S. Kanyal, R. C. Davis, R. Vanfleet, B. M. Lunt, V. Shutthanandan, and M. R. Linford, "Characterization of the plastic substrates, the reflective layers, the adhesives, and the grooves of today's archival-grade recordable DVDs," Optical Engineering **50,** 015201 (2011).

[22] S. Kachi, T. Takada, and K. Kosuge, "Electrical Conductivity of Vanadium Oxides," Journal of the Physical Society of Japan **18,** 1839–1840 (1963).

[23] A. Zylbersztejn, "Metal-insulator transition in vanadium dioxide," Physical Review B **11,** 4383–4395 (1975).

[24] R. M. Wentzcovitch, "VO_2: Peierls or Mott-Hubbard? A view from band theory," Physical Review Letters **72,** 3389–3392 (1994).

[25] V. Eyert, "The metal-insulator transitions of VO2: A band theoretical approach," Annalen der Physik **11,** 650–704 (2002).

[26] A. Liebsch, H. Ishida, and G. Bihlmayer, "Coulomb correlations and orbital polarization in the metal-insulator transition of VO2,", 2005.

[27] S. Biermann, A. I. Poteryaev, A. I. Lichtenstein, and A. Georges, "Dynamical singlets and correlation-assisted Peierls transition in VO2," Physical Review Letters **94,** 5 (2004).

[28] P. P. Boriskov, A. A. Velichko, A. L. Pergament, G. B. Stefanovich, and D. G. Stefanovich, "The effect of electric field on metal-insulator phase transition in vanadium dioxide," Technical Physics Letters **28,** 406–408 (2002).

[29] W. Yin, S. Wolf, C. Ko, S. Ramanathan, and P. Reinke, "Nanoscale probing of electronic band gap and topography of VO[sub 2] thin film surfaces by scanning tunneling microscopy," Journal of Applied Physics **109,** 024311 (2011).

[30] M. M. Qazilbash, K. Burch, D. Whisler, D. Shrekenhamer, B.-G. Chae, H. Kim, and D. N. Basov, "Correlated metallic state of vanadium dioxide," Physical Review B **74,** 5 (2006).

[31] U. Schwingenschlögl and V. Eyert, "The vanadium Magnéli phases VnO2n-1," Annalen der Physik **13,** 475–510 (2004).

[32] K. Kosuge, "The phase diagram and phase transition of the V_2O_3 - V_2O_5, system," Journal of Physics and Chemistry of Solids **28,** 1613–1621 (1967).

[33] R. E. Loehman, C. N. R. Rao, and J. M. Honig, "Crystallography and defect chemistry of solid solutions of vanadium and titanium oxides," The Journal of Physical Chemistry **73,** 1781–1784 (1969).

[34] M. Morinaga and J. B. Cohen, "The defect structure of VOx. I. The ordered phase, VO1.30," Acta Crystallographica Section A: Crystal Physics, Diffraction, Theoretical and General Crystallography **35,** 745–756 (1979).

[35] ASM International, in *Binary Alloy Phase Diagrams*, 2 ed., T. B. Massalski and H. Okamoto, eds., (ASM International, Materials Park, OH, Materials Park, OH, 1990).

[36] H. Katzke, P. Tolédano, and W. Depmeier, "Theory of morphotropic transformations in vanadium oxides," Physical Review B 68 (2003).

[37] K. Kosuge, S. Kachi, H. Nagasaki, and S. Minomura, "Phase Transition in V 6 O 13," Journal of the Physical Society of Japan **20,** 178–179 (1965).

[38] K. Kosuge, H. Okinaka, and S. Kachi, "Metal insulator phase transition and magnetic properties of V_nO_{2n-1}," IEEE Transactions on Magnetics **8,** 581–583 (1972).

[39] S. Horiuchi, M. Saeki, Y. Matsui, and F. Nagata, "Transition of V6O13 to VO2 observed with a high-resolution electron microscope," Acta Crystallographica Section A: Crystal Physics, Diffraction, Theoretical and General Crystallography **31,** 660–664 (1975).

[40] "Inorganic Crystal Structure Database,".

[41] M. Marezio, D. McWhan, J. Remeika, and P. Dernier, "Structural Aspects of the Metal-Insulator Transitions in Cr-Doped VO2," Physical Review B **5,** 2541–2551 (1972).

[42] J. M. Longo, P. Kierkegaard, C. J. Ballhausen, U. Ragnarsson, S. E. Rasmussen, E. Sunde, and N. A. Sø rensen, "A Refinement of the Structure of VO2.," Acta Chemica Scandinavica **24,** 420–426 (1970).

[43] G. Grymonprez, L. Fiermans, and J. Venink, "Structural properties of vanadium oxides," Acta Crystallographica Section A **33,** 834–837 (1977).

[44] G. Andersson, C. Parck, U. Ulfvarson, E. Stenhagen, and B. Thorell, "Studies on Vanadium Oxides. II. The Crystal Structure of Vanadium Dioxide.," Acta Chemica Scandinavica **10,** 623–628 (1956).

[45] T. Maruyama and Y. Ikuta, "Vanadium dioxide thin films prepared by chemical vapour deposition from vanadium(III) acetylacetonate," Journal of Materials Science **28,** 5073–5078 (1993).

[46] H. Verleur, A. Barker, and C. Berglund, "Optical Properties of VO2 between 0.25 and 5 eV," Physical Review **172,** 788–798 (1968).

[47] S. Shin, S. Suga, M. Taniguchi, M. Fujisawa, H. Kanzaki, A. Fujimori, H. Daimon, Y. Ueda, K. Kosuge, and S. Kachi, "Vacuum-ultraviolet reflectance and photoemission study of the metal-insulator phase transitions in VO2, V6O13, and V2O3," Physical Review B **41,** 4993–5009 (1990).

[48] K. A. Khan and M. S. Rahman Khan, "Preparation and properties of vanadium dioxide thermochromic thin films," Pramana **38,** 389–396 (1992).

[49] M. Lee, "Better thermochromic glazing of windows with anti-reflection coating," Thin Solid Films **365,** 5–6 (2000).

[50] C. H. Koo, J. S. Lee, M. W. Kim, Y. J. Chang, T. W. Noh, J. H. Chae, B. G. Jung, and H. T. Kim, "Optical investigations on electronic structure changes related to the metal-insulator transition in VO2 film,", 2005.

[51] Y. Dachuan, X. Niankan, Z. Jingyu, and Z. Xiulin, "Vanadium dioxide films with good electrical switching property," Journal of Physics D: Applied Physics **29,** 1051–1057 (1996).

[52] H. Schlag, "New sputter process for VO2 thin films and examination with MIS-elements and C-V-measurements," Thin Solid Films **366,** 28–31 (2000).

[53] D. McWhan, M. Marezio, J. Remeika, and P. Dernier, "X-ray diffraction study of metallic VO_2," Physical Review B **10,** 490–495 (1974).

[54] D. Watanabe, B. Andersson, J. Gjø nnes, and O. Terasaki, "Determination of structure factors of disordered vanadium monoxide crystals by the intersecting-Kikuchi-line and critical-voltage methods," Acta Crystallographica Section A **30,** 772–776 (1974).

[55] D. Kucharczyk and T. Niklewski, "Accurate X-ray determination of the lattice parameters and the thermal expansion coefficients of VO 2 near the transition temperature," Journal of Applied Crystallography **12,** 370–373 (1979).

[56] R. Lopez, T. Haynes, L. A. Boatner, L. C. Feldman, and R. F. Haglund, "Size effects in the structural phase transition of VO2 nanoparticles," Physical Review B **65,** 1–5 (2002).

[57] T. Mitsuishi, "On the Phase Transformation of VO 2," Japanese Journal of Applied Physics **6,** 1060–1071 (1967).

[58] M. S. Grinolds, V. A. Lobastov, J. Weissenrieder, and A. H. Zewail, "Four-dimensional ultrafast electron microscopy of phase transitions.," Proceedings of the National Academy of Sciences of the United States of America **103,** 18427–31 (2006).

[59] A. Tselev, I. A. Luk'yanchuk, I. N. Ivanov, J. D. Budai, J. Z. Tischler, E. Strelcov, A. Kolmakov, and S. V. Kalinin, "Symmetry relationship and strain-induced transitions between insulating M1 and M2 and metallic R phases of vanadium dioxide.," Nano letters **10,** 4409–16 (2010).

[60] J. Wei, Z. Wang, W. Chen, and D. H. Cobden, "New aspects of the metal-insulator transition in single-domain vanadium dioxide nanobeams.," Nature nanotechnology **4,** 420–4 (2009).

[61] X. Wang, "XRD and Raman study of vanadium oxide thin films deposited on fused silica substrates by RF magnetron sputtering," Applied Surface Science **177,** 8–14 (2001).

[62] B. J. Campbell, H. T. Stokes, D. E. Tanner, and D. M. Hatch, "ISODISPLACE : a web-based tool for exploring structural distortions," Journal of Applied Crystallography **39,** 607–614 (2006).

[63] J. M. Gregg and R. M. Bowman, "The effect of applied strain on the resistance of VO_2 thin films," Applied Physics Letters **71,** 3649 (1997).

[64] A. Cavalleri, T. Dekorsy, H. Chong, J.-C. Kieffer, and R. Schoenlein, "Evidence for a structurally-driven insulator-to-metal transition in VO2: A view from the ultrafast timescale," Physical Review B **70,** 161102 (2004).

[65] R. Lopez, L. A. Boatner, T. E. Haynes, R. F. Haglund, and L. C. Feldman, "Enhanced hysteresis in the semiconductor-to-metal phase transition of VO_2 precipitates formed in SiO_2 by ion implantation," Applied Physics Letters **79,** 3161 (2001).

[66] A. Cavalleri, C. Tóth, C. Siders, J. Squier, F. Ráksi, P. Forget, and J.-C. Kieffer, "Femtosecond Structural Dynamics in VO2 during an Ultrafast Solid-Solid Phase Transition," Physical Review Letters **87,** 237401 (2001).

[67] T. Christmann, "Thermochromic VO2 thin films studied by photoelectron spectroscopy," Thin Solid Films **287,** 134–138 (1996).

[68] S. Chen, H. Ma, X. Yi, H. Wang, X. Tao, M. Chen, X. Li, and C. Ke, "Optical switch based on vanadium dioxide thin films," Infrared Physics & Technology **45,** 239–242 (2004).

[69] L. Q. Mai, C. Wen, P. Qing, J. F. Peng, Q. Y. Zhu, and Y. Hua, "Synthesis and switching property of vanadium dioxide nanorods," Rare Metal Materials And Engineering **32,** 748–751 (2003).

[70] W. Xue-Jin, L. Chun-Jun, G. Kang-Ping, L. De-Hua, N. Yu-Xin, Z. Shi-Oiu, H. Feng, Z. Wei-Wei, and C. Zheng-Wei, "Surface oxidation of vanadium dioxide films prepared by radio frequency magnetron sputtering," Chinese Physics B **17,** 3512–3515 (2008).

[71] D. Ruzmetov, S. Senanayake, and S. Ramanathan, "X-ray absorption spectroscopy of vanadium dioxide thin films across the phase-transition boundary," Physical Review B **75,** 1–7 (2007).

[72] C. S. Blackman, C. Piccirillo, R. Binions, and I. P. Parkin, "Atmospheric pressure chemical vapour deposition of thermochromic tungsten doped vanadium dioxide thin films for use in architectural glazing," Thin Solid Films **517,** 4565–4570 (2009).

[73] M. Nazari, C. Chen, A. A. Bernussi, Z. Y. Fan, and M. Holtz, "Effect of free-carrier concentration on the phase transition and vibrational properties of VO2," Applied Physics Letters **99,** 071902 (2011).

[74] W. Yin, K. G. West, J. W. Lu, Y. Pei, S. A. Wolf, P. Reinke, and Y. Sun, "The metal-insulator transition in vanadium dioxide: A view at bulk and surface contributions for thin films and the effect of annealing," Journal of Applied Physics **105,** 114322 (2009).

[75] T. D. Manning, I. P. Parkin, M. E. Pemble, D. Sheel, and D. Vernardou, "Intelligent Window Coatings: Atmospheric Pressure Chemical Vapor Deposition of Tungsten-Doped Vanadium Dioxide," Chemistry of Materials **16,** 744–749 (2004).

[76] R. Binions, C. Piccirillo, and I. P. Parkin, "Tungsten doped vanadium dioxide thin films prepared by atmospheric pressure chemical vapour deposition from vanadyl acetylacetonate and tungsten hexachloride," Surface and Coatings Technology **201,** 9369–9372 (2007).

[77] B. Felde, W. Niessner, D. Schalch, A. Scharmann, and M. Werling, "Plasmon excitation in vanadium dioxide films," Thin Solid Films **305,** 61–65 (1997).

[78] M. Gatti, F. Bruneval, V. Olevano, and L. Reining, "Understanding Correlations in Vanadium Dioxide from First Principles," Physical Review Letters **99,** 266402 (2007).

[79] R. J. O. Mossanek and M. Abbate, "Optical response of metallic and insulating VO 2 calculated with the LDA approach," Journal of Physics: Condensed Matter **19,** 346225 (2007).

[80] Y. Wang, Z. Zhang, Y. Zhu, Z. Li, R. Vajtai, L. Ci, and P. M. Ajayan, "Nanostructured VO2 photocatalysts for hydrogen production.," ACS nano **2,** 1492–6 (2008).

[81] E. E. Chain, "Optical properties of vanadium dioxide and vanadium pentoxide thin films," Applied Optics **30,** 2782 (1991).

[82] S. B. Choi *et al.*, "Nanopattern enabled terahertz all-optical switching on vanadium dioxide thin film," Applied Physics Letters **98,** 071105 (2011).

[83] R. S. Rana, D. D. Nolte, and F. A. Chudnovski, "Optical bistability from a thermodynamic phase transition in vanadium dioxide," Optics Letters **17,** 1385 (1992).

[84] M. Soltani, M. Chaker, E. Haddad, R. V. Kruzelecky, and D. Nikanpour, "Optical switching of vanadium dioxide thin films deposited by reactive pulsed laser deposition," Journal of Vacuum Science & Technology A: Vacuum, Surfaces, and Films **22,** 859 (2004).

[85] J. M. Tomczak and S. Biermann, "Materials Design using Correlated Oxides: Optical Properties of Vanadium Dioxide," EPL (Europhysics Letters) **86,** 37004 (2008).

[86] E. Donev, J. Suh, F. Villegas, R. Lopez, R. F. Haglund, and L. C. Feldman, "Optical properties of subwavelength hole arrays in vanadium dioxide thin films," Physical Review B **73,** 2–5 (2006).

[87] F. Mendoza and F. Fernandez, "Electrical properties of VO2 thin films grown by PLD," In *2008 17th IEEE International Symposium on the Applications of Ferroelectrics*, pp. 1–2 (IEEE, 2008).

[88] H. Li, N. Wang, and X. Liu, "Optical and electrical properties of Vanadium doped Indium oxide thin films," Optics Express **16,** 194 (2008).

[89] B.-G. Chae and H. T. Kim, "Effects of W doping on the metal-insulator transition in vanadium dioxide film," Physica B: Condensed Matter **405,** 663–667 (2010).

[90] C. Ko and S. Ramanathan, "Stability of electrical switching properties in vanadium dioxide thin films under multiple thermal cycles across the phase transition boundary," Journal of Applied Physics **104,** 086105 (2008).

[91] A. Rata, A. Chezan, M. Haverkort, H. Hsieh, H.-J. Lin, C. Chen, L. Tjeng, and T. Hibma, "Growth and properties of strained VOx thin films with controlled stoichiometry," Physical Review B **69,** 75404 (2004).

[92] F. Dejene and R. Ocaya, "Electrical, optical and structural properties of pure and gold-coated VO2 thin films on quartz substrate," Current Applied Physics **10,** 508–512 (2010).

[93] B. Chen, D. Yang, P. A. Charpentier, and M. Zeman, "Al3+-doped vanadium dioxide thin films deposited by PLD," Solar Energy Materials and Solar Cells **93,** 1550–1554 (2009).

[94] R. Lopez, L. A. Boatner, T. E. Haynes, L. C. Feldman, and R. F. Haglund, "Synthesis and characterization of size-controlled vanadium dioxide nanocrystals in a fused silica matrix," Journal of Applied Physics **92,** 4031 (2002).

[95] R. Lopez, L. A. Boatner, T. E. Haynes, R. F. Haglund, and L. C. Feldman, "Switchable reflectivity on silicon from a composite VO[sub 2]-SiO[sub 2] protecting layer," Applied Physics Letters **85,** 1410 (2004).

[96] M. Borek, F. Qian, V. Nagabushnam, and R. K. Singh, "Pulsed laser deposition of oriented VO2 thin films on R-cut sapphire substrates," Applied Physics Letters **63,** 3288 (1993).

[97] B.-G. Chae, D. H. Youn, H. T. Kim, S. Y. Maeng, and K.-Y. Kang, "Fabrication and Electrical Properties of Pure VO2 Phase Films," Science **44,** 5 (2003).

[98] S. I. Wright, M. M. Nowell, and D. P. Field, "A review of strain analysis using electron backscatter diffraction.," Microscopy and microanalysis : the official journal of Microscopy Society of America, Microbeam Analysis Society, Microscopical Society of Canada **17,** 316–29 (2011).

[99] D. B. Williams and C. B. Carter, *Transmission Electron Microscopy: a textbook for materials science* (Springer, 1996).

[100] EDAX, TSL, and AMETEK, "Introduction to OIM Analysis,", Training in PDF form, 2006.

[101] R. P. Goehner and J. R. Michael, "Phase Identification in a Scanning Electron Microscope Using Backscattered Electron Kikuchi Patterns," Journal of Research of the National Institute of Standards and Technology **101,** 301–308 (1996).

[102] J. K. Farrer, Ph.D. thesis, University of Minnesota, 2004.

[103] B. Yao, R. V. Petrova, R. R. Vanfleet, and K. R. Coffey, "A modified back-etch method for preparation of plan-view high-resolution transmission electron microscopy samples.," Journal of electron microscopy **55,** 209–14 (2006).

[104] K. Biswas and S. Kal, "Etch characteristics of KOH, TMAH and dual doped TMAH for bulk micromachining of silicon," Microelectronics Journal **37,** 519–525 (2006).

[105] B. Yao and K. R. Coffey, "Back-etch method for plan view transmission electron microscopy sample preparation of optically opaque films.," Journal of electron microscopy **57,** 47–52 (2008).

[106] L. A. Giannuzzi, "A review of focused ion beam milling techniques for TEM specimen preparation," Micron **30,** 197–204 (1999).

[107] D. Longo, "Experimental method for determining Cliff-Lorimer factors in transmission electron microscopy (TEM) utilizing stepped wedge-shaped specimens prepared by focused ion beam (FIB) thinning," Ultramicroscopy **80,** 85–97 (1999).

[108] P. M. Nellen, V. Callegari, and U. Sennhauser, "Preparative Methods for Nanoanalysis of Materials with Focused Ion Beam Instruments," CHIMIA International Journal for Chemistry **60,** 735–741 (2006).

[109] D. J. Stokes, F. Morrissey, and B. H. Lich, "A New Approach to Studying Biological and Soft Materials Using Focused Ion Beam Scanning Electron Microscopy (FIB SEM)," Journal of Physics: Conference Series **26,** 50–53 (2006).

[110] J. Li, T. Malis, and S. Dionne, "Recent advances in FIB-TEM specimen preparation techniques," Materials Characterization **57,** 64–70 (2006).

[111] S. Bals, W. Tirry, R. Geurts, Z. Yang, and D. Schryvers, "High-quality sample preparation by low kV FIB thinning for analytical TEM measurements.," Microscopy and microanalysis : the official journal of Microscopy Society of America, Microbeam Analysis Society, Microscopical Society of Canada **13,** 80–6 (2007).

[112] P. R. Munroe, "The application of focused ion beam microscopy in the material sciences," Materials Characterization **60,** 2–13 (2009).

[113] L. Repetto, R. Buzio, C. Denurchis, G. Firpo, E. Piano, and U. Valbusa, "Fast three-dimensional nanoscale metrology in dual-beam FIB-SEM instrumentation.," Ultramicroscopy **109,** 1338–42 (2009).

[114] F. Schmidt, M. Kühbacher, U. Gross, A. Kyriakopoulos, H. Schubert, and R. Zehbe, "From 2D slices to 3D volumes: image based reconstruction and morphological characterization of hippocampal cells on charged and uncharged surfaces using FIB/SEM serial sectioning.," Ultramicroscopy **111,** 259–66 (2011).

[115] M. Cantoni, in *Carbon*, N. Yao, ed., (Cambridge University Press, Cambridge, 2007).

[116] P. E. Russell and F. A. Stevie, "Focused Ion Beam (FIB) Microscopy and Technology," Microscopy and Microanalysis **8,** 558–559 (2002).

[117] J. Melngailis, "Focused ion beam lithography," Nuclear Instruments and Methods in Physics Research Section B: Beam Interactions with Materials and Atoms **80-81,** 1271–1280 (1993).

[118] C. A. Volkert and A. M. Minor, "Focused Ion Beam Microscopy and Micromachining," MRS Bulletin **32,** 389–399 (2007).

[119] S. Yogev, J. Levin, M. Molotskii, A. Schwarzman, O. Avayu, and Y. Rosenwaks, "Charging of dielectrics under focused ion beam irradiation," Journal of Applied Physics **103,** 064107 (2008).

[120] S. Matsui and Y. Ochiai, "Focused ion beam applications to solid state devices," Nanotechnology **7,** 247–258 (1996).

[121] S. Nagamachi, Y. Yamakage, M. Ueda, H. Maruno, and J. Ishikawa, "Focused ion-beam direct deposition of metal thin film," Review of Scientific Instruments **67,** 2351 (1996).

[122] P. E. Russell, "Chemically and geometrically enhanced focused ion beam micromachining," Journal of Vacuum Science & Technology B: Microelectronics and Nanometer Structures **16,** 2494 (1998).

[123] R. Nassar, "Mathematical modeling of focused ion beam microfabrication," Journal of Vacuum Science & Technology B: Microelectronics and Nanometer Structures **16,** 109 (1998).

[124] T. Fujii, K. Iwasaki, M. Munekane, T. Takeuchi, M. Hasuda, T. Asahata, M. Kiyohara, T. Kogure, Y. Kijima, and T. Kaito, "A nanofactory by focused ion beam," Journal of Micromechanics and Microengineering **15,** S286–S291 (2005).

[125] A. Latif, Ph.D. thesis, 2005.

[126] R. M. Langford, "Focused Ion Beam Nanofabrication: A Comparison with Conventional Processing Techniques," Journal of Nanoscience and Nanotechnology **6,** 661–668 (2006).

[127] A. Biance, J. Gierak, E. Bourhis, A. Madouri, X. Lafosse, G. Patriarche, G. Oukhaled, C. Ulysse, J. Galas, and Y. Chen, "Focused ion beam sculpted membranes for nanoscience tooling," Microelectronic Engineering **83,** 1474–1477 (2006).

[128] D. J. Stokes, O. Wilhelmi, S. Reyntjens, C. Jiao, and L. Roussel, "New Methods for the Study and Fabrication of Nano-Structured Materials Using FIB SEM," Journal of Nanoscience and Nanotechnology **9,** 1268–1271 (2009).

[129] R. W. Tjerkstra, F. B. Segerink, J. J. Kelly, and W. L. Vos, "Fabrication of three-dimensional nanostructures by focused ion beam milling," Journal of Vacuum Science & Technology B: Microelectronics and Nanometer Structures **26,** 973 (2008).

[130] M. M. Da Silva, A. R. Vaz, S. A. Moshkalev, and J. W. Swart, "Electrical Characterization of Platinum Thin Films Deposited by Focused Ion Beam," In *ECS Transactions*, **9,** 235–241 (ECS, 2007).

[131] D. A. M. de Winter and J. J. L. Mulders, "Redeposition characteristics of focused ion beam milling for nanofabrication," Journal of Vacuum Science & Technology B: Microelectronics and Nanometer Structures **25,** 2215 (2007).

[132] S. Kim, M. Jeong Park, N. P. Balsara, G. Liu, and A. M. Minor, "Minimization of focused ion beam damage in nanostructured polymer thin films.," Ultramicroscopy **111,** 191–9 (2011).

[133] A. G. Cullis and P. D. Augustus, *Microscopy of Semiconducting Materials* (CRC Press, 1987).

[134] Yue Kuo, *Thin Film Transistors: Materials and Processes*, 1 ed. (Springer, 2003).

[135] Robert A. Street, *Technology and Applications of Amorphous Silicon* (Springer, 2000).

[136] R. Keller, "EBSD measurement of strains in GaAs due to oxidation of buried AlGaAs layers*1," Microelectronic Engineering **75,** 96–102 (2004).

[137] J. K. Farrer, C. B. Carter, and N. Ravishankar, "The effects of crystallography on grain-boundary migration in alumina," Journal of Materials Science **41,** 661–674 (2006).

[138] A. Cavalleri, "Chemistry. All at once.," Science (New York, N.Y.) **318,** 755–6 (2007).

[139] A. Barker, H. Verleur, and H. Guggenheim, "Infrared Optical Properties of Vanadium Dioxide Above and Below the Transition Temperature," Physical Review Letters **17,** 1286–1289 (1966).

[140] A. S. Belozerov, A. I. Poteryaev, and V. I. Anisimov, "Evidence for strong Coulomb correlations in metallic phase of vanadium dioxide," p. 6 (2010).

[141] E. B. Shadrin, "On the Nature of Metal-Semiconductor Phase Transition in Vanadium Dioxide," Physics of the Solid State **42,** 1126 (2000).

[142] S. Westman, I. Lindqvist, B. Sparrman, G. B. Nielsen, H. Nord, and A. Jart, "Note on a Phase Transition in VO2.," Acta Chemica Scandinavica **15,** 217–217 (1961).

[143] J. Brews, "Symmetry Considerations and the Vanadium Dioxide Phase Transition," Physical Review B **1,** 2557–2568 (1970).

[144] R. Heckingbottom and J. W. Linnett, "Structure of Vanadium Dioxide," Nature **194,** 678–678 (1962).

[145] J. Cao *et al.*, "Extended mapping and exploration of the vanadium dioxide stress-temperature phase diagram.," Nano letters **10,** 2667–73 (2010).

[146] B. Hu, Y. Zhang, W. Chen, C. Xu, and Z. L. Wang, "Self-heating and External Strain Coupling Induced Phase Transition of VO(2) Nanobeam as Single Domain Switch.," Advanced materials (Deerfield Beach, Fla.) **23,** 3536–41 (2011).

[147] B.-G. Chae, H.-T. Kim, S.-J. Yun, B.-J. Kim, Y.-W. Lee, D.-H. Youn, and K.-Y. Kang, "Highly Oriented VO_2 Thin Films Prepared by Sol-Gel Deposition," Electrochemical and Solid-State Letters **9,** C12 (2006).

[148] D. H. Kim and H. S. Kwok, "Pulsed laser deposition of VO2 thin films," Applied Physics Letters **65,** 3188 (1994).

[149] P. Mandal, A. Speck, C. Ko, and S. Ramanathan, "Terahertz spectroscopy studies on epitaxial vanadium dioxide thin films across the metal-insulator transition," Optics Letters **36,** 1927 (2011).

[150] H. C. Floresca, J. Jeon, J. G. Wang, and M. J. Kim, "The focused ion beam fold-out: sample preparation method for transmission electron microscopy.," Microscopy and microanalysis : the official journal of Microscopy Society of America, Microbeam Analysis Society, Microscopical Society of Canada **15,** 558–63 (2009).

[151] B. Schaffer, C. Mitterbauer, A. Schertel, A. Pogantsch, S. Rentenberger, E. Zojer, and F. Hofer, "Cross-section analysis of organic light-emitting diodes.," Ultramicroscopy **101,** 123–8 (2004).

[152] R. Spoenak, L. Sauter, and C. Eberl, "Reversible orientation-biased grain growth in thin metal films induced by a focused ion beam," Scripta Materialia **53,** 1291–1296 (2005).

[153] I. W. Hamley and V. Castelletto, "Biological soft materials.," Angewandte Chemie (International ed. in English) **46,** 4442–55 (2007).

[154] A. Minor, "FIB Sample Preparation of Thin Films and Soft Materials," Microscopy and Microanalysis **15,** 1544 (2009).

[155] D. D. Winter, C. Schneijdenberg, M. Lebbink, L. Hekking, J. Post, B. Lich, A. Verkleij, M. Drury, and B. Humbel, "Tomography of Biological Materials using Focused Ion Beam Sectioning and Backscattered Electron Imaging," Microscopy and Microanalysis **15,** 576 (2009).

[156] S. Kooi, "Focused Ion Beam Processing of Polymeric Materials for Analytical Sample Preparation," Microscopy and Microanalysis **14,** 688–689 (2008).

[157] S. Magni, M. Milani, C. Riccardi, and F. Tatti, "FIB/SEM characterization of carbon-based fibers.," Scanning **29,** 185–95 (2007).

[158] M.-W. Moon, J. H. Han, A. Vaziri, E. K. Her, K. H. Oh, K.-R. Lee, and J. W. Hutchinson, "Nanoscale ripples on polymers created by a focused ion beam.," Nanotechnology **20,** 115301 (2009).

[159] M. Mon, S. Lee, J. Sun, K. Oh, A. Vaziri, and J. W. Hutchinson, "Controlled formation of nanoscale wrinkling patterns on polymers using focused ion beam," Scripta Materialia **57,** 747–750 (2007).

[160] B. L. Peterson, P. D, and P. A. Development, "TEM Sample Preparation Tips,", 2007.

[161] P. ThangaduraiI, Y. Lumelsky, M. Silverstein, and W. Kaplan, "TEM specimen preparation of semiconductor-PMMA-metal interfaces," Materials Characterization **59,** 1623–1629 (2008).

[162] L. E. Thompson, P. M. Rice, E. Delenia, V. Y. Lee, P. J. Brock, T. P. Magbitang, G. Dubois, W. Volksen, R. D. Miller, and H.-C. Kim, "Imaging thin films of nanoporous low-k dielectrics: comparison between ultramicrotomy and focused ion beam preparations for transmission electron microscopy.," Microscopy and microanalysis : the official journal of Microscopy Society of America, Microbeam Analysis Society, Microscopical Society of Canada **12,** 156–9 (2006).

[163] C. Aubry, "Polymer gratings achieved by focused ion beam," Synthetic Metals **127,** 307–311 (2002).

[164] H. T. Stokes, D. M. Hatch, and B. J. Campbell, "ISOTROPY,", stokes.byu.edu/isotropy.html, 2007.

Index